On the Use of Indentation Technique to Assess Fracture Properties of Ceramics at the Microscale

Nathalie Payraudeau

A thesis submitted to the University of Dublin in partial fulfilment of the requirements for the degree of

Doctor in Philosophy

School of Engineering
Trinity College Dublin
Ireland

September 2010

Supervisor
Dr. Kevin U. O'Kelly

Internal Examiner
Prof. David Taylor

External Examiner
Prof. Michael Pomeroy

Declaration

I declare that I am the sole author of this thesis and that all the work presented within, unless otherwise referenced, is my own. I also declare that this work has not been submitted, in whole or in part, to any other university or college for a degree or other qualification.

I authorize the library of Trinity College Dublin to lend or copy this thesis on request.

Nathalie Payraudeau
September 2010

Contents

List of Figures

List of Tables

Nomenclature & Abbreviations

Symbol	Definition	Unit
γ	Specific surface energy	J/m^2
ν	Poisson's ratio	non-dimensional
σ	Stress	Pa
σ_c	Fracture stress	Pa
σ_y	Yield stress	Pa
c	Crack length	μm
E	Young's modulus	GPa
E_d	Densification energy	J
E_f	Fracture energy	J
E_p	Plastic energy coming from dislocation movements	J
G	Strain energy release rate	J/m^2
G_c	Critical strain energy release rate	J/m^2
H	Hardness	GPa
J	J-integral	J/m^2
K	Stress intensity factor	$MPa.m^{1/2}$
K_I , K_{II} and K_{III}	Stress intensity factor in modes I, II and III	$MPa.m^{1/2}$
K_c	Fracture toughness	$MPa.m^{1/2}$
P	Porosity	%
R	Crack resistance energy	J/m^2
$\dot{S}$	Entropy creation rate	J/(K.s)
U	Total energy	J
U_A	Potential energy	J
U_E	Strain potential energy	J
U_M	Mechanical energy	J
U_S	Energy associated with the formation of new surfaces	J

Nanoindentation		
Symbol	**Definition**	**Unit**
α	Equivalent cone angle	°
θ	Half-included angle	°
A	Contact area	nm^2
a	Half indent size	nm
E^*	Reduced elastic modulus	GPa
h	Displacement	nm
h_c	Contact depth	nm
h_f	Final residual depth	nm
h_{max}	Maximum penetration depth	nm
P	Indentation load	N
P_{max}	Maximum indentation load	N
S	Contact stiffness	N/m
W_e	Elastic part of the indentation work	J
W_p	Plastic part of the indentation work	J
W_{tot}	Total work of indentation	J

Abbreviations	
BE	Backscattered electrons
CDM	Continuous damage mechanics
CSM	Continuous stiffness measurement
CTOD	Crack tip opening displacement
CVD	Chemical vapor deposition
DL	Deep lateral crack
DM	Damage mechanics
E-SE	Electron induced secondary electron images
FE	Finite element
FM	Fracture mechanics
HCP	Hexagonal close packed
ICL	Indentation crack length
I-SE	Ion induced secondary electron images
ISE	Indentation size effect
ITT	Instrumented indentation testing,
LEFM	Linear elastic fracture mechanics
MEMS	Microelectromechanical systems
NEMS	Nanoelectromechanical systems
O&P	Oliver and Pharr
PHP	Partial half-penny crack
SL	Shallow lateral crack
SR	Shallow radial crack

Fracture toughness test methods	
Abbreviations	
CNB	Chevron notched beam
CT	Compact tension
DCB	Double cantilever beam
IF	Indentation fracture
IS	Indentation strength
SCF	Surface crack in flexure
SENB	Single-edge notched beam
SEPB	Single-edge precracked beam
SEVNB	Single-edge V-notched beam

Spectroscopy techniques	
Abbreviations	
AFM	Atomic force microscopy
EBSD	Electron backscatter diffraction
EDXS or EDX or EDS	Energy-dispersive X-ray
FIB	Focused ion beam
SEM	Scanning electron microscopy
SIMS	Secondary ion mass spectrometry
TEM	Transmission electron microscopy

Acknowledgements

I would first like to thank my supervisor Dr. Kevin O'Kelly for providing me with the opportunity to carry out research and for supporting me throughout with guidance and advice.

I would also like to thank Dr. Damien McGrouther from the University of Glasgow for his exhaustive help with the FIB. I have learnt a lot on this instrument from working with you.

Special thanks go to Dr. Warren McKenzie from Trinity College Dublin who was always useful to fix technical problems with the FIB.

I would like to express my gratitude to Prof. Dominique Schryvers and Ms Shanshan Cao from the University of Antwerp for their hospitality and useful advices during my stay in their laboratory.

My thanks also go to all technical staff of the Mechanical Engineering Department and especially to Peter O'Reilly, Mick Reilly and John Gaynor for helping me solving technical problems. I am also grateful to Joan Gillen, Nicole Byrne and Sheena Brown for aiding me through administrative tasks.

Many thanks to the other postgraduates and postdocs from the Department who made my time at Trinity so enjoyable. I would especially like to thank Iratxe, Gerardo, Kevin, Saeid, Pavel, Oana, Sergio, Eoghan, Martin, Thomas, Stephen, Darren and Tim for his useful tricks on the LaTex software. It was a pleasure working with you all.

I would also like to extend my sincere gratitude to my family who have encouraged me throughout the duration of this PhD.

Finally, I would like to express my heartfelt thanks to my boyfriend Denis for his unconditional support and encouragements throughout these years. Without your love and support, I am sure that I would not have been able to achieve so much.

This work was supported by SFI (Science Foundation Ireland).

The author also acknowledges financial support from the European Union under the Framework 6 program under a contract for an Integrated Infrastructure Initiative. Reference 026019 ESTEEM.

Publications and presentations resulting from this study

Publications:

Payraudeau, N., O'Kelly, K.U.: Scale effects in nano-indentation fracture of brittle ceramics arising from crack-microstructure interactions. *Proceedings of the International Conference on CRACK PATHS 2009.*

Arsecularatne, J. A., Hoffman, M., O'Kelly, K.U., Payraudeau, N. (submitted): FIB tomographic analysis of indents in porous alumina. *Journal of the American Ceramic Society.*

Payraudeau, N., McGrouther, D., O'Kelly, K.U. (submitted): Quantification of subsurface damage in a brittle insulating ceramic by 3D FIB tomography. *Microscopy and Microanalysis.*

Oral presentations:

NanoFIB 2009 (Royal Microscopical Society), Oxford (UK), 16 March 2009.

SF2M JA2009, Rennes (France), 17-19 June 2009.

International Conference on CRACK PATHS 2009, Vicenza (Italy), 23-25 September, 2009.

Abstract

Classic methods to determine fracture properties of ceramics (like Single-Edge Notched Beam or Compact Tension) are accurate at the macroscale but inappropriate to estimate local fracture properties which are decisive at the microscale. The inaccuracy of the indentation crack length method to characterize fracture resistance of ceramics at small scale highlights the need for an accurate method to estimate small scale fracture properties.

This project aimed to address how a material's resistance to fracture can be measured where bulk properties are uninformative. A new technique combining indentation, FIB tomography and 3D reconstruction of the subsurface cracks was implemented and tested on three ceramics with different microstructures. Indentation was used to simulate wear processes which are a huge issue for biomaterials. This technique also allowed assess to local Young's modulus and hardness, two parameters highly influenced by local microstructure. Several adjustments were made to the classical FIB tomography technique in order to overcome issues arising from dealing with highly insulating materials and to study subsurface cracks while causing minimal damage to the original cracks resulting from indentation. FIB tomography and reconstruction of subsurface cracks have permitted the assessment of the total crack surface area as well as some determining fracture parameters like crack size distribution and crack localization. This technique has thus showed its usefulness in comparing fracture behavior of different materials. Quantification of total crack surface area has revealed that this parameter is strongly correlated to the plastic energy dissipated during indentation. This indicates that indentation is a relevant tool for studying small scale fracture properties of ceramics as this technique can capture the total crack surface area which is one important local fracture property.

This work provides a significant contribution to the understanding of fracture resistance of ceramics at small scale. The technique developed in this project also represents an advance in the methods used to study crack-microstructure interactions and to design materials more resistant to fracture.

Chapter 1

Introduction

With the development of microelectromechanical systems (MEMS), nanoelectromechanical systems (NEMS) and small bioengineering devices, materials science is facing new difficulties in the mechanical characterization of the ceramics used in making these small components.

Mechanical properties of materials are well-known at the macroscale level, but some studies [1, 2] have pointed out the inaccuracy of conventional laws for fracture and deformation at small scale.

In fact, it is hypothesized that properties determined at a large scale, cannot be validly extrapolated to reduced characteristic dimensions. Properties at the microscale level (governed by discrete defects, i.e. dislocations, microcracks, microstructural interfaces) and at the nanoscale level (governed by interatomic force laws) are expected to be different from conventional responses at the macroscale (governed by continuum laws).

This is typical for MEMS devices which have different failure mechanisms than their macroscopic counterparts (for instance: by component degradation, charging, vibration...) [1]. Furthermore, as the surface/volume ratio increases, the balance between the competing classical forces will change. Micro-scale devices can have surface area to volume ratios as high as 1,000:1 and 10,000:1 which means that surface effects also have greater influence than in the bulk materials. These are also true for biomaterials as some contain very small components (vascular stents, tissue scaffolds....) where the characteristic dimension is at the same scale as the microstructural features.

Due to their characteristics and their low-cost fabrication processes at small scale, ceramics are interesting materials for uses in microelectromechanical systems (MEMS) and biomaterials.

MEMS are microelectromechanical systems comprising of micron-scale me-

chanical and electrical components. These three-dimensional micro devices can be designed for biological, chemical, optical or thermal applications and are used frequently as micro sensors. The term MEMS also refers to the fabrication processes that provide the means to build these devices with architecture ranging from 1 to 100 microns. MEMS are constructed using semiconductor fabrication processes that incorporate silicon, glass or other sacrificial substrate materials [3].

Since the 1990s, MEMS technology has been used to create a variety of industrial devices such as beams, gears, levers, switches, sensors, accelerometers, diaphragms, and heat controllers, all of them microscopic in size. The mechanical properties of ceramics and their resistance to corrosion at high temperatures make them highly suitable for MEMS applications [4, 3] as they can be used in severe environments or in high-speed devices such as nanoturbines.

Other reasons for using ceramics in MEMS design include their small-scale engineering-low-cost and their reliable mass-scale manufacturing processes. Typical ceramics used in MEMS are silicon, alumina, GaAs and SiO_2.

In the field of medical devices, ceramic-based biomaterials are becoming more and more important. A biomaterial is a synthetic or natural material used to replace part of a living system or to function in intimate contact with living tissue. Biomaterials are intended to interface with biological systems to evaluate, treat, augment or replace any tissue, organ or function of the body. Typically, inorganic (metals, ceramics, and glasses) and polymeric (synthetic and natural) materials have been used for such items as artificial heart-valves, (polymeric or carbon-based), synthetic blood-vessels, artificial hips (metallic or ceramic), medical adhesives, sutures, dental composites, and polymers for controlled slow drug delivery.

In general:

- Metallic biomaterials are used for load bearing applications and must have sufficient fatigue strength to endure the rigors of daily activity eg walking, chewing etc.

- Ceramic biomaterials are generally used for their hardness and wear resistance for applications such as articulating surfaces in joints and in teeth as well as bone bonding surfaces in implants.

- Polymeric materials are usually used for their flexibility and stability, but have also been used for low friction articulating surfaces.

The chemical inertness of ceramics makes them highly suitable for biological applications [5, 4]. Their thermal and chemical stability, their high strength,

wear resistance and durability all contribute to making ceramics good candidate materials for surgical implants. Their low friction coefficient and low wear rate compared to those of metallic materials (stainless steels, titanium and chromium-cobalt alloys) have made them widely used for orthopaedic prostheses. Some ceramics even feature drug-delivery capability (glass microspheres have been employed as delivery systems for radioactive therapeutic agents, for example). Materials for surgical implants and medical devices must, before all else, be non-toxic. Bioceramics meet that test, and can be, in addition bioinert, that is, not interactive with biological systems; bioactive, that is, durable materials that can undergo interfacial interactions with surrounding tissues; biodegradable, soluble, or resorbable (eventually replaced or incorporated into tissue). Furthermore, sugars and proteins can bind to some ceramics. The main ceramics used in biomaterials are alumina, zirconia, calcium phosphates like hydroxyapatite and bioactive glasses.

As ceramics used in MEMS and biomaterials exhibit a brittle fracture behavior, understanding the mechanisms of their fracture is of huge interest. In general, for brittle solids, fracture induced by crack propagation is the main cause of failure. MEMS perform mainly repeated mechanical actions, making them prone to fail by fracture and fatigue. Fracture is also one of the most frequent causes of degradation and failure of brittle biomaterials and it is of particular importance as in many clinical situations, a mechanical breakdown opens the path for biologically mediated failures.

As fracture toughness is an indication of the resistance of the material to fracture propagation, determining it is an essential step in materials design. Large scale determination of fracture toughness is usually done by one of the following methods:

- Single-Edge Precracked Beam (SEPB)
- Single-Edge Notched Beam (SENB)
- Single-Edge V-Notched Beam (SEVNB)
- Chevron Notched Beam (CNB)
- Surface Crack in Flexure (SCF)
- Indentation Strength (IS)
- Indentation fracture (IF)

However, measurement methods become a determining factor as one moves from bulk to micro levels. At small scales, lots of questions arise about the applicability of those methods due to the mismatch between the measurement scale and the fracture scale. Therefore relevance of classical fracture toughness models can be questioned at the microscale.

1.1 Size effects in mechanical properties

Several size effects (like the indentation size effect and the Hall-Petch effect) on mechanical properties have been widely commented in the literature.

Indentation Size Effect (ISE), whereby the hardness of materials increases significantly with decreasing indentation depths has been studied a lot in recent years [6–12]. This effect arises during indentation tests in the micrometer regime even for tests on homogeneous materials. Nix and Gao [6] have shown that ISE can be modeled using the concept of geometrically necessary dislocations, based on the theory of strain gradient plasticity on an idealized nanoindentation process. During indentation, as the indenter is forced into the surface, the amount of dislocation loops necessary to accommodate for the shape of the indenter (i.e. geometrically necessary dislocations) scales linearly with the contact area. However, plastic deformation is confined within a small volume which is assumed to have a hemispherical shape, which results in a strain gradient. The varying density of the geometrically necessary dislocations thus accounts for a size dependence of the plastic strain gradient; i.e. a smaller indent causes a larger strain gradient. Mirshams et al. [12] showed that the ISE is strongly related to each indenter's geometry and less sensitive to the indentation depth.

Another size effect on mechanical properties is the Hall-Petch relationship which describes an increase in yield strength with decreasing grain size. This is due to the fact that grain boundaries impede dislocation movement and that a larger applied stress is required to generate dislocations in the adjacent grains than within one grain. By changing grain size, dislocation movements can be influenced and yield strength as well. The Hall-Petch relation was experimentally found to be an effective model for materials within grain size ranging from 1 millimeter to 1 micrometer. Recent investigations [13, 14] have shown a Hall-Petch type dependence for hardness in alumina. Armstrong et al. [15] have also shown an increase in the indentation fracture mechanics stress intensity K with a decrease in grain size in accordance with a Hall-Petch type dependence at small crack sizes (although larger than the material grain size).

Below a critical grain-size in nanocrystalline materials (typically below 100 nm), the yield stress decreases with decreasing grain size. This is known as the inverse Hall-Petch effect and is thought to be due to dislocation absorption by grain boundaries [16].

1.2 Fracture properties at the microscale level

Unlike size effects on hardness or yield strength, no particular model seems to be able to describe fracture mechanics in brittle solids at the microscale level.

Microstructure has long been recognized as having a strong influence on fracture toughness [17, 18, 2, 19, 20] at small scales.

It also plays an important role in the variation of the toughness curves (R-curves) which plot a material's resistance to crack propagation as a function of crack extension [21–23].

Despite those studies, classical models designed at large scale for fracture toughness are still used at the microscale level.

The most popular model for the determination of fracture toughness by indentation is the one developed by Anstis et al [17].

However, at small scales, many assumptions of this model are not valid anymore. Indeed, this model assumes that the crack patterns remain geometrically well behaved at all times. Anstis et al. indicated that this assumption was not valid for all ceramics which, instead of being deformed readily at constant volume beneath the indenter, experience pile-up or densification. In these cases, the shape of the cracks as well as the size, may be significantly affected. More importantly, they showed that the coarseness of the microstructure influences a lot the value for fracture toughness when this coarseness is comparable with the size of the indentation.

This inaccuracy at small scale is valid for all the existing models based on indentation experiments. None of them takes into account material anisotropy or structural heterogeneity. At bulk level, it may be possible to assume that these local variations are 'averaged out' but these assumptions are not valid at micro- and nano-level and an explicit treatment of anisotropy and heterogeneity is required in any model for fracture toughness.

The fracture toughness models based on indentation experiments are also assuming the fact that material properties (i.e. hardness H and elastic modulus E) are homogeneous and isotropic which is not the case anymore at the microscale level. Some authors [24, 25] have analyzed results of nanoindentation experiments

on various brittle materials and concluded that H and E deduced from the analysis should be treated as the local, rather than the bulk mechanical properties of the test material.

The other assumptions of these models (symmetrical sub-surface stress fields, plastic deformation by shear along slip planes oriented at 45 °, the work done by an indenter equal to the work done against the shear yield strength on the shear planes) are also not valid at these scales because grain morphology and texture, and local compositional heterogeneity influence plasticity and create non-uniform stress fields.

Furthermore, surfaces dominate tribological properties of small scale materials and in particular, they affect the plastic response and the brittle or ductile behavior, leading to significant inaccuracies in the calculation of fracture toughness using conventional models.

Consequently, some work is still needed on the interaction between microstructure and fracture properties of brittle solids at the microscale level and on a possible method to measure them at this scale. This will have significant benefit for the design of MEMS and small biomaterials.

1.3 Focus of present investigation

This project aims to address how a material resistance to fracture can be measured where bulk properties are uninformative. It also aims to quantify the interaction between microstructure and fracture process in these ceramics at the microscale. In this work, the terms 'microscale' and 'small scale' refer to the scale of the microstructure.

The specific objectives of this work include:

- Elaboration of different microstructures by varying the size and the aspect ratio (the width of an object divided by its height) of the grains as well as the phase composition of the material investigated.

- Nanoindentation experiments on these different microstructures to induce cracks and to determine elastic and plastic deformations occurring when the indentation is performed. This will be useful for the understanding of indentation damage.

- Use of Scanning Electron Microscopy (SEM) to provide two-dimensional images of surface cracks, which could also be used to calculate fracture

toughness using conventional indentation fracture toughness models in a comparative purpose.

- Use of Focused Ion Beam (FIB) technique to investigate the three-dimensional morphology of the microstructure and the indentation cracks. The FIB will permit to cut and image cross-sections of indents. Using an image analysis software, serial reconstruction of the cracks and of the microstructure beneath the residual indent impression will then be done. This will permit to reveal the actual microstructure as well as the true crack path within the indent subsurface. Calculation of the crack surface area will also be carried out.

- Comparison of the results obtained with the stress fields given by a Finite Element model based on indentation deformation (another project currently carrying on in Trinity College).

- Comparison of the results between the different microstructures investigated.

Chapter 2

Literature review

Fracture properties of ceramics are well known at the macroscale level but still need some investigations at smaller scales where bulk properties are uninformative. This chapter presents a literature review of mechanics of fracture and highlight their inaccuracy at the microscale. Nanoindentation and Focused Ion Beam (FIB) techniques are then described as well as their applicability in the present study.

2.1 Fracture of brittle solids

Brittle fracture takes place without any appreciable deformation and by rapid crack propagation. This means that there is very little plastic deformation and low energy absorption by the material before failure occurs. If crack propagation corresponds to the successive and repeated breaking of atomic bonds along specific crystallographic planes, this process is termed cleavage and the fracture is said to be transgranular because the fracture cracks pass through the grains. This is the case for most brittle crystalline materials. If crack propagation occurs along grain boundaries, the fracture is termed intergranular and is frequent in weak grain boundary regions or when there are residual tensile stresses across these boundaries [26].

All brittle materials contain a population of small cracks and flaws (surface or interior cracks, internal pores, metallurgical inclusions, grain corners, etc), resulting from their fabrication and which are virtually impossible to all eliminate or control. These flaws act as stress raisers as an applied stress may be amplified or concentrated at the tip of the crack. The degree of stress amplification depends on crack length and tip radius of curvature.

Any fracture process consists of the initiation and propagation of cracks

through the material. Contrary to ductile fracture (characterized by extensive plastic deformation in the vicinity of an advancing crack), for brittle fracture, crack propagation, once started, will continue spontaneously without an increase in magnitude of the applied stress.

There are a large number of possible sources for crack nucleation: machining, impact, erosion, wear, thermal stress, microscopic residual stresses (due to the presence of voids, second-phase inclusions or anisotropy for instance) [27]. Smaller grain size, higher temperature, and lower stress tend to mitigate crack initiation. On the contrary, larger grain size, lower temperatures, and higher stress tend to favor crack propagation.

Two approaches are described in the literature for the analysis of brittle fracture: the Fracture Mechanics (FM) and the Damage Mechanics (DM) models.

2.1.1 Fracture mechanics approach

The FM approach considers the effects of a critical defect which leads to the material failure. The failure criterion is given by the critical strain energy release rate G_c (energy-based approach) or by the critical stress intensity factor K_c (stress-based approach).

2.1.1.1 Griffith's concept and evolution of the theory

The maximum strength expected from a material was first based on the strength of the atomic bonding. Considering two planes of atoms being pulled apart by a tensile stress, at some point, the stress will pass through a maximum as the interatomic forces are overcome. This maximum stress is defined as the theoretical cleavage stress and the strength associated is estimated as $E/10$ where E is the Young's Modulus.

In 1920, Griffith [28] postulated that materials already contain pre-existing flaws or cracks and that it is the stored elastic strain energy associated with these cracks that gives strengths less than the theoretical cleavage strength. Thus, fracture is seen not as the separation of two perfect crystal planes but as the extension of a pre-existing crack. Furthermore, the effect of a stress raiser is more significant in brittle than in ductile materials. For a ductile material, plastic deformation ensues when the maximum stress exceeds the yield strength. This leads to a more uniform distribution of stress in the vicinity of the stress raiser and to the development of a maximum stress concentration factor less than the theoretical value. Such yielding and stress redistribution do not occur to any appreciable

extent around flaws and discontinuities in brittle materials. Therefore, there is a high concentration of stress at the tip of the flaws and fracture occurs when the theoretical cohesive strength of the material is exceeded at this tip.

The work done by Griffith in the 1920s is considered as the first scientific basis for fracture as, in addition to his flaw hypothesis (pertaining to crack initiation), he formulated a criterion for a crack extension from the fundamental energy theorems of classical mechanics and thermodynamics.

He studied the effect of an isolated crack in soda-lime glass subjected to a uniform external load, and formulated the condition for its growth. Using Inglis mathematical equations for stress concentration in an elliptical cavity in a uniformly stressed plate [29], Griffith showed that for brittle materials, surface energy dissipated by forming new crack surfaces was equal to the resistance to the crack growth. This is known as the Griffith criterion:

$$\sigma_c = \sqrt{\frac{2E\gamma}{\pi a}} \tag{2.1}$$

where σ_c is the fracture stress (the critical stress required for crack propagation), γ is the specific surface energy and a is one half the length of an internal crack. This theory was only valid for brittle materials containing a sharp crack and for which there was no plastic deformation. In fact, most metals and many polymers do experience some plastic deformation during fracture; thus crack extension involves more than producing just an increase in surface energy. Furthermore, it was difficult to measure γ from fracture tests because values found were generally much higher than the surface energy.

In 1930, Obreimoff [30] studied the fracture of mica and observed that the value of γ was dependent on the test environment. He showed that fracture was not really an equilibrium process, as treated by Griffith, but that other energy dissipation processes must be present when one forms a fracture surface in a ceramic. These dissipation mechanisms may include acoustic emission, heat generation, inelastic deformation or microstructural interactions. It is these last two groups that have been of particular interest to ceramic scientists because, if controlled, materials could be designed in which the resistance to crack propagation would be higher.

In 1948, Irwin [31] extended Griffith's theory to metals by introducing in Griffith's equation a term that takes into account the plastic deformation energy associated with crack extension. He also introduced a parameter G called the strain energy release rate that represents the elastic energy per unit crack area that is available for infinitesimal crack extension.

For ideally brittle solids, the crack tip profile was described by Barenblatt [32]). He postulated that the forces which bind atoms together and thus provide an intrinsic fracture resistance are evenly distributed within the cohesion region along the crack plane.

2.1.1.2 Energy approach G_c

The energy-balance concept developed by Griffith in 1920 [28] has laid the foundation for the energy approach of fracture. In fact, the Griffith criterion was derived from an energy balance based on the first thermodynamics principle (principle of conservation of energy). Griffith modeled a static crack as a reversible thermodynamic system. He then postulated that the state of minimum total free energy for the system corresponded to the crack being on the verge of extension and that the free energy of a cracked body under stress should decrease during crack extension.

The total energy U of the system is expressed by:

$$U = U_E + U_A + U_S \tag{2.2}$$

where:

U_E is the strain potential energy stored in the elastic body,

U_A is the potential energy of the outer applied loading system (it corresponds to the negative of the work associated with any displacement of the loading points),

and U_S is the energy associated with the formation of new surfaces.

The mechanical energy U_M of the system is:

$$U_M = U_E + U_A \tag{2.3}$$

then the total energy U of the system may be expressed in two parts: U_M and U_S. Thermodynamic equilibrium is attained by balancing the mechanical and surface energy terms over a virtual crack extension $\mathrm{d}c$.

As the crack extends, there is a release of some of the energy stored in the material (elastic strain energy) as it is elastically deformed so the mechanical energy will decrease ($\mathrm{d}U_M/\mathrm{d}c < 0$). This term favors crack extension. On the other hand, during the crack extension process, new free surfaces are created at the faces of a crack, which give rise to an increase in surface energy of the system ($\mathrm{d}U_S/\mathrm{d}c > 0$) since cohesive forces of molecular attraction across $\mathrm{d}c$ must be

overcome during the creation of the new fracture surfaces. This term opposes crack extension. Thus, the equilibrium requirement is given by $(\mathrm{d}U/\mathrm{d}c = 0)$ and is know as the Griffith energy-balance concept.

However, the energy terms U_E, U_A and U_S depend on the crack configuration as well as on the way the load is applied.

For example, the term U_S, in equilibrium conditions, is given by the product of the crack length, the number of surfaces formed and the thermodynamic surface energy per unit area γ.

Some examples of U_S values are given in Table 2.1 with the corresponding systems presented in Figure 2.1:

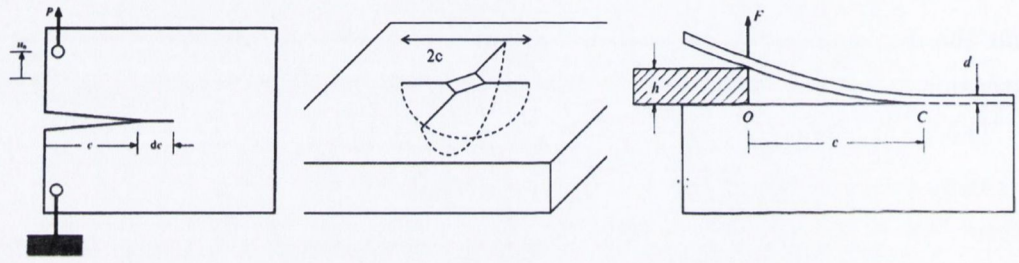

Figure 2.1: i) Static plane-crack system showing incremental extension of crack length c through $\mathrm{d}c$ (Griffith experiment [28]); ii) Two half - penny cracks made by Vickers indentation; iii) Wedge inserted to peel off cleavage flake. In this configuration, both crack origin O and tip C translate with wedge (Obreimoff experiment).

Table 2.1: Examples of values for the energy U_S associated with the formation of new surfaces.

Plane crack of length c and thickness b in uniform tension (Griffith experiment [28])	$U_S = 2cb\gamma$
Two half-penny cracks of diameter $2c$ made by Vickers indentation	$U_S = 2\pi c^2\gamma$
Glass wedge inserted beneath a thin flake attached to a parent block - crack length c and thickness b (Obreimoff experiment)	$U_S = 2cb\gamma$

Irwin [31] defined the strain energy release rate G (also called the mechanical energy release rate) as:

$$G = -dU_M/dC \tag{2.4}$$

with C the crack interfacial area. In the case of a straight crack of length c, this equation becomes:

$$G = -dU_M/dc \tag{2.5}$$

The crack resistance energy R is then given by:

$$R = dU_S/dc \tag{2.6}$$

R represents all the crack resistance processes available in a material. Thus, equilibrium occurs when G reaches a critical value G_c which happens when the crack extension force equals the crack resistance force (i.e. $G_c = R$).

The equations presented above are based on linear elasticity. However, even brittle materials are expected to exhibit some plasticity in the highly stressed region near a crack tip. In order to take into account this inelastic zone, the J-integral has been developed as a fracture criterion for non-linear elastic materials [33]. The Rice line integral J is defined by:

$$J = \int_s (W dy - t\frac{\delta u}{\delta x})ds \tag{2.7}$$

where $W(x, y)$ is the strain energy density, x and y are the coordinate directions, t is the traction vector, n is the normal to the curve s and u is the displacement vector.

J is valid for any reversible deformation response, linear or nonlinear. If the applied loading response is linear elastic, then J=G.

2.1.1.3 Stress approach K_c

At the same period as the strain energy release rate concept was being introduced, an alternative approach based on stress intensity was developed to describe fracture. The notion of stress intensity factor K was introduced to represent the stress distribution around a flaw. It is related to the applied stress σ and the crack length c by the following equation:

$$K = Y\sigma\sqrt{c} \tag{2.8}$$

where Y is a dimensionless parameter or function that depends on both the crack and loading geometries. Some examples of Y values for a crack loaded in uniaxial tension (mode I) are given in Table 2.2.

Table 2.2: Examples of values for the geometric parameter Y (Adapted from Green [34]).

Internal linear crack	$Y = \sqrt{\pi}$
Surface linear crack	$Y = 1.12\sqrt{\pi}$
Internal circular crack	$Y = \frac{2}{\sqrt{\pi}}$

Fracture occurs when the applied stress level exceeds the critical value of σ_c in the vicinity of a crack tip. Fracture toughness is an indication of the amount of stress required to propagate a pre-existing flaw. It is the critical value for K and is defined as:

$$K_c = Y\sigma_c\sqrt{\pi c} \tag{2.9}$$

There are three fundamental modes (Fig. 2.2) by which a load can operate on a crack, and each will effect a different crack surface displacement. Mode I is the opening (or tensile) mode. It corresponds to normal separation of the crack walls under the action of tensile stresses. Mode II is the sliding mode and corresponds to longitudinal shearing of the crack walls in a direction normal to the crack front. Finally, mode III (tearing mode) corresponds to lateral shearing parallel to the crack front. Mode I is encountered most frequently.

All stress fields in the vicinity of a crack can be derived from these three modes of loading. K_{Ic} is unique for a particular material and indicates the conditions of flaw size and stress necessary for brittle fracture to occur. Brittle materials, for which appreciable plastic deformation is not possible in front of an advancing crack, have low K_{Ic} values (below 10 MPa$\sqrt{m}$) and are vulnerable to catastrophic failures. On the other hand, K_{Ic} values are relatively large for ductile materials.

In 1958, Irwin [35] related K_I, K_{II} and K_{III} (stress approach of fracture) to G (energy approach) for plane stress (when one of the three principal stresses is equal to zero) and plane strain (if one dimension is very large compared to the others which implies that the principal strain in the direction of the longest

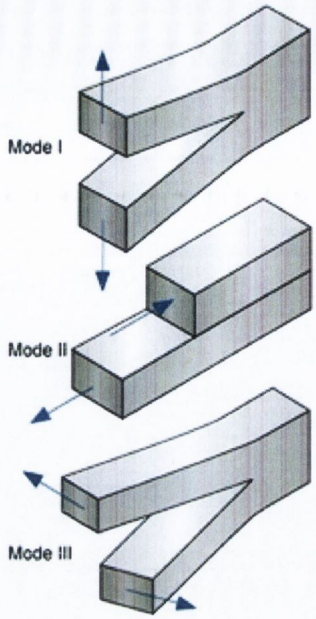

Figure 2.2: The three modes of crack surface displacement. Mode I: tensile mode; mode II: sliding mode; mode III: tearing mode (Adapted from ndt-ed.org).

dimension can be assumed as zero). He suggested that for straight cracks at fixed grips:

$$G = -dU_E/dc \tag{2.10}$$

which leads to the following equation:

$$G = K_I^2/E' + K_{II}^2/E' + K_{III}^2(1+\nu)/E \tag{2.11}$$

with E being the Young's Modulus, ν the Poisson's ratio of the material and E' defined as $E' = E$ in plane stress and $E' = E\ /(1 - \nu^2)$ in plane strain.

Brittle failure appears to occur almost exclusively in mode I loading but cracks that initiate fracture may be oriented such that other loading modes are present. Even for a pure mode I loaded crack, cracks are often deflected at a microstructural level. This crack deflection is a result of variations in the fracture toughness within real materials and the influence of localized stress fields [36].

2.1.2 Kinetics of fracture

The Griffith criterion is based on an energy conservation principle for a system containing a crack in equilibrium, submitted to traction force. In 1978, Rice

[37] proposed an extension of the Griffith criterion in order to take into account kinetic analysis. Applying the second thermodynamic law (the entropy of an isolated macroscopic system never decreases), he showed that the crack driving force (G - R) and the velocity of the crack ν are of the same sign. Then, the crack propagates for G - $R > 0$ and heals for G - $R < 0$.

Rice showed that: $(G - R)\nu = \dot{S} \geq 0$ where $\dot{S}$ is the entropy creation rate. Therefore, the crack velocity is related to irreversible (energy dissipative) mechanisms. Null crack velocity leads to the Griffith criterion $G = R$ as the entropy term is null.

ν - G or ν - K curves can then been drawn for a particular material. The ν term explains that sometimes, crack growth occurs for lower values of K or G than K_c or G_c. This is referred in literature as sub-critical crack propagation [38].

Several mechanisms (stress corrosion, localized creep damage at high temperatures...) can give rise to sub-critical crack growth .

Al_2O_3 exhibits a sub-critical crack growth mechanism due to stress corrosion but Krell et al. [39] have shown that this behavior is independent of the grain size.

2.1.3 Microstructural toughening mechanisms and R-curves

Reinforcement mechanisms of any type can shift the equilibrium given by Griffith towards higher driving force values, giving an increase of crack resistance. Actually, the crack resistance R is not only related to the surface energy but also to additional energy dissipation [38]. Crack tip shielding caused by phase transformation and crack bridging are the two main mechanisms contributing to energy dissipation. Other mechanisms include microcracking, crack deflection and crack arrest on inclusions.

As those mechanisms are functions of the crack length c (the longer the crack the higher the number of crack tip interactions), they explain why, in some materials, crack resistance R and fracture toughness are no longer constant but increase with increasing crack length. This R-curve behavior depends on the toughening mechanisms involved.

Toughening mechanisms in ceramics are classified into three groups: crack tip interactions, crack tip shielding and crack bridging [40].

The crack tip interactions group involves crack bowing and crack deflection processes. Both aim to place obstacles in the crack path to impede crack motion and therefore increase fracture toughness. The obstacles could be second-phase

particles, fibers, whiskers or regions that are difficult to cleave [40]. In the crack bowing process, when the crack is pinned by the obstacles, it by-passes them by remaining on virtually the same plane. In the crack deflection process, the deflection of the crack tip can be accomplished by tilting of the crack path or twisting of the crack front. The change in orientation of the crack plane during deflection leads to a reduction of the crack extension force as the crack is no longer loaded in a simple mode I.

Two mechanisms give rise to crack tip shielding: transformation toughening and microcrack toughening. For both, a non-linear deformation behavior occurs in the high-stress zone at the crack tip. The effect of this process zone is to change the stresses at the crack tip. These stresses are reduced and the process zone is said to shield the crack tip from the applied loads. In the first mechanism, the stress applied induces a phase transformation at the crack tip and a good example is zirconia that is able to transform from tetragonal to monoclinic under the action of mechanical stresses. Microcrack toughening also gives rise to crack tip shielding. Ceramics that contain localized residual stresses are known to be capable of microcracking, usually in regions of low toughness (such as grain boundaries). These residual stresses arise in ceramics as a result of phase transformations, thermal expansion anisotropy in single-phase materials, and thermal expansion or elastic mismatch in multiphase materials [40]. The creation of a microcrack zone around a propagating crack reduces the stresses near the crack tip, giving rise to shielding.

The last toughening mechanism in ceramics is crack bridging. In this mechanism, cracks by-pass an obstacle, leaving it intact and as a ligament behind the crack tip. Crack bridges make it more difficult to open the crack at a given applied stress and increase fracture toughness. This mechanism has been observed in fiber composites, large-grained polycrystals, whisker-reinforced ceramics and cermets. Some authors consider crack bridging to be a form of shielding process, as the bridging decreases the stress intensity factor at the crack tip.

Numerous studies on alumina ceramics have shown that toughening of alumina is made by crack-interface bridging by interlocked grains behind the crack tip [41, 19]. These studies reveal that the crack first propagates through one or two grain diameters, then arrests and thereafter grows erratically during the prefailure growth. To explain this phenomenon, Bennison et al. [42] developed in 1989, a grain-bridging model of crack resistance properties of ceramics, taking into account the internal residual stresses in the constitutive stress-separation relation for pullout of interlocking grains from an embedding matrix. These

residual stresses are due to crystallographic and thermal expansion mismatch between adjacent grains during cooling. Therefore, some grains in the alumina matrix are subjected to compression and play the role of 'bridges'; the remaining grains, subject to tension, are considered as making up the constitutive 'matrix'. As the crack grows, the bridging grains, wedged in the microstructure by this internal compressive stress, lead to an increase in fracture toughness.

Moreover, the extent of toughening also depends upon such factors as the size and shape of the bridging grains and the spacing between the bridges. Based on the model of Bennison et al. [42], Chantikul et al. [21] described the relationships between strength, R-curve behavior and grain size for alumina ceramics in the size range 2-80 μm. They found that the toughness curves become more pronounced as the grain size increases. Tomaszewski et al. [22] later related the role of grain size in the R-curve behavior to residual stresses present in the studied ceramics. They also showed in another study [23] that for alumina based composites with fine microstructures (Al_2O_3-SiC and Al_2O_3-ZrO_2), Al_2O_3 grain size is a stronger parameter than internal stresses introduced by a second phase in controlling R-curve properties of ceramics.

For SiAlONs, toughening mechanisms have been studied less. Microstructurally, these ceramics are composed of grains of α- or β-SiAlON with sizes distributed in the range 1 to 3 μm and separated by an intergranular amorphous yttrium-aluminosilicate-oxynitride glass. Crack bridging and crack deflection have been identified as the two main toughening mechanisms in these ceramics. Crack deflection occurs as the crack path is deflected around the grains in order to pass through the weaker intergranular phase [43].

The different materials investigated (alumina and SiAlONs) are expected to present significant crack-microstructure interactions while indenting, making them a relevant choice for the present study.

2.1.4 Fracture toughness measurements

Fracture toughness is usually determined by introducing a crack of known size into the specimen, which is then loaded to failure. The geometric parameter Y is determined and the crack length c and the strength applied σ_c are measured in order to calculate K_{Ic} according to equation (2.9).

At large scale, determination of fracture toughness is usually done by one of the following methods (From British Standards 14425-1 [44]):

- Single-Edge Precracked Beam (SEPB): a flexural test on a beam into the

tensile side of which a short straight sharp crack has been introduced.

- Single-Edge Notched Beam (SENB): a flexural test on a beam in which a narrow notch has been made on the tensile side.
- Single-Edge V-Notched Beam (SEVNB): a development of the SENB method with the notch tip sharpened by honing with diamond paste.
- Chevron Notched Beam (CNB): a flexural test on a beam with two coplanar angled notches leaving a sharp-tipped triangular shaped region to fracture.
- Surface Crack in Flexure (SCF): a flexural test on a beam in which a small semi-circular flaw has been introduced by indentation on the tensile side, and with the indentation damage removed.
- Indentation Strength (IS): a flexural test on a beam into which has been placed an indentation on the tensile side.
- Indentation fracture (IF): a test in which the length of cracks emanating from the corners of a Vickers hardness indentation is measured.
- Compact tension (CT): a tensile test on a specimen of full plate thickness containing a notch. The sides of the specimen are approximately twice the specimen thickness.
- Double Cantilever Beam (DCB): a test in which the ends of the sample are pulled apart, forcing a crack to propagate down the beam from one end.

For all the flexural methods, three- and four-point flexure tests exist. The force applied to the specimen, specimen displacements (notably the crack-mouth opening), loading rate and temperature are recorded during the experiment. The most widely used fracture toughness test configurations are the SENB and CT methods. Figure 2.3 shows some of these fracture test methods.

During flexural tests, three fracture parameters can be calculated: K_c (stress-based estimate of fracture toughness), J-integral (energy-based estimate of fracture toughness) and the opening displacement of the original crack tip ($CTOD$).

$CTOD$ can be considered as a strain-based estimate of fracture toughness. Like J, $CTOD$ can be divided in an elastic and a plastic term, whereas K_c only includes elastic components.

The crack tip opening displacement ($CTOD$) of a crack at the edge of a three-point bending specimen is shown in Figure 2.4:

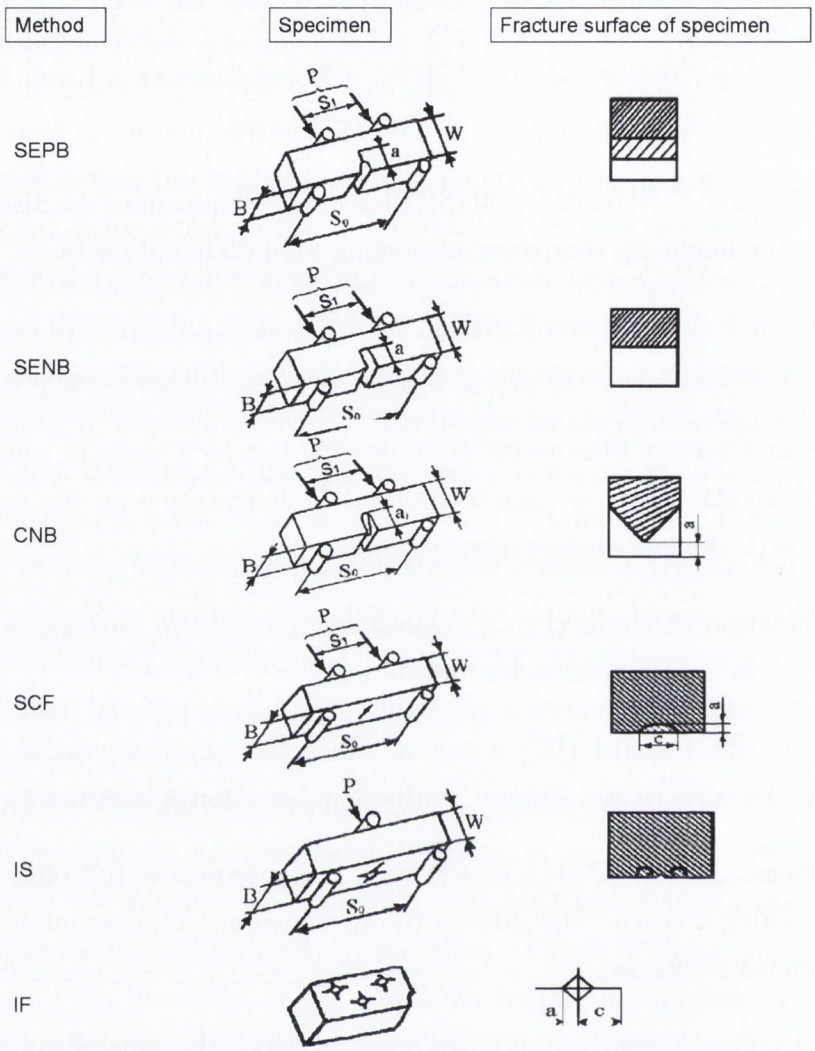

Figure 2.3: Schematic diagrams of some existing fracture toughness test methods (Adapted from Gogotsi [45]).

where $CTODm$ is the measured crack tip opening displacement, usually near the edge of the specimen for ease of access, $CTOD$ is the real crack tip opening displacement, a is the length of the crack and b is the width of the rest of the specimen. Thus:

$$CTOD \equiv \delta = \frac{\rho b}{a + \rho b} CTOD_m \tag{2.12}$$

where ρ is a dimensionless rotational factor used to locate the center of the hinge.

Considering a linear elastic body containing a crack, the J-integral and the $CTOD$ have the following relationship:

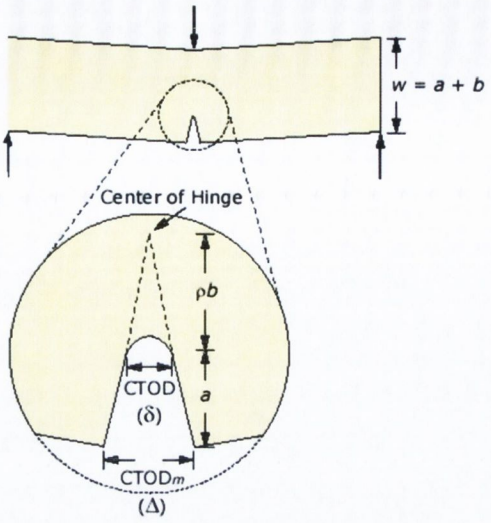

Figure 2.4: CTOD of a crack at the edge of a three-point bending specimen (Adapted from efunda.com).

$$J = \frac{K_I^2}{E} = m\sigma_{ys}\delta \tag{2.13}$$

where σ_{ys} is the small scale yielding stress and m is a dimensionless constant that depends on the material properties and the stress states.

Most of the methods cited above require a minimum number of samples of sufficiently large dimensions, which limits their application range. Microfabrication techniques permit to make specimens of only a few microns in size for fracture toughness testing but this application is limited by the difficulty in preparing specimens.

The recent development of depth-sensing nanoindentation instruments has allowed indentation tests to be made in very small volumes (e.g. depths < 500 nm) and to measure several material properties like Young's modulus and hardness during the test. As this study focuses on the microscale level, indentation measurements seem to be the best method to determine fracture toughness at this scale. Moreover, this method permits many tests on the same small sample and to run tests on small areas with dimensions on the micrometer scale, such as individual grains or grain boundaries. For materials with R-curve behavior, it is also a good method to investigate the short-crack domain compared with the long-crack domain tested by traditional toughness methods. Furthermore, the fracture initiating crack made by indentation can be considered as a model for natural defects, contact and wear.

More importantly, the cracks formed during indentation testings are equilibrium cracks, i.e. they grow and stop before the complete fracture of the sample. When a crack stops growing, it means that the energy for opening it has been balanced by the resistance of the material to crack propagation. Therefore, the crack resistance of the material can be accessed. On the contrary, conventional tests end by the breaking of the sample, which means that the energy needed to overcome the crack resistance has been attained but may have also been exceeded. The resulting energy given to the sample has been transformed to kinetic energy, increasing crack velocity. In this case, it is more difficult to access the crack resistance of the material unlike in indentation testings where the kinetic energy remains very low. Finally, in high energy tests, there is little interaction of the crack front with the microstructure as the crack grows very quickly due to the high energy accumulated. Contrary to these methods, indentation fracture presents an equilibrium condition (when a crack arrests in the material) that makes more accessible the study of crack-microstructure interactions.

All the reasons cited above have lead to the choice of indentation technique for this study of crack-microstructure interaction in small scale ceramics fracture toughness measurements.

A review of mechanics of indentation fracture is presented in the next subsection.

2.1.5 Mechanics of indentation fracture

To access material properties like fracture toughness, one method consists in studying the morphology and growth behavior of the cracks formed by indenting the surface of a brittle material, usually with a Vickers indenter. This method has been widely used over the past decades.

In indentation fracture, the contact stress field induced in the specimen by the indenter is principally determined by geometrical factors (indenter shape) and material properties (elastic modulus, hardness, fracture toughness). The indentation shape can be blunt or sharp [46, 47] depending on the existence of irreversible deformation at contact. Spherical indenters are considered as blunt because the contact prior to fracture remains predominantly elastic. On the contrary, sharp indenters like cones or pyramids (Vickers, Berkovich or Knoop indenters) induce plastic flow (i.e. irreversible deformation process). This type of contact is called elastic-plastic due to the presence of an elastic matrix around the plastically deformed region. However, at high loads, spherical indenters can behave more like sharp indenters. Both blunt and sharp indenter crack patterns

can be used to determine fracture toughness, but sharp indenters are more often used for several reasons. In opaque materials, they enable fracture toughness to be determined by producing radial surface cracks. In addition, sharp indents are more close to real contact situations, where severity of surface damage is a prime concern [48]. Furthermore, sharp indenters can induce crack formation at lower loads than blunt indenters [46]. Finally, the shape of sharp indenters remain constant as the indenter penetrates in a specimen, making the contact pressure independent of indent size. This is useful for measuring the hardness.

2.1.5.1 Contact stress fields

In 1885, Boussinesq [49] described the contact stress field beneath an indenter. This stress field is represented by an isotropic, linear, elastic half-space subjected to a normal point load P on its surface.

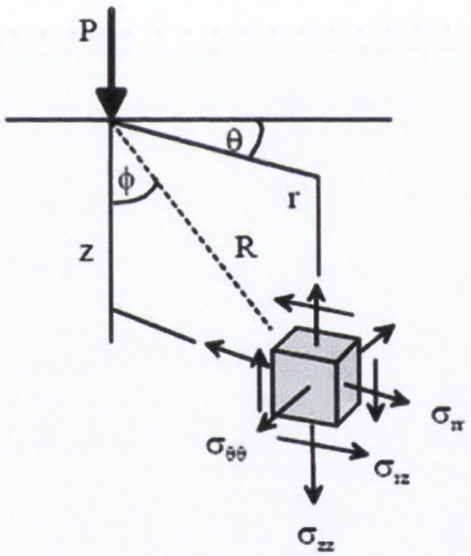

Figure 2.5: Coordinate system for axially symmetric point loading P (Adapted from Burghard [50]).

For an isotropic material of Poisson's ratio ν, the stress components in the curvilinear coordinate system of Fig.2.5 are seen to assume the general form:

$$\sigma_{ij} = (P/\pi R^2)[f_{ij}(\phi)]\nu \tag{2.14}$$

Thus, at fixed indenter load, the stress field varies as the inverse square of the radial distance R from the contact point, times an independent angular term.

Trajectories and contours of the three principal normal stresses formed under contact for the case $\nu = 0.25$ are plotted in Fig.2.6.

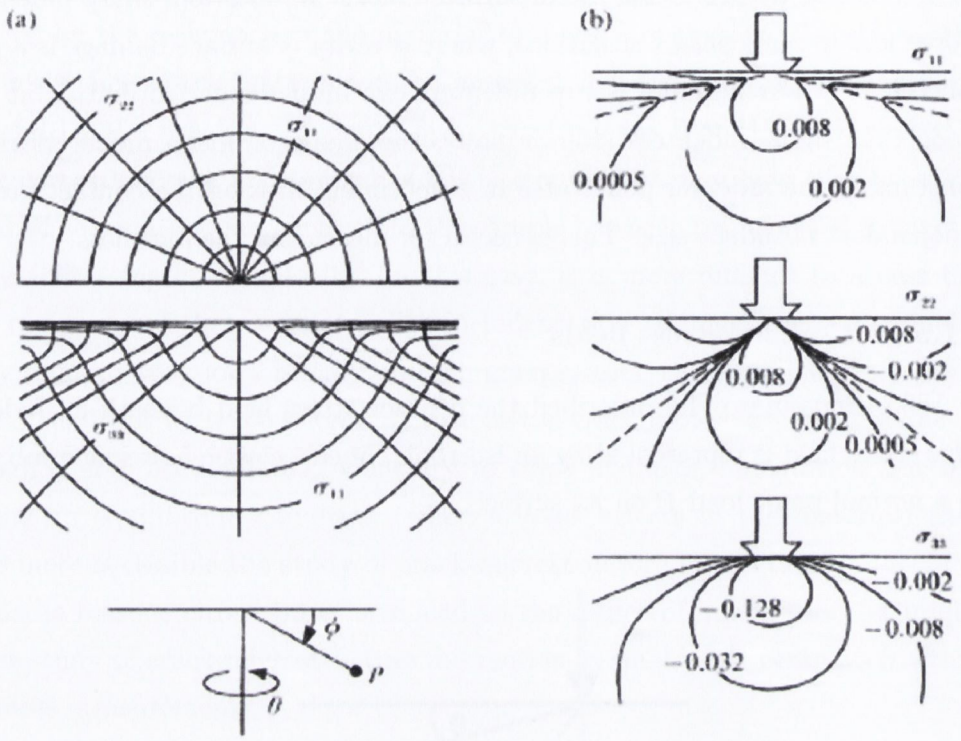

Figure 2.6: Boussinesq field for principal normal stresses σ_{11}, σ_{22}, and σ_{33} plotted for $\nu = 0.25$. (a) stress trajectories (tangents to which denote direction of the principal stresses) shown in half surface view (top) and side view (bottom); (b) contours (numbers on which denote magnitude) shown in plane containing contact axis (side view). Note: sharp minimum in σ_{11} and zero in σ_{22}, indicated by broken lines (Adapted from Burghard [50]).

The stress field is axisymmetric around the force direction (Fig.2.6 (a)) and the stress components are defined such as $\sigma_{11} \geq \sigma_{22} \geq \sigma_{33}$ at any point in the field. In the context of crack initiation and propagation, it is the tensile component of the field that commands most attention. The σ_{11} stress is tensile at all points in the field and shows a maximum at the surface ($\phi = 0$) and along the contact axis ($\phi = \pi/2$) [51](Fig.2.6(b)) Therefore, the crack will tend to initiate at one of these favored locations. Thus, provided the surface does not contain severe handling damage, crack initiation would be expected to occur preferentially below the contact point. σ_{22} is tensile within a conical region below the indenter but compressive near surface. In contrast, σ_{33} is everywhere compres-

sive. Once initiated, a crack will at any point tend to propagate along trajectories of lesser principal normal stresses, thereby maintaining near-orthogonality to a major tensile component [48].

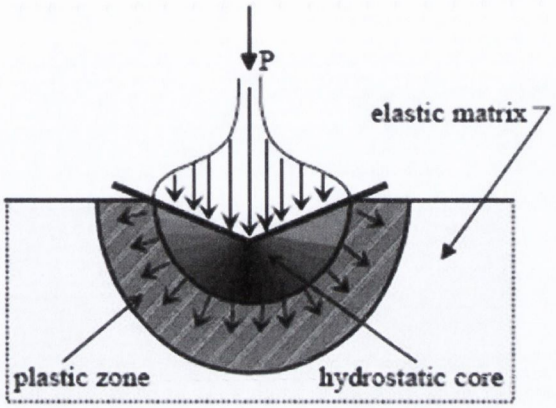

Figure 2.7: Schematic representation of the model for elastic-plastic indentation according to Marsh [52]. P is the applied load (Adapted from Burghard [50]).

The theoretical stress fields described by Boussinesq work well for homogeneous and isotropic materials subject to an indentation by a sharp indenter. However, these idealized patterns are unlikely to be well-representative of the real stress fields encountered in the materials investigated in this study for which local heterogeneities (complex microstructures and/or residual stresses) will create non-uniform stress fields patterns.

A model for inelastic deformation within ideal elastic-plastic contacts in glasses was proposed by Marsh in 1964 [52] and is presented in Figure 2.7. This model assumes that:

- Immediately below the indenter the material behaves as an expanding core, exerting a uniform hydrostatic pressure on the surrounding material. The hydrostatic pressure is equal to the mean indentation pressure.
- An ideally plastic region encases the core and beyond the plastic region lies the elastic matrix.
- The plastic component of the deformation is a constant volume, with a radial displacement process and characterized by a well-defined yield stress.
- The deformation field below the indenter is spherical.

The vast majority of indentation studies are based on the assumptions made within Marsh's model. During indentation experiments, the irreversible deformation within the contact zone does not allow full recovery of the initial stress-free state in the surrounding elastic matrix after one complete loading and unloading cycle. This results in the creation of a residual stress field in the unloaded solid, which provides the primary driving force for the radial crack formation in the final stage [53].

As previously highlighted for the idealized stress fields, the assumptions underlying Marsh's model are unlikely to be checked in materials with complex microstructures.

In the next two subsections are presented the different types of cracks observed in glasses and ceramics and a focus is made on those induced by a sharp indenter and on their use to estimate fracture toughness of the material.

2.1.5.2 Type and formation of major indentation-induced cracks observed in glasses and ceramics

A diversity of cracks may be generated in the surface of a brittle material by indentation contact. They are usually divided in four major crack types: cone, median, shallow radial and lateral cracks [50]. In each case, the indenter sets up a contact stress field, the tensile component of which provides the driving force for the ensuing fracture.

Cone cracks are commonly generated by the elastic loading of spherical or blunt indenters [54, 48]. They are sometimes called Hertzian cone cracks due to their first observation by Hertz in 1881 [55] during his examination of solids under elastic contact.

The cone crack formation is schematically illustrated in Fig. 2.8 (i). Cone cracks nucleate at the material surface as a circular crack (indicated by dashed line). It starts generally from pre-existing flaws (short dashes) just outside the contact circle (shaded region), where the principal tensile component reaches its maximum (a). When reaching a critical load, the surface circular crack becomes unstable and propagates from the surface downward at a characteristic angle to the load axis, which results in a cone crack (b). During unloading, the cone cracks tend to close (but rarely to heal), leaving a circular crack on surface (c).

Figure 2.8 (ii) shows the evolution of the median crack system associated with Vickers indentation.

Median cracks nucleate at the bottom of the plastic zone (depicted as a grey region) at the elastic-plastic interface where the stress concentration is maximal

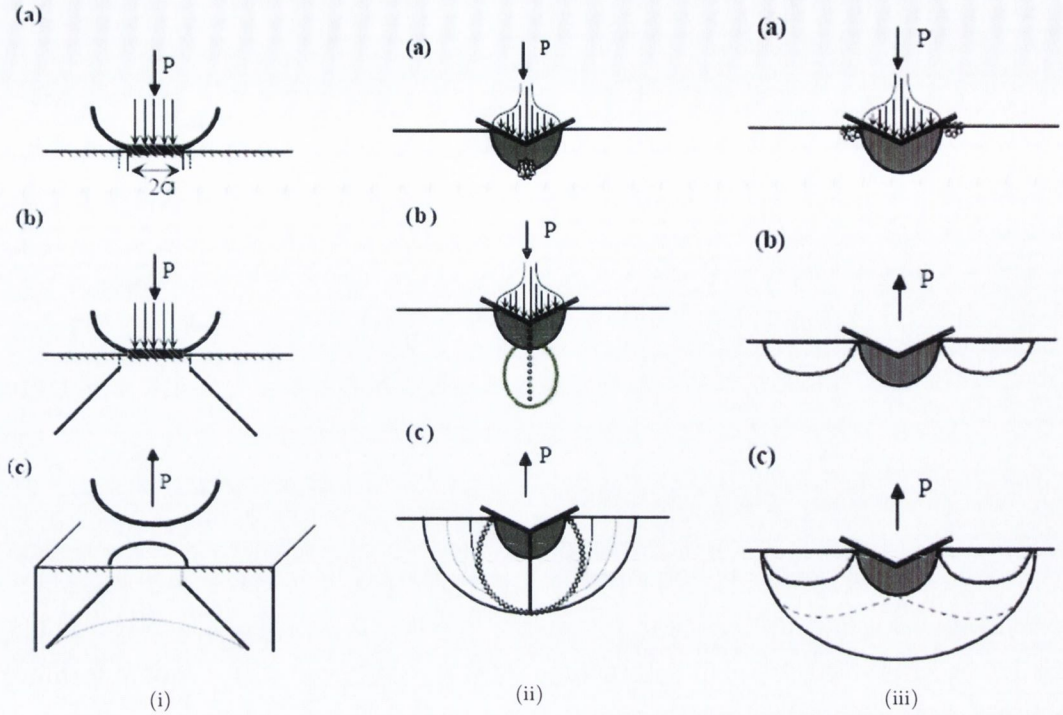

Figure 2.8: Cone, median and shallow radial crack systems (Adapted from Burghard [50]).

(a) [46]. In general, the nucleation sites are created by the actual deformation process that causes intersecting shear or slip bands beneath the indenter (named 'shear faults') [56]. Pre-existing surface flaws can also sometimes act as crack initiators [57]. Median cracks consist of two mutually perpendicular penny shaped cracks parallel to the axis of loading. During loading, the median cracks become unstable and propagate downward, reaching their maximum size at peak load (b). If the loading is severe, the cracks may break through to the material surface. Upon unloading, they close up below the surface but simultaneously expand towards the indented surface forming the final crack with half-penny shape (indicated by the dashed lines in Figure 2.8 (ii) (c)) [48]. The stress field driving the crack is composed of an elastic component, responsible for the growth of the crack during loading, and a plastic component, responsible for the extension of the surface trace on unloading [54]. The terminology has recently changed: the median cracks which have reached the surface cracks are referred to as radial, whilst the subsurface cracks are still referred to as median [50]. The combined system is often termed 'median-radial' crack system in the literature.

Shallow radial cracks can form when applied loads are smaller than the critical load for median crack formation [58] or when the specimen has a rough surface.

These cracks are sometimes called 'Palmqvist' crack after their discoverer, who first observed them in 1957 [59]. The evolution of the shallow radial crack system associated with Vickers indentation is shown in Figure 2.8 (iii). The formation of shallow radial cracks can also occur with materials which have a very high toughness, or when small spherical indenters are used. With increasing load, nucleation of shallow radial cracks occurs parallel to the load axis, emanating from the edge of the plastic contact impression (usually at an indentation corner), and remaining close to the surface (a) [54]. However, propagation of these cracks only occurs during unloading. They start to grow both in length and depth parallel to the load axis (b) just prior to complete removal of the indenter. This leads to the formation of four mutually perpendicular, semi-elliptically-shaped cracks (c) with a maximum depth in the same order as the indentation depth. The crack shape can be elliptical (for cemented carbides) or circular (in case of ceramics). These cracks tend to propagate downward and merge beneath the plastic zone into half-penny geometry, either during unloading [60] or post-indentation growth, forming a semi-elliptical crack system.

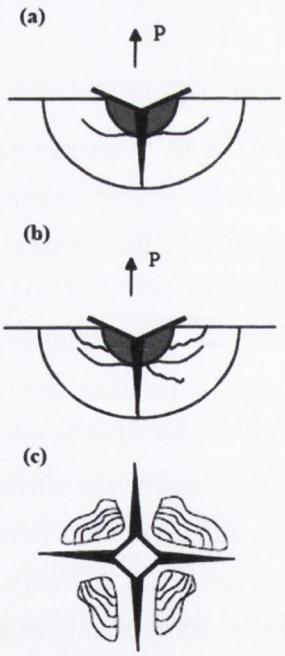

Figure 2.9: Lateral crack system (Adapted from Burghard [50]).

Figure 2.9 shows the formation of lateral cracks during Vickers indentation. This type of cracks is generated below the surface independently of other crack type formation. Lateral cracks nucleate beneath the deformation zone at the be-

ginning of the unloading part of the cycle (usually at about 90 % of the maximum load) and grow in a plane parallel to the surface (a). It has been found that the maximum stress for lateral crack propagation occurs at the depth of the contact impression. At very high loads, lateral cracks tend to divert upwards toward the surface, resulting in material removal at the surface; this process is termed 'chipping' ((b): cross-sectional view, (c): plane view).

Lateral cracks appear during the unloading of sharp indenters, or blunt indenters with associated plastic deformation. In some materials, lateral cracking occurs on loading, suggesting that the driving force and initiation mechanisms for lateral cracks depend in a more subtle way on elastic and plastic material properties than do radial or median cracks [54].

2.1.5.3 Cracks observed under a sharp indenter

Fig.2.10 shows the final configuration of the median-radial and lateral crack systems resulting from Vickers indentation.

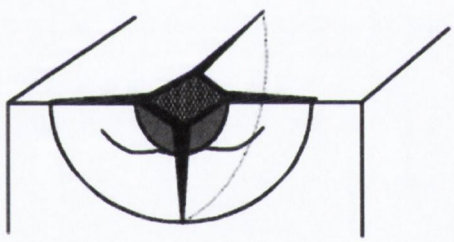

Figure 2.10: Median-radial and lateral cracks resulting from Vickers indentation (Adapted from Burghard [50]).

The radial cracks visible on the surface can be the manifestation of either shallow radial cracks (Palmqvist cracks) or median cracks which have reached the surface.

Unlike median cracks which are closed during unloading, radial and lateral cracks grow to their final length as the indenter is unloaded [48]. This has led to the assumption of the creation of a residual stress, resulting from the mechanical mismatch between the deformation zone (plastic) and the surrounding elastic material. At the end of the unloading, this residual stress starts to dominate the field of the applied loading and act as the prime driving force for crack propagation [51].

This residual stress field contains a component of tension sufficiently intense

to generate lateral cracks. It is also responsible for the final half-penny shape of the median cracks [48].

Median and radial cracks are usually associated with strength degradation caused by a contact event, whereas lateral cracks are linked to spalling and erosion that can occur during contact [61, 60].

However, the idealized crack pattern resulting from Vickers indentation and represented above is unlikely to be observed in brittle ceramics with complex microstructures (those having multiple phases for instance). In this case, crack paths are expected to be disrupted by local heterogeneities, leading to a final crack configuration different from theoretical ones.

2.1.5.4 Evaluation of fracture toughness by indentation

In 1957, Palmqvist [59] demonstrated that the length of cracks, which emanate from the corner of an indent, can be empirically related to the toughness of the investigated material. Based on these observations and using Marsh's elastic-plastic model, Lawn et al. [48, 57] developed a method for determining fracture toughness by crack length measurements. The indentation crack length (ICL) method, usually performed using a Vickers indenter, only requires measurement of the half indent size a, the lengths of the cracks c that emanate from its corners and the applied indentation load P. It has since been widely applied for fracture toughness determination, especially for glasses and ceramics.

During the 1970s and the 1980s, many researchers have established equations relating material fracture toughness to the measured indentation parameters using the ICL method. In 1989, Ponton et al. [62] reviewed existing models for K_c. They noticed that all models derived from three basic models which are described below:

- Elastic models [48, 57, 63]: These models are based on the elastic stresses during loading and assume the formation of median-radial cracks beneath the indenter. The calculation of K_c depends on the indenter load P, on the length of the surface radial crack c and on a coefficient based on the indenter geometry.

- Elastic-plastic models [64, 58, 65]: These models assume the existence of a plastic deformation during loading. They are also based on the median-radial crack system. K_c is calculated using c, the half-diagonal of the indentation a and material's properties such as the Young's modulus E, the

standard hardness based on the indentation contact area H_s and the plastic constraint factor Φ defined as the indentation pressure over the material flow stress.

- Residual stress models [53, 17]: These models are based on the residual stress fields arising from the mismatch between the deformation zone which is plastic and the surrounding elastic material. The calculation of K_c is made using shallow radial cracks. It involves P, c, E, the true hardness based on the projected indentation area H_T and a material dependent constant.

As such equations have led to significantly varying fracture toughness values, the most accurate of these models seems to be the one proposed by Anstis et al. [17] presented in Figure 2.11, which gives results close to the experimental ones obtained in ceramics. This model leads to a simple relation between the fracture toughness K_c, and the lengths of the radial cracks c, of the form:

$$K_c = \alpha \left[\frac{E}{H}\right]^{\frac{1}{2}} \left[\frac{P}{c^{\frac{3}{2}}}\right] \tag{2.15}$$

with P the peak indentation load, H and E respectively the hardness and Young's modulus of the indented material and α an empirical constant which depends on the geometry of the indenter. α is defined as:

$$\alpha = \xi(\cot\phi)^{2/3} \tag{2.16}$$

where ξ is a dimensionless constant and ϕ the indenter half-angle.

Anstis et al. [17] empirically found that the constant $\alpha = 0.016$ gave the best results and therefore, this model has been used extensively.

The basic assumptions of this model are:

- The different elastic and plastic regions are described by Marsh's model (cf. section 2.1.5.1).

- A residual stress field will remain in the unloaded specimen providing the primary driving forces for the radial crack configuration in the final stage, where the cracks tend to near half-penny geometry. Thus, the final size of the radial crack is determined by this residual stress field.

- This residual stress is concentrated at the point located at the crack center at the elastic/plastic interface, and acts as crack mouth opening point force.

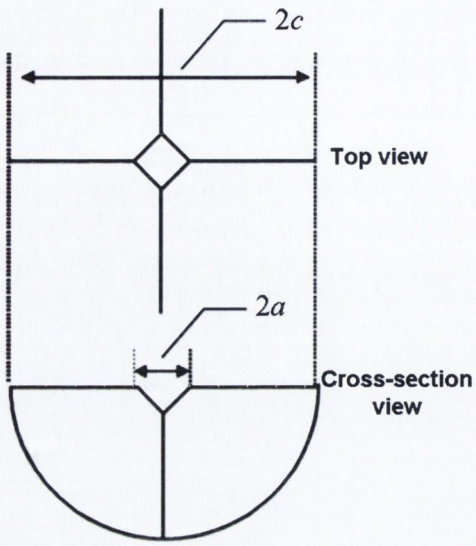

Figure 2.11: Schematic representation of geometry and characteristic parameters a and c of the median/radial crack system around a Vickers indent (Adapted from Burghard [50]).

- The volume of the indentation plastic zone can be equated to that of an internally pressurized spherical cavity, allowing the use of Hill's solution for the expanding spherical cavity.

- E and H are isotropic and homogeneous properties.

- This model is valid for a limited range of materials: those where indentation leads to well-developed half-penny shaped cracks (described in the equation by the exponent $\frac{3}{2}$). Well developed cracks are defined by $c \geq 2a$.

- The analysis is confined to loads below the chipping threshold where lateral cracks turn upward to intersect the surface, causing severe disruptions of the radial crack pattern.

The relevance of using Anstis model to calculate fracture toughness in small-scale ceramics with complex microstructures has to be questioned as many of the assumptions underlying this model can't be validated anymore. Specific issues concerning the applicability of conventional fracture toughness models from indentation tests on these ceramics at small scale are discussed in the next subsection.

2.1.6 Limitations of existing models for indentation fracture toughness at small scales in ceramics

Indentation techniques have been widely applied in the characterization of fracture toughness of engineering materials, using the model developed by Anstis et al. [17], even if this model only permits to calculate K_c with an accuracy of 30 to 40 % [17, 66] compared to the values obtained by conventional methods (i.e DCB or SENB).

Quinn et al. [67], in a comparative study between Vickers indentation and standardized fracture toughness tests (i.e. CNB, SEPB, SCF) in ceramics, show that the indentation test produces a complex three-dimensional crack system and complex residual stresses which cannot be directly correlated with K_c, contrary to the single crack produced by standardized techniques. They strongly recommend not to use the indentation technique on ceramics as they describe this technique as 'not reliable' for brittle materials. They pointed out many issues related to the indentation technique such as the various deformation behaviors of ceramics and the interacting cracks. According to them, instead of measuring any crack propagation parameter, indentation fracture toughness only represents a 'complex crack arrest phenomenon'.

In addition to these concerns about the reliability of indentation fracture toughness tests at the macroscale for ceramics, the use of this technique at small scales presents several other issues. Indeed, many assumptions underlying Anstis model are not checked anymore at small scales. Three main issues have been highlighted when using Anstis model for the measurement of fracture toughness in micro-ceramics:

- The influence of microstructural heterogeneity
- The presence of densification, pile-up or phase transformation phenomena
- The influence of surface properties and indenter geometries

Because of microstructural heterogeneities (i.e. grain morphology and texture, porosity, residual stresses, etc), the stress fields created are non-uniform leading to the formation of crack shapes different from the well-formed median or Palmqvist cracks described in the model [68]. Thus, the complex and tortuous crack pattern obtained can produce on the surface: side cracks, corner cracks with non-equal crack length, crack deflection, crack branching, angle cracking, etc, making it difficult to determine the crack length c and impeding the calculation of fracture

toughness using the Anstis model [17]. Moreover, toughening mechanisms like crack deflection, crack branching, etc, induce a greater surface area of median-radial cracks than the one predicted, as Anstis model rely on idealized subsurface crack shapes. Low indentation loads can also result in low values of c/a ratio (i.e. a great proportion of the crack is within the dimension of the deformed region), in which case the crack length c is meaningless and Anstis model not applicable [68]. In fact, the inaccuracies at the small scale described above are valid for all the existing models based on indentation experiments (cf. 2.1.5.4). None of them takes into account material anisotropy or structural heterogeneity. They all assume that H and E are homogeneous and isotropic which is not the case anymore at the microscale level, where the E and H values measured represent local rather than bulk properties [24, 25].

Another basic assumption of Anstis model is that the plastic component of the deformation beneath the indenter is a constant volume. Anstis et al. [17] indicated that this was not valid anymore for ceramics which experience pile-up (for materials with low H/E values), densification or phase transformation. Such phenomena induce a diminution in residual stress intensities at indentation sites, which leads to changes in crack shape and reduced radial crack lengths. Thus, evaluation of crack lengths in these materials using equations with calibrated parameters can lead to gross overestimates of fracture toughness. Indeed, when densification or phase transformation occur, the indentation strain can be relaxed by compaction (as well as by elastic compression) within the deformation volume. Therefore, the constant ξ in Equation 2.16 would be smaller than for a volume conserving process [51]. This implies that the value of ξ will depend on the nature of deformation and that the constant α in Equation 2.15 is no longer material independent.

Little importance is also given to surface properties (like the fracture-inhibiting effect of residual compressive stresses in a toughened surface) which yet have a greater influence on plastic response and on the brittle or ductile behavior of the material at this scale where the indentation cracks remain within the sphere of influence of the near-contact region [47]. Residual surface stresses and surface defects (grain pull-out and micro-scratching) usually originating from polishing, can also serve as initiators for subsurface micro-cracks then inducing a decrease in the material properties (notably E)[69]. Furthermore, the indenter geometry is an important factor to be considered at small scale, as its interaction with the brittle surface is a determining factor in crack initiation (with blunt indenters, preexisting surface flaws determine fracture initiation process whereas sharp in-

denters induce their own flaws [47]). At higher loads, when the contact damage is severe, the differences due to details in the near-contact conditions tend to lose in importance. The indenter geometry is also important as it can determine the types of cracks induced in the specimen.

For all these reasons, conventional models used at macroscale to determine fracture toughness in ceramics do not seem to be valid anymore at small scale, as microstructure and surface properties begin to have great influence on fracture properties.

An alternative method of capturing fracture behavior of brittle solids is to use a damage mechanics approach.

2.1.7 Damage mechanics approach

When the location of an expected crack and its direction of propagation are unknown, fracture mechanics can hardly be used because the critical flaw from which cracking initiates needs to be determined first. Alternatively, a damage mechanics approach permits the prediction of the location of this critical flaw.

Based on stress and strain histories of a material, damage mechanics studies the situation that precedes the appearance of a macrocrack. The propagation of this macrocrack can then be predicted using fracture mechanics or by considering that the evolution of this crack is the evolution of the damaged zone as calculated element by element with recalculation of the state of stress and strain [70, 71]. Another approach to investigate rupture conditions was defined by Lemaitre [70] and consists in coupling strain and damage equations in one step as damage decreases the rigidity and the strength of materials. In the last two approaches presented above, continuous damage mechanics (CDM) encompasses both description of initiation and crack propagation.

Unlike the fracture mechanics approach, which considers the effects of a single dominant effect, damage mechanics is based on the presence and effects of a large number of microdefects distributed randomly throughout the material.

Damage mechanics describes the process of transformation of microvoids and microdefects into a macrocrack. In the CDM approach, this is done by the introduction of a new internal variable called damage D and its evolution law [70–72]. D characterizes the density of microcracks, micropores, plastic microstrains and other defects. Damage reduces the elastic properties of the material, such as the Young's modulus, and induces anisotropy in elastic properties. Therefore, D also represents the state of deterioration of the mechanical properties of a volume element in a continuum and is defined as:

$$0 \leq D \leq 1 \tag{2.17}$$

$D = 0$ corresponds to the undamaged state, while $D = 1$ is equivalent to complete local rupture of the material.

To model isotropic damage processes, a scalar damage variable is needed whereas tensor valued damage variables (second or fourth order) are required in order to account for anisotropic damage [73, 70].

For brittle materials, plastic strains are neglected and a damage function g is introduced. This function depends on some adequate invariant of the strain tensor ε_{eq}, called equivalent strain, and on a hardening term $K(D)$, such as:

$$g = \varepsilon_{eq} - K(D) \tag{2.18}$$

Damage remains constant if the function g is negative or if it is decreasing and it evolves if g is equal to zero.

Materials exhibiting microcracking are also referred as quasi-brittle materials. When quasi-brittle materials are subjected to external mechanical loads, they exhibit a non-linear response. Contrary to perfectly brittle materials which fail as soon as a few microcracks appear, a quasi-brittle material will sustain a greater number of cracks. Beyond its maximum strength, a quasi-brittle material accumulates inherent damage (microcracks) which leads to a strain softening phenomenon: a reduction in the principal stress with the increase in the corresponding principal strain (i.e. negative slope of the stress-strain curve).

For these materials, the overall toughness depends on both the degree of prefailure damage accumulation and of the properties of the final fracture surface [74]

Mazars et al. [71] developed relationships between FM and CDM approaches, based on thermodynamic considerations (i.e the equivalence of energy dissipated during failure process according to the two theories). They modeled a damage zone by an equivalent crack and inversely, transformed a crack into a volume distribution of damage on a 'band" around this crack. Lee at al. [72] followed the same reasoning and associated local damage with an equivalent elliptical (non-circular) microcrack.

Damage mechanics is a powerful theoretical tool for the description of the gradual degradation of brittle material mechanical properties, such as elastic modulus, due to growth and coalescence of microvoids or microcracks. However, in practical cases, it remains difficult to determine analytically and experimentally evolution equations for microcracking (such as the evolution of crack density) and

reduced elastic properties, two parameters which are needed in the formulation of damage mechanics models.

An investigation done in 1996 on geological materials showed interesting hypotheses which could be tested with our small scale ceramics. Studying Utah limestone, Middlemiss et al. [18] found that crack density (i.e. crack surface area per unit volume) was a material property and was relatively insensitive to variations in the local microstructure of the material (they made tests at grain boundaries and within grains). They also postulated (but didn't prove) that the crack density of their material can be correlated with the particulate fracture energy of that material.

The aim of this work is to quantify the influence of the microstructure on fracture behavior and to develop an accurate method to measure fracture properties of ceramics at the microscale level.

2.2 Nanoindentation

Nanoindentation, also known as depth-sensing indentation, ultra-low-load indentation and instrumented indentation testing (ITT), has been extensively used in the past decades to characterize mechanical response of materials at micrometer and nanometer length scales. This technique allows the continuous control and monitoring of the loads and displacements of an indenter as it is driven into and withdrawn from a material [75–77].

Oliver and Pharr [75] first introduced a method for determining hardness (H) and Young's modulus (E) using nanoindentation techniques. These properties could be calculated for isotropic materials exhibiting no time dependence in their deformation behavior (creep or viscoelasticity). Although this method was originally developed for sharp and geometrically self-similar indenters, it also applies to axisymmetric indenter geometries including the sphere [75, 78].

Fig 2.12 presents the geometries of the most common used indenters (sphere, cone, Berkovich, cube corner, Vickers and Knoop). The standard Knoop indenter is usually defined by two angles: $d = 172.50\,^\circ$ and $g = 130.00\,^\circ$ and is commonly used to investigate anisotropy of the surface of the specimen.

The important geometric parameters of these indenters are presented in Table 2.3. The half-included angle θ represents the angle between the axis of the indenter and any of the faces. In order to use Oliver and Pharr's equations, actual pyramidal geometries are mathematically transformed to equivalent rigid cones. The half-included cone angle α is defined as the angle that gives the same

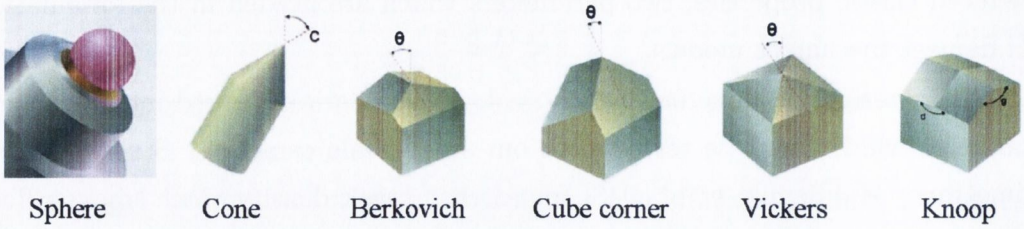

Figure 2.12: Indenter tip geometries (Adapted from Micro Star Technologies website).

projected area-to-depth ratio as the pyramidal indenter.

Table 2.3: Geometric parameters of the different indenters (Adapted from Fischer-Cripps [79]). R is the sphere radius and h_p the indentation depth.

Indenter type	**Half-included angle θ**	**Equivalent cone angle α**	**Projected area**
Sphere	...	...	$A \approx 2\pi R h_p$
Cone	α	α	$A = \pi h_p^2 tan^2\alpha$
Berkovich	$65.3\,^\circ$	$70.2996\,^\circ$	$A = 3\sqrt{3}h_p^2 tan^2\theta$
Cube corner	$35.26\,^\circ$	$42.28\,^\circ$	$A = 3\sqrt{3}h_p^2 tan^2\theta$
Vickers	$68\,^\circ$	$70.32\,^\circ$	$A = 4h_p^2 tan^2\theta$
Knoop	$\theta_1 = 86.25\,^\circ; \theta_2 = 65\,^\circ$	$77.64\,^\circ$	$A = 2h_p^2 tan\theta_1 tan\theta_2$

The most frequently used indenter in nanoindentation testing is the Berkovich. It is preferred to the Vickers because a three-sided pyramid can be ground to a point, thus maintaining its self-similar geometry to very small scales [77]. A four-sided pyramid, on the other hand, terminates at a line of conjunction at the tip rather than at a point, causing its small-scale geometry to differ from that at larger scales. The Berkovich indenter is designed to have the same projected area as the Vickers indenter at any given indentation depth.

An ideal Berkovich indenter tip has an infinitely sharp radius but this is impossible to achieve in practice. As a result of the finite radius of the indenter tip, it is necessary to employ contact mechanics equations appropriate to a spherical indenter (Hertzian theory) for the initial part of the loading/unloading cycle as the deformation is almost purely elastic [80]. Once the penetration depth becomes

larger than the tip radius (usually in the order of 50 - 150 nm for a Berkovich), the pyramidal shape of the indenter becomes the dominant geometrical feature of the indentation and the behavior becomes elastic-plastic. Thus the deformation has the property of geometrical similarity and equations of contact for a conical indenter can be used [81].

The Oliver and Pharr (O&P) method as well as some refinements introduced in their analysis since 1992 are developed in the next subsections. A focus is made on the possible sources of errors and uncertainties arising during the experiments and on their influence on the mechanical properties calculated.

2.2.1 Oliver and Pharr's method: determination of hardness and Young's modulus

Hardness and Young's modulus are the two mechanical properties measured most frequently using nanoindentation techniques. Based on previous work done by Sneddon [82], the O&P method consists in the analysis of indentation load-displacement data according to a model of the penetration of a flat elastic half space by a paraboloid of revolution, assuming the unloading behavior of the material is characterized by elastic recovery only [75].

Figure 2.13 shows the schematic of the indentation process for an axisymmetric indenter of arbitrary profile.

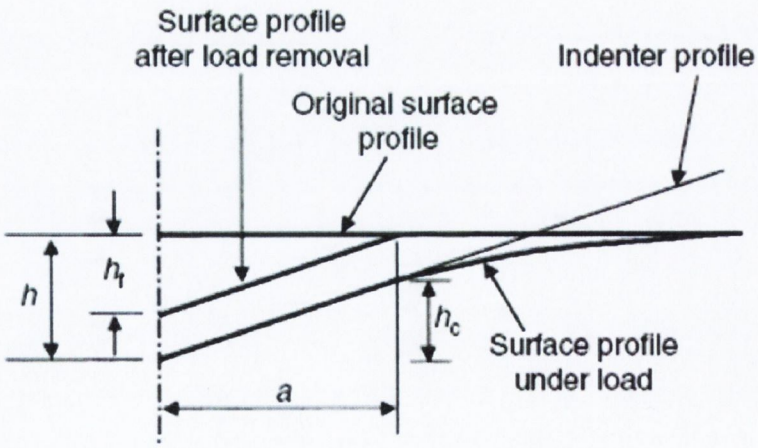

Figure 2.13: Schematic representation of a section through an axisymmetric indentation showing various quantities used in analysis (From Hay et al. [77]).

An example of the load (P) - displacement (h) curve obtained during one cycle of loading and unloading is drawn in Figure 2.14.

During loading, both elastic and plastic deformation processes occur, producing a hardness impression that conforms to the shape of the indenter to some contact depth h_c, with a circle of contact of radius a. If the contact is fully elastic, the unloading curve lies on top of the loading curve. For an elastic-plastic contact, the unloading curve is different from the loading curve and the area enclosed between them is related to the energy lost during plastic deformation (the plastic part of the work of indentation is represented by the blue area in Fig. 2.14). The elastic part of the indentation work is represented in Fig. 2.14 by the purple area and corresponds to the area under the unloading curve. The total work of indentation is the area under the loading curve.

The O&P method assumes there is no plastic deformation occurring during unloading. Thus, the unloading curve can be used for the calculation of both E and H.

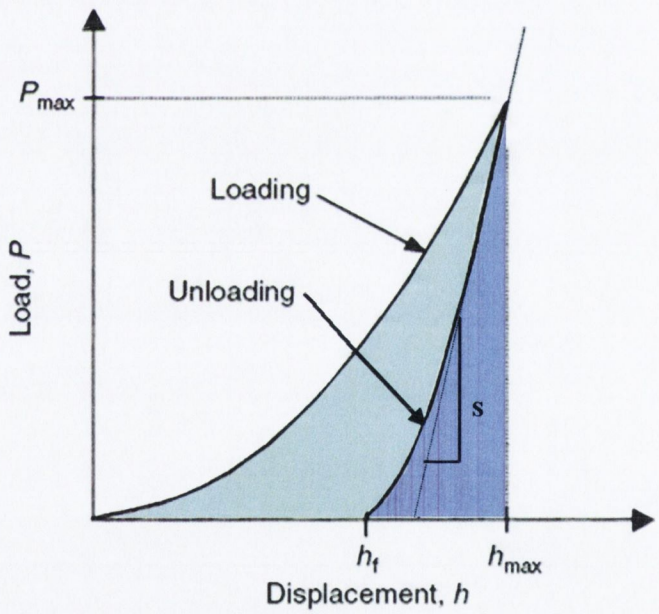

Figure 2.14: Schematic representation of indentation load-displacement data during one complete cycle of loading and unloading (Adapted from Hay et al. [77]).

During the initial loading of the indenter, elastic and plastic deformations occur and the indenter conforms perfectly to the shape of the hardness impression. However, during unloading, elastic recovery causes the hardness impression to

change its shape. Thus, the unloaded shape is not perfectly conical but exhibits a subtle convex curvature [78]. This induces a continuous change in the contact area as the indenter is withdrawn from the material and this continuous change in the contact area produces non-linear unloading curves.

The unloading curve can be accurately described by the power law relation:

$$P = B\,[h - h_f]^m \tag{2.19}$$

where h_f is the final residual depth measured from the original specimen free surface, (h - h_f) is the elastic displacement and B and m are material constants.

The contact stiffness is defined as the slope of the upper portion of the unloading curve evaluated at the maximum depth of penetration h_{max}:

$$S = \left.\frac{dP}{dh}\right|_{h=h_{max}} \tag{2.20}$$

Assuming that that pile-up is negligible, the elastic model shows that the depth h_c along which contact is made between the indenter and the specimen is:

$$h_c = h_{max} - \epsilon \frac{P_{max}}{S} \tag{2.21}$$

where P_{max} is the maximum indentation load and ϵ is a geometric constant equal to 0.75 for a paraboloid of revolution.

Then, the fundamental relation from which the hardness is calculated is:

$$H = \frac{P_{max}}{A} \tag{2.22}$$

where A is the projected contact area evaluated at peak load and is a function of h_c. In this case, the hardness is defined as the mean pressure the material will support under load and is called the standard hardness. If there is significant elastic recovery during unloading, the standard hardness may be different from the true hardness, in which the area is obtained by direct measurement of the size of the residual hardness impression during traditional hardness tests at higher length scales. As H can be determined at any stage during loading, the term 'mean contact pressure' may be more appropriate than 'hardness' because it may characterize plastic as well as elastic contact [24].

Measurement of the elastic modulus is obtained through the two following relations:

$$E^* = \frac{\sqrt{\pi}}{2} \frac{S}{\sqrt{A}} \tag{2.23}$$

where E^* is the reduced elastic modulus. It is used to account for the fact that elastic displacements occur in both the indenter and the sample so E^* is the combined elastic modulus of the bodies in contact. E^* is given by:

$$E^* = \left[\frac{1-\nu^2}{E} + \frac{1-\nu_i^2}{E_i} \right]^{-1} \tag{2.24}$$

where E and ν are Young's modulus and Poisson's ratio for the material indented and E_i and ν_i are the same parameters for the indenter. For a diamond indenter, $E_i = 1141\ GPa$ and $\nu_i = 0.07$.

2.2.2 Corrections of nanoindentation data

The method developed in 1992 by Oliver and Pharr has been widely adopted for characterization of small-scale mechanical behavior. Since its original development, this method has undergone numerous refinements and changes.

2.2.2.1 Refinements of Oliver and Pharr's method

As described previously, the power law describing the unloading curve is:

$$P = B\,[h - h_f]^m \tag{2.25}$$

and the contact stiffness is defined as the slope of the upper portion of this curve. The calculation of S is based on the initial stages of unloading; therefore, the portion of the curve used for calculation of the slope S should be chosen with caution. The ISO standard on instrumented indentation testing (ISO 14577 [83]) recommends using 80% of the unloading data, in which case the fitting procedure becomes very important.

As B, m and h_f are unknown quantities, the best fitting of the unloading curve is obtained by using an iterative procedure based upon a least squares approach [83, 81].

Moreover, determination of the depth h_c along which contact is made between the indenter and the specimen is done using a constant ϵ. Based on previous work done by Sneddon [82], Martin at al. [80] showed that the geometric constant ϵ can be directly determined from m, which is obtained from the fit of the unloading curve:

$$\epsilon = m \left[1 - \frac{m-1}{m\left[\chi\left[\frac{m}{m-1}\right]\right]} \right] \tag{2.26}$$

with:

$$\chi(k) = \int_0^1 \frac{x^k \, dx}{\sqrt{1-x^2}} = \frac{\sqrt{\pi}}{2} \frac{\Gamma(\frac{k+1}{2})}{\Gamma(\frac{k+2}{2})} \tag{2.27}$$

and:

$$\Gamma(k) = \int_0^\infty e^{-x} \, x^{k-1} \, dx \tag{2.28}$$

As in the original O&P method, the unloading deformation is assumed to be purely elastic.

Furthermore, experiments and finite element analysis done by Hay et al. [77] showed that the introduction of a correction factor γ in the calculation of S was needed to take into account radial displacements of surface points inside the circle of contact. This has led to a new equation for E^*:

$$E^* = \frac{1}{\gamma} \frac{\sqrt{\pi}}{2} \frac{S}{\sqrt{A}} \tag{2.29}$$

γ depends on the half-included angle α of the equivalent cone of the indenter and on Poisson's ratio ν of the indented material. It is calculated as follows:

$$\gamma = 1 + \frac{1-2\nu}{4(1-\nu)\tan\alpha} \tag{2.30}$$

2.2.2.2 Use of the Atomic Force Microscopy for pile-up or sink-in corrections

One of the most important sources of errors during the calculation of H and E is due to the fact that the method proposed by Oliver and Pharr is based on the assumption that the contact periphery sinks-in into the sample (cf Fig 2.13). However, either sink-in or pile-up can occur depending on the specific mechanical properties of the material (E, ν, the yield stress σ_y and the work hardening rate η) [84, 78]. Figures 2.15 and 2.16 show the phenomena of sink-in and pile-up and their incidence on the calculation of h_c.

When pile-up occurs, the material which has piled-up supports part of the load applied to the indenter and so the indenter penetrates less compared to the case where there is no piling-up. Classical methods for analyzing nanoindentation data do not take this phenomenon into account and the material appears to be stiffer and harder. Consequently, the analysis may underestimate the true contact area by as much as 60 %, leading to over-estimations of hardness and Young's modulus [84, 85, 81]. Moreover, pile-up of material can induce a relief in strain energy underneath the indenter, thus disturbing stress fields and crack initiation and propagation. Pile-up can be expected for instance in ductile soft materials

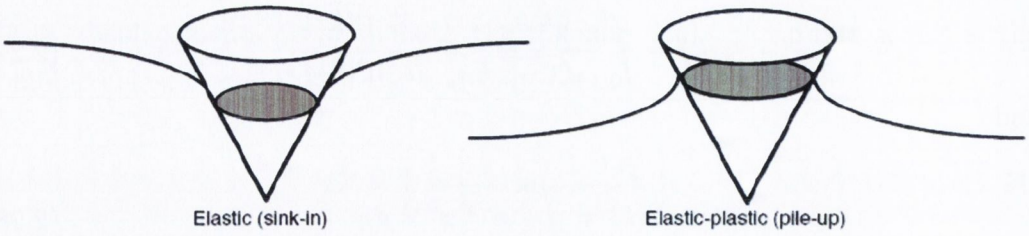

Figure 2.15: Sink-in and pile-up during indentation (From Hay et al. [77]).

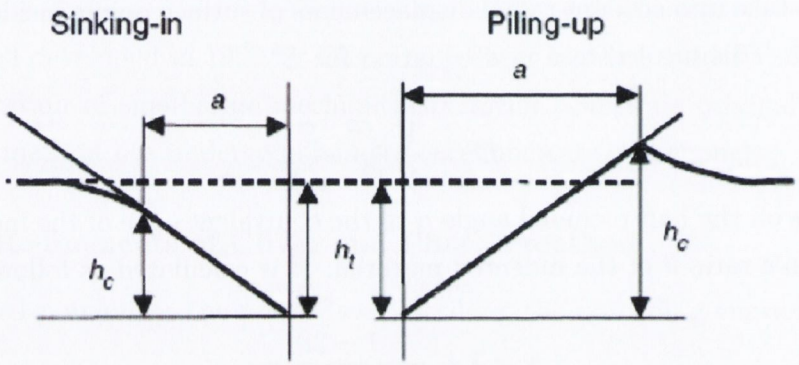

Figure 2.16: Schematic of piling-up compared to sinking-in (From Fischer-Cripps [81]).

or in soft films on a hard stiff substrate. In this last case, the plastic flow or displacement of the film material radially away from the indenter is restrained by the substrate [24, 86, 76].

Several authors have tried to find accurate means of determining the contact area with minimal errors in the E and H values measured in nanoindentation due to pile-up effect. This has involved measurement of the residual impression with a SEM [86], modifications to the way in which the contact depth is defined [87] and the use of finite element simulations [84, 76, 88, 78]. In recent years, Kese et al. [89–91] have introduced a method to take the pile-up phenomenon into account in the calculation of E an H from nanoindentation data, when using a Berkovich indenter. This method is based on approximating the area projected by the pile-up contact perimeter as a semi-ellipse and including this pile-up area in the analysis. Using the Atomic Force Microscopy (AFM) technique, indents are imaged and cross-sectional profiles of each of them are drawn, leading to an estimation of the pile-up contact area. This method gives results that are in good

agreement with reference data.

The AFM consists of a microscale cantilever with a sharp tip (probe) at its end that is used to scan the specimen surface. The tip radius of curvature is on the order of nanometers and when the tip is brought into proximity of a sample surface, forces between the tip and the sample lead to a deflection of the cantilever. Depending on the situation, forces that are measured in AFM include mechanical contact force, Van der Waals forces, capillary forces, chemical bonding,... The deflection of the cantilever is measured using a laser spot reflected from the top surface of the cantilever into a photodetector.

Used in non-contact mode, the AFM avoids alteration of the sample by tip contact. In this mode, the cantilever is oscillated at a frequency slightly above its resonant frequency where the amplitude of oscillation is typically a few nanometers ($<$ 10 nm). The Van der Waals forces, which are strongest from 1 nm to 10 nm above the surface, or any other long range tip-sample interaction forces which extend above the surface act to modify the oscillation amplitude, phase and resonance frequency of the cantilever. The feedback loop system then maintain a constant oscillation amplitude or frequency by adjusting the average tip-to-sample distance. The measurement of the tip-to-sample distance at each (x,y) data point allows the scanning software to construct a topographic image of the sample surface.

Figure 2.17 shows a schematic diagram of a Berkovich indent with only one pile-up lobe represented (for clarity of illustration), and a radial cross-section through this pile-up lobe. Kese et al. [89] showed that the projected pile-up area at every indent made with a Berkovich indenter could be calculated by approximating each pile-up lobe as a projected semi-ellipse of major axis b and minor axis a_i. b is calculated as the side of an equilateral triangle at the contact depth h_c while a_i is measured on the indent profile image as the horizontal distance of the pile-up contact perimeter T from the edge L of the indentation. Using the AFM, cross-section profiles of every indent can be drawn and used for the measurement of a_i for the determination of the projected pile-up area.

Then, the total area of contact is simply obtained by the addition of the projected pile-up area to the area calculated using Oliver and Pharr's method.

2.2.2.3 Specimen preparation and detection of the surface

Surface roughness is extremely important in nanoindentation testing because the contact area from which E and H are deduced is calculated from the contact depth and area function on the presumption that the surface is flat [77]. Moreover,

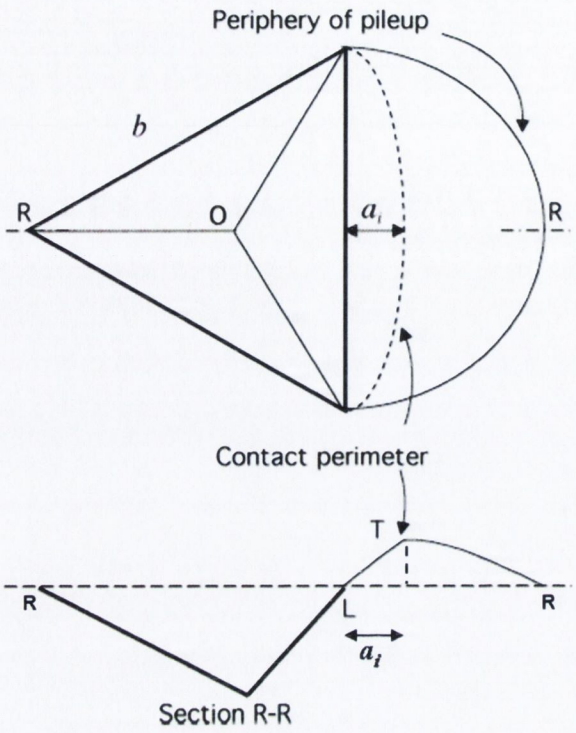

Figure 2.17: Schematic diagram of a Berkovich indent with one pile-up lobe drawn and its cross-sectional profile (Adapted from Kese et al. [89]).

surface roughness causes an uncertainty in contact area due to asperity contact at very shallow indentation depths. This highlights the importance of polishing and surface preparation.

In many materials, residual stresses, tensile or compressive, may be present within the specimen as a result of processing (temperature induced) or surface preparation (cold working from polishing). These residual stresses, as well as the specimen surface states (presence or not of micro-asperities and pre-existing micro-cracks) can affect the indentation deformation and should be taken into account during specimen preparation.

Another important parameter is the determination of the initial contact between the indenter and the specimen. The initial zero penetration needs to be carefully identified as an error in determining it could lead to inaccuracies in the final depth h_f determination and in all the mechanical properties calculated from h_f.

The Continuous Stiffness Measurement (CSM) technique permits the continuous measurement of the contact stiffness S during the loading portion of the test. This is accomplished by superimposing a small oscillation on the force signal and

measuring the displacement response at the same frequency. The data obtained using this technique can be used to provide a continuous measurement of H and E as a function of depth in a single experiment. More importantly, the CSM technique permits accurate determination of the initial contact with the surface as for hard materials such as ceramics, the harmonic contact stiffness increases dramatically after contact [78].

2.2.2.4 Environmental control

Uncertainties and errors in measured displacements can arise from two separate environmental sources: vibrations and variations in temperature. To minimize vibrations, most testing systems are mounted on vibration-isolation systems. The second source of uncertainties, thermal drift, is particularly important for small indentations. Small thermal fluctuations cause thermal expansion or contraction of both the sample and testing system. However, the expansion of the machine components is manifested in the data as an apparent displacement in the specimen [75] and this may lead to inaccuracies. To account for thermal drift, the rate of displacement can be measured during an hold period at low load (to minimize any creep effects) and the displacement data corrected by assuming that this drift rate is constant throughout the test. In this procedure, it is implicitly assumed that the displacements measured at the low load during the hold period are due mostly to thermal expansion rather than to time dependent plasticity in the specimen. Good technique requires thermal drift correction to be performed individually for each indentation [77]. It is usually done by including a period near the end of the test during which the load is held constant at 10 % of the maximum indentation load.

2.2.2.5 Calibration issues

As with most measurement systems, calibration is essential for limiting uncertainties and achieving reproducible and repeatable measurements. Calibration of load and displacement (the two main parameters recorded during the experiment) are usually provided by the manufacturer using procedures specific to the machine.

Two other very important parameters need to be calibrated in order to obtain accurate measurements of mechanical properties by nanoindentation: the area function of the indenter and the load frame compliance.

The area function of the indenter relates its cross-sectional area A to the distance back from its tip (i.e the contact depth h_c). Determination of the area

function of the indenter is of great importance as both H and E values are calculated from it through equations 2.22 and 2.29. Area function calibration is usually done by performing several indents over the whole load range of the instrument [81] in a reference material of well-known elastic properties such as fused quartz. Due to its amorphous nature, this material is isotropic and because it is not subject to oxidation, its near surface properties are similar to its bulk properties and do not depend to a large degree on the depth of penetration [77]. Furthermore, fused quartz is not subject to pile-up and exhibits no time dependence when indented at room temperature, thus making it an interesting material for calibration purpose.

A general form that is often used for the area function is:

$$A = C_1 h_c^2 + C_2 h_c + C_3 h_c^{1/2} + C_4 h_c^{1/4} + C_5 h_c^{1/8} + ... + C_8 h_c^{1/128} \tag{2.31}$$

where C_1 through C_8 are constants. The first term $C_1 h_c^2$ represents the area function of a perfect indenter while the additional terms describe deviations from this perfect geometry (due to blunting of the tip for instance). In a reference material having both E and H independent of depth, tip shape calibration can be checked by plotting the E vs h data which should give a constant line [92].

Another method used for the indenter area function calibration is the AFM imaging of the indenter tip [92].

The second calibration issue concerns the load frame compliance. In fact, the measured displacements are the sum of the displacements in the specimen and in the load frame. Thus, to access the specimen displacement, the load frame compliance must be known with precision, especially during large indentations made in materials with high E value for which the load frame displacement can be a significant fraction of the total displacement [75]. Calibration of the load frame compliance is usually done using a reference materials (such as fused silica) that is homogeneous and isotropic and for which both E and ν are known [78, 81]. Checking of the load frame compliance calibration can be done in a reference material by plotting the ratio of load to contact stiffness squared P/S^2 vs h data at depths greater than a few hundred nanometers. This ratio should be independent of depth regardless of the tip shape function [92, 78]. The area function can then be calculated using a standard material using the frame compliance value found.

2.2.2.6 Indentation Size Effect

One of the most well-known issues of nanoindentation results is the Indentation Size Effect (ISE). In some materials, indentation tests at scales on the order of

one micron have shown that the measured hardness and/or modulus increase significantly with decreasing indent size [12, 7]. This effect is due to the presence of strain gradients in the vicinity of the indentation and as been described by Nix and Gao [6]. As shown schematically in Fig 2.18, when the indenter is loaded into the surface, the indentation is accommodated by circular loops of geometrically necessary dislocations with Burgers vectors normal to the plane of the surface. These dislocations are required to account for the permanent shape change at the surface. When loading, the amount of dislocation loops necessary to accommodate for the shape of the indenter (i.e. geometrically necessary dislocations) scales linearly with the contact area. However, as plastic deformation is confined within an hemispherical shape, this results in a strain gradient. The varying density of the geometrically necessary dislocations with the indent size thus accounts for a size dependence of the plastic strain gradient. As the indentation depth becomes smaller, the increase in yield strength due to these dislocations becomes more pronounced and this in turn means an increase in hardness.

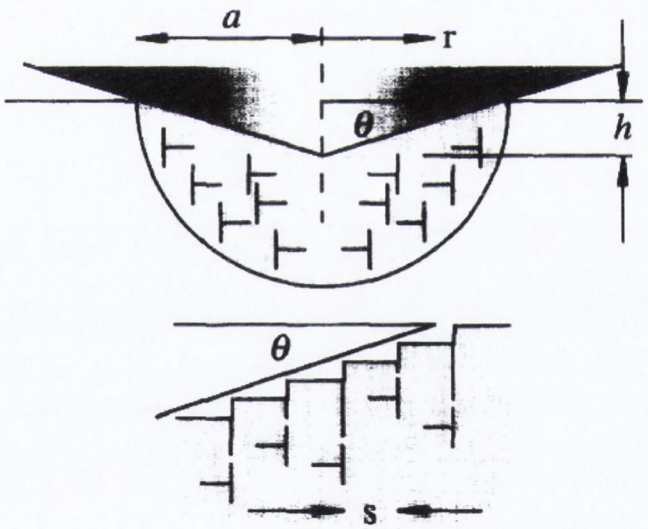

Figure 2.18: Geometrically necessary dislocations created by a rigid conical indentation. The dislocation structure is idealized as circular dislocation loops. θ is the angle between the surface of the conical indenter and the plane of the surface, a the contact radius, h the depth of indentation and s the spacing between individual slip steps on the indentation surface (Adapted from Nix et al. [6]).

2.2.2.7 Other issues

The O&P method is based on the fact that the unloading behavior of the material is purely elastic. However, this is not always the case.

Performing multiple loadings and unloadings is a current method to examine the reversibility of the deformation in a given material in order to be sure that the unloading data used for analysis are mostly elastic [75, 93].

When performing repeated loadings/reloading cycles, the behavior of the materials studied may exhibit some variability. If the unloading and reloading curves of a material trace one another perfectly, this suggests that deformation in this material after the initial loading is entirely elastic. This is the case for fused silica, sapphire and quartz for instance [75].

In some materials, displacements recovered during first unloading may not be entirely elastic but this small amount of reverse plasticity tends to disappear with consecutive loadings/unloadings. This is the case for soda-lime glass for instance.

Finally, some specimens may experience time dependent deformation (creep or viscoelasticity) like aluminium or tungsten. In these case, part of the measured displacement is due to some plastic deformation occurring after the initial loading. Time-dependent creep and/or viscoelastic deformation manifest themselves as a change of the indentation depth with a constant test force applied, giving abnormally high contact stiffnesses that affect the calculation of E and H.

Because of these two nonelastic effects (reverse plasticity and time dependent deformation), the use of the first unloading curve in the analysis of elastic properties can lead to inaccuracies. One way to minimize this is to include peak load hold periods in the loading sequence to allow time dependent plastic effects to diminish (for materials exhibiting short-lived creep responses)[77], and to use unloading curves obtained after several cycles of loading to minimize effects of reverse plasticity [75]. Then analyses are performed using the final unloading data only.

Another good practice during nanoindentation testing is to separate successive indentations by at least 20 to 30 times the maximum depth when using a pyramid indenter (Berkovich or Vickers) to avoid interferences between residual stress fields or crack systems of successive indents. Moreover, the test piece thickness should be at least ten times the indentation depth or three times the indentation diameter, whichever is greater [83].

Finally, as suggested by Petit et al. [69], care should be taken when using nanoindentation instruments in the micrometer range on brittle materials. They pointed out some issues like the critical influence of microcracking and the effect

of instrument compliance and/or fixture device. These two effects cannot be neglected at elevated loads and can lead to wrong H and E estimates. In order to use instrumented micro-indentation technique to evaluate E and H using O&P method, they recommend to avoid any micro-displacement during indentation by rigidly maintaining the samples, to prevent any surface damage during polishing and finally, to work at moderate loads (typically below 1000 mN) in order to avoid cracking and crushing of samples during indentation. Krell et al. [94] also pointed the influence of cracking on the increasing compliance and penetration in the specimen. Following Petit et al. recommendations, E and H values obtained by instrumented indentation could be in good agreement with those obtained using conventional techniques. The small difference they found for hardness values between instrumented indentation and conventional techniques is probably due to the elastic recovery occurring during unloading, as classical methods for determining H are based on the measurement of the residual impression whereas ITT uses the contact area prior to unloading [69].

2.2.3 Influence of microstructure on nanoindentation results

Microstructure has long been recognized as having an influence on nanoindentation results on polycrystalline ceramics [17, 18, 2, 20, 19, 25, 69] although nanoindentation tests have still been applied to characterize their mechanical properties. In fact, microstructural inhomogeneity can significantly change the material compliance and affect the load/depth curves in a critical manner. The microstructural heterogeneity of polycrystalline ceramics results from the presence of porosity, different phases, anisotropy, etc.

This heterogeneity can induce internal residual stresses or micro-cracks. In alumina, these stresses result from thermal expansion anisotropy and crystallographic misorientation across the grain boundaries. The magnitude of these residual stresses depends on the grain size and degree of texture in the materials [69]. For instance, coarse-grained alumina is more sensitive to residual stresses with a higher risk of grain boundary cracking and pull-out during polishing or indenting. These internal residual stresses and micro-cracks have a significant influence on the indentation behavior. For instance, they may induce matrix grains pull-out during indentations which leads to a decrease in E values [69].

The other effect of heterogeneity is that below a certain load or depth of penetration, the indentation only concerns a part of the material (indentation

in one particular phase for instance) and the response is dominated by the local rather than the bulk properties. This in turn leads to a large scatter in the E and H values measured.

The same effect (scatter in H and E values measured) arises in polycrystalline isotropic materials when the volume indented becomes of the same order as the mean grain size. If the mean grain size is much smaller than the indentation size, indentation modulus and Young's modulus are expected to be equivalent for an isotropic material because of the weighted averaging over a large number of grains. In this case, the indentation results are representative of the bulk material property. In the other case (when the volume indented becomes of the same order as the mean grain size), the indentations can only concern single isolate grains rather than a larger part of the microstructure, leading to a large scatter in the E and H values obtained. For instance, Gong et al. [25] have analyzed results of nanoindentation experiments on high-purity, fine-grained alumina ceramics and concluded that H and E deduced from the analysis should be treated as the local, rather than the bulk mechanical properties of the test material.

Another example of the influence of grain size on mechanical properties is given by the Hall-Petch effect, which is the increase observed in yield strength of polycrystalline materials with decreasing grain size. This effect is due to the fact that grain boundaries impede dislocation movement and that with decreasing grain size, a larger applied stress is required to generate dislocations in the adjacent grains than within one grain. The Hall-Petch relation concerns mechanical properties like the yield strength, the hardness [13, 14] or even the stress intensity K [15] in materials within grain size ranging from 1 millimeter to 1 micrometer. It is another example of the influence of microstructure on mechanical properties measured at small scale.

Below a critical grain-size in nanocrystalline materials (typically below 100 nm), the inverse effect exists and is called the inverse Hall-Petch effect. In this case, the yield stress decreases with decreasing grain size and this thought to be due to dislocation absorption by grain boundaries [16].

For anisotropic materials, a question still remains as to what the modulus and hardness measured by load and displacement sensing indentation techniques represent [75]. On the one hand, it can be argued that the most appropriate modulus is that in the direction of testing, since the elastic displacements are primarily in this direction. On the other hand, since the formation of the contact impression involves deformation in many directions, it can be argued that the measured modulus should be some average quantity.

2.2.4 Fracture toughness measurement

Fracture toughness at small scales can be measured by nanoindentation using techniques similar to those developed at larger scale (cf section 2.1.5.4). These techniques are based on the measurement of the length c of surface cracks which occur when brittle materials are indented by a sharp indenter such as a Vickers or Berkovich diamond.

The most popular model used in micro- and nanoindentation experiments is the one from Anstis et al. [17] and is directly derived from the equation defined at larger scale. The evaluation of K_c is done using different values for the constant α depending on the geometry of the indenter. This constant is evaluated at 0.016 for both the Vickers and Berkovich indenters [95]. For a cube-corner indenter, Harding et al. [66] found a value of 0.036 for α while Pharr et al. [95] found a value of 0.0319.

All models for K_c are based on several assumptions previously described in section 2.1.5.4. They are all derived from Linear Elastic Fracture Mechanics and can be classified in three basic types: elastic models, elastic-plastic models and residual stress models (see section 2.1.5.4).

An attractive feature of using these methods in nanoindentation is that P, E and H can be determined directly from the analysis of the nanoindentation load-displacement data and c from direct observation of the surface. However, one difficulty of the technique consists in indenting above the cracking threshold, which is the load below which indentation cracking does not occur. This cracking threshold is material specific and also depends on the indenter geometry. For example, indenting with a cube-corner will produce an approximately equal projected contact area as when indenting with a Berkovich but the cube-corner indenter displaces more than three times the volume of material displaced by the Berkovich. Thus, the cube-corner produces greater stresses and strains in the surrounding material, enabling crack nucleation and propagation at lower loads than when using the Berkovich indenter [95, 66]. Nevertheless, the cube-corner geometry can't always be used for fracture toughness measurements as sharp indenters can produce the pushout of individual grains from around the indenter in polycrystalline materials. It can also induce the chipping of lateral cracks, especially at high loads, creating pile-up and impeding the calculation of K_c as the fracture toughness measurement method relies on the formation of radial cracks [95, 66].

However, indentation on polycrystalline ceramics presents many challenges to the assumptions underlying all the existing models. Application of these models

to indentation of ceramics face many issues, especially at small scale, which have been described in details in section 2.1.6. As a consequence, a simple measurement of P, E, H and c is unlikely to reflect adequately the balance between elastic and plastic behavior on these materials and the influence of microstructure on crack initiation and propagation. A complete change is expected in actual crack shape and area from the idealized median-radial and shallow radial crack ones, due to all the phenomena described in section 2.1.6. In this case, contrary to the classical approaches for the determination of indentation fracture toughness which are based on assumptions of linear elastic mechanics, an energy approach may be more appropriate to describe the indentation fracture process in polycrystalline ceramics at small scale.

Although subject to questions about its applicability in the measurement of fracture toughness in the case of ceramics at small scale, microindentation testing has been used in this study to induce cracks and to determine elastic and plastic deformations occurring when the indentation is performed. In order to investigate the subsurface cracking behavior of these optically opaque ceramics after microindentation experiments, Focused Ion Beam (FIB) microscopy has been used in this project. A review of FIB technology is presented in the next section.

2.3 Focused Ion Beam microscopy

Focused Ion Beam (FIB) is a recent technique that has been developed during the late 1970s and the early 1980s. FIB systems operate in a similar way to Scanning Electron Microscopes (SEM). However, instead of using an electron beam, FIB microscopes use a finely focused beam of ions (usually Ga^+) that can be operated at low beam currents for imaging or at high beam currents for site specific sputtering or milling. Coupled with a SEM, FIB can be used to mill and image cross-sections of a volume of interest. This technique is referred to as FIB tomography and allows the image reconstruction of 3D microstructural data.

One of the biggest advantages of FIB-SEM over other tomography techniques (3D atom probe tomography, tomographic transmission electron microscopy, X-ray microtomography) is that it is suitable to study submicrometer- and micrometer-size samples [96]. The ion column also contains a wide range of apertures and the associated beam currents vary from a few picoamps to several nanoamps, enabling the study of materials in a large magnification range. Moreover, contrary to other high-resolution microscopy techniques like SEM, TEM (Transmission

Electron Microscopy) or AFM (Atomic Force Microscopy) which are limited to two-dimensional imaging, it is possible with the FIB to access 3D geometries. Using X-ray microtomography, it is also possible to investigate 3D microstructure but this technique doesn't have a sufficient resolution to detect microcracks in a massive specimen.

All these reasons have made the FIB as a relevant tool in this study to investigate subsurface cracks formed during indentation experiments as well as their interaction with the microstructure.

2.3.1 Principle of the FIB instrument

Like the SEM, the FIB requires a high vacuum environment. The ion beam is generated from a liquid metal ion source by the application of a strong electric field. The charged particles emitted by the liquid source under the electric field are then focused onto the sample surface by lenses. Contrary to SEM, electromagnetic lenses are not of sufficient strength to focus the heavy ion beam and so ion columns use electrostatic lenses [97].

Most FIB microscopes use a gallium ion source although ion sources based on elemental gold and iridium are also available. Ga is more often used as it has a low melting point (29.8 °C) and therefore exists in the liquid state near room temperature and also because Ga can be focused to a very fine probe size ($<$ 10 nm in diameter) [98]. The most recent ion source seen in commercially available instruments is a helium ion source, which is less inherently damaging to the sample than Ga ions.

The FIB can raster the beam across the surface of a specimen to generate a signal that can be used for imaging. Alternatively, the beam can be fixed on a specific location. This leads to localized sputtering and milling on the specimen surface.

Fig. 2.19 shows the three different uses of the incident ion beam: imaging (a), milling (b) and deposition (c).

When the gallium ion beam hits the sample surface, it sputters a small amount of material, which leaves the surface as either secondary ions or neutral atoms. This effect is exploited for substrate milling (Fig. 2.19 (b)). Modern FIBs can deliver tens of nanoamperes of current to a sample and this high energy beam can be applied to remove material locally in a highly controlled manner, down to the nanometer scale.

The interaction of the primary ion beam with the sample surface also produces secondary electrons which like the sputtered secondary ions can be collected to

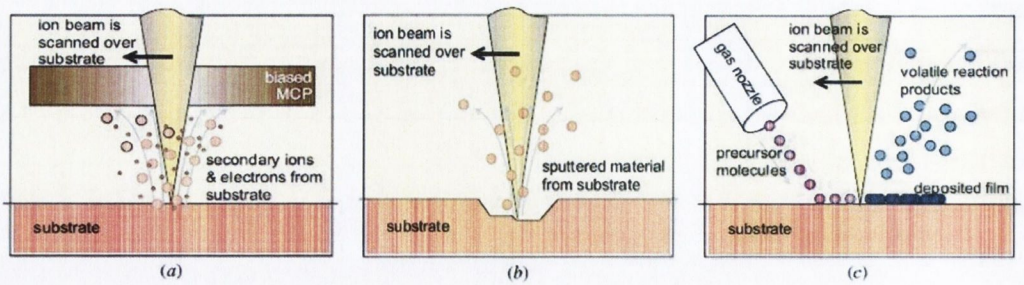

Figure 2.19: FIB applications: (a) imaging, (b) milling, (c) deposition (Adapted from Reyntjens et al. [99]).

form an image as the primary beam rasters on the sample surface. This permits to obtain electron and ion images (Fig. 2.19 (a)). At low primary beam currents, very little material is sputtered and modern FIB systems can easily achieve 5 nm imaging resolution. FIB secondary electron images show intense grain orientation contrast as a result of a variation in the ion penetration depth. This is due to ion channeling through different crystallographic directions in the different grains exposed to the ion beam at different angles of incidence [98, 99]. As a result, grain morphology can be readily imaged and grain size determined without resorting to chemical etching. FIB secondary ion images reveal chemical differences, and are especially useful in corrosion studies as FIB secondary ion images are particularly sensitive to the presence of oxides and carbides in metallic systems.

Incident ions hitting the surface of a solid sample induce other physical effects like displacement of atoms in the solid (induced damage) and emission of phonons (heating) [99].

Finally, they induce chemical interactions including the breaking of chemical bonds and thereby the dissociation of molecules (this effect is exploited during deposition (Fig.2.19 (c))). Localized maskless deposition of metal or insulator materials can be made by FIB-assisted Chemical Vapor Deposition (CVD). This technique consists of introducing a gas to the vacuum chamber so that it can be adsorbed onto the sample. By scanning the region of interest with the ion beam, the precursor gas will be decomposed into volatile and non-volatile components; the volatile reaction product will desorb from the surface and be removed through the vacuum system while the non-volatile component will remain on the surface as a thin film [99]. This deposited material can be used as a sacrificial layer for instance, to protect the underlying sample from the destructive sputtering of the beam. Materials such as platinum, cobalt, carbon, tungsten, silicon dioxide and

gold are the most commonly deposited elements.

The ejected secondary ions can also be collected for Secondary Ion Mass Spectrometry (SIMS) of the target material in a mass spectrometer attached to the system [99].

Unlike SEM, FIB is inherently destructive to the specimen. High energy gallium ion beam induces damaged artifacts on the surface of the specimen and this has been reported widely in literature [98–100]. The expected damage caused by the Ga^+ ion beam on the surface of the sample includes implantation of gallium ions, amorphization of the outer layer of the specimen, loss of fine structural detail and mixing of components due to Ga ions implanted and to redeposited material [98, 99]. Most of the Ga^+ ions that arrive at the surface enter the sample. Therefore, some of them stay implanted in it into the top few nanometers of the surface. As ions are much larger than electrons, they cannot easily penetrate within individual atoms of the sample. Interaction then mainly involves outer shell interaction resulting in atomic ionization and breaking of chemical bonds of the substrate atoms. The penetration depth of the ions is much lower than the penetration of electrons of the same energy and when the ion has come to a stop within the material, it is caught in the matrix of the material. Energetic ions that enter the sample can also create point defects (vacancies and interstitials) which congregate to generate a large number of dislocations. This effect occurs mostly in softer or more weakly bonded materials like metals [97]. The depth of the implanted region and the thickness of the amorphous layer depend on the material, the ion energy and the angle of incidence [101]. These effects can be prevented by depositing a layer of platinum or other metal on the area of interest prior to FIB processing or by using a finer ion beam. However, even when using a fine ion beam (fine spot and low ion current), some milling always occurs when the ion beam is scanned across the sample surface.

Devices referred to as Dual Beam instruments combine an ion column together with an electron column in one single apparatus. These instruments thus combine all the capabilities of FIB with SEM, allowing the same feature to be investigated using either of the beams. Fig. 2.20 presents a schematic of the column layout of the dual beam system with the electron and ion columns separated by an angle of around 52 °.

In such instruments, the ion beam is predominantly used for sputtering and the electron beam for imaging due to its non-destructive property. Electron Backscatter Diffraction (EBSD) and Energy-Dispersive X-ray (EDXS or EDX or EDS) analysis can also be done using Dual Beam instruments as, contrary to the

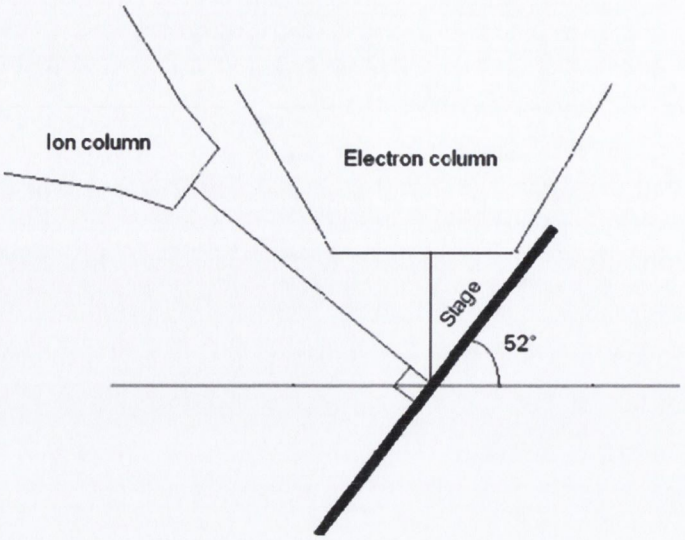

Figure 2.20: Geometry of a dual beam instrument.

ion beam, the energetic electron beam generates signals such as characteristic X-rays and backscattered electrons. EBSD is a particularly powerful tool to measure textures, grain size and misorientation of individual grains in a sample.

2.3.2 Applications of the FIB

FIB technology has a wide range of applications, especially in the semiconductor industry, due to its ability to mill and deposit conductors and insulators with high precision. It is widely used in device modification, wafer repair, maskless fabrication, lithography, process control, failure analysis and micromachining applications for MEMS [99, 100, 97].

FIB is often used in the semiconductor industry to patch or modify an existing semiconductor device. For instance, in an integrated circuit, the gallium beam can be used to cut unwanted electrical connections, and/or to deposit conductive material in order to make a connection. FIB is also used as a maskless micromachining tool, to machine materials at the micro- and nanoscale by milling and deposition [101]. FIB micromachining is particularly useful because it permits a high flexibility in the shapes that can be realized and because of the attainable resolution (5 nm for imaging, a bit less for milling and deposition). Moreover, during fabrication process, FIB can be used to check and measure the dimensions and shapes of the realized structures [99].

The FIB is also widely used in physical and biological sciences for Transmis-

sion Electron Microscopy (TEM) sample preparation due to its small beam size and imaging capabilities [98, 100, 101]. The TEM requires very thin samples to transmit an electron beam, typically 100 nanometers or less and is used to investigate chemical composition and structural information (i.e. dislocation activity, crystal structure, crystallinity) of a solid-state sample on the nanometer scale [98, 99, 101]. Using the FIB, material can be removed from both sides of the desired section which can be polished using a thin ion beam to make it transparent to electrons. Thin samples machined with the FIB are also needed in integrated circuit failure analysis.

Other applications of the FIB in material sciences include the characterization of the material microstructure and analysis of subsurface damage. These applications are reviewed in more details in the next two subsections.

2.3.2.1 FIB tomography

Inkson et al. [102] first introduced a method commonly referred to as FIB tomography. It involves serial sectioning with the ion beam followed by imaging of each section using either the ion beam or the electron beam. This method allows the acquisition and image reconstruction of 3D microstructural data, specifically spatial distribution of phases, real feature shape and size and feature connectivity.

The principle of FIB tomography is illustrated in Fig. 2.21. A rough and fast single pass-mill is first use to remove material adjacent to the location of interest. This results in a steep sidewall on the side near the feature of interest. This sidewall is made perfectly vertical and smoothly polished with using a finer ion beam. Then the newly exposed surface is imaged with the electron beam. Repeating these steps several times until the desired volume has been removed results in a stack of images that can be combined with an appropriate software package to form a 3D image of the sputtered volume.

The technique consists in computer alignment and reconstruction of the 2D slices to generate a 3D data set of the analyzed zone. In order to investigate possible errors occurring during FIB tomography, Steer et al. [104] have compared the 3D FIB maps of the surface of a residual indent to the ones obtained using the AFM. They showed good correspondence between the two results even if the AFM maps are more accurate in this case. Actually, the main source of errors in the FIB mapping technique was caused by some inaccuracy in the alignment of the 2D slices and therefore in the determination of 3D position of material features which were to be mapped.

Using the combination ion beam for milling - electron beam for imaging, cross-

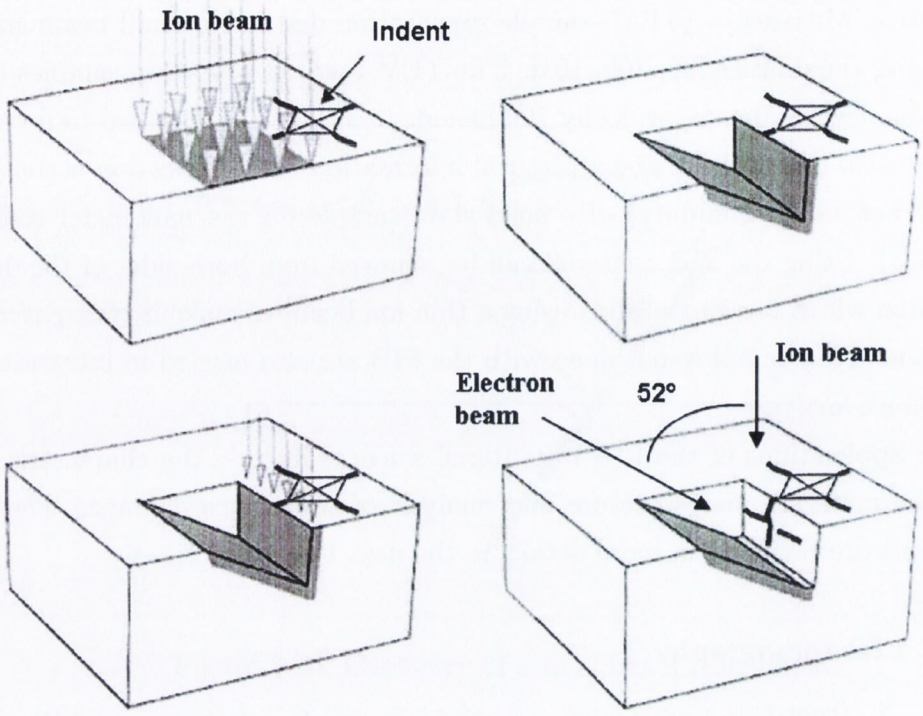

Figure 2.21: Schematic of FIB tomography technique (Adapted from Moon et al. [103]).

sectional 'slices' of the subsurface of the indent can be taken with few nanometers between each slice.

During a tomography experiment, EDXS analysis can be added on each freshly produced surface in order to make chemical microanalysis [105, 106]. Furthermore, in each serial section, electron backscattering diffraction (EBSD) analysis can also be made. It allows the identification of the difference phases, grains and interfaces in terms of their lattice parameters and crystallographic orientation respectively [106, 101].

However, during FIB tomography, EBSD analysis can only be performed on sample edge or on specimen surface. In the case of EBSD of cross-sections perpendicular to the sample surface, there is a problem of geometrical shadowing of the observed area, which impedes the collection of backscattered electrons.

2.3.2.2 Observation of subsurface microstructure and cracks with the FIB

The use of highly focused ion beams for subsurface microstructure investigation is a huge growth area. In materials science, FIB tomography is a powerful tool

to investigate complex microstructural features and capture the 3D morphology of complex materials. Many FIB applications for the characterization of three-dimensional (3D) micro- and nanostructures have been reported in the last few years [102, 107–111, 106, 112, 105, 113].

Another successful use of the FIB is the investigation of subsurface damage following surface contact [114, 104, 115, 116, 103, 117–120]. as subsurface cross-sections can be prepared rapidly with minimal damage. Metals and semiconductors are the more often studied materials [114, 108–110, 106, 111, 112, 121, 96], but recently, this method has also been applied on insulators, including biological materials or ceramics [107, 105, 113].

Previous investigations to study the subsurface cracking behavior of optically opaque materials have used different methods including:

- Sample sectioning perpendicular to the surface containing the cracks
- Decoration of cracks (the indentations are made into a solution dropped on the surface of the sample and this solution impregnates the cracks which open during the indentation cycle. After drying of the solution, the sample is broken in 4-point-flexure test and the impregnated cracks studied) [122]
- Stepwise surface layer removal by ceramographic polishing [122]

However, these methods introduce further damage to the material studied and are difficult to apply to small cracks. Moreover, the poor accuracy of the stepwise surface layer removal technique can result in the fact that the extent of the layers removed exceed the crack depth.

In recent years, FIB microscopy has begun to be used to produce 2D cross-sectional images through specific sites such as cracks or indents [116, 103, 114]. This technique permits the user both to mill precise sections in the observed area and to image them without the disadvantages of the other techniques presented above. Indeed, ion milling is a relatively gentle and damage-free process as compared to conventional mechanical grinding or polishing methods. Therefore, features such as pores or soft phases are preserved and can be studied.

Focused Ion Beam could be used to investigate crack profile (transgranular or intergranular, crack position, crack aspect ratio...), its interaction with the grain structures (morphology, orientation...) under a surface crack [114] or underneath an indent [116, 103, 123]. Accurate measurements of the crack length and of the crack positions around the indents can also be done as well as the investigation of the plastic deformation under nanoindentation sites [115].

Furthermore, FIB tomography is a very useful tool to investigate subsurface cracking behavior of optically opaque materials. Using FIB tomography, the position of distinguishable features can be mapped, for instance the position of interfaces and cracks in 3D around an indentation site. This method has been applied to different materials like Cu-Ti multilayers grown on an Al_2O_3 substrate [104, 115], Al_2O_3-5vol%SiC nanocomposite [102], single crystal alumina and soda-lime-silicate [119] and to an amorphous carbon coating [117] for instance. Holzapfel et al. [121] studied the interaction of microcracks with grain boundaries and precipitates in a Ni-based superalloy during fatigue tests. They showed that FIB tomography was a powerful tool for the reconstruction of the crack path of short cracks with respect to the local microstructure.

Using FIB tomography and 3D crack mapping, Wu et al. [124] studied the subsurface cracks made in alumina and in a nanocomposite after a scratch test and found a high density of microcracks under the scratches.

These investigations reveal that the FIB is a very interesting tool for the determination of the cracks developed during a nanoindentation experiment. For example, Inkson et al. [102], in their analysis of the subsurface of a 1N load indentation site (Vickers diamond tip) in an Al_2O_3-5vol%SiC nanocomposite, found radial and deep lateral cracks at the indent periphery, surface localized crack clusters and a crack deficient zone close to the indent center (zone of compressive stress with significant dislocation activity). This observation is in agreement with the cracks usually found under indentation sites of brittle materials at higher scale.

2.3.3 Limitations of using the FIB in our study

FIB tomography technique seems to be the most relevant tool to use in this project to study subsurface cracks produced during microindentation in ceramics. However, some inconveniences, due both to the nature of the material studied and to the FIB technique itself, can limit the applicability of FIB tomography in this study.

FIB tomography applications on insulators face several difficulties due to charging effects occurring either during ion milling or during electron imaging. For instance, during a fully automated slice&view sequence, it is necessary to compensate for beam shift or sample drift between the individual milling steps. Beam shift is caused by charging of the specimen due to insufficient conductivity of the milled trenches. The classical way to compensate this beam shift is by using reference markers on the surface (e.g., milled crosses) which are cut into the

surface near the milling site. Moreover, during FIB operations, a small amount of Ga^+ ions are implanted in the sample and large number of electrons leave the sample, resulting in positive charging building up at the surface of the specimen. This may lead to electrostatic damage in semiconductors or deflection of the ion beam. This issue can be avoided by flooding the substrate with electrons from a separate electron source [99, 97] but this method can only be used when collecting secondary ions for imaging. Although several authors have proposed some refinements to Inkson's technique in order to eliminate these charging effects [107, 105, 113], these developments are not all suitable in the case of our investigation, considering both the nature of the material studied (insulating) and the purpose of this study (the analysis of subsurface damage). All the difficulties coming from the insulating nature of our material have to be fixed in order to produce a set of 2D images suitable for the reconstruction of the microstructure and crack paths surrounding an indent. Charging effects will also produce artifacts within the specimen so the results need to be interpreted accordingly.

Although FIB has become widely used to produce cross-sectional images through indents and cracks, only a few studies have been made on localized geometry changes and surface damage generated by FIB processing on initial material stress states and existing cracks [118, 119, 125, 120]. Inkson et al. [118] have studied evolution of stress states under nanoindents and scratches in alumina samples during FIB processing. They have shown that for FIB cross-sections through indentation sites, the density of cracks observed depends on the location and milling procedure because cross-sectioning with the FIB alters local stress states. In a unidirectional sequential FIB sectioning of an indent, there is a systematic considerable decrease in the crack density observed from the first side of the indent to be sectioned to the second side. This can be explained by the fact that changes in surface geometry in a highly stressed region leads to some stress release. As the first side observed is close to the high residual stress concentration localized under the indent center, some stresses are released during the milling process participating to the opening of new cracks. On the contrary, when the second side of an indent is analyzed, the residual high stress zone present at the indent center has already been removed so the local stress are reduced and less cracks can open. This important result has to be taken into account later on in this study when interpreting images from the FIB, as it could lead to include cracks opened during the milling process in the crack pattern due to the indentation. Other researchers have also studied changes in local residual stresses during FIB tomography of indent sites in alumina using Cr^{3+} fluorescence spectroscopy

[125]. Soda-lime-silicate-glass has also been studied [120] and for both materials, a clear reduction in local residual stresses was observed in the second half of indents sectioned unidirectionally. This reduction in the local stresses lowers the driving force for crack opening at the FIB cross-section surface and some cracks close in this reduced stress environment. This in turn leads to a reduction in the observed crack density in the second half of the indent studied. As FIB sputtering induces changes in residual stress fields, existing cracks may also undergo an alteration of their topography, length and width of opening. Finally, during FIB milling, it may also happen that some FIB sputtering of material into fine cracks will mask their presence [118, 119, 125, 120], leading to an underestimation of the total crack surface area. However, Elfallagh et al. [120] found good correspondence between the major crack morphologies investigated with the FIB and the ones identified using optical methods, this highlighting the usefulness of the FIB technique in subsurface cracks analysis.

The changes in residual stress fields due to FIB processing, leading to errors when estimating the actual crack surface area or crack paths due to indentation and the issues coming from the insulating nature of the material studied are the two main difficulties to overcome in order to use FIB in this study. However, indentation experiments coupled with FIB tomography remain the most relevant tool in order to investigate fracture properties in ceramics at small scale. It will also permit to study any interaction between microstructure and small scale fracture process in these ceramics.

2.4 Summary

The determination of fracture properties of brittle materials at small scale is facing difficulties due to the influence of microstructure and surface properties. Indeed, conventional macroscale techniques to characterize fracture properties have shown their limits in the case of polycrystalline or multiphase ceramics at the microscale. Most of these techniques are based in Linear Elastic Fracture Mechanics for which the main assumptions are not valid anymore at small scale for brittle materials. The purpose of this work is to understand scale effects of microstructure on small scale fracture behavior using a novel approach: microindentation and study of the induced subsurface cracks using FIB tomography. An analysis of results, based on the quantification of energy dissipated during fracture process will be prioritized.

Chapter 3

Experimental methods

This project aims to investigate fracture properties of ceramics at the microstructural scale as conventional indentation fracture toughness models have shown their limitations.

A process flow chart for the experimental methods is shown in Fig. 3.1. Different microstructures have been indented in order to induce cracks. The use of the FIB reveals the actual microstructure as well as the true crack path within the indent subsurface and its interaction with the local microstructure. Calculation of the crack surface area has also been carried out and related to the energy dissipated during indentation.

3.1 Materials

Three materials with different microstructures have been studied in this project: alumina, Syalon 101 and Syalon 050.

Alumina (Al_2O_3) was chosen as the starting material for the following reasons: the alpha form (corundum) of the crystal has a simple microstructure of equiaxed grains that can be controlled by addition of small amounts of magnesia (MgO) or yttria (Y_2O_3) allowing for the influence of grain size on crack propagation to be analyzed. This material also has an average submicrometer grain size which is comparable to the scale of an indenter penetration depth during nanoindentation and this would permit to examine the effect of microstructural inhomogeneity. This high-purity, fine-grained alumina was also chosen because it is widely used in bioengineering (for example in wear applications in joint replacements) and in the micro-electronics industry (Al_2O_3 is commonly used as substrate in MEMS). It is also widely used as an abrasive and for wear-resistant components.

Alumina used in this project is the corundum form which is the naturally

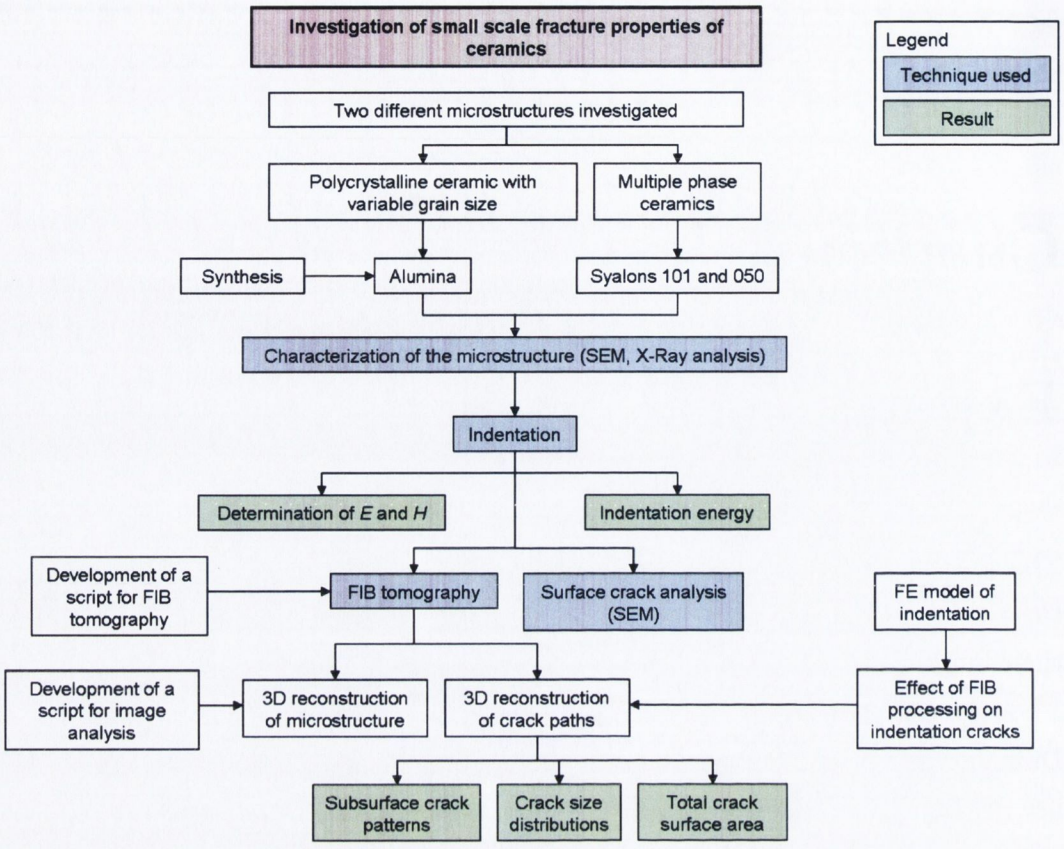

Figure 3.1: Flow chart of the experimental methods employed in this project.

occurring crystalline form of aluminium oxide. It has a rhombohedral unit cell but is often described by its larger hexagonal close packed (HCP) unit cell. The oxygen ions are packed in the HCP lattice structure with aluminium ions in two-thirds of the octahedral sites. Alumina is a hard refractory oxide with the following property values for sintered α-alumina at 20 °C (from [126]):

- Theoretical density : 3.984(2) g/cm^3
- Compressive strength : 3.0(5) GPa
- Elastic modulus : 416(30) GPa
- Flexural strength : 380(50) MPa
- Fracture toughness for crack length of 300 μm : 3.5(5) MPa·m$^{1/2}$
- Hardness Vickers, 1kg : 15(2) GPa
- Poisson's ratio : 0.231(1)

- Tensile strength : 267(30) MPa

Numbers in parentheses are representative combined standard uncertainties of the final digits. These are the properties for the bulk material (with a nominal grain size of 5 μm) but many of them (flexural strength, tensile strength, hardness, fracture toughness) will be sensitive to variations in the microstructure of the material as discussed later.

SiAlONs are ceramic alloys based on silicon nitride (Si_3N_4) and developed in the 1970s. SiAlONs exist in three different forms: β-sialon, α-sialon and O-sialon. Each form is isostructural with one of the two common forms of Si_3N_4, beta (β) and alpha (α) or with silicon oxynitride (Si_2N_2O). Their synthesis from Si_3N_4 requires the substitution of Si by Al with corresponding atomic replacement of N by O to satisfy valency requirements.

β-sialon and α-sialon are commercialized by International Syalons, Wallsend, UK under the trade names Syalon 101 and Syalon 050 respectively.

Syalon 101 and Syalon 050 were chosen as second materials in this project in order to study the influence of a complex microstructure with several phases on crack propagation. Syalon 101 consists of crystalline grains of β-sialon bonded in an amorphous intergranular yttrium-alumino-silicate glass. Syalon 050 contains crystalline β-sialon grains, crystalline α-sialon grains and an amorphous intergranular yttrium-alumino-silicate glass.

The grain size of α- and β-sialon is in the order of a few microns, a fact that also makes these materials relevant for the study of the influence of microstructural features on crack propagation at the microscale. Futhermore, due to their good mechanical strength, hardness, thermal shock resistance and chemical stability, Syalon 101 and Syalon 050 are very good candidates for extreme industrial wear applications.

Table 3.1 presents some of the mechanical properties of Syalons 101 and 050 (From International Syalons, Wallsend, UK).

3.1.1 Review of sintering cycle and manipulation of grain size for alumina

Polycrystalline sintered alumina ceramics are formed by sintering compacted powders. Sintering is the process of manufacturing advanced ceramics by heating a fine powder to approximately two thirds of its melting point. During the sintering process, the reduction of distance between grains leads to a densification of the compacted powder and a shrinkage of the starting ceramic. Sintering of pure

Table 3.1: Mechanical properties of Syalon 101 and Syalon 050 (From International Syalons, Wallsend, UK).

Property	**Syalon 101**	**Syalon 050**
3 point RT modulus of rupture (MPa)	945	800
RT Young's modulus (GPa)	288	306
RT hardness (HRA)	92	94
RT hardness Vickers $Hv_{0.3}$ (kg/mm^2)	1500	2000
Fracture toughness ($MPa.m^{1/2}$)	7.7	6.5
Poisson's ratio	0.23	0.27
Density (g/cm^3)	3.23	3.23
Porosity (%)	0	0

alumina is a solid-state sintering, which means that no liquid phase is formed and all densification is achieved by reshaping (neck formation) of the powder. He et al. [127] showed that densification during sintering of fine-grained alumina ceramics is mostly controlled by interface reaction (boundary diffusion) while grain growth is mostly dominated by surface diffusion. Densification mechanism is driven by the reduction of the energy associated with the total particle surface area and is achieved by elimination of the solid-gas interface and its replacement by a solid-solid interface (surface energies are larger in magnitude than grain boundary energies).

Some additives (such as MgO, Y_2O_3, SiC, TiO_2...) can be added to control the rates of densification and grain growth during the sintering process. Lots of studies have been dedicated to this phenomenon [128–138] and to its consequences on mechanical properties of the bulk material [139–144]. They show some contrasts in the grain growth and densification process of alumina, depending on the additive used. For example, titania (TiO_2) accelerates grain growth but beyond the solubility limit, grain growth decreases as the TiO_2 content increases because the presence of a secondary phase between the α-Al_2O_3 grains inhibits their growth [143]. This is a slightly different phenomenon with yttria (Y_2O_3) doping. Below its solubility limit in bulk alumina, Y_2O_3 segregates to grain boundaries and beyond it, it precipitates on grain boundaries or surfaces. In both cases, it reduces grain boundary mobility and therefore retards both grain growth and densification of Al_2O_3 compacts during sintering [130, 133, 136]. MgO is a traditional additive to Al_2O_3 since it can reduce the sintering temperature

and grain size. Indeed even small amounts of MgO enable Al_2O_3 to sinter to near theoretical density and increase the densification rate. Furthermore, it inhibits grain growth [142]. Rare earth dopants (La, Gd, Yb) are also known to reduce both grain growth kinetics and densification rate by segregating at grain boundaries [130, 144]. Furthermore, grain growth is promoted with manganese oxide addition, leading sometimes to exaggerated grain growth behavior when increasing the sintering time [143]. When pure alumina is sintered, normal grain growth occurs (equiaxial grains and curved grain boundaries without any facets). However, with the addition of some impurities like SiO_2, CaO [132] or Fe_2O_3 [137], abnormal grain growth (AGG) occurs in alumina (large grains elongated with straight grain-boundary segments in the direction of the basal planes). Although the overall impurity level is below the solubility limit, these oxides accumulate at the grain boundaries as grain growth occurs during sintering and induce AGG in alumina. Some authors attribute this effect to the production of intergranular liquid or glassy phases, which induce AGG in alumina by increasing the rate of grain-boundary migration abruptly [128] but others propose that AGG would be directly related to the grain-boundary structure in alumina, which could be influenced by SiO_2 and CaO [134]. However, when MgO is added together with SiO_2 and CaO, normal growth occurs [129, 131, 134].

3.1.2 Preparation of alumina

A first step in this study was to determine the ideal sintering conditions for alumina to obtain a microstructure suitable for later crack analysis. In order to induce cracks by indentation, the material should be as dense as possible. One of the challenges of this work was to obtain the right microstructure, as an incomplete sintering leads to remaining porosity and a full sintering to a huge increase in grain size insofar as the last step in the sintering process is both a densification and a grain growth. Considering the discrepancy between results found in literature for the sintering of alumina, a parametric study was implemented to determine the best sintering conditions to obtain full density but also to control alumina grain size by using appropriate amounts of sintering additives. The experimental work of this parametric study was carrying out by an internship student from Trinity College, Stéphanie Touchefeu.

As the sintering temperature and the duration of the dwell at this maximum temperature are parameters that strongly influence alumina grains size, they were two of the parameters investigated in the parametric study. Both MgO and Y_2O_3 control grain growth of alumina during sintering without forming abnormal

grains. As literature about them is quite abundant, they have been chosen for this project.

An initial experiment was performed using different amounts of MgO (0 and 500 ppm) and Y_2O_3 (0, 1000 and 3000 ppm). Results showed that the addition of magnesium oxide induced a reduction in the average alumina grain size, which was not the case for yttrium oxide with the quantities tested [145]. Furthermore, magnesia is known to help to obtain full density which is not the case for yttria. Therefore, magnesium oxide was chosen as the sintering additive for the manipulation of grain size. The amount of MgO dopants was also added as another variable in the parametric study.

Finally, two different pressures were applied in order to look at the influence of the green density on the fired one. Therefore, there were four parameters investigated in the parametric study:

- the pressure applied during the compaction of the powder
- the amount of MgO additive
- the sintering temperature
- the duration of the dwell at this maximum temperature

The samples were prepared from α-alumina powder (Accumet Material, Co.) for which the manufacturer claimed 99.99% purity and 0.5-1.2 μm average particle size. The powder was dispersed in high purity ethanol (99.99 %) with different concentration of magnesium oxide powder (99.9% purity, 1-5 μm average particle size, Accumet Material, Co): 0, 100, 200, 300, 500 or 800 ppm. The resulting preparation was mixed in a Turbula for one hour and left to dry under a fume cupboard at room temperature. After evaporation of the solvent, the dried preparations were ground in a ceramic mortar. In order to facilitate the grains displacement during pressing and to obtain best green densities, 15 wt% of an organic binder (quantity determined empirically) based on polyvinyl acetate and polyethylene glycol (Bindemittel B11/V, Degussa, Germany) were added. The samples were pressed isostatically at 335 MPa or 670 MPa and then sintered in air, following the sintering cycle presented in Fig. 3.2. The cycle used was the same for each sample except the sintering temperature (1600, 1650 or 1700 °C) and the duration of the sintering dwell (2, 4, 8 or 12 hours). Three samples were prepared for each combination of the four main parameters studied.

- Phase A: The samples were quickly heated to 120 °C at the rate of 8 °C/min.

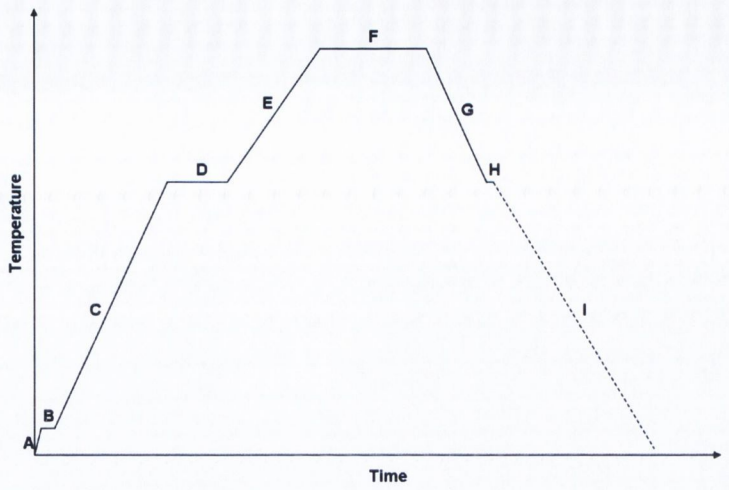

Figure 3.2: Cycle of sintering of alumina samples.

- Phase B: They were held at 120 °C during 30 min to get rid of the moisture and other volatile substances present in the binder.
- Phase C: A reduced heating rate of 4 °C/min was applied until 1000 °C.
- Phase D: The samples were then calcinated at 1000 °C for 2h to remove any carbon contamination.
- Phase E: They were heated at a reduced rate of 2 °C/min to the sintering temperature (1600, 1650 or 1700 °C).
- Phase F: They were kept at this temperature for 2, 4, 8 or 12 hours.
- Phase G: Cooling was done to 1000 °C at the rate of 4 °C/min.
- Phase H: The samples were then held at 1000 °C for 10 min.
- Phase I: A reduced cooling rate (to prevent thermal stresses and therefore cracking from shrinkage) of 2 °C/min was applied, followed by an ambient (in furnace) cooling to room temperature.

The diameter, height and mass of the sintered cylindrical pellets were measured in order to estimate the fired density. Some of the pellets were cut in half, finely diamond-polished and thermal etched at 1400 °C during 30 min in order to reveal grain boundaries. Their grain size distribution was determined using a SEM after gold coating them to ensure conductivity.

3.1.2.1 Results of the parametric study

The densities obtained for each samples were analyzed with the software Minitab and the results obtained are presented below.

Among the four parameters investigated in the parametric study, only three of them appear to have a significant effect on the density obtained. These three parameters are the amount of MgO added (noted MgO), the sintering temperature (T) and the duration of the dwell (t) at this maximum temperature. The pressure applied during the compaction process didn't have any significant effect. Moreover, the following interactions also had a significant effect on the final density:

- MgO and t
- MgO and T
- T and t

Fig. 3.3 presents the main effects and interaction plots of the parameters having a significant effect on the final density obtained.

The addition of MgO seems to have a great effect on the density obtained when the amount added is different from zero but few changes were observed between the other amounts (100, 200, 300, 500 and 800 ppm). This statistical study also suggests that the best density is obtained with 200 ppm of MgO and sintering at 1700 °C during 12 hours. Interaction curves show that the sintering time is the most important of the three parameters investigated in order to obtain a high density. Indeed, full density was only obtained for samples sintered for 12 hours.

3.2 Characterization of the microstructure

3.2.1 Alumina

As the overall aim of the parametric study was to create samples with two different grain sizes (but both having as little porosity as possible), the average grain size of alumina samples containing 200 ppm of MgO and sintered 12 hours at 1600 or 1700 °C was investigated. These two sets of samples were also chosen for the following reasons: grain size is known to be strongly influenced by the sintering time but also by the sintering temperature, and the interaction plots only show

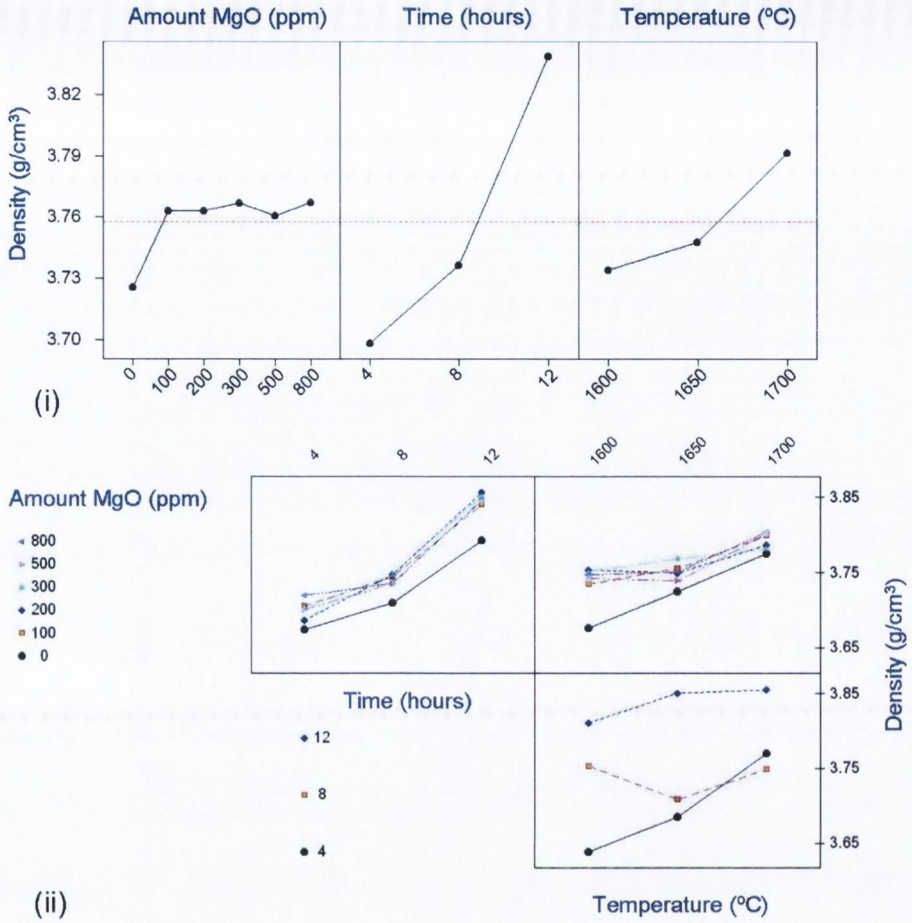

Figure 3.3: (i) Main effects and (ii) Interaction plots using data means for density.

a small variation in the obtained density when sintering 12 hours at 1600 or 1700 °C. The results of the grain size analysis is presented below.

The 12 hours-sintered samples (alumina + 200 ppm of MgO) at 1600 °C (samples D2) or at 1700 °C (samples L2) were cut in half and their cross-section was carefully polished until a 1 μm diamond paste finish. The samples were observed under a SEM after being thermally etched at 1400 °C during half an hour and then gold coated to ensure conductivity.

The density of the cylindrical pellets was calculated geometrically by measuring and weighing them and was determined as 3.84 g/cm^3 for D2 and 3.86 g/cm^3 for L2.

The SEM used in this study was a Mira XMU (Tescan). Typical microstructure of samples D2 and L2 are presented in Fig. 3.4. From the SEM images, the

porosity was calculated and is 7.0% for D2 and 3.3% for L2.

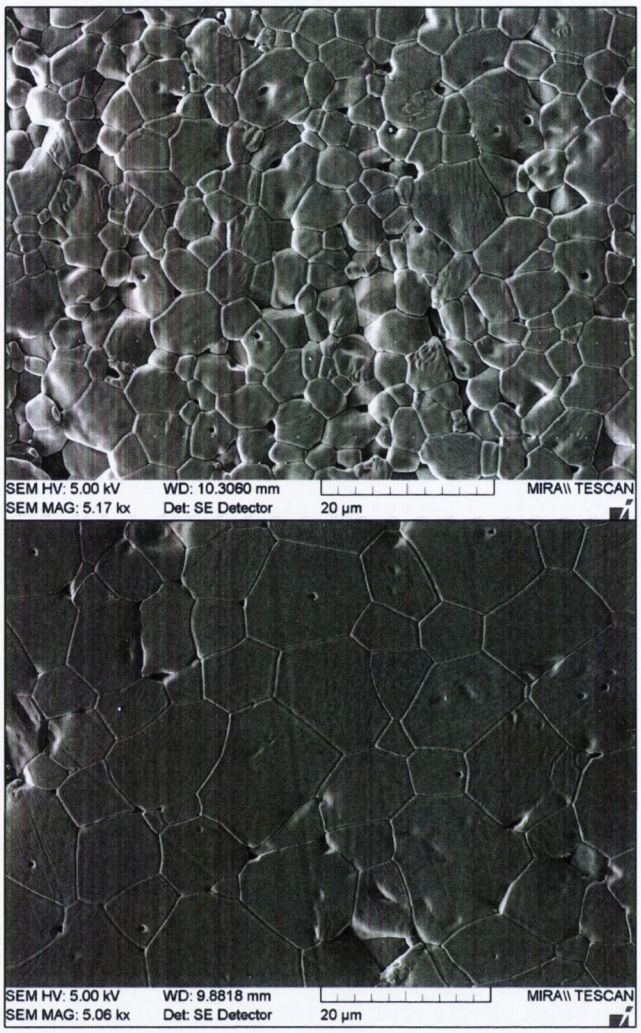

Figure 3.4: SEM images taken at the same magnification of samples D2 (top) and L2 (bottom) after thermal etching.

Thermal etching at 1400 °C was used to reveal grain boundaries. Therefore, grain size distribution of samples D2 and L2 were analyzed using ImageJ and are presented in Fig. 3.5.

The microstructure obtained is dense with average grain sizes of 4.7±2.0 μm for D2 and of 9.7±3.8 μm for L2. The grains are equiaxed and no abnormal grain growth has been observed.

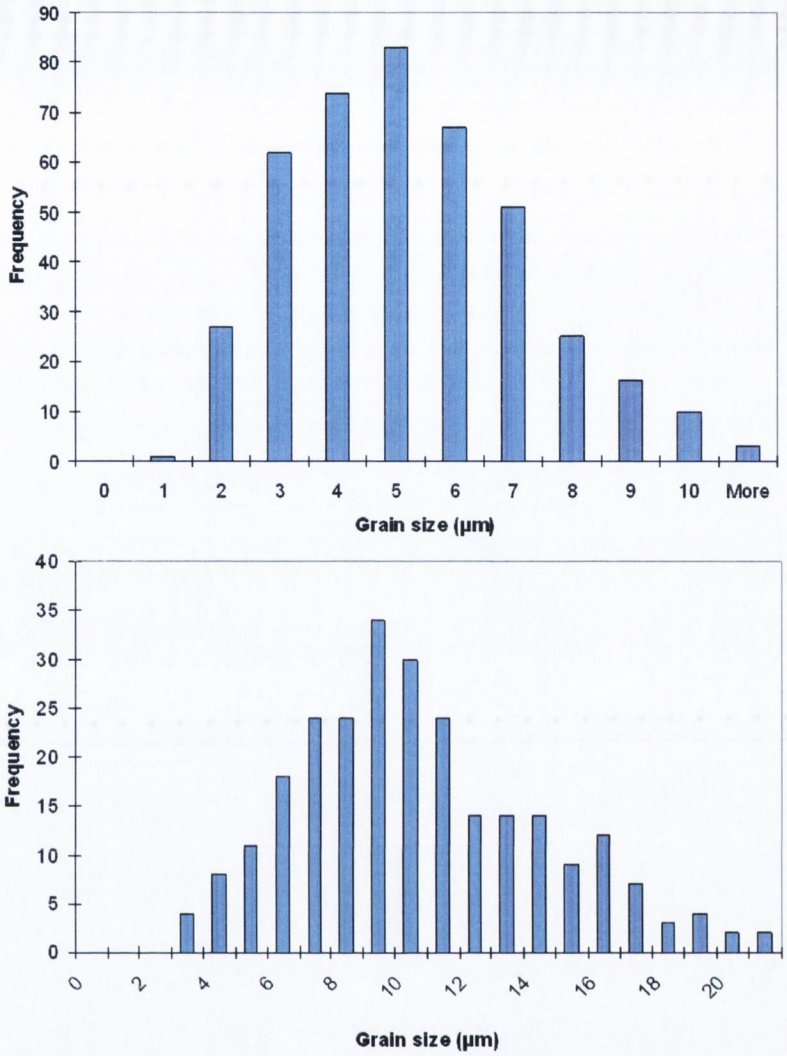

Figure 3.5: Histogram of grain sizes for D2 (top) and L2 (bottom).

It can be noticed that the average grain size found for Al_2O_3-200ppm MgO samples sintered 12 hours at 1700 °C is twice the average grain size of samples of the same composition sintered 12 hours at 1600 °C. Considering the good density of these two sets of samples, they have been chosen as two different representative microstructures for the rest of this study in order to investigate the influence of grain size on crack propagation in ceramics at the microscale.

3.2.2 Syalons 101 and 050

Cylindrical samples received from International Syalons were cut in half perpendicular to the axial direction and the cross-sections were mounted on epoxy resin for microstructure analysis and indentation experiments. The specimens were

carefully polished using 78 μm, 46 μm and 15 μm grain sizes SiC papers then 6 μm and 1μm diamond pastes in succession.

In order to analyze the repartition of the different phases and their composition by X-ray analysis, the samples were carbon-coated ($\simeq$ 20 nm thickness) to avoid charging effect. The average grain size and typical grain shape (aspect ratio) were also determined, using backscattered electrons (BE) imaging and image analysis with ImageJ.

Fig. 3.6 presents a BE image of Syalon 101. The β-sialon grains appear in black in the BE image. They are separated by an amorphous intergranular yttrium-alumino-silicate glass (in white) which gives a strong BE signal due to the presence of yttrium which has a higher atomic number than the other elements present in the sample.

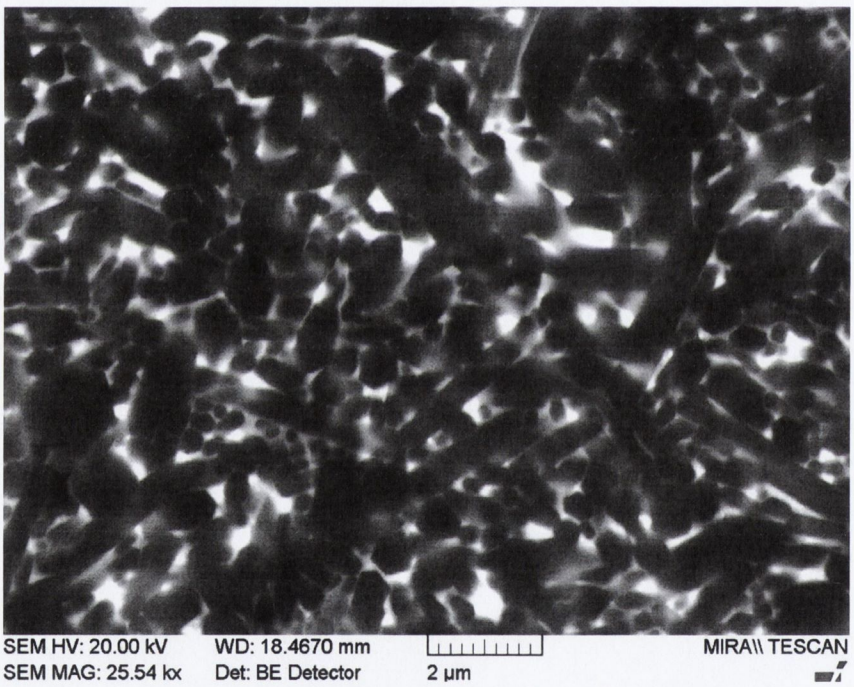

Figure 3.6: Backscattered electron image of Syalon 101.

Analysis of BE images gave an average grain size of 1.9 μm with grains ranging from 0.5 μm to 3 μm on average. The average grain aspect ratio was 1.7. Repartition of the β and intergranular phases was quite uniform in the volume studied with the intergranular phase representing between 12 an 13% of the total volume.

Table 3.2 presents the elemental composition of the two phases present in Syalon 101.

The atomic percentages found were close to the ones given by the manu-

Table 3.2: Compositional analysis of the β and intergranular phases of Syalon 101.

	β-phase		Intergranular phase	
Element	**Atomic %**	**Sdt. deviation**	**Atomic %**	**Sdt. deviation**
Si	39.8	1.4	34.1	2.0
Al	1.5	0.1	2.1	0.2
O	4.8	0.9	17.2	3.4
N	53.9	1.4	43.8	3.5
Y	0	0	2.8	0.5

facturer as International Syalons claims that the composition of the β phase is $Si_{5.5}Al_{0.5}O_{0.5}N_{7.5}$.

Concerning Syalon 050, it was not possible to differentiate the α phase from the β phase neither with electron microscopy nor with X-ray analysis. Consequently, the composition given by the manufacturer (45% of α-sialon, 45% of β-sialon, the balance being an amorphous yttrium-alumino-silicate glass) was taken as the reference. According to International Syalons, the α phase consists in $Y_{0.3}Si_{10}Al_2ON_{15}$. Analysis of BE images showed that the intergranular phase was representing approximately 4% of the total volume in Syalon 050.

3.3 Determination of elastic and plastic properties by nanoindentation

Once the compositional and microstructural analysis of alumina and Syalons samples were carried out, the work progressed to mechanical testing, fracture analysis and crack morphology study. The matrix of testing and analysis is shown in Table 3.3.

A part of this project involved a collaboration with the University of New South Wales (UNSW) in Australia. They carried out the FIB tomographies on alumina. The analyzed alumina samples consisted of 99.85 wt% Al_2O_3 (99.99% purity), 0.1 wt% Y_2O_3 (99.9% purity) and 0.05 wt% MgO (99.9% purity), all powders coming from Accumet Material, Co. The compacts formed had a density of 3.77 g/cm^3 and a porosity of around 4%. These samples are labeled as Alumina UNSW in the rest of this project.

Indentation experiments were performed using an MTS nanoindenter XP

Table 3.3: Matrix of testing and analysis showing the number of tests performed for each step.

Material	Indenter	Different loads investigated	Indents performed	Calculation of E, H and W_p	SEM	FIB tomography	Crack pattern reconstruction
Alumina D2	Vickers	n=9	n=203	n=178	n=178	-	-
Alumina L2	Vickers	n=9	n=205	n=112	n=112	-	-
Alumina UNSW	Vickers	n=3	n=30	-	n=30	n=3	n=3
Syalon 101	Vickers	n=15	n=980	n=173	n=139	n=7	n=6
Syalon 101	Customized	n=8	n=485	n=168	n=81	n=4	n=3
Syalon 050	Vickers	n=13	n=842	n=304	n=114	n=3	n=3
Syalon 050	Customized	n=12	n=622	n=90	-	n=3	-

(MTS Systems).

Prior to the experiments to induce cracks in the specimens, the indentation behavior of the different materials (alumina D2 and L2, Syalons 101 and 050) was checked by successive loadings and unloadings in order to identify any possible reverse plasticity in the unloading part of the indentation.

Two different indentation cycles were used in this project. The XP High Load Basic Hardness, Modulus, Load Control is a load-control method designed by the manufacturer for the application of high loads (typically between 1 and 10 N) while the CSM Load Control method has been built especially for this study and consists in a load-control method using the CSM. The latter method can only apply loads until 700 mN. The two methods use either a constant loading time (High Load method) or a constant strain rate (CSM Load Control method) for loading until the indenter reaches the preset maximum load. After a 10 to 30 s holding peak at this maximum load, the indenter is unloaded at a constant unloading time or unloading rate. A thermal drift correction is then performed at the end of the unloading segment.

Although the most frequently used indenter in nanoindentation testing is the Berkovich, a Vickers and a customized four-facets pyramid tip with a 45 ° half-included angle have been used in this project. The main advantage of the Berkovich lies in the fact that a three-sided pyramid can be ground to a point (causing its small-scale geometry to be the same as at larger scales), making it very useful at low indentation depth. However, the Vickers and customized tips were used at relatively high loads in this study in order to induce cracks so the fact that a four-sided pyramid terminates at a line of conjunction at the tip rather than at a point was of reduced importance. Moreover, the theoretical crack shapes beneath a four-sided pyramid are well known and widely commented in literature [48, 57, 146, 53, 17, 147, 61, 58, 54, 65, 63, 50] which is not the case

for cracks induced by a Berkovich indenter, as less studies have been dedicated to fracture toughness determination using this indenter [148].

Typically, sets of 25 to 36 indents were run for every load investigated on each different material using the two methods cited above.

Special attention was given to possible sources of errors in nanoindentation measurements, as highlighted in the section on nanoindentation (cf 2.2.2): compliance of the measuring system, thermal drift, surface roughness, determination of the initial depth of penetration, indenter tip shape and pile-up. Both frame compliance and thermal drift can be corrected respectively before and during the measurements using the appropriate methods given by the software. Another useful tool provided with the nanoindenter XP is the CSM technique. With this option, the stiffness is measured continuously during the loading of the indenter and is used in order to detect surface location. Indeed, stiffness rises rapidly when contact is achieved with the specimen, thus providing a very accurate estimate of the surface location. In parallel, the AFM technique was used to check any pile-up effect.

Automatic calculations of Young's modulus and hardness provided by the software were refined using the equations defined in section 2.2.2. The corrections consist notably in the insertion of the correction factors γ and ϵ in the calculation of S and h_c respectively.

Finally, the energy dissipated during indentation was evaluated from the indentation curves. The unloading curve was fitted to draw the last 10 % of the curve then calculation of the area under the loading and unloading curves was performed using Visual Basic for Applications (VBA).

3.4 Investigation of surface cracks and fracture threshold

Indents performed at loads ranging from 0.05 to 10 N were imaged using the SEM in order to look at their surface cracking behavior. Any material effect such as pile-up or sink-in was studied and surface crack lengths recorded for calculation of fracture toughness using classical models. Any crack with a length superior to 10% of the length of the residual impression diagonal was recorded. In addition, the surface fracture threshold was determined for each material investigated. If the majority of indents with no close hole around had cracks then surface fracture threshold was considered to be reached.

3.5 Investigation of 3D crack structure beneath the indent

The three-dimensional crack pattern underneath several indents and its interaction with the microstructure were studied using the FIB-tomography technique as described in section 2.3.2.1.

Two Dual Beam FIBs have been used in this project: a FEI Nova 200 Dualbeam FIB system from the Kelvin Nanocharacterisation Centre (University of Glasgow) and another FEI Nova 200 from the Electron Microscopy for Materials Science group (University of Antwerp). The sample to study was placed in the Dual Beam FIB at the eucentric point (where the ion and electron beams converge). Hence, while the ion beam is used for milling, the sectioned planes can be imaged with the electron beam without having to reorient the sample. It is of great importance to avoid any stage rotation or movement during the experiment in order to minimize any drift of either the electron beam or the ion beam. During the serial sectioning process, the stage tilt was kept constant at 52° so that the sample surface was perpendicular to the ion beam. The geometry used during these FIB tomographies is presented in Fig. 3.7.

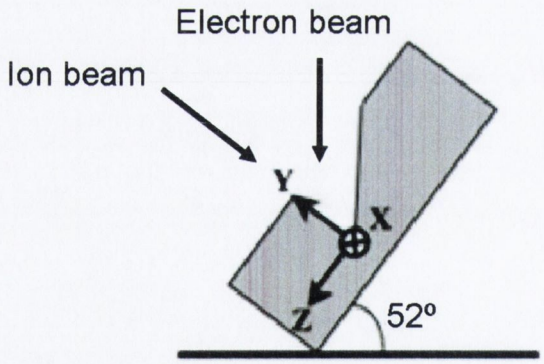

Figure 3.7: Geometry of a dual beam instrument during FIB tomography.

Areas of interest were protected with a 1 μm thickness platinum film. This coating has three principal functions. First, it serves as a protective layer and prevents unwanted sputtering or beam damage of the outer surface of the specimen. Second, this film may inhibit the formation of artifacts such as 'curtaining' (also called 'waterfalling') since the metallic coating has the effect of applying a smoother layer on the specimen surface. Such features arise because sputtering

rates are sensitive to local changes in surface topology. This effect often occurs below pores or cracks for instance. And finally, the metallic layer reduces charging effects on the surface as alumina and SiAlONs are non-conductive.

For every indent, the highest available ion beam current (20 nA) was chosen to mill the large first trench out of the region of interest, prior to the start of the serial cross-sectioning.

Because the average particle size of both Syalons and alumina samples was in the range of few micrometers, a sectioning step size of 100 nm was considered as being ideal for capturing the microstructural features without spending too much time with FIB processing. Exceptionally, two FIB tomographies of 5 N indents in Syalon 101 were investigated using a milling step of 250 nm.

The ion beam current used during serial sectioning was adjusted for every indent studied depending on the volume of material to remove. A higher beam current enables to mill quicker the volume of interest. The current chosen was a compromise between the maximum time allowed for the entire experiment (run overnight) and the need for the lowest possible beam current in order to mill slices of precise thickness and without creating too much damage to the features of interest. A list of ion beam currents used for every indent studied is presented in Appendix A.

The use of EBSD was first considered in order to access the material texture on each slice during FIB tomography. However, this technique is only applicable on the edge or on the surface of a sample but not on a cross-section perpendicular to the sample surface. In the latter case, walls surrounding the imaged cross-section shadow the area of interest, thus impeding the collection of backscattered electrons for EBSD analysis.

3.5.1 Development of a protocol with the FIB

Although FIB tomography is now widely used in material characterization (cf 2.3.2.2), a set of difficulties appeared while using this technique in this project. The issues were coming both from the highly insulating nature of the material investigated and from the purpose of the FIB study (the analysis of subsurface cracking patterns). As the large dimensions of the volume studied implied a long process time, there also was a need for the development of an automated method capable to correct any beam instability during the experiment. The next subsections present the fully automated method developed in collaboration with Dr McGrouther (from the Kelvin Nanocharacterisation Centre of the University of Glasgow). This method is valid on insulating materials and produces reliable

2D image datasets for 3D reconstruction of a large volume in the analysis of subsurface damage.

An initial experiment was performed on a 500 mN indent in Syalon 101 and involved cutting a trench with the ion beam midway through an indent and acquiring SEM images to view the crack structure. A number of phenomena (causing difficulty) were observed related to the insulating nature of the material. They are listed below and our solutions are presented in the text thereafter.

3.5.1.1 Charging and non-uniformity in image contrast

On the newly cut cross-section, charging effects were important, resulting in some image distortions and voltage contrast (some areas appeared extremely bright due to negative charging whereas others appear black because they charge positively). In a previous study on FIB tomography of porous $BaTiO_3$, Holzer et al.[107] suggested the use of low-kV imaging in order to minimize charging effects by reducing the energy of the incident beam. It resulted that the balance between the charges injected by the beam and the ones leaving the specimen as secondary and backscattered electrons was not too important, limiting charging effects.

Such an approach has been used here and the beam current was reduced to minimize the effects of charging. On the other hand, a sufficient contrast was needed to differentiate the amorphous and crystalline phases.

A beam energy of 5 keV was found to be the best compromise as it was giving a contrast enough to differentiate the amorphous and crystalline phases and to resolve clearly the subsurface cracks without leading to important charging effects. Further reduction in the levels of voltage contrast due to electrical charging was obtained by choosing a low beam current (98 pA, to reduce the amount of implanted charge) and by using a relatively quick scan rate (dwell time = 3 μs) averaged over 16 frames.

Using the imaging conditions defined above (5 keV, 16 frames, 3 μs), another freshly cut cross-section was repeatedly imaged 20 times in order to estimate the remaining charging effect. The variation of the mean intensity between the 20 images is presented in Fig. 3.8.

The repeated imaging of the same cross-section with the electron beam led to a global increase by 24% of the mean intensity of the pixel values, between the 1^{st} and the 21^{st} image taken in this experiment. This can be explained by an accumulation of charge on the cross-section, which leads to an enhancement of the secondary electrons collected by the detector. The increase followed a second degree polynomial trend line.

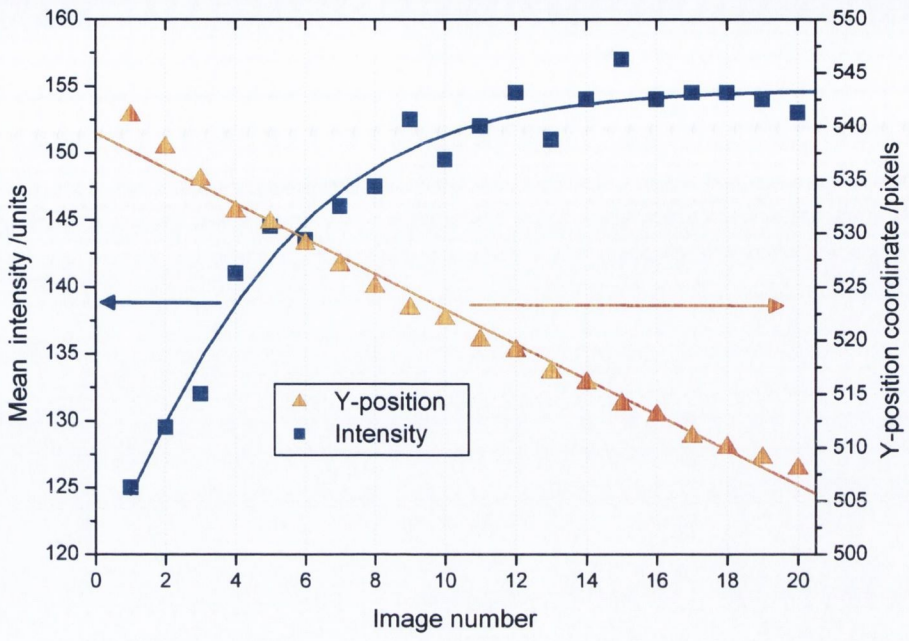

Figure 3.8: Graph showing changes in mean intensity and position of the selected region against image number.

This experiment also showed an almost linear displacement of the image in the y-axis (Fig. 3.8). This is again due to the negative charge accumulated on the cross-section, which causes a rise in its surface potential and provokes a deflection of the incident electron beam.

Even if the milling step of the slice&view process counterbalances this negative charging, this experiment highlighted the need for accurate alignment of the electron images in any FIB tomography technique to compensate for any drift between the images.

Another difficulty arising during FIB-SEM tomography of insulators is the creation of shadow effects from the side walls. This effect is due to charging and is material dependent. A common approach to overcome this problem is by milling a 'U-shaped' trench around the investigated sample location prior to the slice&view process [107, 105, 113]. However, in the case of the study of subsurface damage, this technique can't be used as the creation of the 'U-pattern' would lead to significant changes in the stress fields surrounding the area of interest, resulting in the opening or closing of cracks.

Charging effects during electron imaging also result in a brightness gradient

from the top to the bottom of the section. It can then induce difficulties during image processing (segmentation) by introducing gray levels within the same phase. Data segmentation by a global threshold value is then no longer possible.

A customized script using linear filters was developed in Matlab to overcome these last two difficulties, transforming the gray level images to binary ones and therefore enabling segmentation by a global threshold.

Fig. 3.9 presents some of the charging effects encountered while imaging cross-sections of Syalon 101. It also indicates the different phases present in the material.

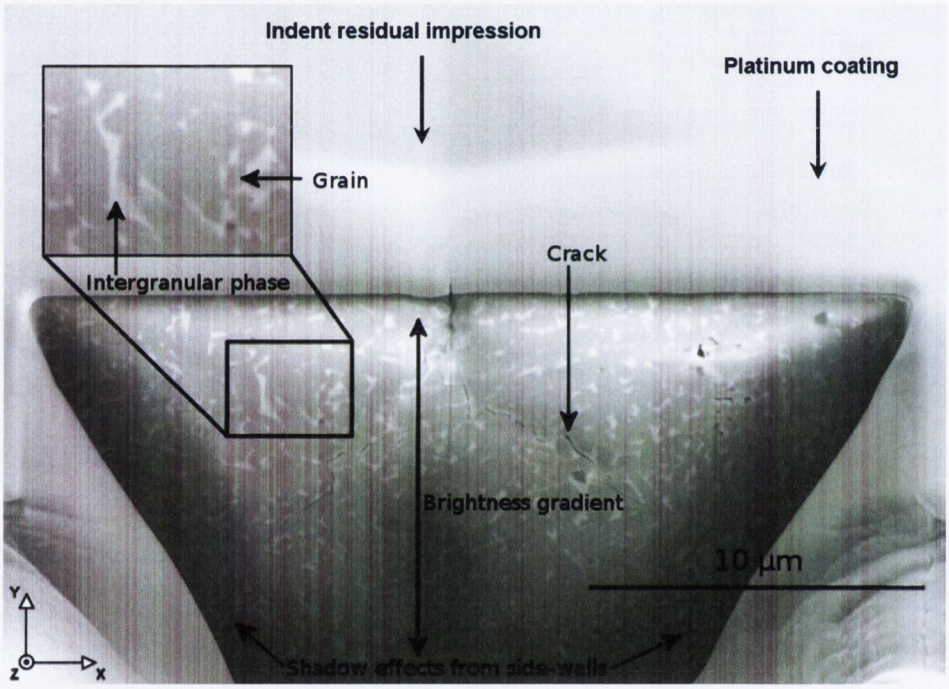

Figure 3.9: Cross-section of a 2 N Vickers indent in Syalon 101. The relevant contrast features in the image are indicated (phases, cracks, charging effects).

3.5.1.2 Electron beam drift

Considering the duration of each experiment (typically twelve to fifteen hours) and the presence of charging effects, a drift of the scanning electron beam can also occur. Introducing markers, the traditional technique for correcting this drift, was not possible in this study as milling these references would change local stress fields. However, the low magnification used during the imaging process (around *5000) enabled to see part of the surface so that electron images could

be aligned using distinguishable features, prior to 3D reconstruction.

An automatic adjustment of the electron beam focus has also been used as the total investigated volume was quite important (typically 30 μm * 30 μm * 10 μm).

3.5.1.3 Material dependent contrast and brightness changes between consecutive electron images

During the slice and view process, the ion beam removes part of the negative charge accumulated on the cross-section when scanning with SEM. However, previous experiments on the same material had shown a linear increase of the brightness between consecutive slices. This sometimes led to unusable saturated electron images and highlighted the need for a dynamic detector adjustment. Based on these results, an automatic correction of brightness was applied to compensate for the increase in brightness due to charging effect. The value of the correction was determined empirically and was increasing with the number of the cross-section being milled.

Fig. 3.10 shows two electron beam images of the same area of interest (Syalon 101 2 N Vickers indent), one taken without brightness correction (i) and one with (ii). It can be seen that the automated reduction of brightness value during slice&view has avoided saturation of pixels on some images due to charging.

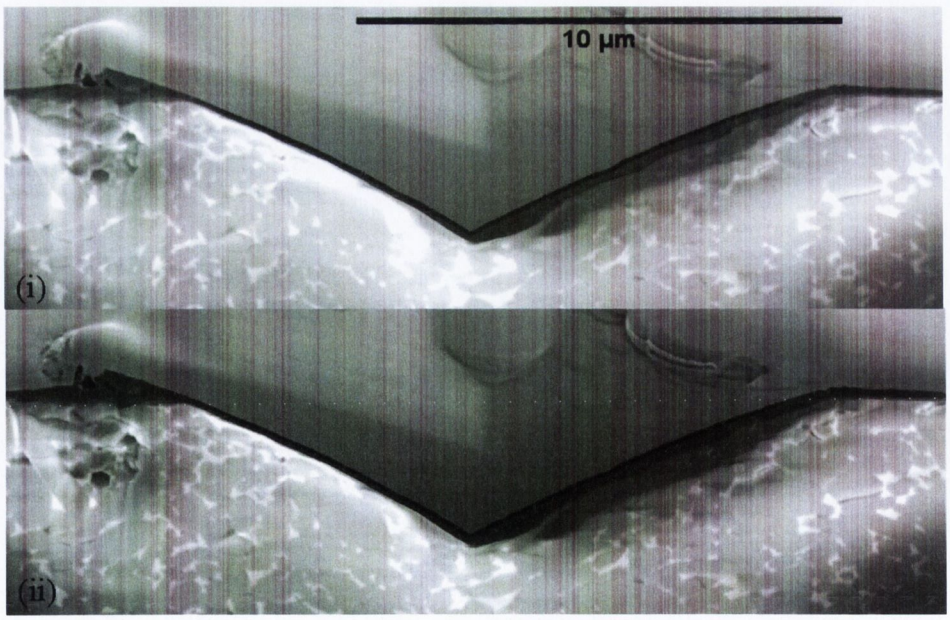

Figure 3.10: Electron beam images taken (i)without and (ii)with brightness correction.

3.5.1.4 Correction of ion beam drift

More importantly, charging can also cause a drift of the ion beam in the z-direction leading to irregular slicing step sizes. In order to correct this drift, ion beam images (I-SE images) can be taken before each slicing step and reference markers used to realign the ion beam [107]. However, considering the high ion beam currents used during the slice&view process (typically 3.0 nA and sometimes 6.5 nA), repeatedly imaging the sample surface can destroy the references and cross-correlation of reference images fail.

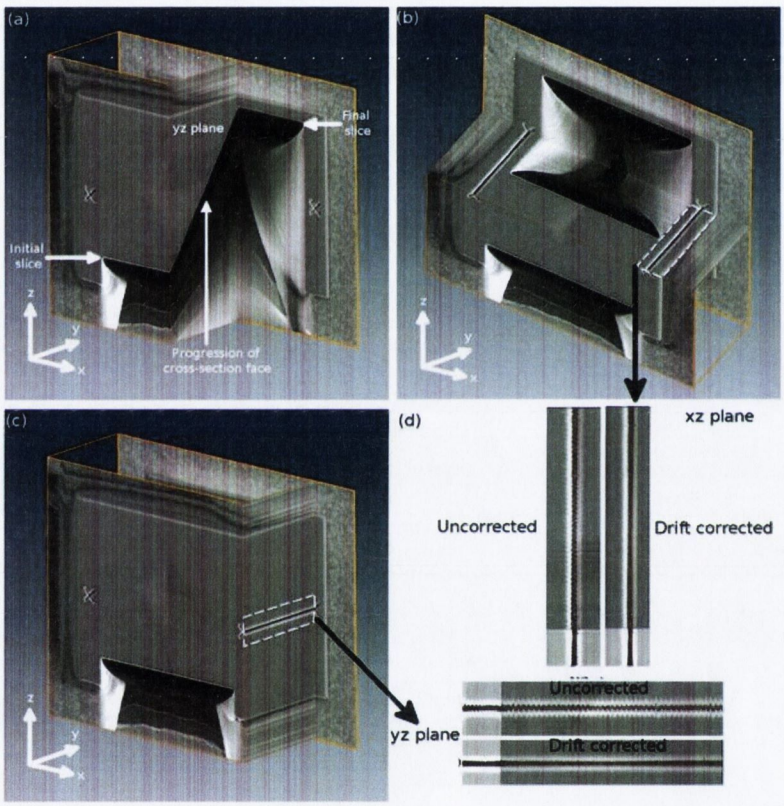

Figure 3.11: Analysis of I-SE images. (a) yz cut plane through stack of drift corrected I-SE images showing smooth progression of cross-section face. (b & c) xz & yz cut planes through right most reference cross of drift corrected I-SE image stack. (d) Comparison of xz and yz cut planes through the reference cross for uncorrected and drift-corrected I-SE image stacks highlighting the need for drift correction.

In this study, milling and ion beam imaging processes were automated using the scripting capabilities of the FIB software, using an automated drift correction as described by Holzer et al. [107]. Two crosses were milled out of the region

of interest prior to the slice&view process and recorded as references for the automatic ion beam drift correction.

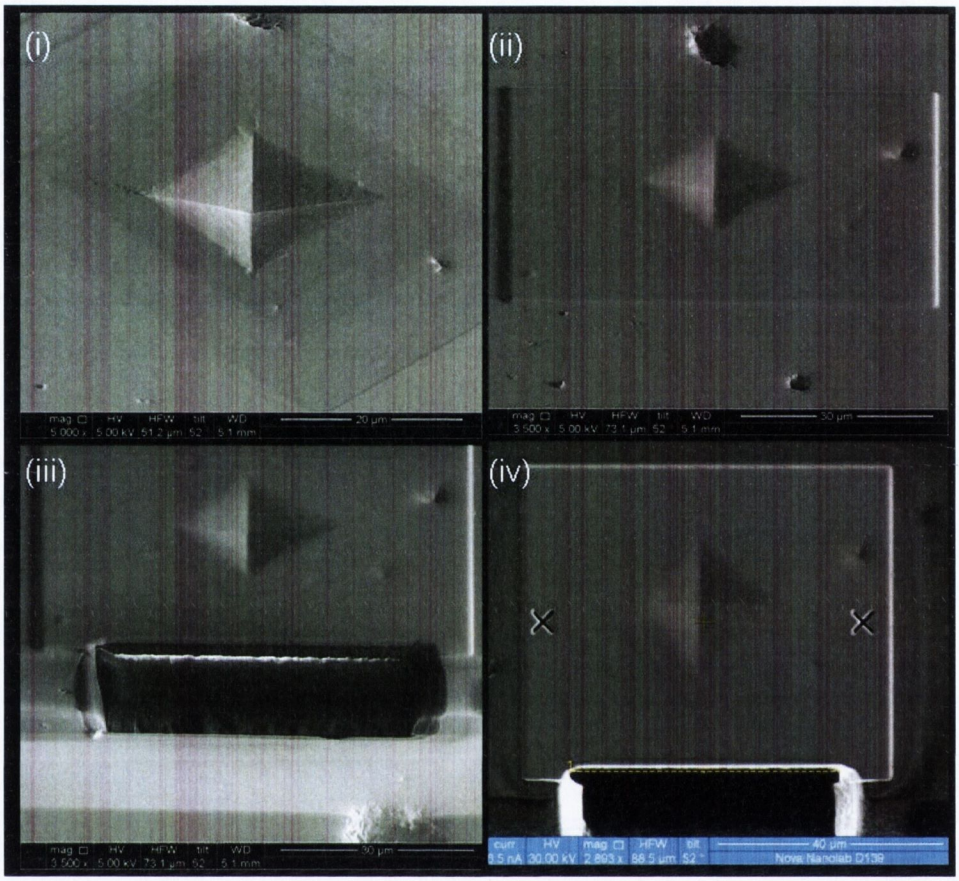

Figure 3.12: An example of the FIB tomography process on a Syalon 101 5 N Vickers indent: (i) the uncoated indent with four radial cracks. (ii) the same indent covered with a 1 μm Pt layer, (iii) after the rough milling and (iv) a top view of the indent before starting the automated procedure, showing the two crosses used as references for ion beam automatic alignment. In this image, the bright contrast visible on the edges of the newly cut cross-section is due to redeposited and sputtered material.

Fig. 3.11 presents the results of the automated drift correction procedure (for a Syalon 101 5 N indent). The projections of a reference (the center of the right cross) on the z-axis (direction of the slice&view process) clearly show ion beam movements before drift correction (Fig. 3.11 (b) & (c)). It also shows a good realignment of the beam after drift correction with the center of the cross being kept at the same position during the entire experiment. Comparison of ion beam images taken between each slicing step has also permitted to measure

the thickness of each slice which was constant at 250 nm during all slice&view process for the indent studied.

As milling was performed using a high ion beam current (6.5 nA for FIB tomography of this 5 N indent in Syalon 101), ion beam images used for automated drift correction were taken at a high scan rate in order not to damage the reference crosses. Therefore, an image of the real crosses was taken before starting the experiment to improve the recognition score, and recorded as the reference. This has permitted the 15 hours slice&view experiments with a high and constant recognition score (> 90 %).

A summary of the steps during FIB tomography is presented in Fig 3.12 for a Syalon 101 sample indented at 5 N with a Vickers tip.

3.6 Image analysis

The serial sectioning and imaging process produced a stack typically consisting of 200 - 300 images. Because of oblique SEM imaging at an angle of 52 °, distances in the y-direction had to be corrected for projection effects using $y' = y$ * sin(52 °). After tilt correction, SEM images were aligned using the commercial software package Avizo (Visualization Sciences Group). Then subsurface crack contours were drawn on each slice using the image analysis software IMOD from the University of Colorado-Boulder [149] while the microstructure was reconstructed using Avizo.

3.6.1 Reconstruction of crack paths

Using the software IMOD, the crack paths were identified by manual inspection in each slice and marked by manual segmentation. Fig. 3.13 presents an example of the manual crack reconstruction process. Each color represents a different crack.

FIB tomography of indents produced on average 200 to 300 slices, each of them containing several cracks. Therefore, for a typical indent, reconstruction of cracks took between one and two weeks thus explaining that only twelve indents have been reconstructed for this project compared to the high number of indentation tests performed.

The crack surface area was then calculated by interpolating between consecutive slices as presented in Fig. 3.14. The area of a crack between three consecutive slices (hatched area on Fig. 3.14) is calculated as follows:

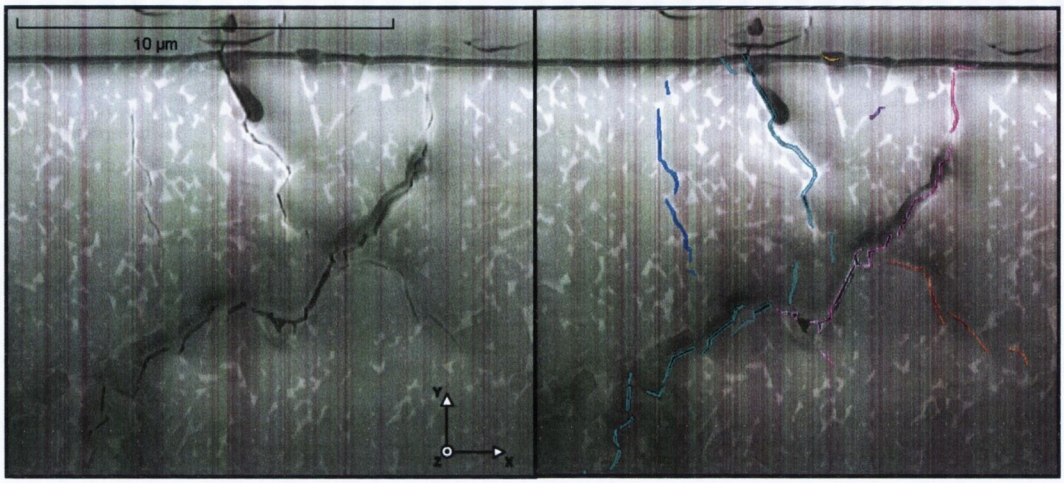

Figure 3.13: An example of the crack reconstruction process from a 2D image. The pictures were taken from a 2 N indent made with the customized tip in Syalon 101 and represent before (left) and after (right) crack path reconstruction.

$$A = 2 * (L_{n-1} * 0.5z_n + L_n * 0.5z_n + L_n * 0.5z_{n+1} + L_{n+1} * 0.5z_{n+1}) \qquad (3.1)$$

with L_n representing the length of the crack on slice n and z the distance between two consecutive slices.

On ion beam images, as the projections of a reference on the z-axis showed a constant slice thickness for the indents studied, estimation of the crack surface area was done using z as a constant value.

3.6.2 Reconstruction of the microstructure

For the reconstruction of the microstructure, the stack of images obtained were processed in Matlab with a customized script in order to remove brightness gradients due to charging effects. This script used linear filters and two local thresholds in order to transform the grey level images to binary ones (with the intergranular phase in white and the grains in black). Then a filter to remove small objects (noise) was used and the binary images obtained were superimposed to the original ones to check the filtering process. Binary images were then segmented in Avizo using a global threshold.

Fig. 3.15 shows an example of a microstructure reconstructed from the set of 2D images obtained by FIB tomography.

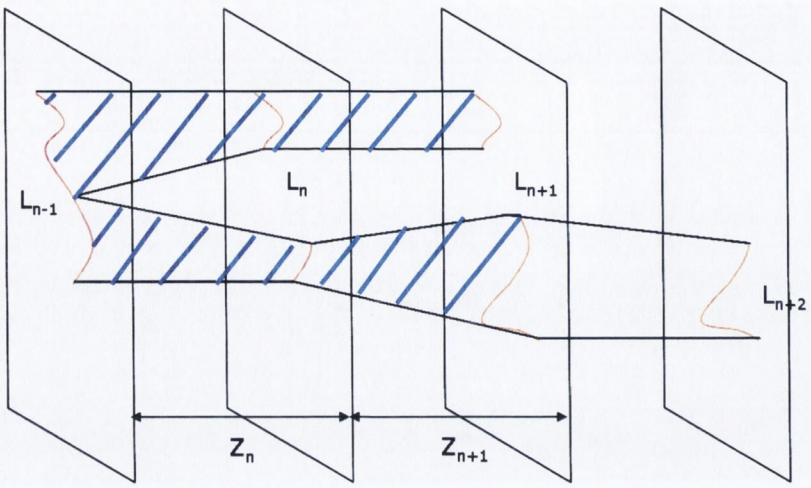

Figure 3.14: Illustration of the method used to calculated the crack surface area.

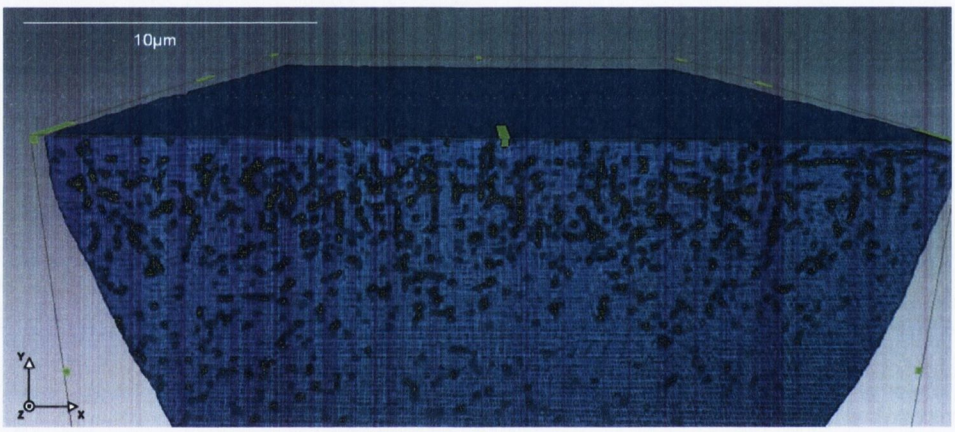

Figure 3.15: An example of the reconstruction of microstructure: Syalon 101 2 N indent made with the Vickers tip. The crystalline phase is drawn in purple while the intergranular phase is in green.

Finally, 3D visualization of the reconstructed microstructure combined with the crack system was performed by recombining both of the segmented stacks in Avizo, in order to investigate crack-microstructure interactions in three dimensions.

3.7 Estimation of uncertainties

Indentation experiments and reconstructions of crack path and microstructure using FIB tomography can be subject to many sources of uncertainties. A con-

siderable effort was made to reduce each source of uncertainty, the main ones being presented in the next subsections.

3.7.1 Calibration issues

Calibration procedures were performed on the nanoindenter and on the FIB before each set of experiments. Possible sources of uncertainties during indentation experiments (compliance of the measuring system, thermal drift, surface roughness, determination of the initial depth of penetration, indenter tip shape) were minimized by applying calibration procedures as described in details in the section 2.2.2. SEM micrographs of the indenter tip have shown damage induced to the tip by repeated indentations in hard Syalons material. Calibration of the indenter tip shape was therefore performed regularly but the damage induced to the tip can constitute a source of uncertainty between indents inside the same batch .

3.7.2 Uncertainties on the image acquisition and analysis

Considering the precision of the automated drift correction process (as presented in section 3.5.1.4), experimental errors and uncertainties during image acquisition (such as the regularity of the distance between the slices) have been minimized in this study. Furthermore, the samples were not moved during the whole tomography process and this also reduced the possible drifts that may happen during long-time experiments.

However, non negligible sources of errors exist, especially while processing the stack of images. Even done with great care, the alignment of the image stack can be subject to small deviations. Moreover, recognition and drawing of cracks were done manually and thus are subject to user interpretation. These two effects can affect the crack surface area calculated.

Concerning the reconstruction of the microstructure, uncertainty can come from both the filtering and segmentation processes by thresholding.

3.7.3 FIB processing effect on indentation cracks

Finally, a possible source of uncertainty in the results comes from the influence of the FIB process on indentation cracks. This influence needs to be assessed and has been considered when evaluating results of this project.

3.8 Finite element modeling

Although finite element modeling was not part of this work, the results obtained experimentally were correlated to the ones given by a finite element model of indentation developed by another PhD student, Iratxe Mijangos. The development of this model was complementary to the experimental project and permitted to localize and estimate the stress fields around the indentation, as they couldn't be determined experimentally. The model also highlighted the interaction of stress fields with the local microstructure and gave an estimation of the energy dissipated during cracking as well as the change in the stress fields during FIB processing.

Chapter 4

Results

4.1 Alumina

4.1.1 Indentation results

A basic assumption for using the Oliver&Pharr method is that the unloading is purely elastic. In order to check this assumption, successive loadings and unloadings at the same location were performed in the two materials D2 and L2. Typical loading-unloading-reloading curves obtained for D2 and L2 are presented in Fig. 4.1. As previously noticed by Gong et al. [25], in most cases, the unloading and reloading curves are nearly the same, i.e the two curves overlap with each other. The small difference observed reveals the presence of a small amount of reverse plasticity which may be due to cracking (shallow radial cracks for instance grow during unloading). For few experiments, distinct hysteresis loops were observed showing considerable reverse plasticity upon unloading.

One important result of the indentation test is the maximum penetration into surface as material properties E and H are deduced from it. Table 4.1 shows statistical variations of the recorded penetration depth h_{max} at different peak loads for D2 and L2 indented with the Vickers tip. A poor reproducibility in the indentation curves obtained (as shown in Fig. 4.2) and a large scatter in the maximum depth has been noticed for every load studied. For instance, at 200 mN in D2 , the maximum depth varies between 504 and 1215 nm, which is a considerable interval. At the same peak load in L2, the maximum depth varies between 560 nm and 1768 nm. This huge scatter in the penetration depth for the same load applied is also found at larger loads as the maximum depth at 10 N varies between 5259 nm and 6100 nm for D2 and between 4084 nm and 6827 nm for L2.

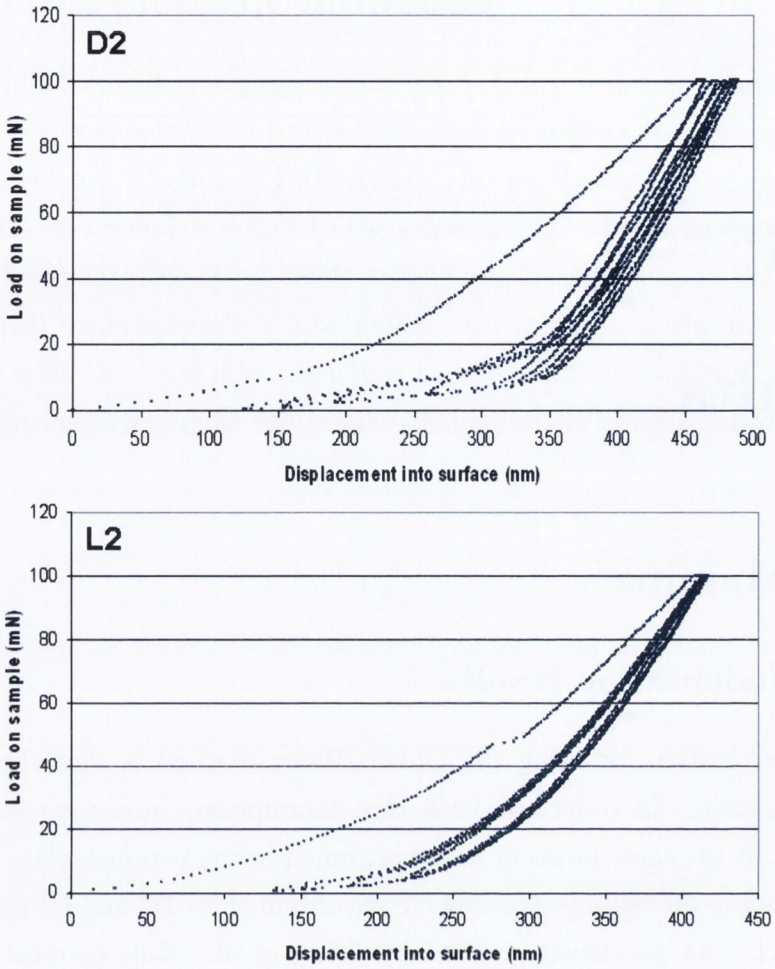

Figure 4.1: Representative load-displacement curves obtained during successive loading-unloading-reloading cycles at 100 mN for alumina samples D2 and L2.

Interestingly, as can be seen in Table 4.1, the coefficient of variation of h_{max} has a decreasing tendency with increasing the maximum load. Cv represents the normalized measure of dispersion so this result means that as the load increases, there is less scatter in the maximum depth.

Some curves exhibit a sudden and dramatic increase in the penetration depth during loading (Fig 4.3) which may reflect the presence of softer region (pores or grain boundaries) or cracking in the material during loading. These sudden increases were often observed in L2 but rarely in D2.

Each set of curves was examined individually and any spurious test removed (tests presenting dramatic increases in penetration depths or bad surface detection). Thus, on a total of 203 tests on D2, 25 were removed and on 205 tests done

Table 4.1: Statistical properties of the maximum penetration depth h_{max} measured at different peak loads for alumina samples D2 and L2.

				D2					
P_{max} (mN)									
Mean	206.6	516	824	1028	2069	3319	4141	5170	10274
Stdev	0.9	3	12	12	19	12	15	24	36
h_{max} (nm)									
Mean	772	1215	1453	1761	2423	2825	3319	3883	5806
Stdev	166	164	200	247	238	274	286	317	239
Cv	0.22	0.14	0.14	0.14	0.10	0.10	0.09	0.08	0.04
				L2					
P_{max} (mN)									
Mean	206.6	515	824	1029	2075	3111	4150	5177	10238
Stdev	0.9	3	11	11	15	19	24	26	60
h_{max} (nm)									
Mean	910	1345	1530	1954	2450	3144	3711	4038	5806
Stdev	354	567	220	509	353	569	717	519	619
Cv	0.39	0.42	0.14	0.26	0.14	0.18	0.19	0.13	0.11

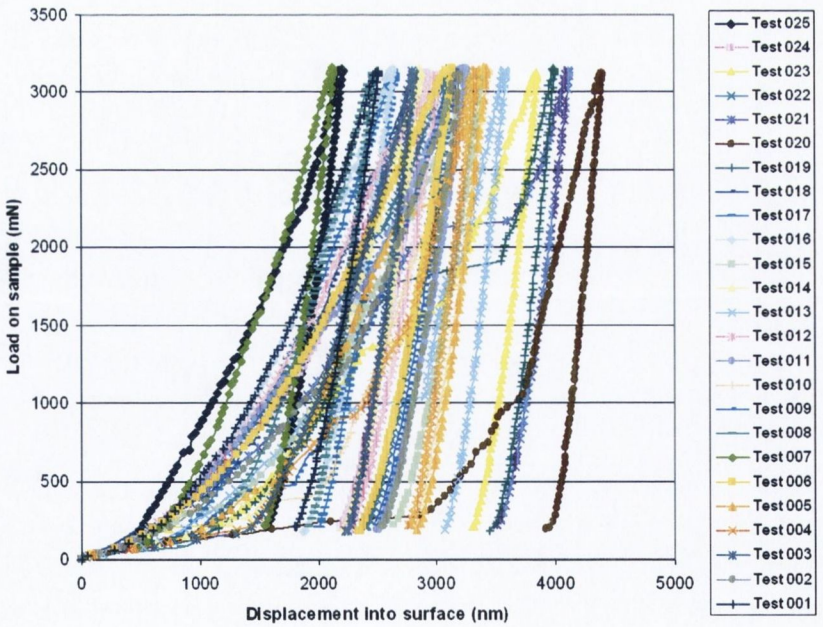

Figure 4.2: Load-displacement curves of 25 indentations performed at 3 N in L2 showing the poor reproducibility of indentation curves.

in L2, 93 were removed. Indentation results were analyzed with great care and all possible sources of errors corrected as seen in the Literature Review (fitting

Figure 4.3: Load-displacement curve of an indent performed at 3 N in L2 showing a dramatic increase in the penetration depth between 2500 and 3500 nm.

of the unloading curve, tip calibration, thermal drift correction, detection of the surface, etc). Consequent to the large scatter found in the maximum penetration depths for the same load applied, the calculated Young's modulus and hardness values exhibit large variations for the same load applied, even after removing spurious tests. Table 4.2 presents a summary of E and H values calculated for different peak loads. It can be noticed that standard deviations are huge for each load investigated (sometimes more than 25 % of the value), probably due to the large scatter in the maximum penetration depth values. The value of H seems to follow a decreasing tendency with increasing the load. This could be due to an indentation size effect but these results have to be used carefully on looking at the high standard deviation values.

On average over all loads studied (178 good tests for D2 and 112 good tests for L2), H is equal to 21±4 GPa for D2 and to 19±4 GPa for L2 and E is equal to 434±90 GPa for D2 and to 464±101 GPa for L2.

The previous results are in accordance with the fact that the Young's modulus of porous polycrystalline ceramics decreases when porosity increases.

Table 4.2: Summary of E and H values calculated from indentation tests in D2 and L2.

Load (mN)	$\mathbf{E}_{D2}$ **(GPa)**	$\mathbf{E}_{L2}$ **(GPa)**	$\mathbf{H}_{D2}$ **(GPa)**	$\mathbf{H}_{L2}$ **(GPa)**
206±1	450±106	419±51	24±5	23±2
515±2	449±118	453±67	22±5	24±3
827±11	442±84	436±66	22±5	21±4
1030±11	427±84	476±71	21±5	20±3
2080±13	431±69	485±48	20±4	19±3
3110±24	488±90	507±84	23±5	19±4
4162±17	464±46	534±91	21±2	17±4
5170±36	434±80	564±39	20±4	18±3
10221±69	324±29	366±148	19±2	16±3

The following equation is usually given for describing the influence of porosity on Young's modulus of porous polycrystalline ceramics:

$$E(P) = E_0(1 - 1.9P + 0.9P^2) \tag{4.1}$$

where E_0 is the theoretical modulus of elasticity with no porosity and P is the volume fraction porosity.

The calculated porosity is 7.0 % for D2 and 3.3 % for L2 using image analysis. Applying the previous equation gives an average value of 495 GPa for E_0, which is a bit high compared to literature values (416(30) GPa) [126] but again, these results should be taken with great care considering the high standard deviation values and the poor reproducibility of the indentation curves. Less variation might be found using porosity values determined from density measurements.

From the indentation curves, the total work of indentation W_{tot} and the elastic part of the work of indentation W_e were calculated. The plastic part of the work of indentation W_p was then deduced from the previous values. Results are presented in Table 4.3 and Fig. 4.4 for D2 and L2. As expected, the indentation energy increases with the load applied as can be seen in Fig. 4.4 and both elastic energy and plastic energy follow the same trend. Results are quite similar for D2 and L2 especially at loads inferior to 1 N. However, standard deviation values are large and this again is due to the scatter observed in the maximum penetration depths. Despite the high standard deviation, it was possible to fit the curves with a polynomial trendline.

Table 4.3: Summary of total indentation work W_{tot}, elastic work W_e and plastic work W_p values calculated from indentation tests in D2 and L2.

Load (mN)	**W_{tot} D2 (10^{-7}J)**	**W_{tot} L2 (10^{-7}J)**	**W_e D2 (10^{-7}J)**	**W_e L2 (10^{-7}J)**	**W_p D2 (10^{-7}J)**	**W_p L2 (10^{-7}J)**
206±1	0.54±0.07	0.57±0.04	0.22±0.02	0.22±0.01	0.32±0.07	0.35±0.04
515±2	2.2±0.3	2.1±0.2	0.8±0.1	0.8±0.1	1.4±0.3	1.3±0.2
827±11	4.4±0.6	4.6±0.6	1.7±0.1	1.7±0.1	2.7±0.6	2.9±0.6
1030±11	6±1	5.9±0.9	2.4±0.1	2.2±0.2	4±1	4±1
2080±13	18±2	17±2	6.5±0.3	5.8±0.4	11±2	11±2
3110±24	30±3	33±5	11.6±0.5	10.4±0.7	19±3	22±5
4162±17	48±3	48±6	17.7±0.6	15±1	30±3	33±6
5170±36	70±6	70±6	26±2	20±1	45±7	50±6
10221±69	209±10	222±20	82±3	77±16	127±11	145±25

An additional parameter was considered to characterize mechanical behavior of the material in the present study. It consists in the ratio between the plastic and total deformation energies during a depth-sensing indentation test. The W_p/W_{tot} ratio is called the energy dissipation coefficient and represents the tendency of the material to dissipate energy through irreversible plastic deformation. W_p/W_{tot} seems to be constant over all loads studied for D2 and L2 and was 0.62±0.04 on average over all loads for D2 and 0.65±0.05 on average for all loads for L2, which means that the indentation behavior of L2 is slightly more plastic than D2's behavior.

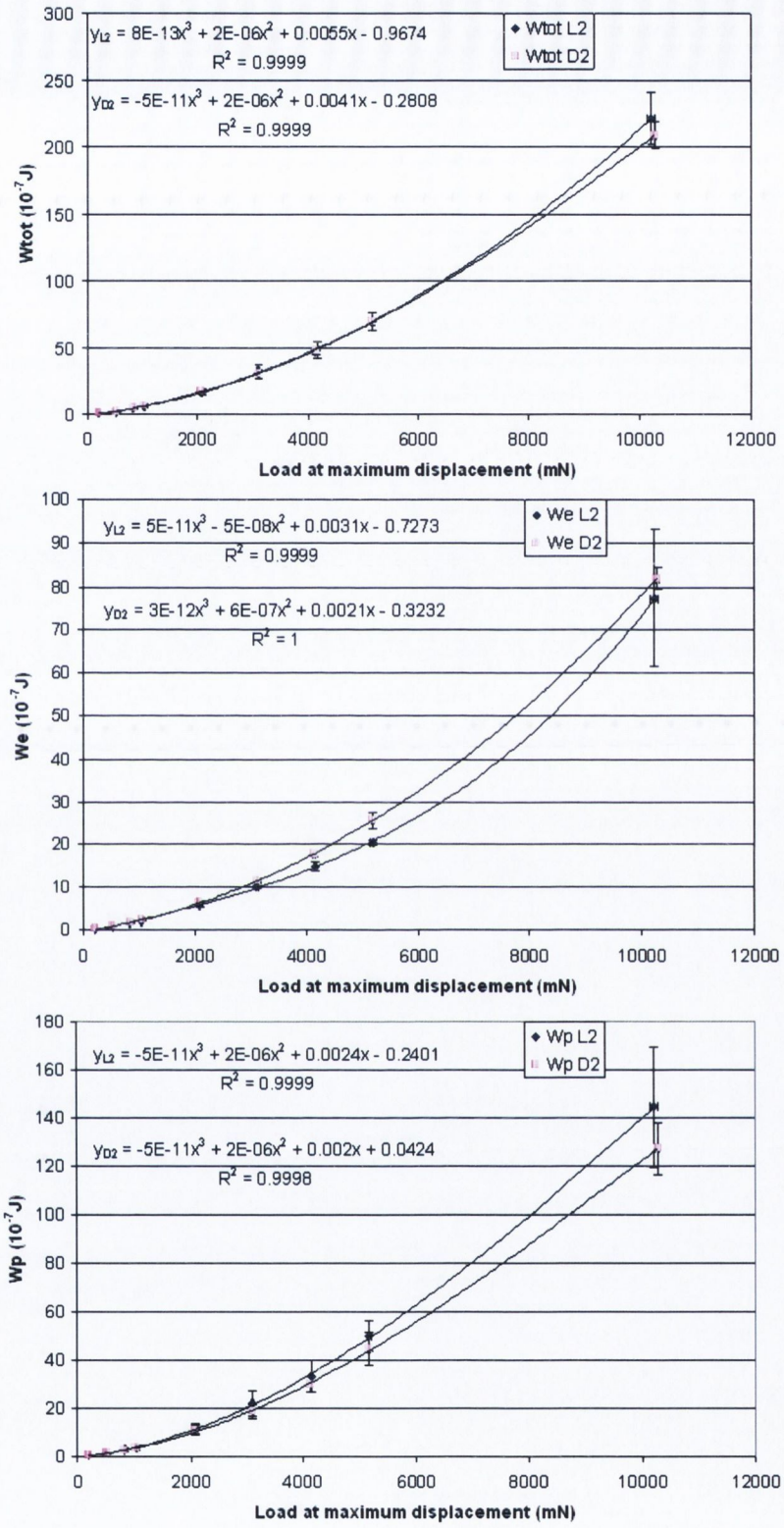

Figure 4.4: Total indentation work W_{tot}, elastic work W_e and plastic work W_p values function of the maximum load for D2 and L2.

4.1.2 Surface crack analysis

Fig. 4.5 presents two 5 N indents made with the Vickers tip in D2 (left) and L2 (right). These micrographs are representative of all the indents in alumina studied with the SEM: they show densification of the material and some grains pulled out on the edges of the indent. It should be noticed that the size of the grains is on the same order of magnitude as the size of the indent impression which means that the microstructure probably greatly influences the results. Few cracks were visible on the images, probably due to the porosity which favors densification during the indentation process. On 25 indents observed at 5 N in L2, only 4 of them had four corner cracks. The majority of the indents only had one or two corner cracks and some side cracks. However, the porosity and grain pull-out made the crack study difficult for most of the indents. The observed cracks were short with a length much lower than the diagonal of the indentation and were often deflected. Consequently, the calculation of fracture toughness using the indentation crack length method was not applicable. The same results were found on every load studied for both samples.

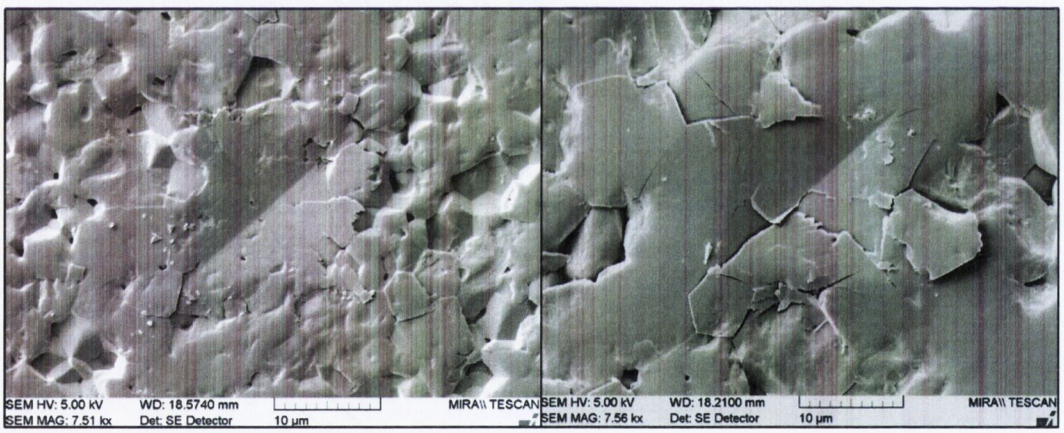

Figure 4.5: Micrographs of 5 N indents in D2 (left) and in L2 (right).

4.1.3 FIB and image analysis results: alumina crack systems

FIB tomographies on alumina were carried out by the University of New South Wales (UNSW) in Australia. The analyzed alumina samples were indented at three different loads: 50, 100 and 200 g using a Vickers tip and then gold coated before FIB tomography.

A typical image of the subsurface of an indent is presented in Fig. 4.6.

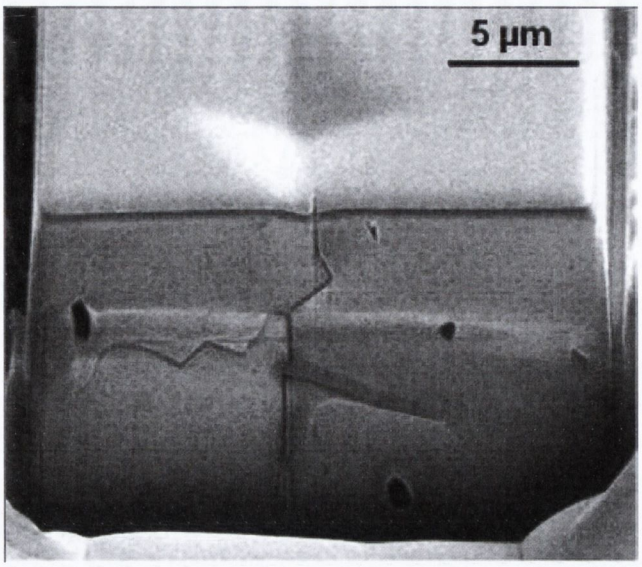

Figure 4.6: Subsurface SEM images of a 50 g load indent in alumina.

Due to topographic contrast, cracks are resolved as dark lines surrounded by brighter edges (due to enhanced secondary electron emission at edges). Pores were also visible but not grain boundaries, the voltage contrast dominating over any channeling contrast. Therefore, individual alumina grains couldn't be identified on the images for all the samples studied. This difficulty had already been noticed by Inkson in 2001 [102] while working on a Al_2O_3-5 vol%SiC nanocomposite. Consequently, crack-microstructure interactions couldn't be investigated in alumina.

The subsurface cracks found during FIB tomography have facetted and quite tortuous crack paths. On a first observation, it is quite obvious that these cracks don't follow classical well-defined paths as the indentation loads used here are too small to create real indentation cracks in alumina (well developed cracks are defined by $c \geq 2a$). Consequently, on a strict point of view, the cracks observed can hardly be related to well known types of cracks (i.e. median, shallow radial or laterals). However, when reconstructing the 3D crack patterns for the three loads investigated, these cracks can be described as parts of traditional crack types. Fig. 4.7 to Fig. 4.12 show the 3D reconstruction of cracks under 50, 100 and 200 g indentations. Pores are represented in green, cracks in red and the specimen surface in yellow. For clarity, alumina material has been removed from the picture.

Under the 50 g indent, a partial half-penny crack (noted as PHP-1 in Figs. 4.7 and 4.8) is visible. It lies from the center of the indent impression to the

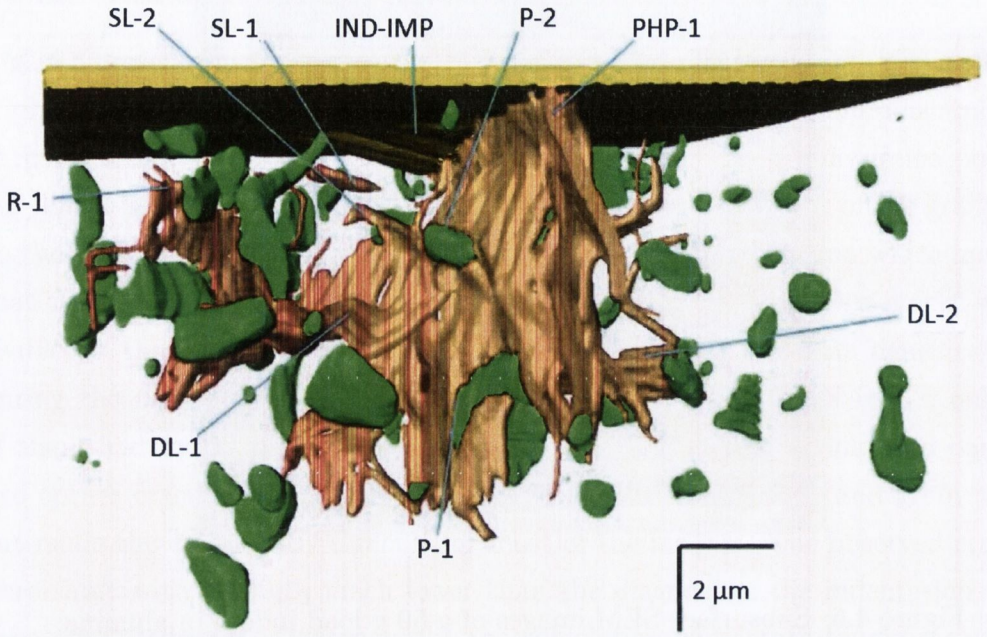

Figure 4.7: Front view of a 3D reconstruction of indentation at 50 g load. Legend for features: CD = a part of a larger crack extending in a downward direction (into the material); DL = deep lateral crack; IND-IMP = indent impression; P = pore; PHP = partial half-penny crack; R = radial crack; SL = shallow lateral; SR = secondary radial crack.

indent corner where FIB tomography has started. It is perpendicular to the serial sectioning direction and in the downward direction, it has propagated in a plane perpendicular to the surface, without any bifurcation and through two pores (named P-1 and P-2 in Figs. 4.7 and 4.8). Its maximum depth is approximately four times the depth of the residual indent impression. The partial half-penny crack observed can represent a part of the final crack shape of a median crack or of two shallow radial cracks which have merged beneath the plastic zone with a median crack. In addition to PHP-1, two deep lateral cracks (DL-1 and DL-2) and two shallow lateral cracks (SL-1 and SL-2) have formed under the 50 g indent (lateral cracks situated at depth greater than three times the depth of impression are called deep laterals whereas the others are considered as shallow laterals). A second radial crack (R-1), smaller than PHP-1 can also be seen. R-1, DL-1 and DL-2 have merged with PHP-1 to form a larger crack system. Finally, a part of a radial crack (named R-2) can be seen in Fig. 4.8 in the second half of the

indent studied during tomography. Interestingly, it is situated at some distance from the corner of the residual impression.

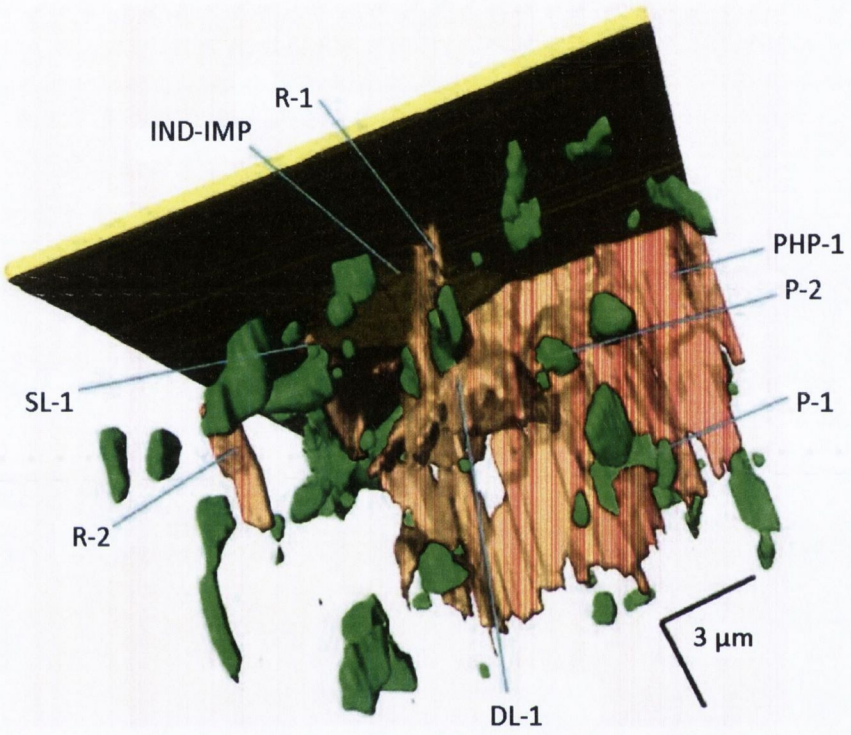

Figure 4.8: Side view of a 3D reconstruction of indentation at 50 g load. Legend for features is same as in Fig. 4.7.

Like under the 50 g indent, the largest crack formed under the 100 g indent is a partial half-penny crack (named PHP-2 in Figs. 4.9 and 4.10) but contrary to PHP-1, PHP-2 shows a tendency to turn sideways and extend as a lateral crack. However, a part of PHP-2 (marked CD-1) has propagated downward in a more classic direction. There is also a partial radial crack (named R-3) in the second half of the indent studied. Moreover, several small cracks (noted SC in Fig. 4.9) have formed under the 100 g indent as well as two deep lateral cracks (DL-3 and DL-4) and two shallow lateral cracks (SL-3 and SL-4). DL-3, CD-1 and PHP-2 have joined together to form a larger crack system.

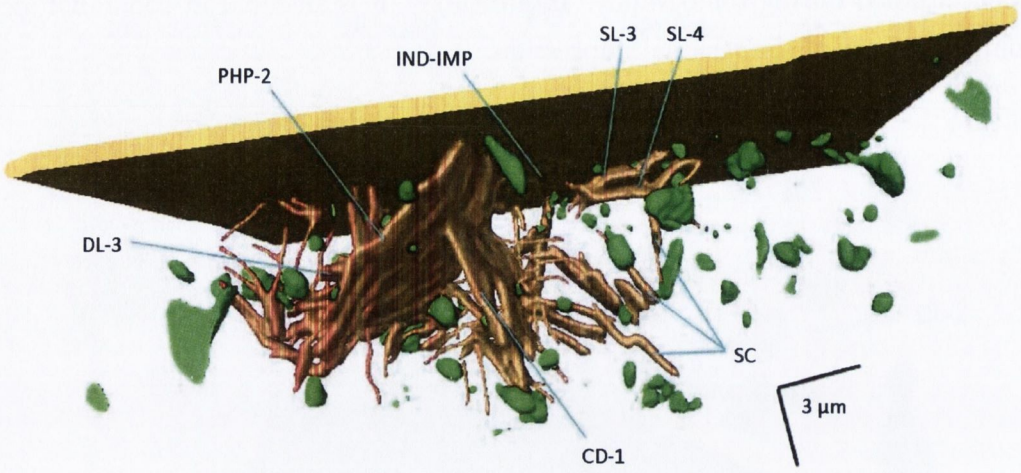

Figure 4.9: Front view of a 3D reconstruction of indentation at 100 g load. Legend for features is same as in Fig. 4.7.

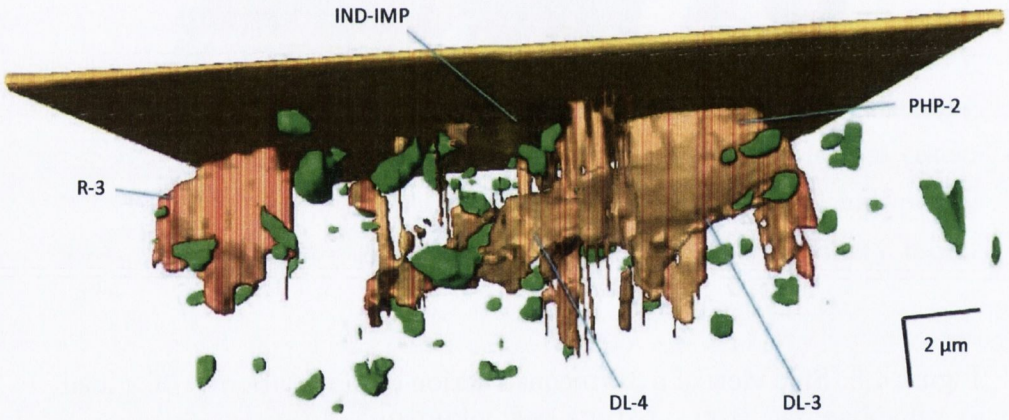

Figure 4.10: Side view of a 3D reconstruction of indentation at 100 g load. Legend for features is same as in Fig. 4.7.

Under the 200 g indent, a higher number of cracks have been generated. However, the largest crack observed is also a partial half-penny crack (marked PHP-3 in Figs. 4.11 and 4.12). PHP-3 is very similar to PHP-2 found under the 100 g indent as it bifurcates and extends as a lateral crack. A part of it (named CD-2) has propagated in a downward direction. There have been several deep lateral cracks generated (DL-5, DL-6, DL-7 and DL-8), which are bigger than under 50 and 100 g loads and two shallow lateral cracks (SL-5 and SL-6). Again, a partial radial crack (R-4) is found on the second half of the indent studied.

It can be noticed from these observations that increasing load seems to lead to an increasing tendency to form deep lateral cracks under the indents.

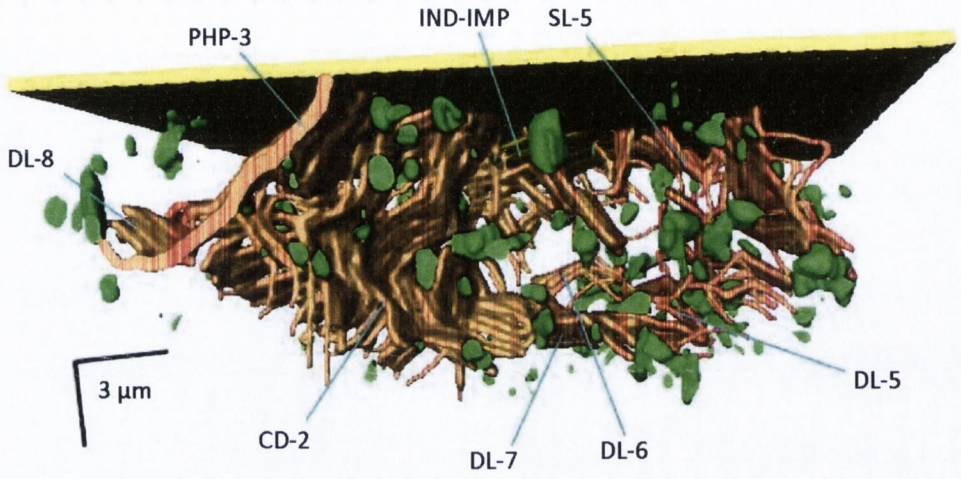

Figure 4.11: Front view of a 3D reconstruction of indentation at 200 g load. Legend for features is same as in Fig. 4.7.

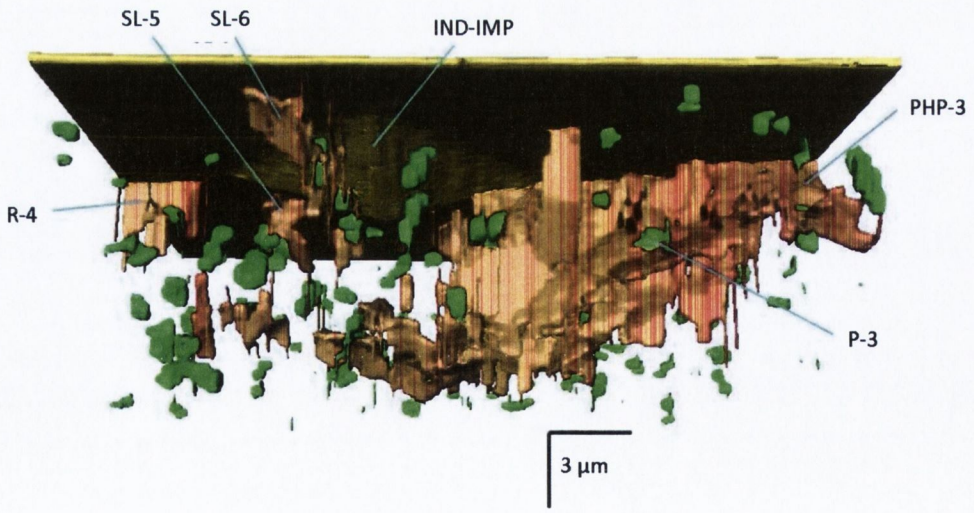

Figure 4.12: Side view of a 3D reconstruction of indentation at 200 g load. Legend for features is same as in Fig. 4.7.

The subsurface crack patterns observed are in accordance with the ones found by Elfallagh [125] in single crystal alumina, notably the presence of a crack free zone directly underneath the indent (which corresponds to a zone of compressive stress). and the interconnection between deep lateral cracks and partial half-penny cracks.

In addition to the study of the different cracks formed under the indents, other interesting observations have been done during FIB tomography of alumina samples.

One of these observations concerns pores, which are distributed randomly in the material and appear to be frequently linked to the cracks, as shown in Fig. 4.13. This may indicate they are involved in crack initiation and/or propagation.

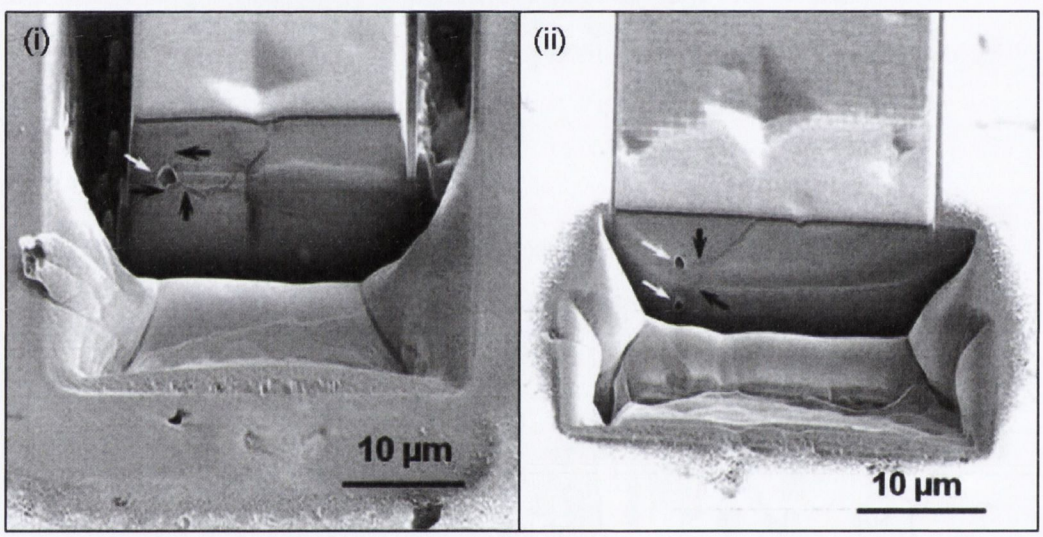

Figure 4.13: Pores involved with crack generation and/or crack propagation: (i) At 50 g load; (ii) At 100 g load.

It has also been noticed that there were few radial cracks observed on surface at the corner of the indentations made at 50, 100 and 200 g. This is very different from the large multiple radial cracks usually observed at the four corners of indent impressions when indenting polycrystalline dense alumina at those loads. This could indicate that the presence of pores tends to reduce the ability to generate or propagate radial cracks, which has been previously noticed by Jiang et al. [150] in carbon nanotube-toughened alumina-based composites.

Moreover, FIB tomography on alumina also revealed an interesting phenomenon. As presented in Fig. 4.14, some cracks opened on the platinum layer which has been deposited after the indentation test. This highlights the influence of the FIB process on existing cracks in a highly stressed environment.

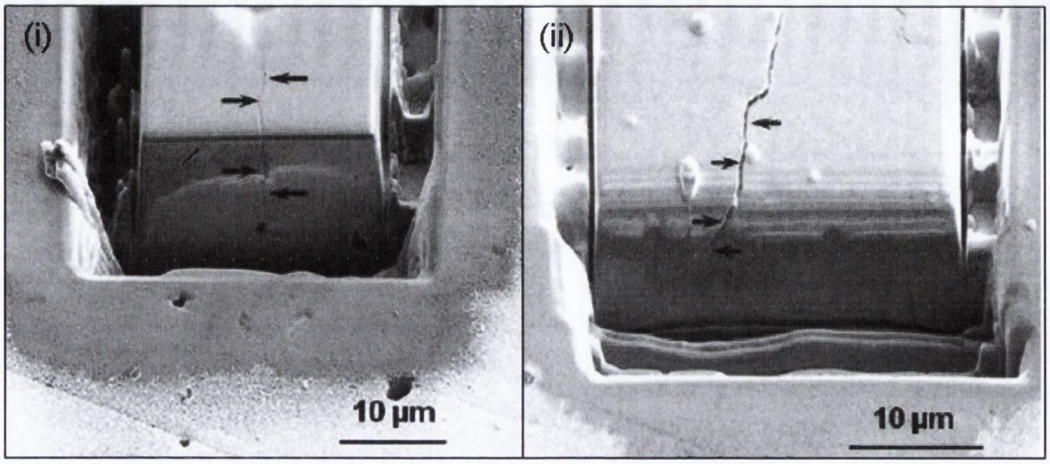

Figure 4.14: Possible crack propagation due to material removal by FIB milling of (i) 50 g indent and (iii) 200 g indent. The cracks designed by the arrows have opened on the Pt layer which has been deposited after indentation.

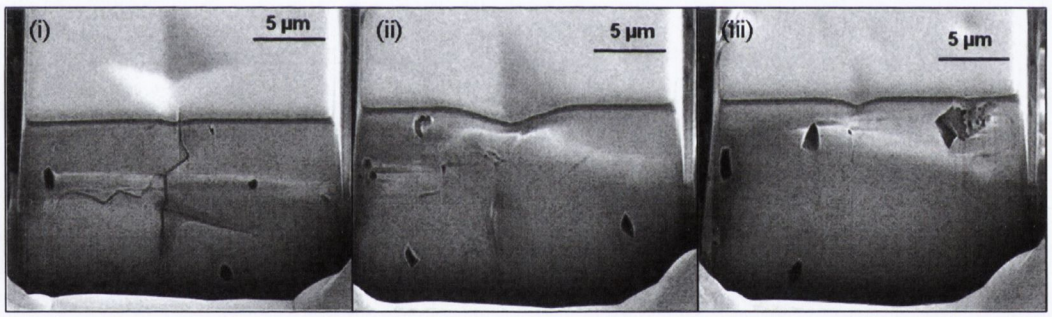

Figure 4.15: Variation in the subsurface crack density at different locations in the indentation site: (i) in the first half; (ii) at the centre; (iii) in the second half.

Finally, contrary to pore distribution, crack distribution is not uniform in the three indents studied. This is clearly visible when comparing the left (second half of the indent studied during FIB tomography) and the right (first half of the indent studied) parts of the side views for each indent (Figs. 4.8, 4.10 and 4.12). Fig. 4.15 also shows this variation of crack density through one indent during FIB tomography. Crack density in the second half of the indent is reduced compared to crack density in the first half studied. This again, is an indication of the influence of FIB processing on existing crack patterns and has been previously highlighted by Inkson et al. [118] under nanoindents and scratches in alumina

samples.

4.2 SiAlONs

Syalon 101 and Syalon 050 were chosen as second materials to study as they comprise an intergranular phase which strongly contrasts with the other phases present in SiAlON materials. Therefore, grain boundaries were visible, contrary to alumina where subsurface crack-microstructure interactions couldn't be investigated.

4.2.1 Indentation results

All Syalon 101 and 050 samples came from the same batches. However, significantly different results were obtained when indenting in the middle or in the periphery of the samples. In the following study, only indents made in the center of the samples were considered.

Successive loadings and unloadings at the same location were performed in Syalon 101 and Syalon 050 in order to check the assumption that the unloading was purely elastic. Typical loading-unloading-reloading curves obtained for Syalon 101 and Syalon 050 are presented in Fig. 4.16. In all cases, unloading and reloading curves are nearly overlapping with each other which means that the unloading is quasi-entirely elastic. The very small difference reflects reverse plasticity which may be due to small cracking during unloading.

As in alumina, a poor reproducibility of indentation curves was observed due to a scatter in the depth reached at peak load. However, the scatter in h_{max} was lower in Syalons 101 and 050 than in alumina samples as can be seen when analyzing the coefficient of variation of h_{max}. Table 4.4 shows statistical variations of the recorded penetration depth h_{max} at different peak loads for Syalons 101 and 050 indented with the Vickers tip. As already observed with alumina, this coefficient of variation exhibits a clear decreasing tendency when load increases, (Fig. 4.17), which means the dispersion in the results decreases as the load increases.

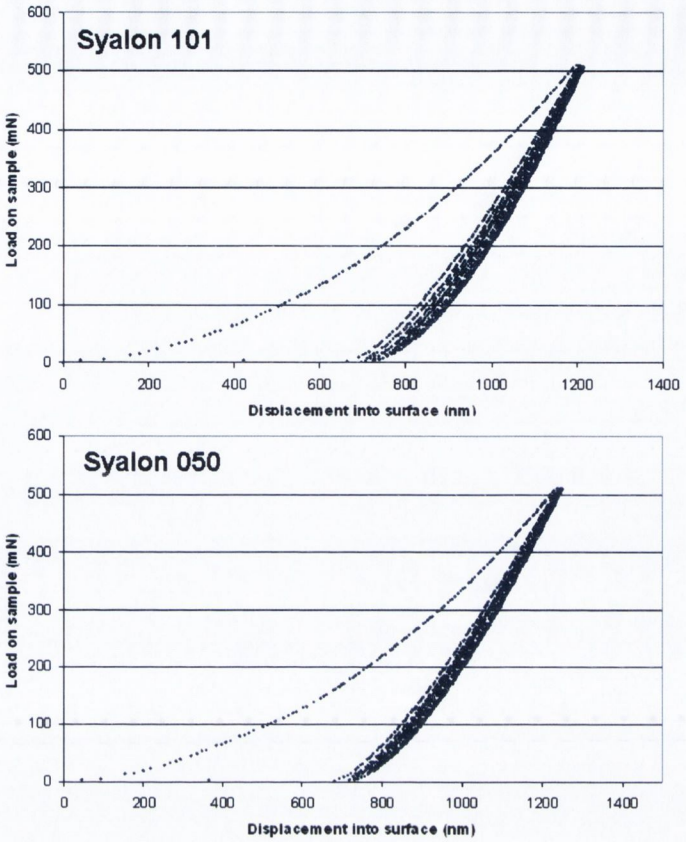

Figure 4.16: Representative load-displacement curves obtained during successive loading-unloading-reloading cycles at 500 mN for Syalon 101 and Syalon 050.

4.2.1.1 Indentation in Syalon 101 and Syalon 050 with the Vickers tip

Each set of curves was examined individually and any spurious test removed. Contrary to the previous study in alumina, only few tests exhibited a dramatic increase in penetration depths, resulting in a higher number of tests kept for analysis. Corrections on calculated E and H values were applied in accordance with the issues detailed in the Literature Review (fitting of the unloading curve, tip calibration, thermal drift correction, detection of the surface, etc) and results for E, H and the ratio H/E are presented in Table 4.5.

The scatter found in E and H values is quite large, probably due to the variation found in the maximum penetration depths for the same load applied. Figs. 4.18, 4.19 and 4.20 show the variation of H, E and H/E with the maximum load applied.

Table 4.4: Statistical properties of the maximum penetration depth h_{max} measured at different peak loads for Syalon 101 and Syalon 050 indented with the Vickers tip.

Syalon 101									
$\mathbf{P}_{max}$ **(N)**									
Mean	0.515	0.713	1.03	2.07	5.18	10.28			
Stdev	0.003	0.006	0.01	0.01	0.03	0.02			
$\mathbf{h}_{max}$ **(nm)**									
Mean	1282	1578	1897	2797	4437	6211			
Stdev	86	119	141	162	157	130			
Cv	0.067	0.076	0.075	0.058	0.035	0.021			
Syalon 050									
$\mathbf{P}_{max}$ **(N)**									
Mean	0.515	0.822	1.028	2.06	3.11	4.15	5.185	8.28	10.26
Stdev	0.002	0.009	0.009	0.01	0.02	0.01	0.020	0.05	0.04
$\mathbf{h}_{max}$ **(nm)**									
Mean	1224	1616	1792	2572	3152	3643	4080	5210	6095
Stdev	65	209	125	171	135	208	107	115	85
Cv	0.053	0.129	0.070	0.067	0.043	0.057	0.026	0.022	0.014

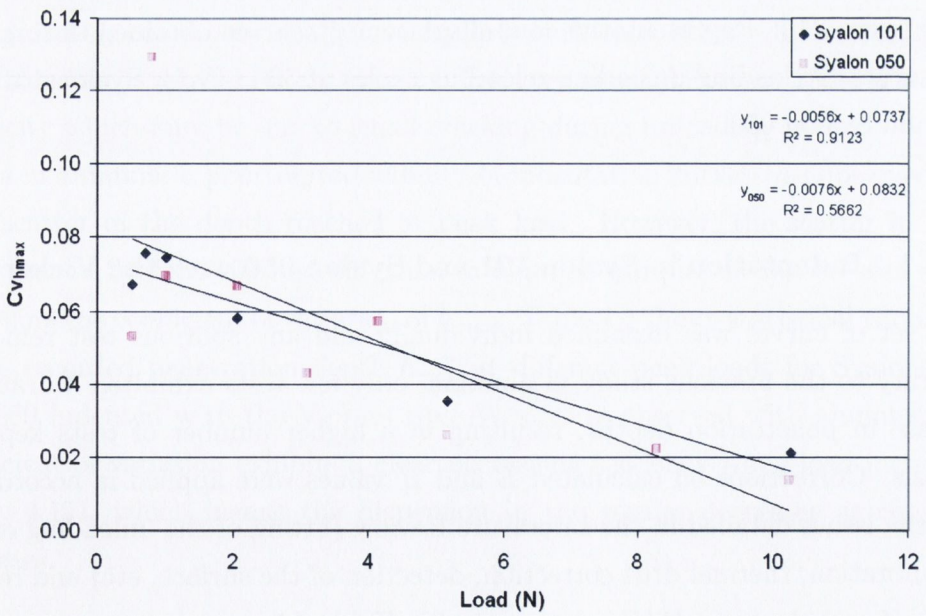

Figure 4.17: Coefficient of variation of h_{max} function of the maximum peak load for Syalon 101 and Syalon 050 indented with the Vickers tip.

Table 4.5: Summary of E, H and H/E values calculated from indentation tests in Syalons 101 and 050 (Vickers tip).

Load (N)	$\mathbf{H}_{Syalon101}$ **(GPa)**	$\mathbf{H}_{Syalon050}$ **(GPa)**	$\mathbf{E}_{Syalon101}$ **(GPa)**	$\mathbf{E}_{Syalon050}$ **(GPa)**	$\mathbf{H/E}_{Syalon101}$	$\mathbf{H/E}_{Syalon050}$
0.515±0.003	20.3±0.4	24±1	279±5	290±9	0.073±0.002	0.083±0.005
0.713±0.006	18.7±0.9	-	280±9	-	0.067±0.004	-
0.822±0.009	-	22±1	-	276±9	-	0.081±0.005
1.03±0.01	18.8±0.6	22±1	266±6	273±11	0.071±0.003	0.081±0.006
2.07±0.01	19.0±0.7	23±1	234±6	261±8	0.081±0.004	0.089±0.005
3.11±0.02	-	22±1	-	257±13	-	0.085±0.007
4.15±0.02	-	22.2±0.8	-	264±5	-	0.084±0.003
5.19±0.03	17.7±0.9	21±1	239±10	266±20	0.074±0.005	0.080±0.007
8.28±0.05	-	20.4±0.6	-	260±7	-	0.078±0.003
10.26±0.03	17.7±0.6	19.0±0.6	239±12	227±4	0.074±0.005	0.084±0.003

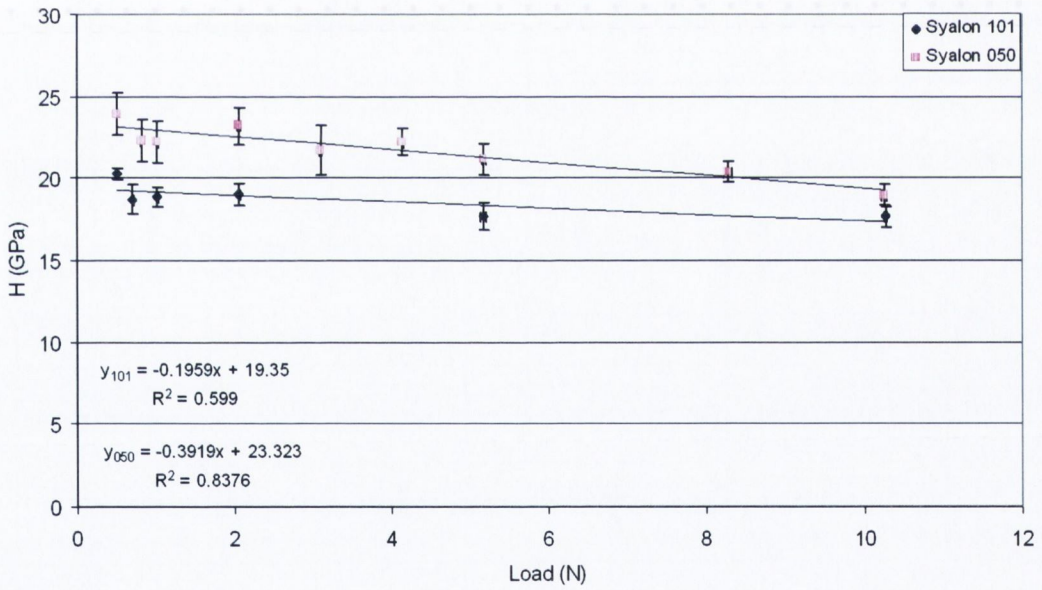

Figure 4.18: Variation of hardness with the maximum load applied for Syalons 101 and 050 indented with the Vickers tip.

A decrease in hardness when increasing the load was observed in both Syalon 101 and Syalon 050 with H ranging from 20.3 to 17.7 GPa between 0.515 and 10.26 N for Syalon 101 and H varying between 24 and 19 GPa for Syalon 050 on the same range of loads. This indentation size effect was a bit more marked in Syalon 050 than in Syalon 101 as can be seen in Fig. 4.18. It can be noticed that despite

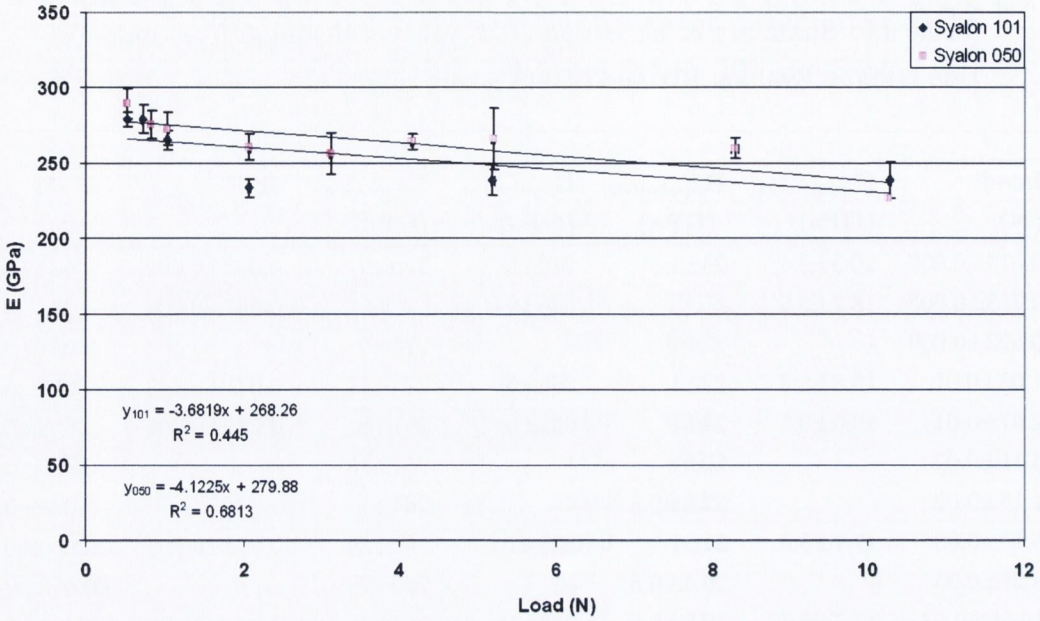

Figure 4.19: Variation of Young's modulus with the maximum load applied for Syalons 101 and 050 indented with the Vickers tip.

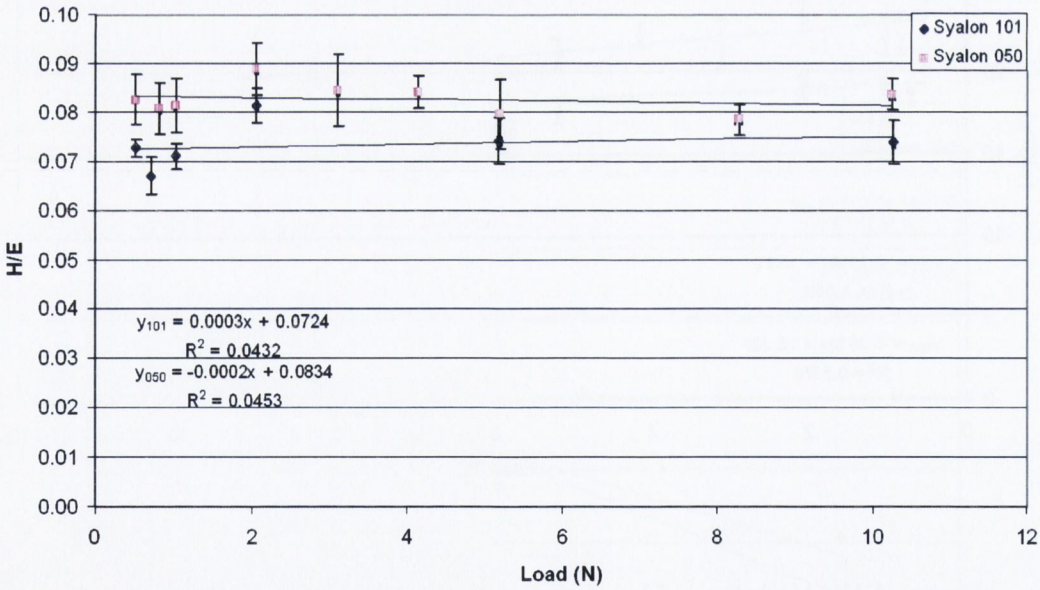

Figure 4.20: Variation of H/E with the maximum load applied for Syalons 101 and 050 indented with the Vickers tip.

the decrease in H when increasing the maximum load, Syalon 050 hardness value is always higher than Syalon 101 value on the range of loads investigated. This is in accordance with the manufacturer specifications but the values found in this

study are higher than the ones claimed by International Syalons (14.7 GPa for Syalon 101 and 19.6 GPa for Syalon 050). Their tests were done at 2.94 N using a Vickers microindenter.

An indentation size effect was also observed for Young's modulus in both Syalons 101 and 050 with E ranging from 280 to 234 GPa between 0.515 and 10.26 N for Syalon 101 and E varying between 290 and 227 GPa for Syalon 050 on the same range of loads. As for the hardness value, a difference was found between Young's modulus bulk value given by International Syalons (288 GPa for Syalon 101 and 306 GPa for Syalon 050) and the ones obtained in this study which were significantly lower than the values claimed by the manufacturer. On average, E value was higher for Syalon 050 than for Syalon 101 which is in accordance with International Syalons specifications.

No significant variation of the ratio H/E has been observed in the range of loads investigated. On average of all loads, this ratio was 0.073 for Syalon 101 and 0.083 for Syalon 050. It can be noticed that Syalon 050 presents a H/E value always higher than Syalon 101 which is in accordance with the bulk values given by International Syalons (0.051 for Syalon 101 and 0.064 for Syalon 050).

The total work of indentation W_{tot} and the elastic part of the work of indentation W_e were calculated from the indentation curves and are presented in Table 4.6 with the plastic part of the work of indentation W_p and the ratio W_p/W_{tot}. As expected, the total indentation energy W_{tot} increases with the load applied as can be seen in Fig. 4.21 and can be fitted with a power law curve. Both elastic (Fig. 4.22) and plastic (Fig. 4.23) energies follow the same trend. It can be noticed from these curves that Syalon 050 has a more elastic response to indentation than Syalon 101, which is confirmed by the ratio W_p/W_{tot} lower in Syalon 050 than in Syalon 101 for all loads studied (Fig. 4.24). Interestingly, for both materials, the W_p/W_{tot} ratio slightly tends to increase with the maximum load applied, which would significate a small change in the elasto-plastic indentation response of these materials when increasing the maximum load applied.

Table 4.6: Summary of W_{tot}, W_e, W_p and W_p/W_{tot} values calculated from indentation tests in Syalons 101 and 050 (Vickers tip).

Load (N)	**W_{tot} Syalon101 (10^{-7}J)**	**W_{tot} Syalon050 (10^{-7}J)**	**W_e Syalon101 (10^{-7}J)**	**W_e Syalon050 (10^{-7}J)**
0.515±0.003	2.40±0.03	2.26±0.07	1.12±0.02	1.15±0.02
0.713±0.006	4.1±0.1	-	1.88±0.03	-
0.822±0.009	-	4.7±0.2	-	2.40±0.06
1.03±0.01	7.0±0.1	6.6±0.2	3.26±0.06	3.36±0.09
2.07±0.01	20.5±0.4	18.6±0.4	9.7±0.1	9.6±0.3
3.11±0.02	-	35±1	-	17.5±0.6
4.15±0.02	-	52.7±0.8	-	26.9±0.4
5.19±0.03	82±2	75±3	38±1	37±2
8.28±0.05	-	154±3	-	74±1
10.26±0.03	230±7	222±4	104±4	112±1
Load (N)	**W_p Syalon101 (10^{-7}J)**	**W_p Syalon050 (10^{-7}J)**	**W_p/W_{tot} Syalon101**	**W_p/W_{tot} Syalon050**
0.515±0.003	1.28±0.03	1.12±0.08	0.53±0.02	0.49±0.04
0.713±0.006	2.2±0.1	-	0.54±0.03	-
0.822±0.009	-	2.3±0.2	-	0.49±0.04
1.03±0.01	3.8±0.1	3.2±0.2	0.54±0.02	0.49±0.04
2.07±0.01	10.8±0.4	9.0±0.5	0.53±0.02	0.48±0.03
3.11±0.02	-	17±1	-	0.50±0.05
4.15±0.02	-	25.8±0.9	-	0.49±0.02
5.19±0.03	45±3	38±3	0.54±0.04	0.50±0.05
8.28±0.05	-	79±3	-	0.52±0.02
10.26±0.03	127±8	110±4	0.55±0.04	0.50±0.02

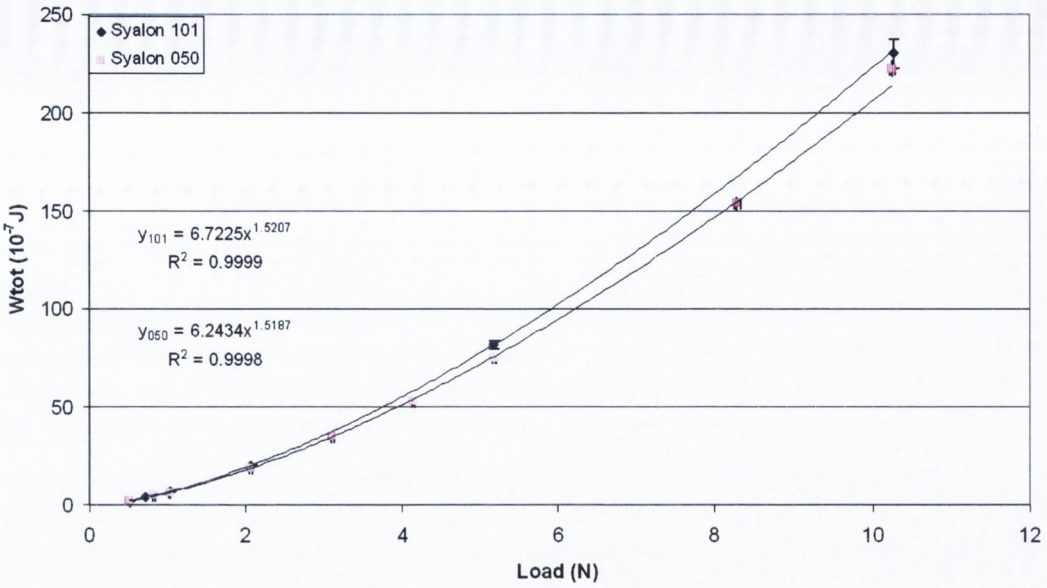

Figure 4.21: Variation of W_{tot} with the maximum load applied for Syalons 101 and 050 indented with the Vickers tip.

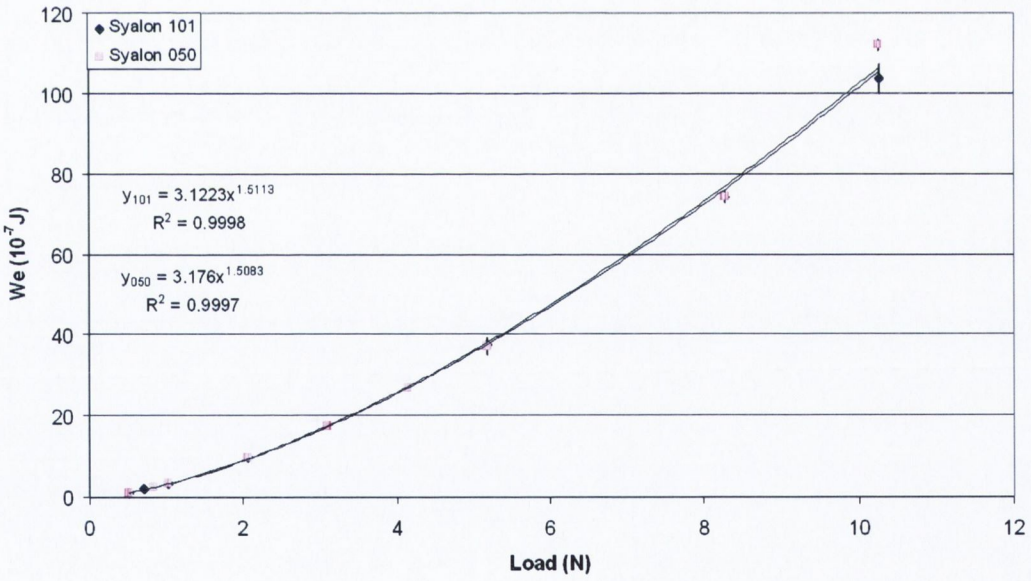

Figure 4.22: Variation of W_e with the maximum load applied for Syalons 101 and 050 indented with the Vickers tip.

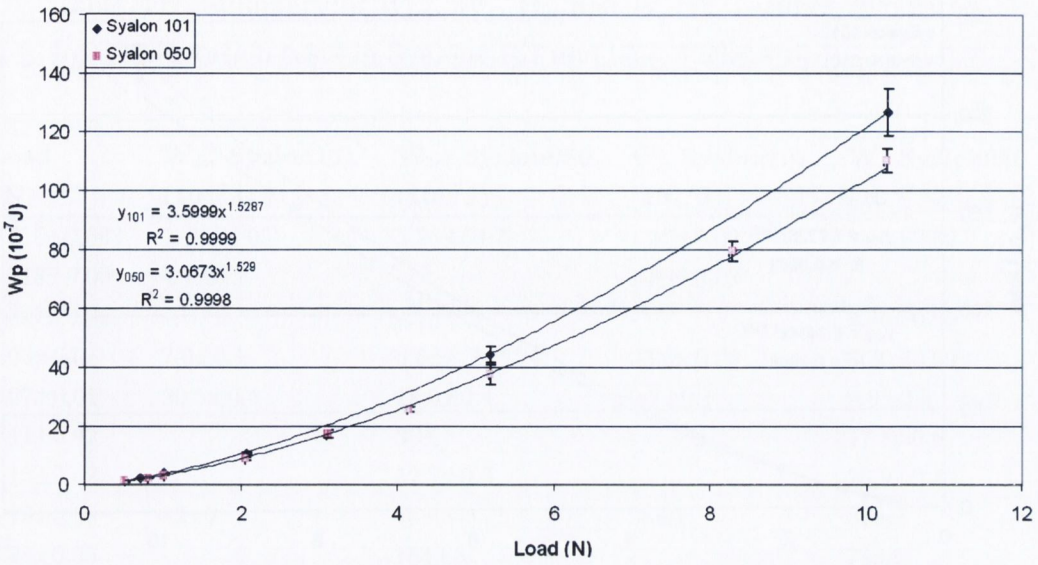

Figure 4.23: Variation of W_p with the maximum load applied for Syalons 101 and 050 indented with the Vickers tip.

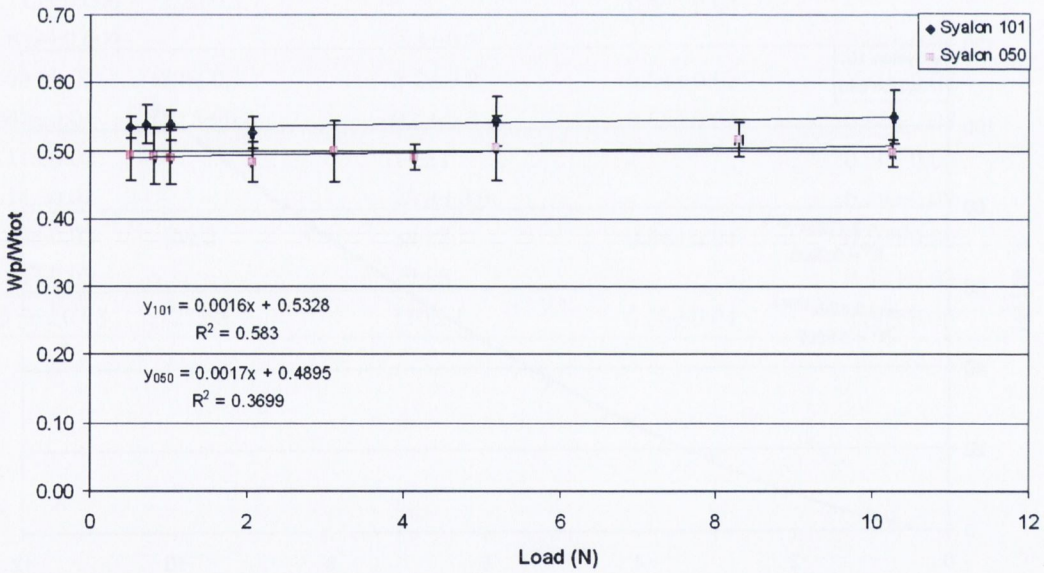

Figure 4.24: Variation of W_p/W_{tot} with the maximum load applied for Syalons 101 and 050 indented with the Vickers tip.

4.2.1.2 Indentation in Syalon 101 and Syalon 050 with the Customized tip

A summary of the values of H, E and the ratio H/E obtained for the tests performed with the customized tip (a four-facets pyramid tip sharper than the Vickers tip) is presented in Table 4.7 and the corresponding curves are drawn in Figs. 4.25, 4.26 and 4.27. Contrary to the Vickers tip, the customized tip is expected to create pile-up on the edges of the indent, thus leading to an apparent increase in H and E values calculated from indentation tests. This is in accordance with the results obtained in this study for H (Figs. 4.28 and 4.29) as the results obtained are higher than those obtained using the Vickers tip. It is also the case for E in Syalon 101 (Fig. 4.30) but surprisingly not in Syalon 050 as can be noticed in Fig. 4.31. As previously found with the Vickers tip, an indentation size effect was observed in both Syalon 101 and Syalon 050 for H and E but no particular variation of the ratio H/E was noticed over the range of loads studied. This ratio was found to be equal to 0.074 for Syalon 101 on average over all loads studied and to be equal to 0.090 for Syalon 050.

Table 4.7: Summary of E, H and H/E values calculated from indentation tests in Syalons 101 and 050 (customized tip).

Load (N)	$\mathbf{H}_{Syalon101}$ **(GPa)**	$\mathbf{H}_{Syalon050}$ **(GPa)**	$\mathbf{E}_{Syalon101}$ **(GPa)**	$\mathbf{E}_{Syalon050}$ **(GPa)**	$\mathbf{H/E}_{Syalon101}$	$\mathbf{H/E}_{Syalon050}$
0.514±0.002	21.2±0.8	25±2	296±9	268±6	0.071±0.004	0.095±0.006
0.72±0.01	20.5±0.4	24±1	279±6	256±7	0.073±0.002	0.095±0.006
1.03±0.01	21.3±0.7	25±2	281±7	276±8	0.076±0.003	0.089±0.006
2.07±0.01	20.6±0.4	-	260±6	-	0.079±0.002	-
3.11±0.02	-	22±1	-	232±5	-	0.097±0.004
5.18±0.03	19±1	22±1	268±10	274±9	0.070±0.005	0.079±0.005
8.28±0.04	-	20±2	-	220±16	-	0.09±0.01

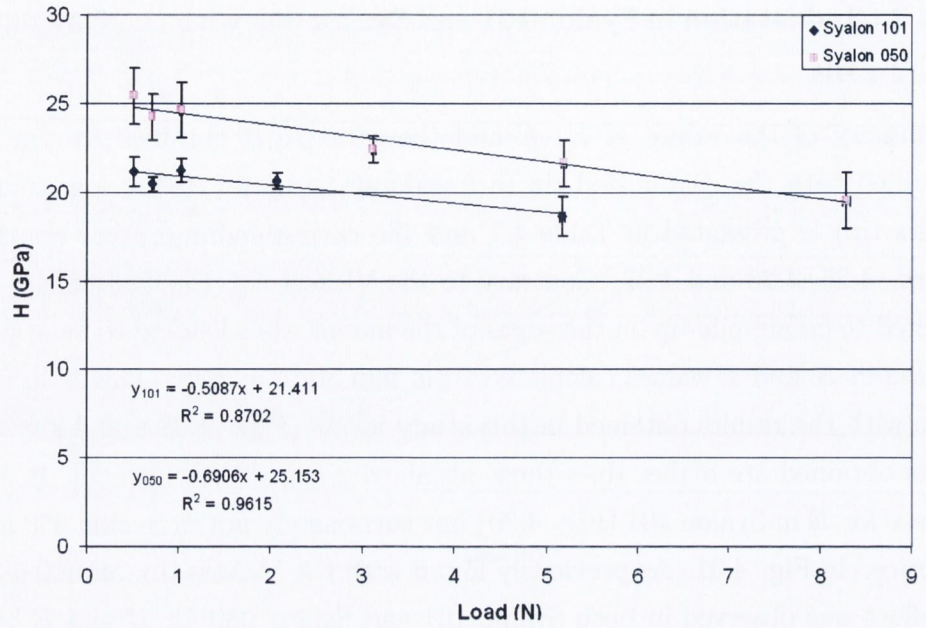

Figure 4.25: Variation of hardness with the maximum load applied for Syalons 101 and 050 indented with the customized tip.

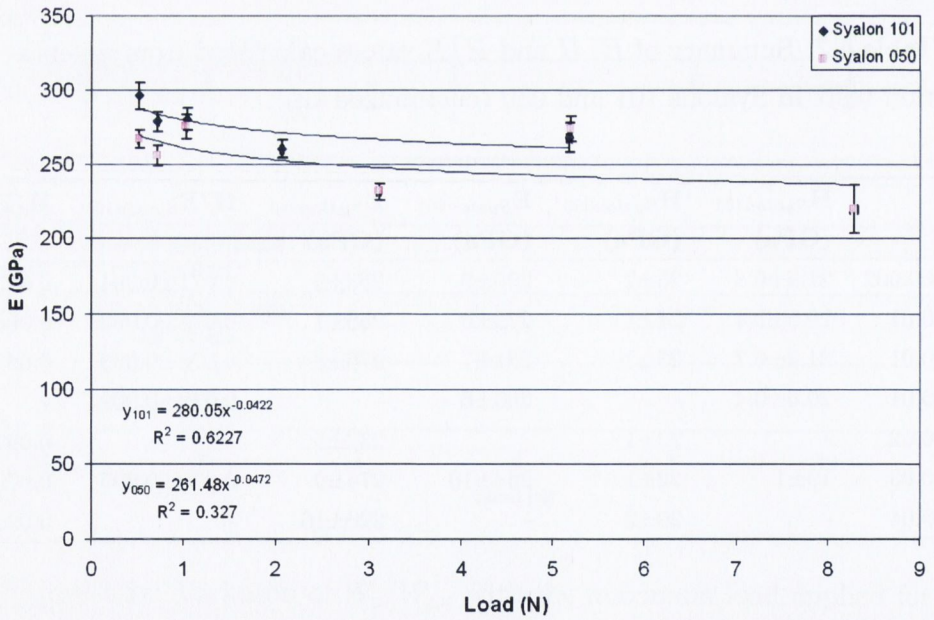

Figure 4.26: Variation of Young's modulus with the maximum load applied for Syalons 101 and 050 indented with the customized tip.

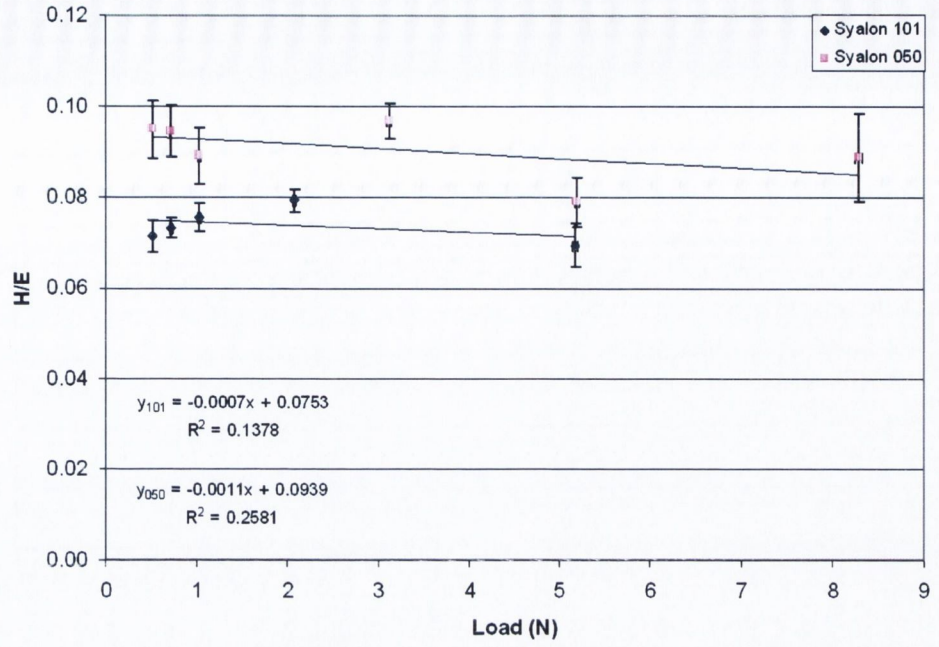

Figure 4.27: Variation of H/E with the maximum load applied for Syalons 101 and 050 indented with the customized tip.

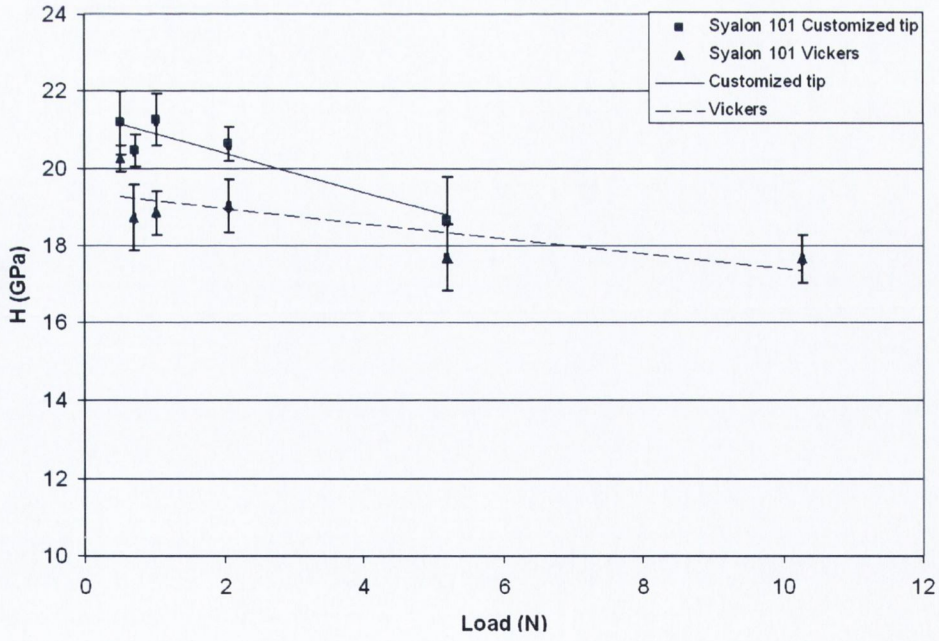

Figure 4.28: Variation of H with the maximum load applied for Syalon 101 indented with Vickers and customized tips.

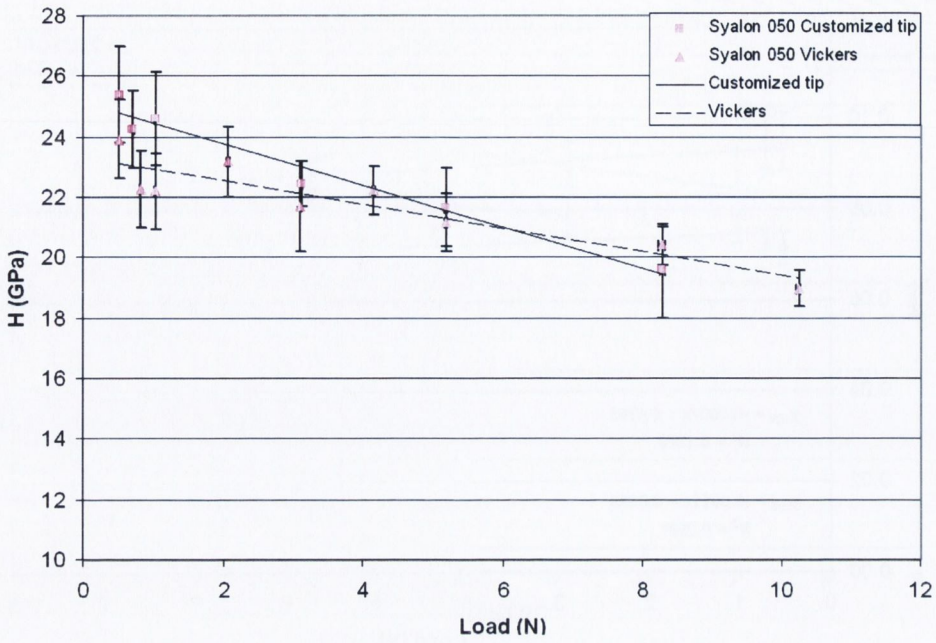

Figure 4.29: Variation of H with the maximum load applied for Syalons 050 indented with Vickers and customized tips.

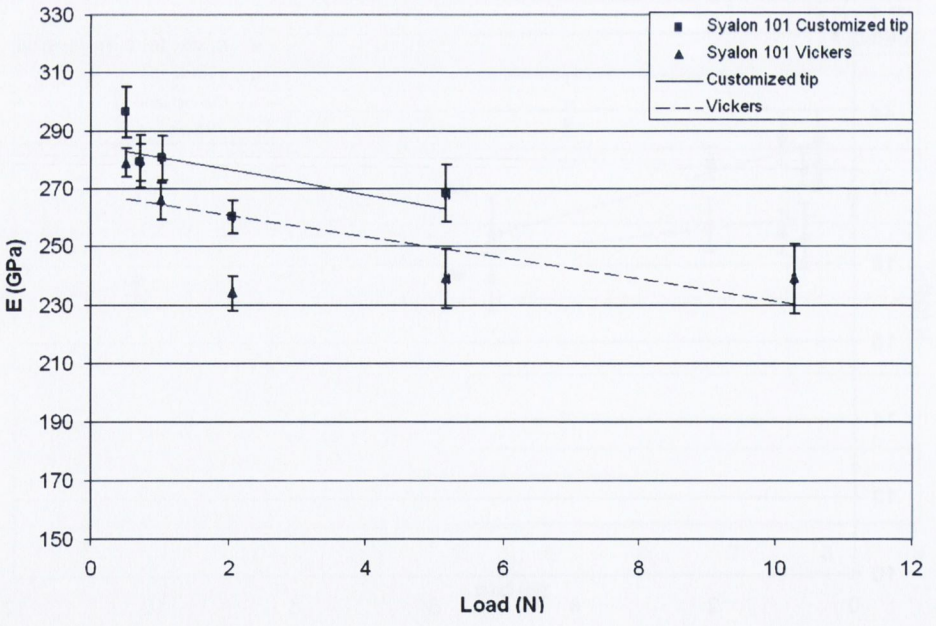

Figure 4.30: Variation of E with the maximum load applied for Syalon 101 indented with Vickers and customized tips.

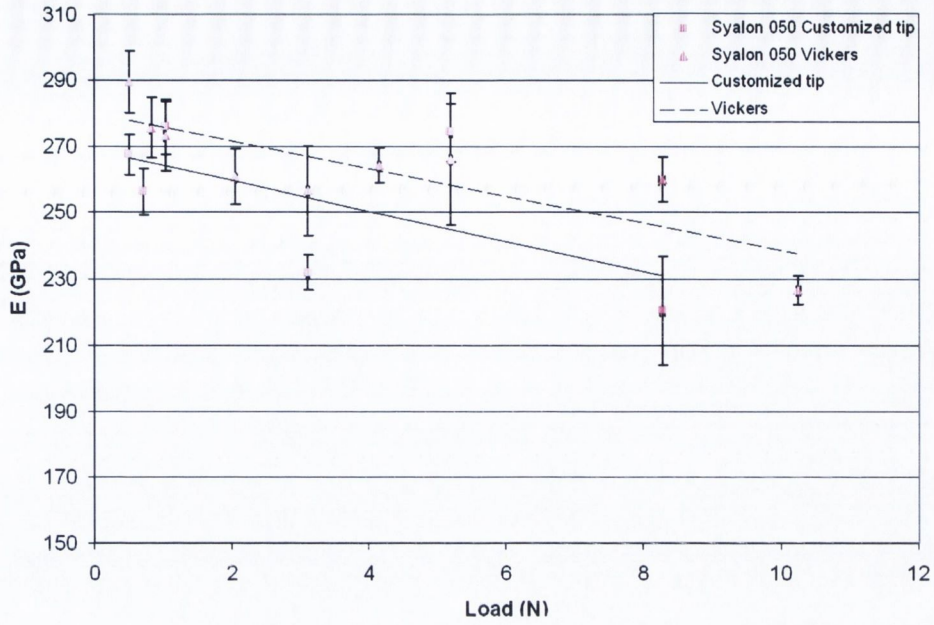

Figure 4.31: Variation of E with the maximum load applied for Syalon 050 indented with Vickers and customized tips.

The energies W_{tot}, W_e and W_p were calculated from the indentation curves. Results are presented in Table 4.8 and the variation of the total (Fig. 4.32), elastic (Fig. 4.33) and plastic (Fig. 4.34) energies follow the same trend and can be fitted with a power law curve. As already noticed with the Vickers tip, Syalon 101 has a more plastic response to indentation than Syalon 050 as can be seen with the W_p/W_{tot} ratio (Fig. 4.35) which is always lower for Syalon 050 on the range of loads investigated. This ratio also follows an increasing tendency with the maximum load applied as previously noticed with the Vickers tip.

Table 4.8: Summary of W_{tot}, W_e, W_p and W_p/W_{tot} values calculated from indentation tests in Syalons 101 and 050 (customized tip).

Load (N)	**W_{tot} Syalon101 (10^{-7}J)**	**W_{tot} Syalon050 (10^{-7}J)**	**W_e Syalon101 (10^{-7}J)**	**W_e Syalon050 (10^{-7}J)**
0.514±0.002	5.0±0.2	4.6±0.2	1.14±0.02	1.28±0.03
0.72±0.01	8.5±0.2	7.6±0.4	2.03±0.04	2.13±0.03
1.03±0.01	14.5±0.3	13.6±0.6	3.46±0.07	3.58±0.05
2.07±0.01	42±1	-	9.9±0.2	-
3.11±0.02	-	75±3	-	20.0±0.3
5.18±0.03	175±8	159±10	37.1±0.9	38±1
8.28±0.04	-	367±35	-	84±2
Load (N)	**W_p Syalon101 (10^{-7}J)**	**W_p Syalon050 (10^{-7}J)**	**W_p/W_{tot} Syalon101**	**W_p/W_{tot} Syalon050**
0.514±0.002	3.9±0.2	3.3±0.2	0.77±0.04	0.72±0.05
0.72±0.01	6.5±0.2	5.5±0.4	0.76±0.02	0.72±0.06
1.03±0.01	11.0±0.3	10.0±0.6	0.76±0.03	0.74±0.05
2.07±0.01	32±1	-	0.76±0.03	-
3.11±0.02	-	55±3	-	0.73±0.05
5.18±0.03	138±8	121±10	0.79±0.06	0.76±0.08
8.28±0.04	-	283±35	-	0.8±0.1

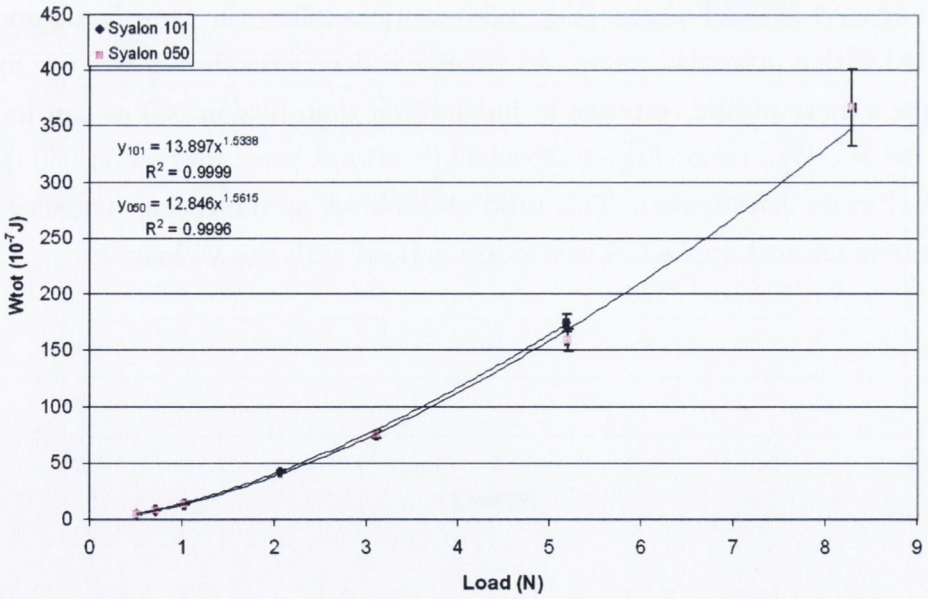

Figure 4.32: Variation of W_{tot} with the maximum load applied for Syalons 101 and 050 indented with the customized tip.

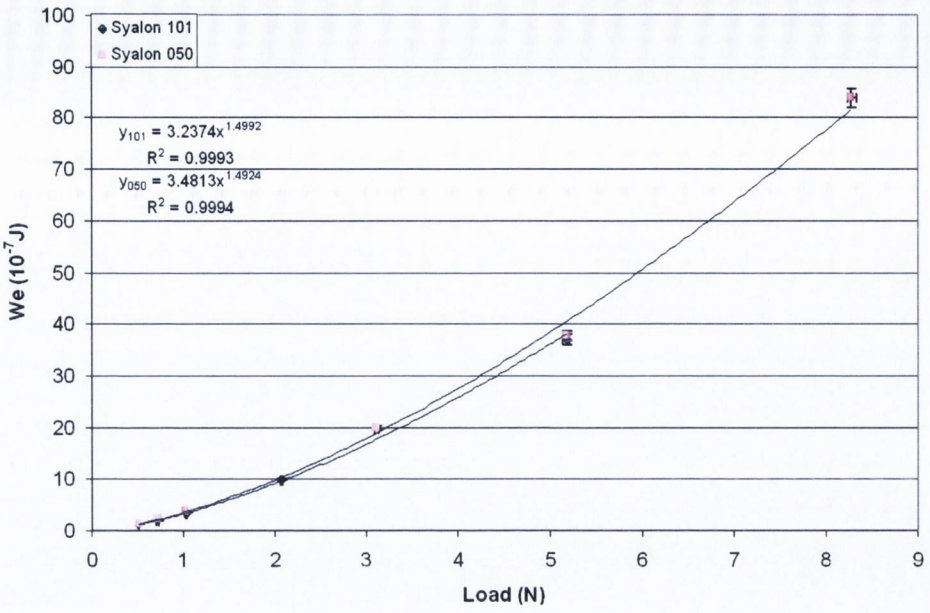

Figure 4.33: Variation of W_e with the maximum load applied for Syalons 101 and 050 indented with the customized tip.

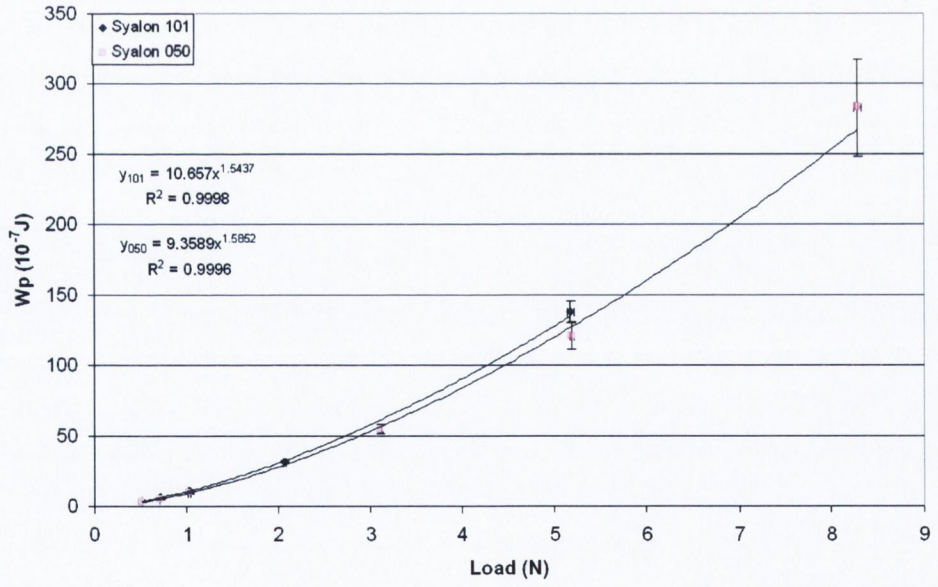

Figure 4.34: Variation of W_p with the maximum load applied for Syalons 101 and 050 indented with the customized tip.

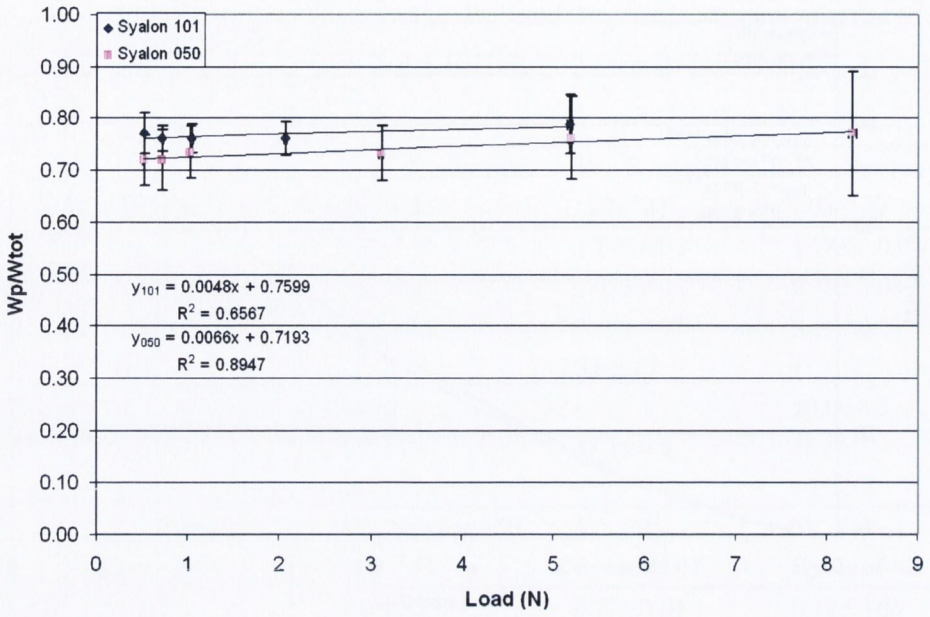

Figure 4.35: Variation of W_p/W_{tot} with the maximum load applied for Syalons 101 and 050 indented with the customized tip.

When comparing the energies from the indentation curves (Figs. 4.36 to 4.43), it is interesting to note that the elastic energy value is nearly identical when performing the indents with the Vickers or the customized tip at all loads studied . This result is valid for both Syalons 101 and 050. The difference of energy observed in W_{tot} between the customized and the Vickers tips is therefore entirely plastic. This result can also be correlated to the ratio W_p/W_{tot} which is much more higher for the customized tip than for the Vickers.

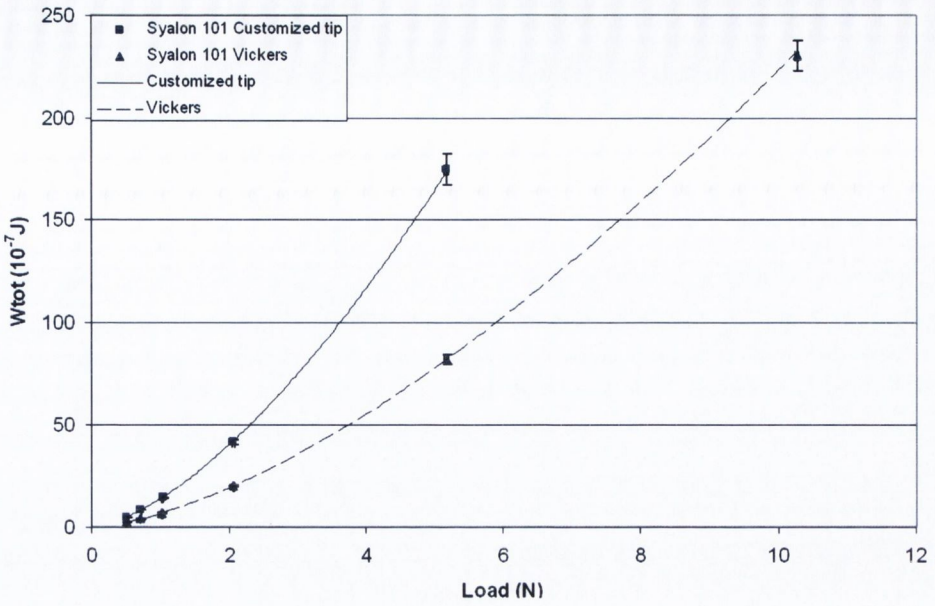

Figure 4.36: Variation of W_{tot} with the maximum load applied for Syalon 101 indented with Vickers and customized tips.

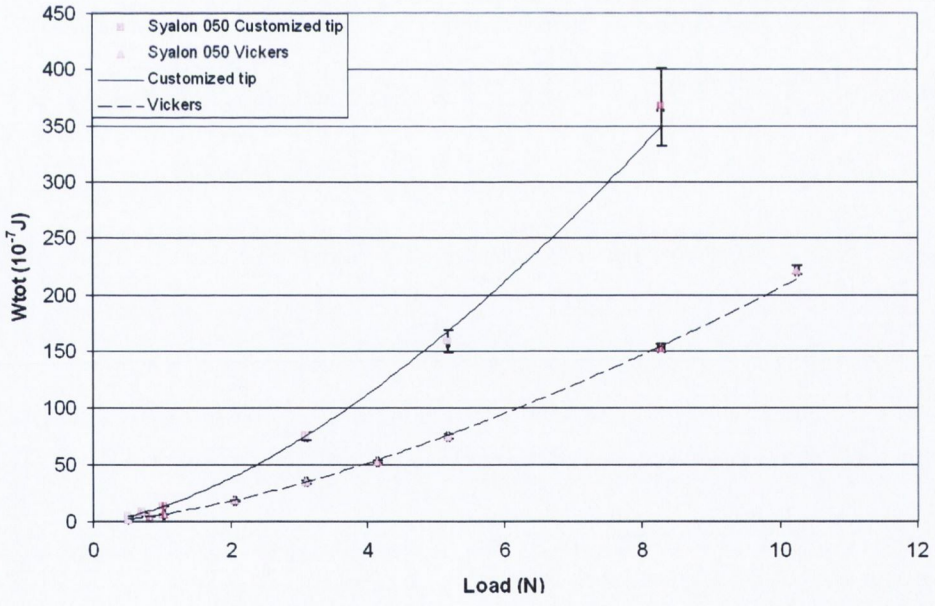

Figure 4.37: Variation of W_{tot} with the maximum load applied for Syalon 050 indented with Vickers and customized tips.

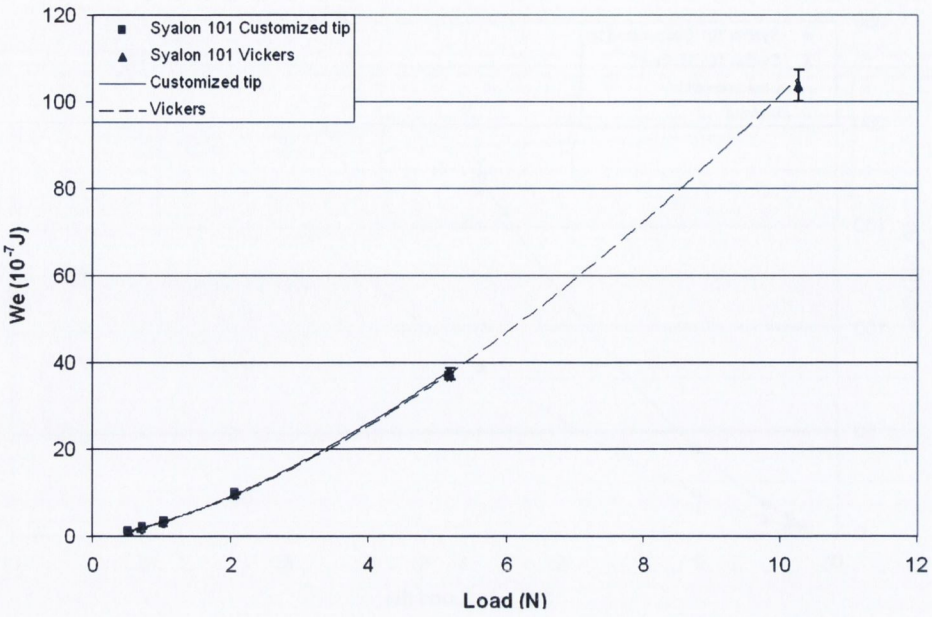

Figure 4.38: Variation of W_e with the maximum load applied for Syalon 101 indented with Vickers and customized tips.

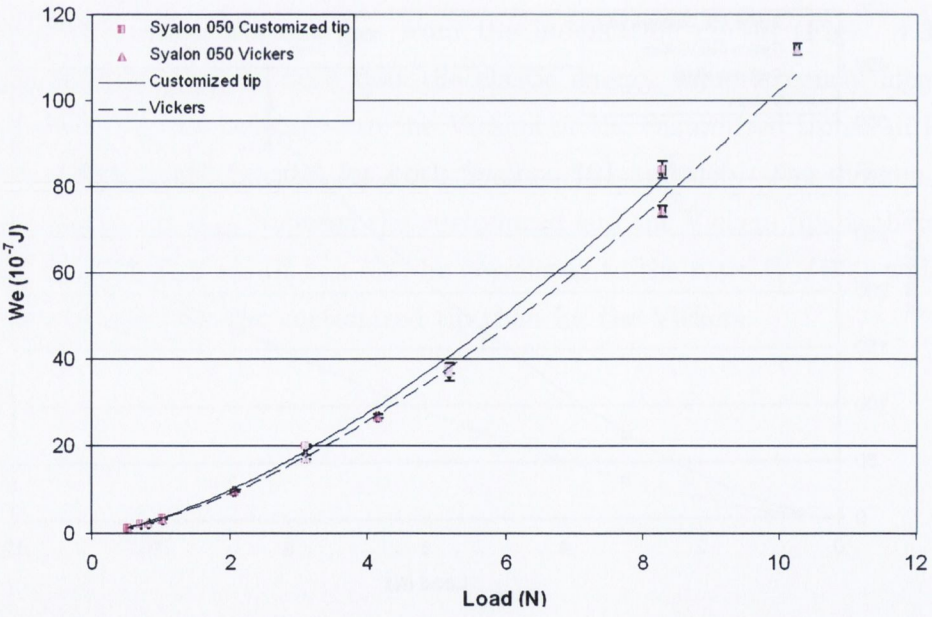

Figure 4.39: Variation of W_e with the maximum load applied for Syalon 050 indented with Vickers and customized tips.

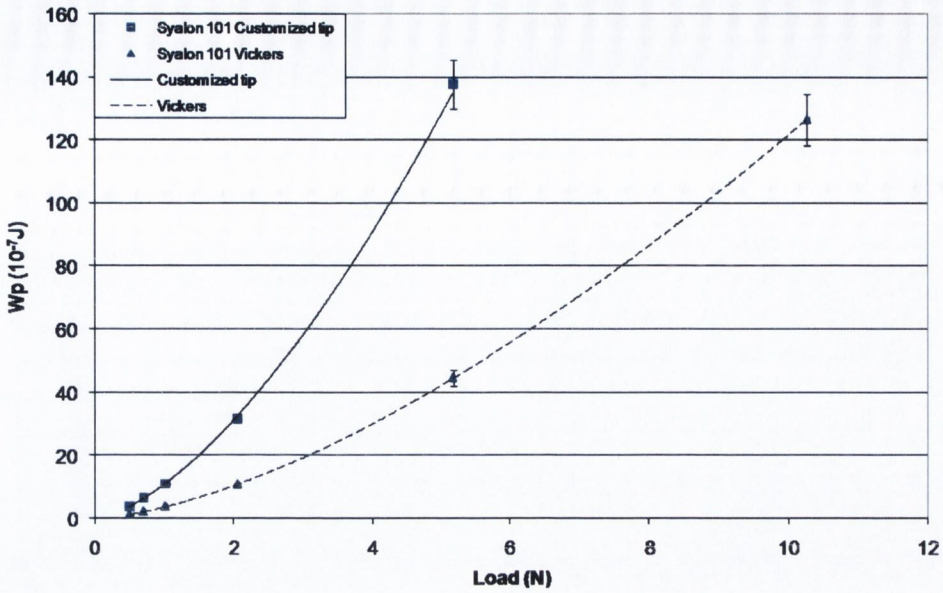

Figure 4.40: Variation of W_p with the maximum load applied for Syalon 101 indented with Vickers and customized tips.

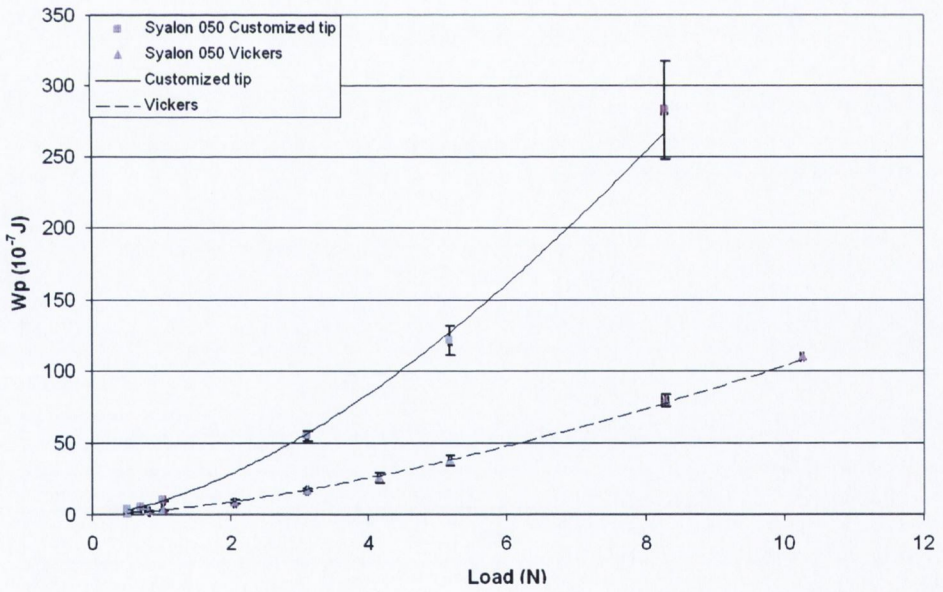

Figure 4.41: Variation of W_p with the maximum load applied for Syalon 050 indented with Vickers and customized tips.

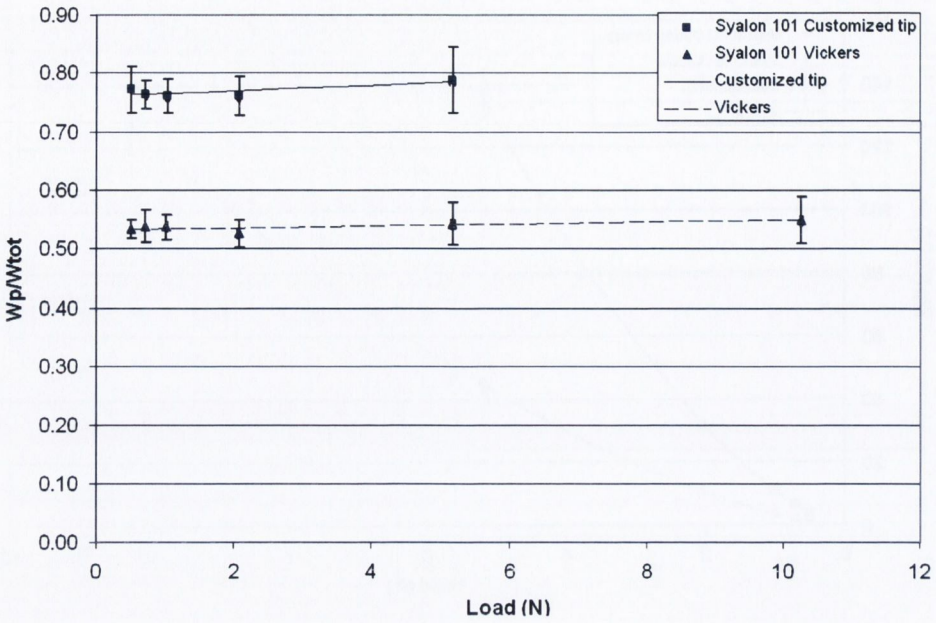

Figure 4.42: Variation of W_p/W_{tot} with the maximum load applied for Syalon 101 indented with Vickers and customized tips.

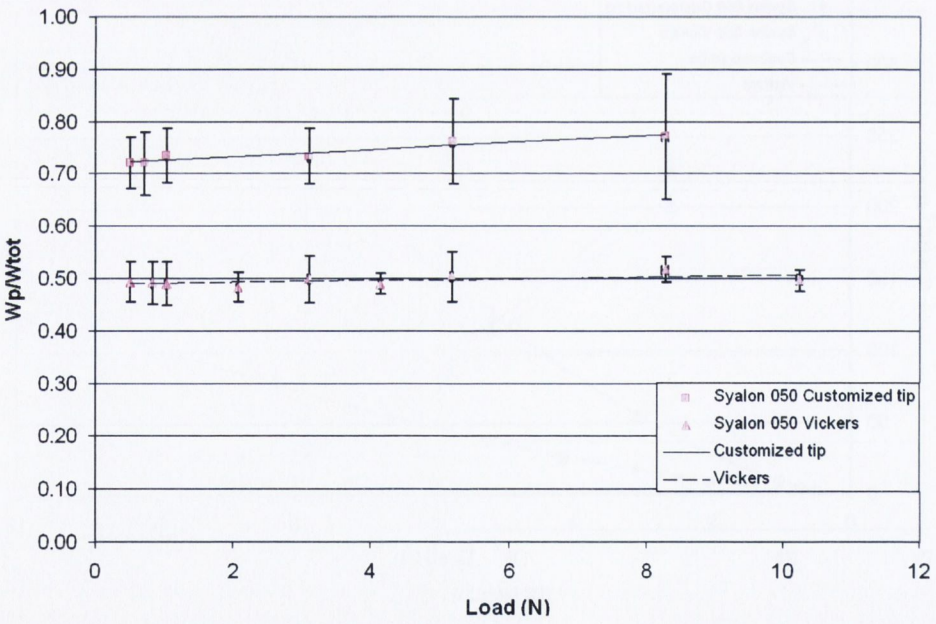

Figure 4.43: Variation of W_p/W_{tot} with the maximum load applied for Syalon 050 indented with Vickers and customized tips.

4.2.2 Surface crack analysis

For each load studied, an average of 25 indents were imaged with the SEM when cracks were visible on the surface. The diagonal length $2a$ of the indent and the length c of corner cracks were measured. For the same load applied, surface indentation crack shape or length were varying considerably from one indent to another. Indentations performed with the customized indenter showed extensive spalling of material from around the indentation. Some SiAlON grains were clearly pulled out on the edges of the indents as can be observed in Fig 4.44. The observed surface cracks are often emanating from the side of the residual indent impression and have very tortuous paths.

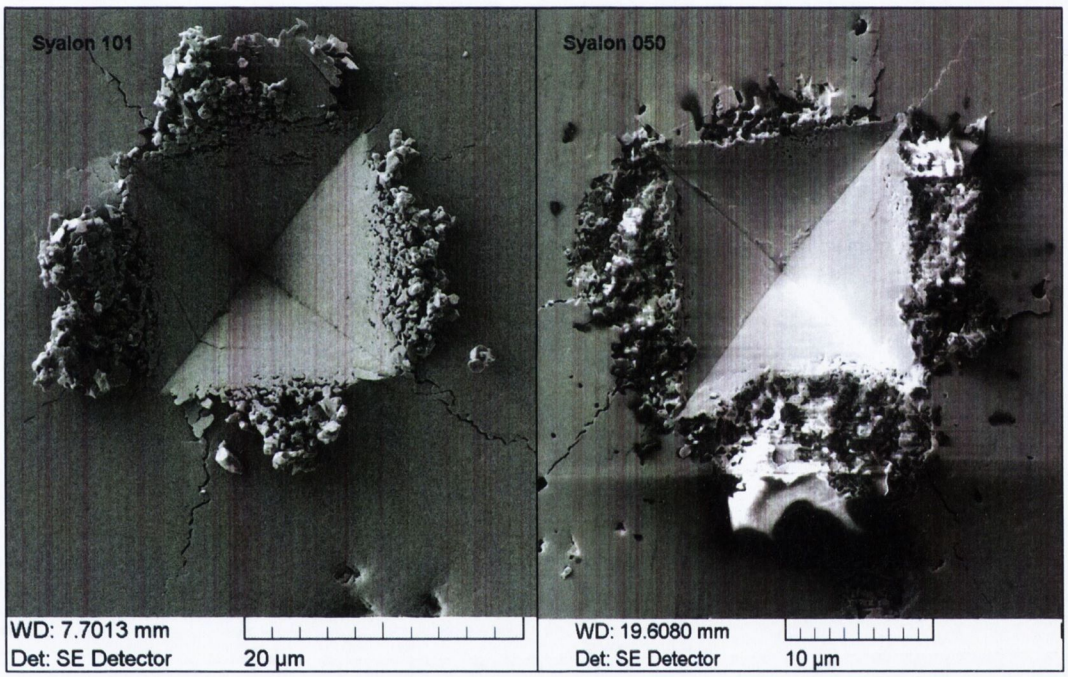

Figure 4.44: Pile-up phenomenon on two indents performed at 5 N with the customized tip in Syalon 101 and Syalon 050.

No pile-up phenomenon has been noticed on indentations performed with a Vickers tip and the cracks observed often start from the corner of the indent impression. A summary of the recorded lengths is presented in Table 4.9 for Syalons 101 and 050 indented with the Vickers tip.

A first observation is that even at 10 N, the crack length c is inferior to the diagonal length $2a$ for both Syalon 101 and 050. But one of the basic assumptions of using the ICL method is that cracks are well defined and of length $c \geq 2a$. Other observations include a wide range of crack shapes that impede the application of the ICL method. The observed crack shapes include side cracks, the presence

Table 4.9: Summary of diagonal length $2a$ and length c of corner cracks measured on Syalons 101 and 050 indented with the Vickers tip.

Load	**Syalon 101**		**Syalon 050**	
(N)	**$2a$ (μm)**	**c (μm)**	**$2a$ (μm)**	**c (μm)**
0.5	-	0	6.6±0.3	0
0.8	-	0	8.4±0.1	0
1	-	0	9.8±0.3	0
2	15.6±0.9	0	13.6±0.2	0
3	20±2	0	17.8±0.8	10.3±0.8
4	22±1	13±1	20.2±0.6	11.6±0.9
5	26±1	16±2	22.6±0.9	14±1
10	37±1	23±2	33.5±0.9	26±2

of cracks of non-equal lengths, angle cracking and crack deflection, discontinuous cracks and non-symmetric cracks (i.e only one, two or three corner cracks observed instead of four). Some illustrations of these crack shapes are presented in Figs. 4.45 and 4.46.

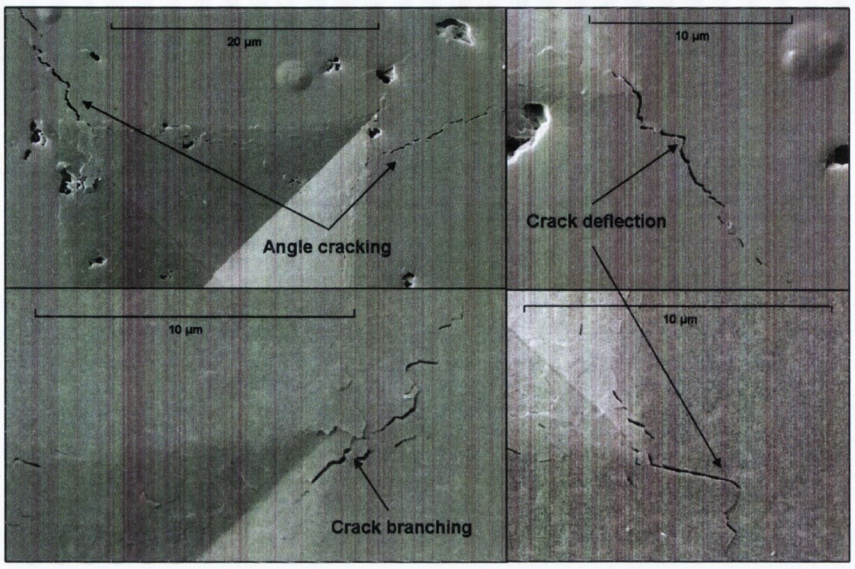

Figure 4.45: Particular crack shapes observed in Syalon 101 and 050 indented with the Vickers tip at loads ranging from 3 to 10 N: angle cracking, crack branching and crack deflection.

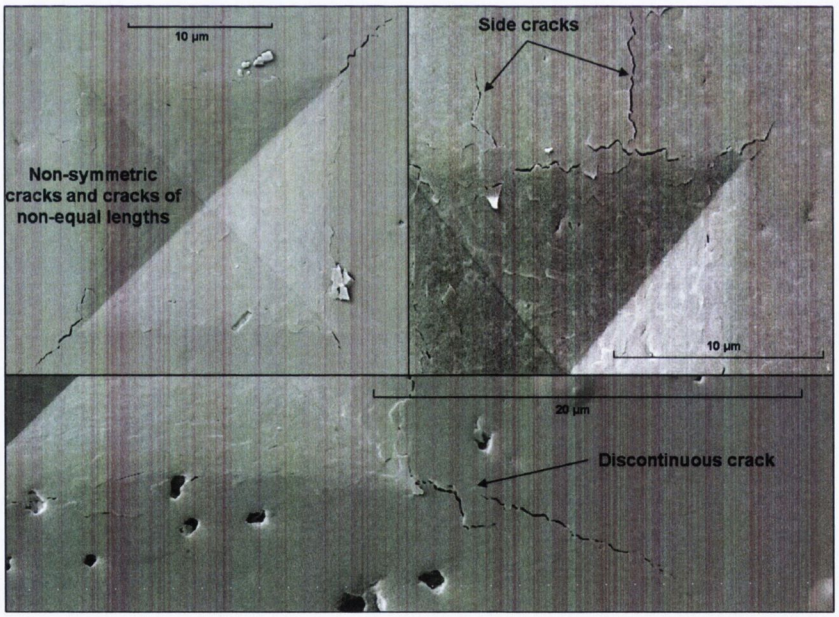

Figure 4.46: Particular crack shapes observed in Syalon 101 and 050 indented with the Vickers tip at loads ranging from 3 to 10 N: non-symmetric cracks, cracks of non-equal lengths, side cracks and discontinuous crack.

The observations made above (tortuous crack shapes, short crack lengths, pile-up) clearly impede the use of the classical ICL method in order to determine

fracture toughness as the results obtained would be meaningless. In fact, trying to apply this method would lead to a large underestimation of the surface area of cracks opened during fracture which is directly linked to the material resistance to fracture. On the range of loads investigated, it is now clear that the ICL method is not applicable and that a method is missing to estimate fracture toughness in Syalons 101 and 050 at this scale as the indentations performed with the Vickers or customized tip can represent real contact events.

It can be noticed from Table 4.9 that the residual indent impression in Syalon 101 is always bigger than the residual indent impression in Syalon 050 for the same load applied. This means that H_{050} is superior to H_{101} which is in accordance with International Syalons specifications. Surprisingly, except for 10 N, crack length is bigger for Syalon 101 than for Syalon 050. This means that K_{c101} is inferior to K_{c050}, which is in contradiction with the manufacturer specifications. At 10 N however, $c_{101} < c_{050}$ so $K_{c101} > K_{c050}$. It should also be noticed that surface crack threshold is slightly lower for 050 (between 2 and 3 N) than for 101 (between 3 and 4 N).

4.2.3 FIB and image analysis results

4.2.3.1 Reconstruction of 3D crack patterns

There were only a few subsurface cracks found during FIB tomography of Syalon 101 indented at 500 mN with the Vickers tip. The cracks found were partial cracks and had very tortuous patterns. Crack bridging and crack deflections were often observed. Fig. 4.47 shows the 3D reconstruction of cracks under this indent. The surface is drawn in green and each different crack is represented with a different color. Under this indent, a partial half-penny crack is visible (noted as PHP-1). It emanates from the corner of the indent impression where FIB tomography has started and propagates downward until around 5.5 μm below the surface. Two partial deep lateral cracks (DL-1 and DL-2) are also noticed as well as one shallow lateral crack (SL-1) and a shallow radial crack (noted SR-1). A few microcracks are also visible. Interestingly, there is a crack-free zone underneath the indent and most of the cracks start at a depth greater than twice the maximum depth of the indent residual impression. Other views of this indent are presented in Appendix B.

Fig. 4.48 presents the crack pattern found below a Vickers indentation at 1 N. This crack pattern is very similar to the one done at 500 mN, except that the observed cracks are longer. There is a high number of crack bridging and

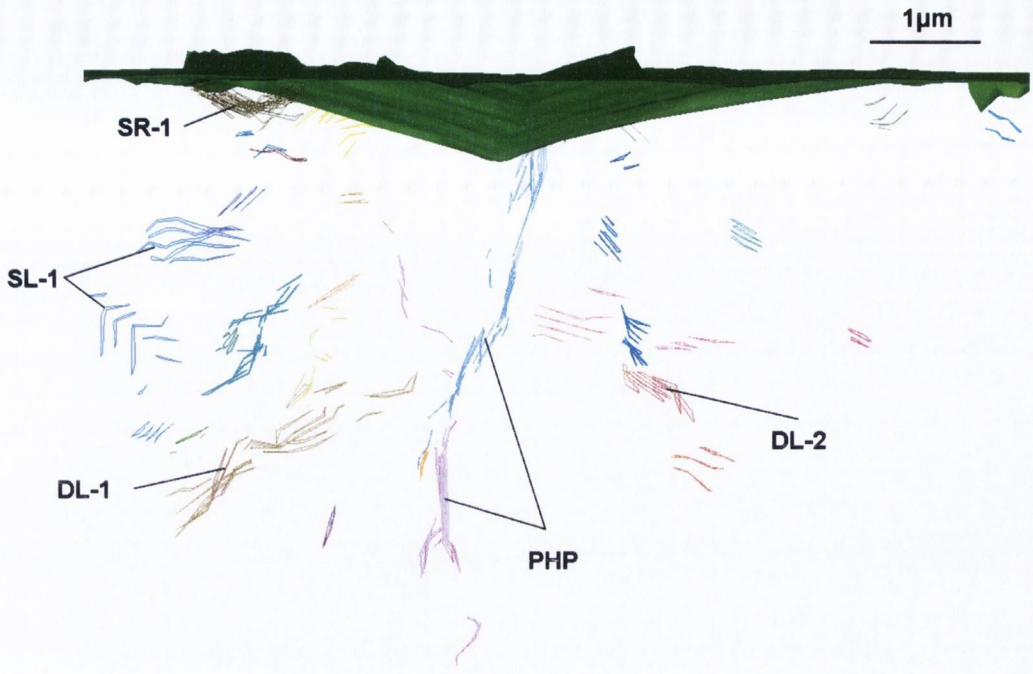

Figure 4.47: Front view of a 3D reconstruction of a Vickers indentation at 500 mN in Syalon 101. Each line represents a contour drawn on a different slice. Contours of the same color belong to the same crack.

deflection phenomena. The largest crack observed is a partial half-penny crack (PHP-1) starting from the indent corner and propagating downward until 9 μm below the surface. Two deep lateral cracks have also formed (DL-1 and DL-2) as well as one shallow lateral (named SL-1) and one shallow radial crack (noted SR-1). A number of microcracks are also observed underneath the indent. Again, the area immediately below the residual indent impression is free of crack.

The 3D reconstruction of cracks underneath a 2 N Vickers indent in Syalon 101 is shown in Fig. 4.49. Under the 2 N indent, a very high number of cracks has been generated. The biggest crack observed is a partial half-penny crack (marked PHP-1) starting from the indent corner and propagating downward until 13 μm below the surface but two very big deep lateral cracks (named DL-1 and DL-2) are also present. A high number of microcracks is also observed in the two halves of the indent studied.

There are few cracks underneath the 500 mN Vickers indent in Syalon 050, as shown in Fig. 4.50. A partial half-penny crack (PHP-1) starts from the corner of the indent impression and propagates downwards until 5 μm below the surface but shows a tendency to turn sideways and extend as a lateral crack. Two additional

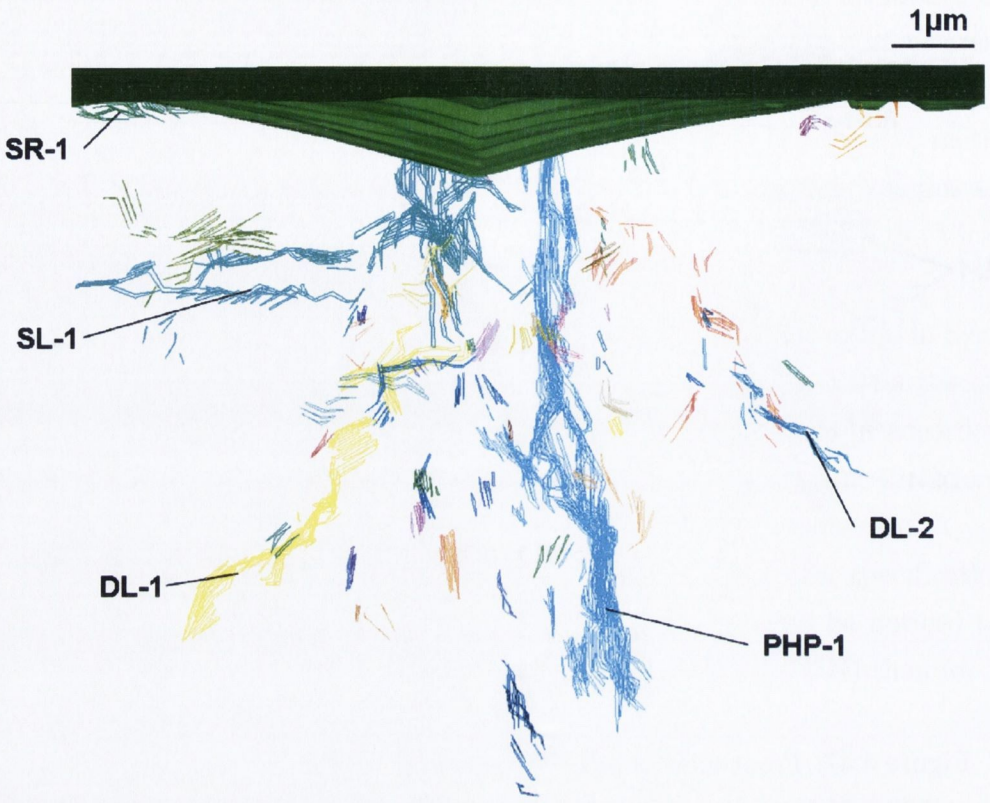

Figure 4.48: Front view of a 3D reconstruction of a Vickers indentation at 1 N in Syalon 101.

deep lateral cracks (noted as DL-1 and DL-2) were also observed.

The 3D reconstruction of cracks underneath a 1 N Vickers indent in Syalon 050 is shown in Fig. 4.51. Again, a big partial half-penny crack (PHP-1) starts from the corner of the indent impression and propagates downwards until 10 μm below the surface. The presence of two shallow lateral cracks (noted as SL-1 and SL-2) and of a deep lateral crack (DL-1) is also noticed as well as the presence of a shallow radial crack (named SR-1).

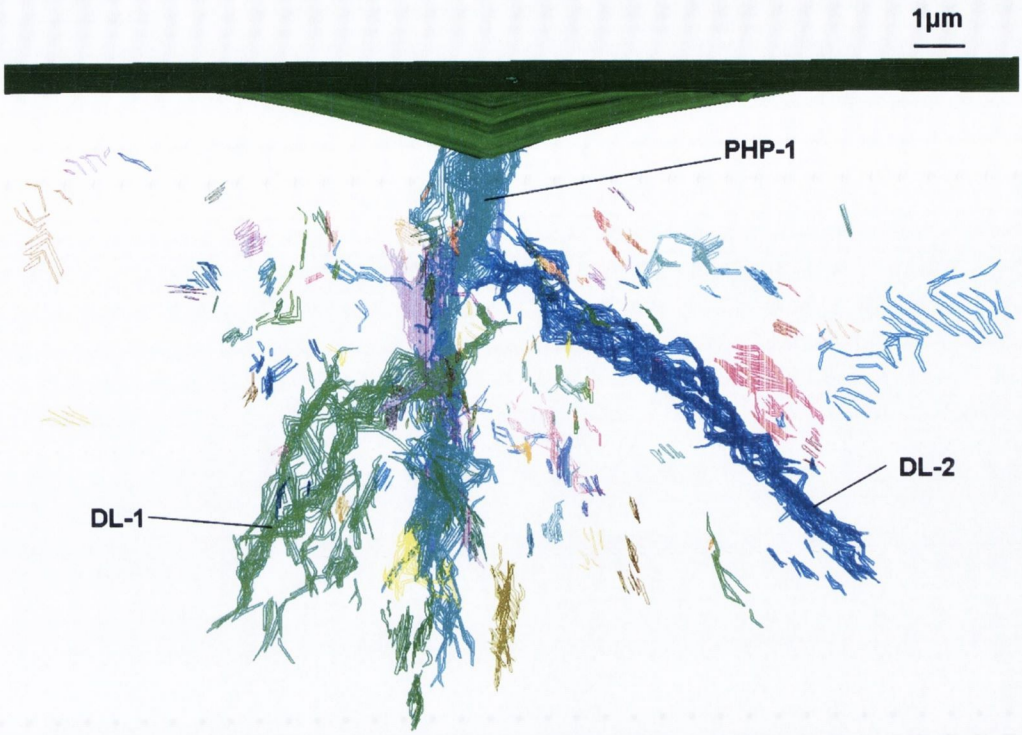

Figure 4.49: Front view of a 3D reconstruction of a Vickers indentation at 2 N in Syalon 101.

Fig. 4.52 presents the crack pattern found below a Vickers indentation at 2 N in Syalon 050. The biggest crack observed is a partial half-penny crack (marked PHP-1) starting from the indent corner and propagating downward until 15 μm below the surface but two other partial half-penny cracks (named PHP-2 and PHP-3) are also observed. The presence of two shallow lateral cracks (SL-1 and SL-2) and of a deep lateral crack (DL-1) is also noticed.

FIB tomography of indents performed in Syalon 101 with the customized tip reveals the presence of a high number of cracks close to the surface and to the residual indent impression. For the three indents studied (500 mN, 1 N and 2N), the majority of the cracks are close to the surface, contrary to what was observed underneath Vickers indents.

The 3D reconstruction of cracks underneath a 500 mN indent made with the customized tip in Syalon 101 is shown in Fig. 4.53. It is quite difficult to relate the crack pattern obtained to well-known crack types. Nevertheless, a partial half-penny crack (named PHP-1) can be identified. It starts from the corner of the indent impression and propagates downwards until 7 μm below the surface. A shallow radial crack (SR-1) and a shallow lateral crack (SL-1) are also observed.

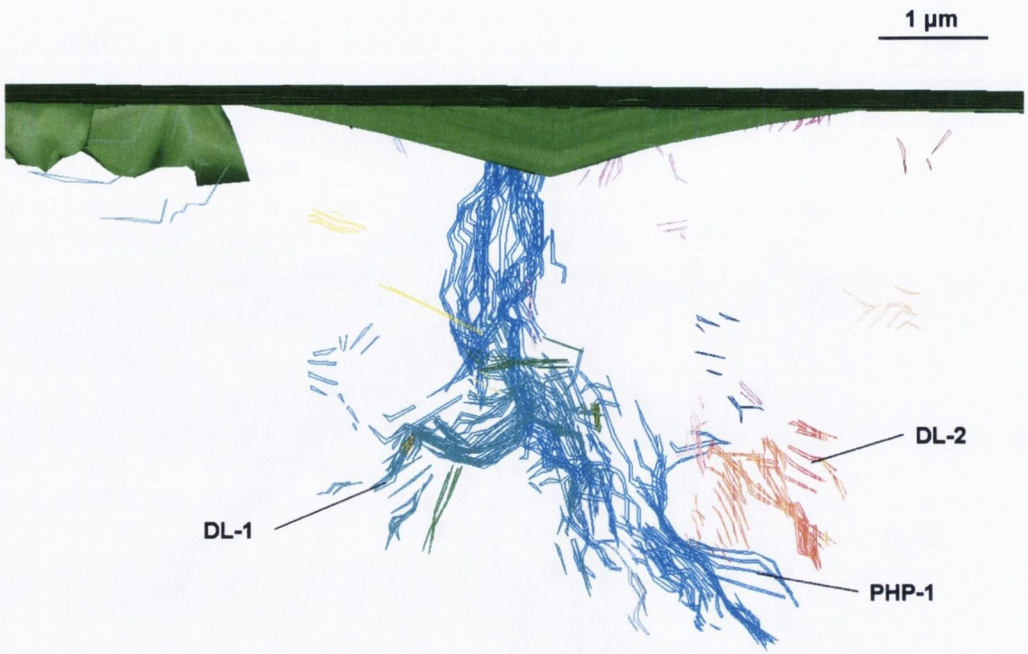

Figure 4.50: Front view of a 3D reconstruction of a Vickers indentation at 500 mN in Syalon 050.

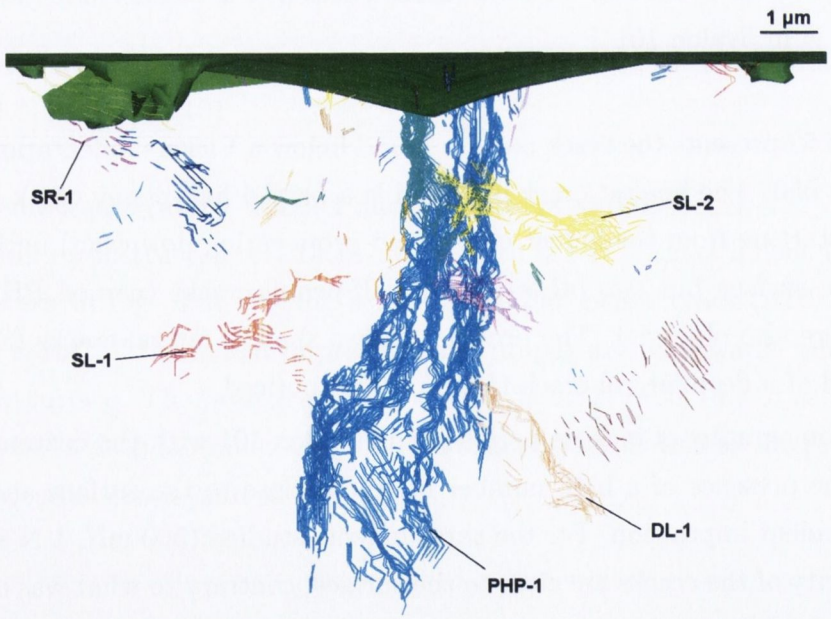

Figure 4.51: Front view of a 3D reconstruction of a Vickers indentation at 1 N in Syalon 050.

Fig. 4.54 presents the crack pattern found below a 1 N indent made with the customized tip in Syalon 101. A partial half-penny crack (noted as PHP-1)

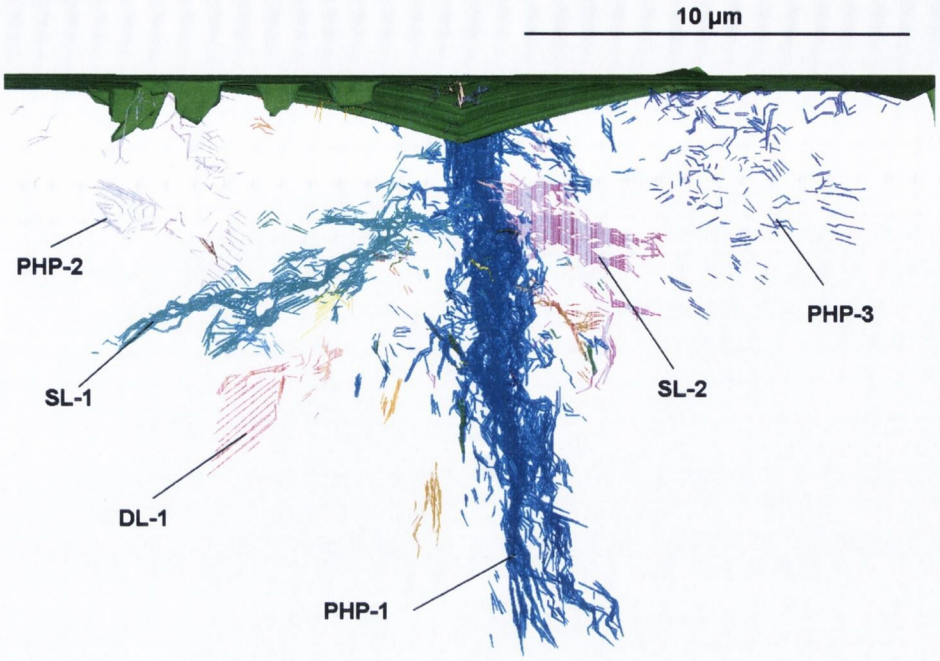

Figure 4.52: Front view of a 3D reconstruction of a Vickers indentation at 2 N in Syalon 050.

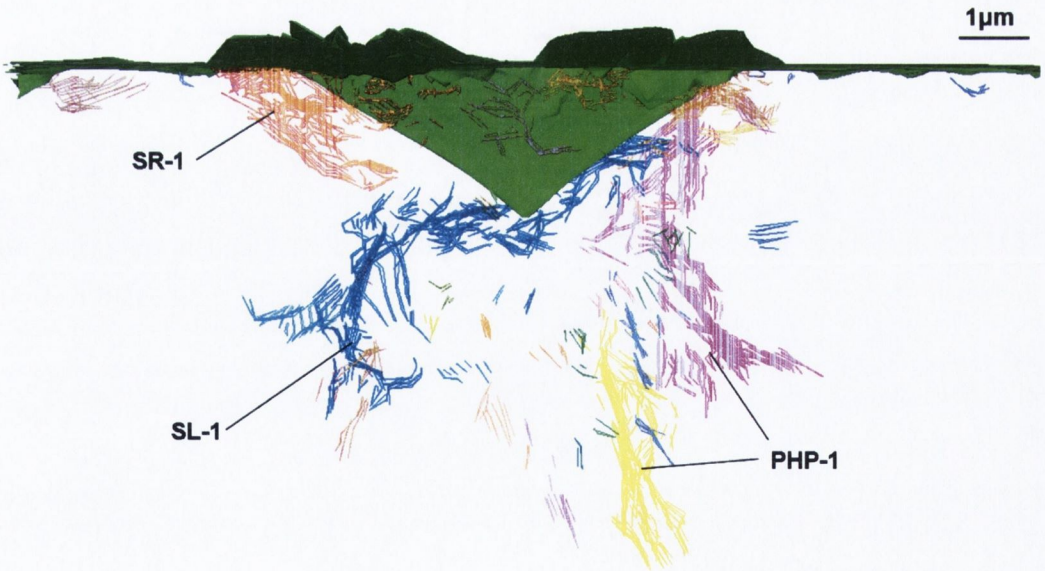

Figure 4.53: Front view of a 3D reconstruction of an indentation at 500 mN in Syalon 101 with the customized tip.

starts from the indent corner and propagates downward until 11 μm below the surface. Two shallow radial cracks (SR-1 and SR-2) are also observed at two

different indent corners. Finally, a shallow lateral (SL-1) and a deep lateral crack (DL-1) are observed underneath this indent. There are also lots of other cracks that can't be easily related to a defined crack type.

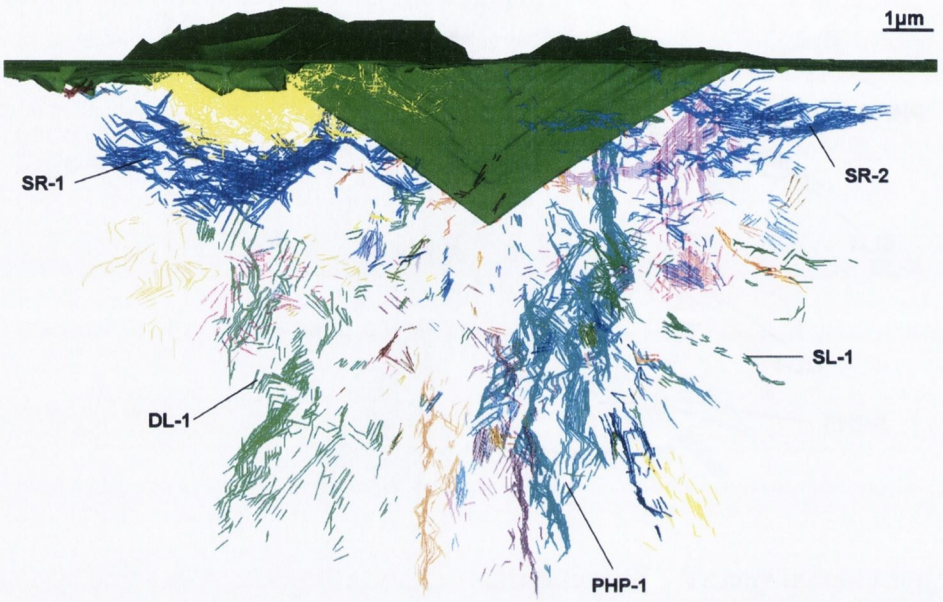

Figure 4.54: Front view of a 3D reconstruction of an indentation at 1 N in Syalon 101 with the customized tip.

A 2 N indent made with the customized tip in Syalon 101 is shown in Fig. 4.55. A very high number of cracks are observed underneath this indent, creating a complicated crack pattern. However, some cracks can be identified, like a partial half-penny (PHP-1) starting from the indent corner and propagating 16 μm downward. Four shallow lateral cracks (noted as SL-1, SL-2, SL-3 and SL-4) are also identified under the indent.

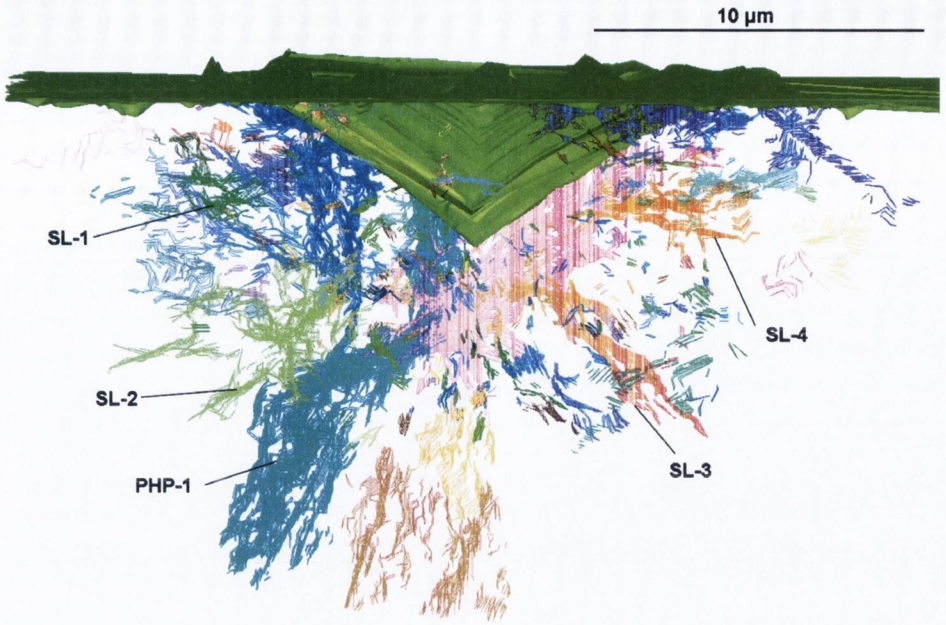

Figure 4.55: Front view of a 3D reconstruction of an indentation at 2 N in Syalon 101 with the customized tip.

Finally, FIB tomography has been performed on three different 5 N indents in Syalon 101 (indents num7, 18 and 20) in order to test the reproducibility of the results. 3D reconstruction of the subsurface crack pattern of indent num7 is presented in Fig. 4.56. As observed with the previous indents studied, a partial half-penny crack (PHP-1) emanates from the indent corner and propagates downward until 24 μm below the surface. There are also two deep lateral cracks (DL-1 and DL-2) and one shallow lateral crack (SL-1). Furthermore, two partial shallow radial cracks (SR-1 and SR-2) are also visible at two indent corners.

Fig. 4.57 presents the 3D reconstruction of the 5 N indent num18. Under this indent, a partial half-penny crack is visible (noted as PHP-1). It emanates from the corner of the indent impression where FIB tomography has started and propagates downward until around 22 μm below the surface. The presence of two other partial half-penny cracks (PHP-2 and PHP-3) at two other corners of the indent is also noticed. Finally, two shallow lateral cracks (named SL-1 and SL-2) are also visible and join PHP-1.

FIB tomography of 5 N indentation num20 (Fig. 4.58) reveals the presence of a very high number of micro-cracks underneath the indent. Again, the biggest crack is a partial half-penny crack (PHP-1) starting from the corner of the indent and propagating 21 μm downward. It is joined by two deep lateral cracks (noted

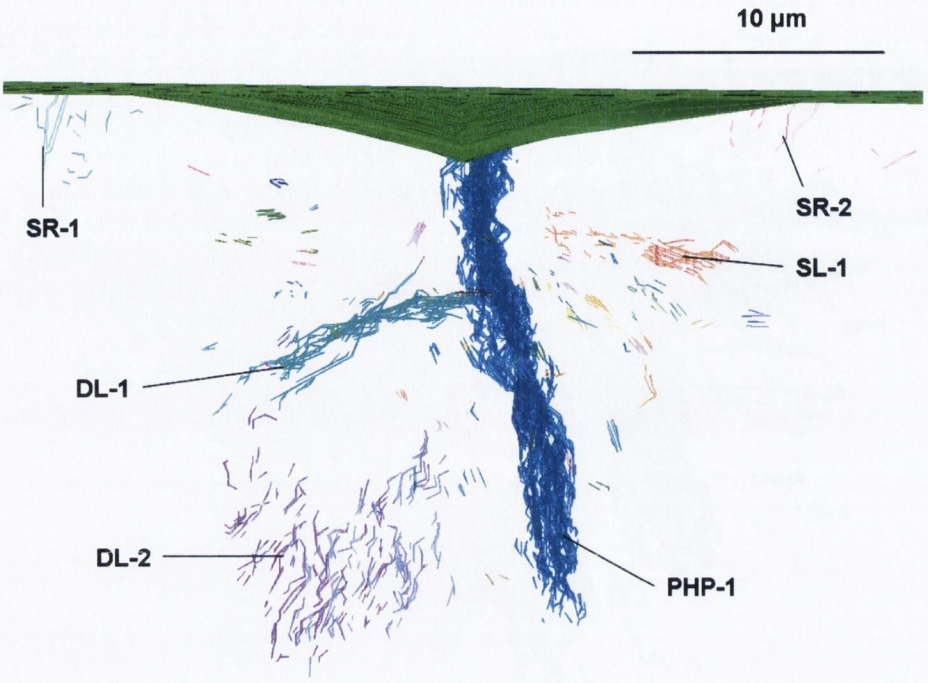

Figure 4.56: Front view of a 3D reconstruction of a Vickers indentation at 5 N (indent num7) in Syalon 101.

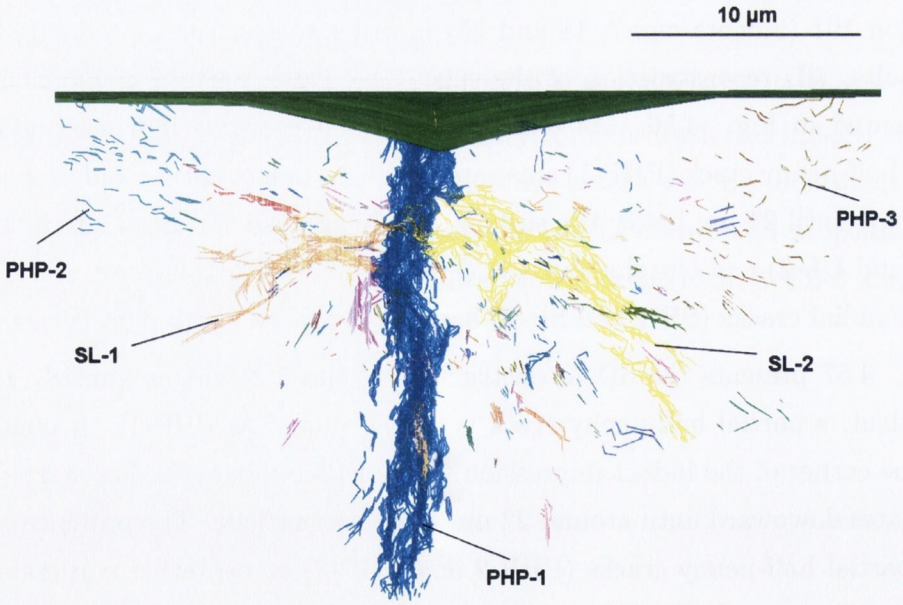

Figure 4.57: Front view of a 3D reconstruction of a Vickers indentation at 5 N (indent num18) in Syalon 101.

as DL-1 and DL-2). Two other partial half-penny cracks (PHP-2 and PHP-3) are also observed at two other corners of the indent.

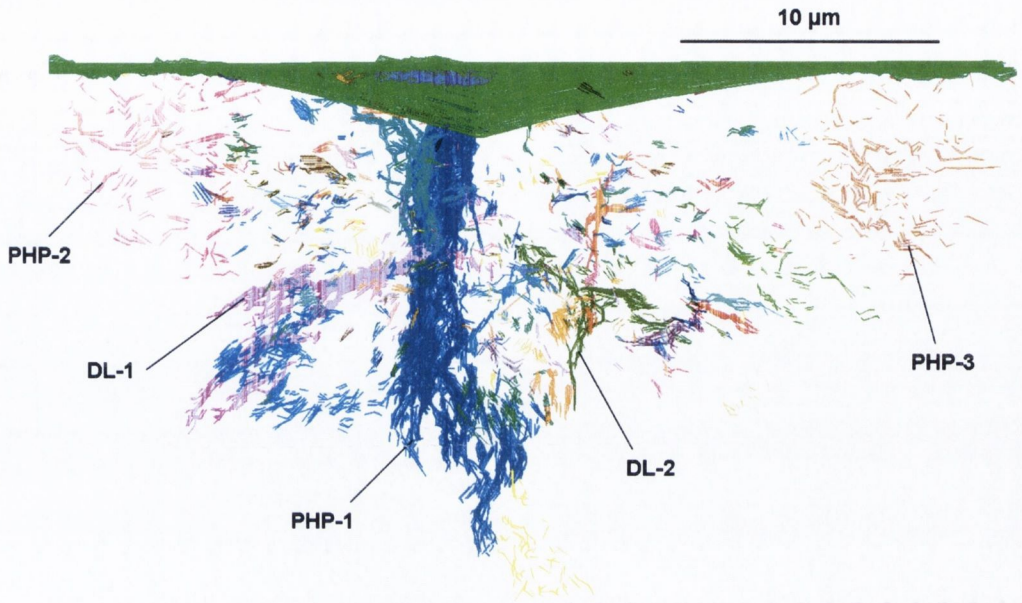

Figure 4.58: Front view of a 3D reconstruction of a Vickers indentation at 5 N (indent num20) in Syalon 101.

A summary of some characteristics of the three 5 N Vickers indents studied is presented in Table 4.10.

Table 4.10: Some characteristics of the three different 5 N Vickers indents reconstructed.

Indent	**E** (GPa)	**H** (GPa)	$\mathbf{W}_p$ (10^{-7}J)	**Total number of cracks**	**Total crack surface area** (μm^2)	**Predicted crack surface area** (μm^2)
101V 5 N num7	251	18.8	42.7	66	934	2166
101V 5 N num18	223	17.4	43.6	122	1177	1466
101V 5 N num20	203	16.5	46.7	265	903	623

Figs. 4.59 to 4.64 show the histograms of crack surface area of the twelve indents studied.

Bin	Frequency	Cumulative %
0	0	0.00%
1	23	82.14%
2	2	89.29%
3	3	100.00%
4	0	100.00%
5	0	100.00%
6	0	100.00%
7	0	100.00%
8	0	100.00%
9	0	100.00%
10	0	100.00%
11	0	100.00%
12	0	100.00%
13	0	100.00%
14	0	100.00%
15	0	100.00%
16	0	100.00%
17	0	100.00%
18	0	100.00%
19	0	100.00%
20	0	100.00%
More	0	100.00%

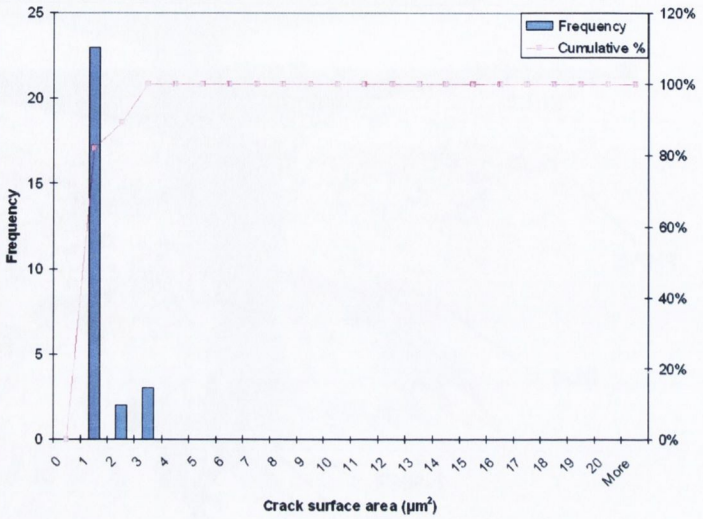

Figure 4.59: Histogram of crack surface areas of Syalon 101 indented at 500 mN with the Vickers tip.

Bin	Frequency	Cumulative %
0	0	0.00%
1	40	81.63%
2	4	89.80%
3	2	93.88%
4	0	93.88%
5	0	93.88%
6	0	93.88%
7	0	93.88%
8	0	93.88%
9	1	95.92%
10	0	95.92%
11	0	95.92%
12	0	95.92%
13	0	95.92%
14	0	95.92%
15	0	95.92%
16	1	97.96%
17	0	97.96%
18	0	97.96%
19	0	97.96%
20	0	97.96%
More	1	100.00%

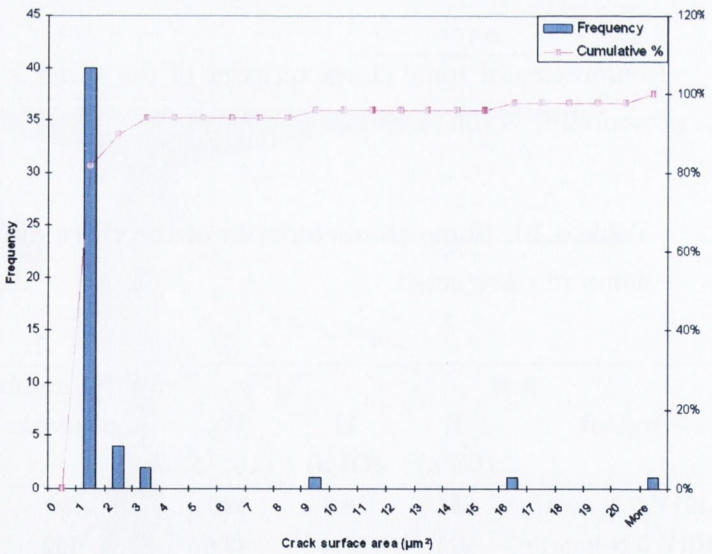

Figure 4.60: Histogram of crack surface areas of Syalon 101 indented at 1 N with the Vickers tip.

Bin	Frequency	Cumulative %
0	0	0.00%
1	70	72.92%
2	13	86.46%
3	1	87.50%
4	3	90.63%
5	3	93.75%
6	1	94.79%
7	1	95.83%
8	0	95.83%
9	0	95.83%
10	0	95.83%
11	0	95.83%
12	0	95.83%
13	0	95.83%
14	0	95.83%
15	0	95.83%
16	0	95.83%
17	0	95.83%
18	0	95.83%
19	0	95.83%
20	0	95.83%
More	4	100.00%

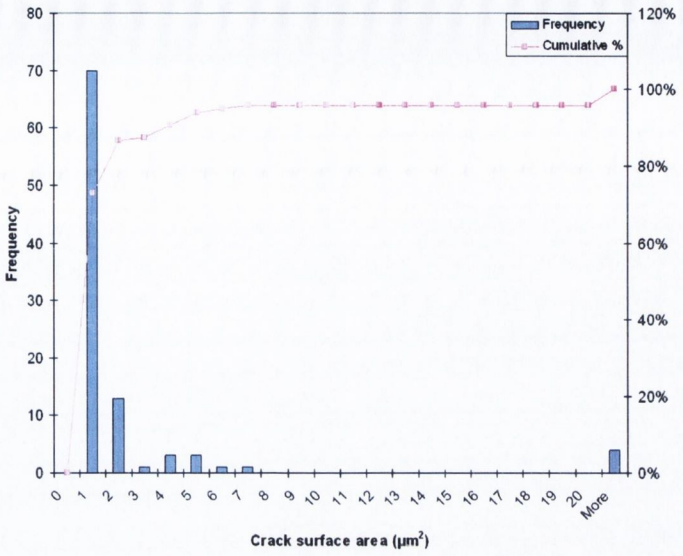

Figure 4.61: Histogram of crack surface areas of Syalon 101 indented at 2 N with the Vickers tip.

Bin	Frequency	Cumulative %
0	0	0.00%
1	16	80.00%
2	0	80.00%
3	1	85.00%
4	0	85.00%
5	1	90.00%
6	0	90.00%
7	0	90.00%
8	0	90.00%
9	0	90.00%
10	0	90.00%
11	0	90.00%
12	0	90.00%
13	1	95.00%
14	0	95.00%
15	0	95.00%
16	0	95.00%
17	0	95.00%
18	0	95.00%
19	0	95.00%
20	0	95.00%
More	1	100.00%

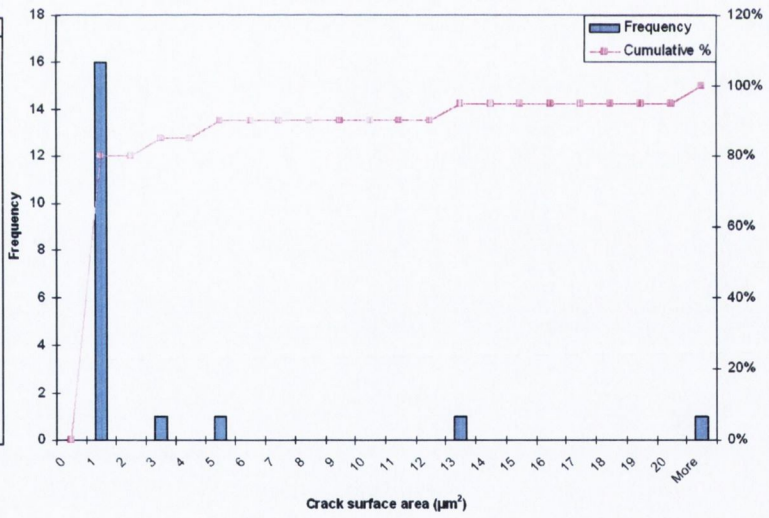

Figure 4.62: Histogram of crack surface areas of Syalon 050 indented at 500 mN with the Vickers tip.

Bin	Frequency	Cumulative %
0	0	0.00%
1	31	75.61%
2	1	78.05%
3	2	82.93%
4	2	87.80%
5	1	90.24%
6	1	92.68%
7	0	92.68%
8	0	92.68%
9	0	92.68%
10	0	92.68%
11	0	92.68%
12	1	95.12%
13	0	95.12%
14	0	95.12%
15	0	95.12%
16	0	95.12%
17	0	95.12%
18	0	95.12%
19	0	95.12%
20	0	95.12%
More	2	100.00%

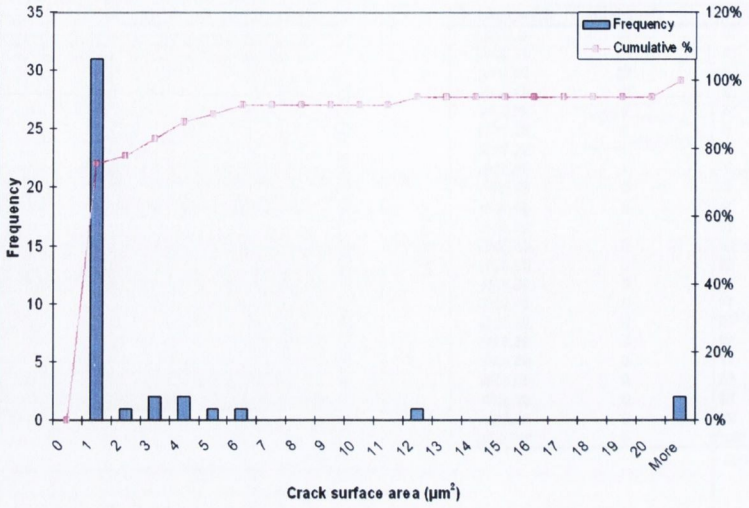

Figure 4.63: Histogram of crack surface areas of Syalon 050 indented at 1 N with the Vickers tip.

Bin	Frequency	Cumulative %
0	0	0.00%
1	33	66.00%
2	7	80.00%
3	2	84.00%
4	1	86.00%
5	1	88.00%
6	0	88.00%
7	1	90.00%
8	0	90.00%
9	0	90.00%
10	0	90.00%
11	1	92.00%
12	0	92.00%
13	0	92.00%
14	1	94.00%
15	0	94.00%
16	0	94.00%
17	0	94.00%
18	0	94.00%
19	0	94.00%
20	0	94.00%
More	3	100.00%

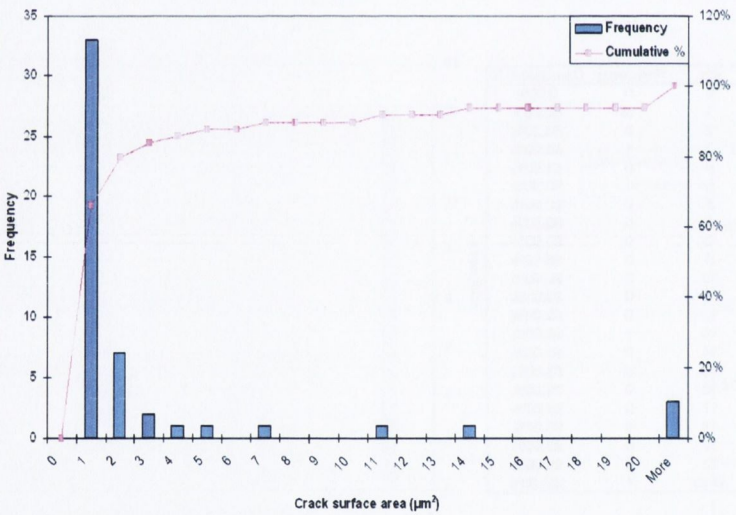

Figure 4.64: Histogram of crack surface areas of Syalon 050 indented at 2 N with the Vickers tip.

Bin	Frequency	Cumulative %
0	0	0.00%
1	27	65.85%
2	4	75.61%
3	3	82.93%
4	1	85.37%
5	0	85.37%
6	0	85.37%
7	0	85.37%
8	0	85.37%
9	0	85.37%
10	1	87.80%
11	1	90.24%
12	0	90.24%
13	0	90.24%
14	0	90.24%
15	1	92.68%
16	0	92.68%
17	0	92.68%
18	0	92.68%
19	1	95.12%
20	1	97.56%
More	1	100.00%

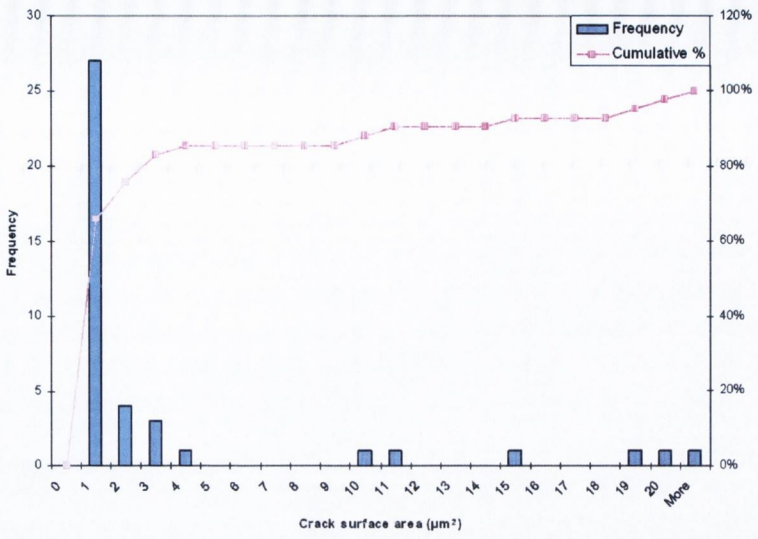

Figure 4.65: Histogram of crack surface areas of Syalon 101 indented at 500 mN with the customized tip.

Bin	Frequency	Cumulative %
0	0	0.00%
1	74	75.51%
2	7	82.65%
3	3	85.71%
4	1	86.73%
5	1	87.76%
6	1	88.78%
7	0	88.78%
8	0	88.78%
9	0	88.78%
10	2	90.82%
11	2	92.86%
12	0	92.86%
13	0	92.86%
14	0	92.86%
15	0	92.86%
16	0	92.86%
17	0	92.86%
18	0	92.86%
19	1	93.88%
20	0	93.88%
More	6	100.00%

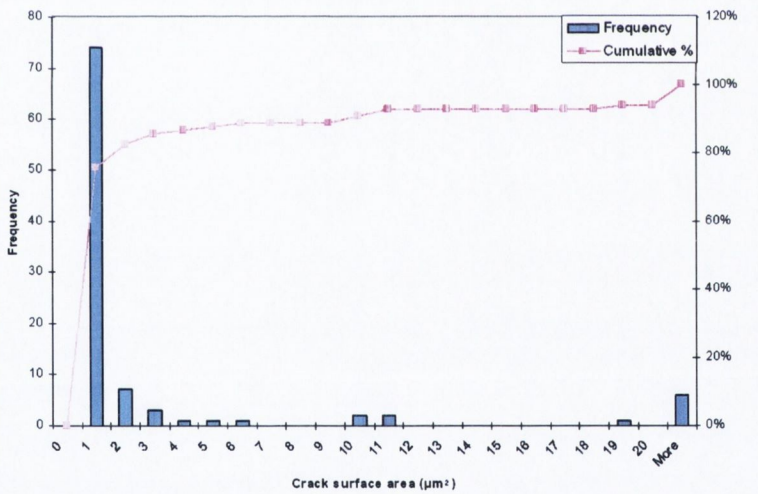

Figure 4.66: Histogram of crack surface areas of Syalon 101 indented at 1 N with the customized tip.

Bin	Frequency	Cumulative %
0	0	0.00%
1	166	74.44%
2	17	82.06%
3	9	86.10%
4	6	88.79%
5	2	89.69%
6	5	91.93%
7	2	92.83%
8	1	93.27%
9	0	93.27%
10	1	93.72%
11	0	93.72%
12	2	94.62%
13	1	95.07%
14	1	95.52%
15	1	95.96%
16	0	95.96%
17	0	95.96%
18	0	95.96%
19	0	95.96%
20	0	95.96%
More	9	100.00%

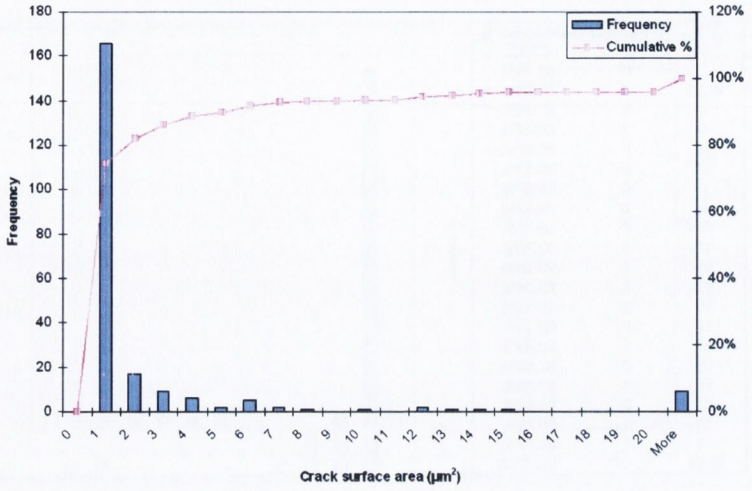

Figure 4.67: Histogram of crack surface areas of Syalon 101 indented at 2 N with the customized tip.

Bin	Frequency	Cumulative %
0	0	0.00%
1	40	60.61%
2	12	78.79%
3	7	89.39%
4	1	90.91%
5	1	92.42%
6	0	92.42%
7	0	92.42%
8	1	93.94%
9	0	93.94%
10	0	93.94%
11	0	93.94%
12	0	93.94%
13	0	93.94%
14	0	93.94%
15	0	93.94%
16	0	93.94%
17	0	93.94%
18	0	93.94%
19	0	93.94%
20	0	93.94%
More	4	100.00%

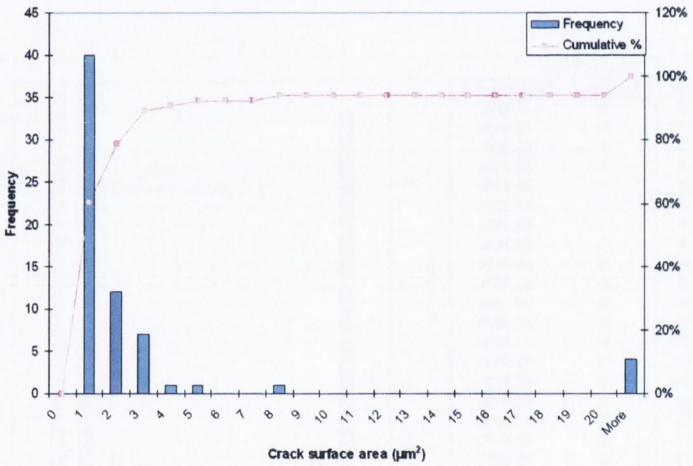

Figure 4.68: Histogram of crack surface areas of Syalon 101 indented at 5 N (indent num7) with the Vickers tip.

Bin	Frequency	Cumulative %
0	0	0.00%
1	79	84.75%
2	19	80.33%
3	9	87.70%
4	4	90.98%
5	2	92.62%
6	0	92.62%
7	1	93.44%
8	0	93.44%
9	0	93.44%
10	0	93.44%
11	2	95.08%
12	0	95.08%
13	0	95.08%
14	0	95.08%
15	0	95.08%
16	0	95.08%
17	0	95.08%
18	0	95.08%
19	0	95.08%
20	1	95.90%
More	5	100.00%

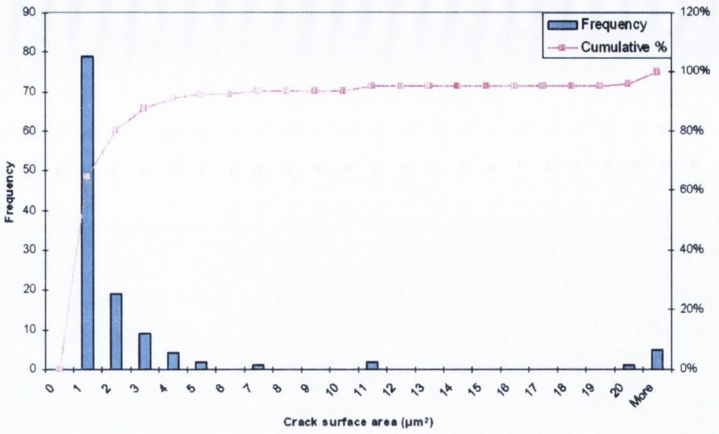

Figure 4.69: Histogram of crack surface areas of Syalon 101 indented at 5 N (indent num18) with the Vickers tip.

Bin	Frequency	Cumulative %
0	0	0.00%
1	198	74.72%
2	37	88.68%
3	5	90.57%
4	6	92.83%
5	1	93.21%
6	3	94.34%
7	4	95.85%
8	0	95.85%
9	1	96.23%
10	0	96.23%
11	0	96.23%
12	2	96.98%
13	0	96.98%
14	0	96.98%
15	0	96.98%
16	0	96.98%
17	0	96.98%
18	1	97.36%
19	0	97.36%
20	0	97.36%
More	7	100.00%

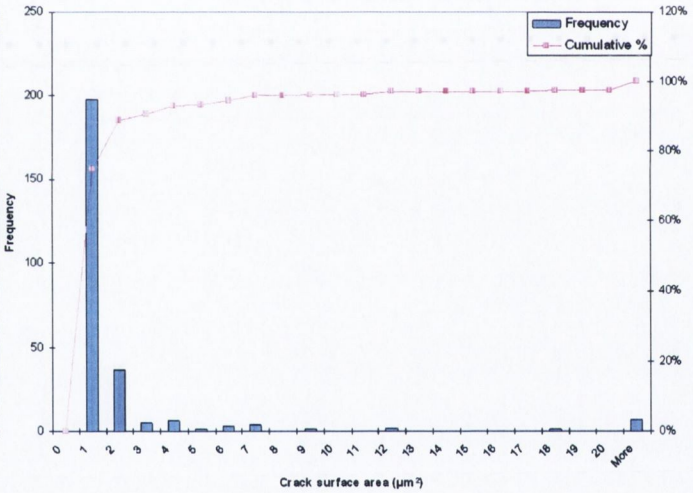

Figure 4.70: Histogram of crack surface areas of Syalon 101 indented at 5 N (indent num20) with the Vickers tip.

Comparison of the different cracks formed under the indents and of the histograms of crack surface areas has lead to interesting observations. No particular change in crack patterns has been observed in Syalons 101 and 050 when increasing the load. The crack types are the same (partial half-penny, shallow and deep lateral cracks) but cracks become longer when the load increases. It can also be noticed that for the same indentation load, Syalon 101 and Syalon 050 present approximately the same number of cracks and more or less the same crack patterns. However, the total crack surface area is higher for 050 than for 101 which implies that cracks are longer on average in Syalon 050. This result is confirmed by the comparison of histograms of crack surface areas of indents performed in Syalons 101 or 050 and may indicate that Syalon 050 resistance to fracture is lower than Syalon 101. This is in agreement with the manufacturer specifications at bulk level. The same kind of observations can be done for Syalon 101 indented with a Vickers or a customized tip. There are more cracks underneath indents performed with a customized tip and these cracks are closer to the surface than when indenting with a Vickers tip. Cracks are also longer with the customized tip, leading to a crack surface area much higher than in indentations performed with the Vickers tip.

The three 5 N Vickers indents performed in Syalon 101 and studied in order to test the reproducibility of the results have shown different subsurface crack patterns. There are more cracks underneath indent num20 (265 cracks) than underneath the two others (122 cracks for indent num18 and 66 for num7). These indents also have different surface behavior: indentations num7 and num18 present four well-defined corner cracks although these cracks are longer for indent num7. Indentation num20 only shows two surface cracks.

FIB tomography of the subsurface of the indents has also revealed that crack bridging and crack deflection were present in all indents studied, for both Syalons 101 and 050.

Finally, from 3D reconstructions of the microstructure, the porosity has been calculated and is equal to 0.05 % for Syalon 101 and to 1.3 % for Syalon 050.

4.2.3.2 Density of cracks influenced by the FIB process

FIB tomography of unindented regions in Syalons 101 and 050 didn't show any influence of the FIB process on the local microstructure. The grains and the intergranular phase present in Syalon 101 and 050 could be clearly identified and their shape didn't seem to be influenced by the highly energetic ion beam used to remove every slice during the slice&view experiment. Therefore, the use of

the FIB is highly interesting in studies of microstructure of these ceramics due to the minimal amount of subsurface damage caused by this instrument during the tomography process.

However, FIB tomography of indented areas has highlighted the influence of the FIB process on existing stress fields. As previously noticed with alumina during slice&view experiments, some cracks have opened on the platinum layer which has been deposited after the indentation test. Fig. 4.71 presents SEM micrographs of two consecutive slices during FIB tomography of a 5 N Vickers indent in Syalon 101. On the second image, a crack has opened on the Pt coating during the material removal phase performed with the ion beam.

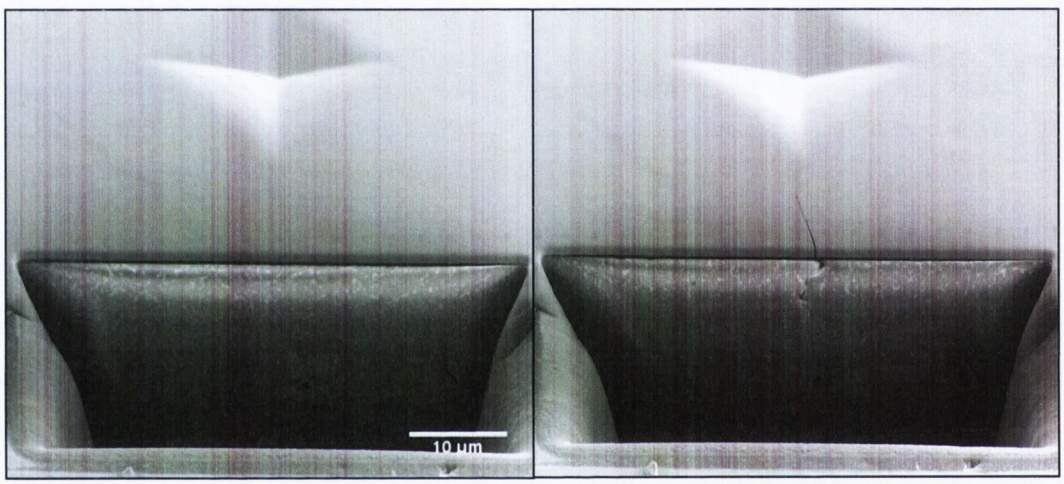

Figure 4.71: SEM micrographs of two consecutive slices during FIB tomography of a 5 N Vickers indent in Syalon 101. The second image shows a crack opened on the Pt layer due to stress relief.

Furthermore, crack distribution is not uniform in the twelve indents studied. There is a huge difference between the density of cracks observed in the first and in the second halves of the indents studied during FIB tomography. Crack density in the second half of each indent is much less compared to crack density in the first half studied. Moreover, the cracks observed in the second half of the indents are only microcracks, which contrasts with the long cracks often observed in the first half of the indent.

In order to quantify the changes in the crack pattern during FIB tomography, simulations of the material removal process using the ion beam were run on a Finite Element model of indentation developed in Trinity College Dublin [151]. The validity of this FE model had previously been checked and a good correlation obtained between modeled and experimental energy results. The purpose of this

was to estimate the changes in stress fields and the effect on crack surface area due to material removal during the FIB process. The model assumed homogeneous structure therefore the results are indicative only. It gave an estimation of 4 % of cracks being opened in a 5 N Vickers indent in Syalon 101 when using the FIB and around 8 % for a 2 N indent performed with the customized tip in Syalon 101 [151]. However, these values seem very low on looking at the big difference experimentally found in the crack density between the first and the second halves of the indents studied during FIB tomography. This is particularly obvious when looking at side views of the indents (cf. Appendix B).

Comparisons of crack patterns of Syalon 101 and Syalon 050 indented with the Vickers tip didn't show big differences although these two materials have different microstructures and therefore are expected to behave differently. For all indents studied, a partial half-penny crack was observed emanating from the indent corner where the FIB tomography begins. Then on the first half of the indent studied, few shallow or deep lateral cracks were observed as well as one or two shallow radial cracks. The second half of the indent only presents microcracks.

4.2.3.3 Comparison of total crack surface area obtained with energy data

The total crack surface area was calculated for each crack pattern reconstructed. Results are presented in Table 4.11 and compared with the predicted crack surface area (calculated from the length of the surface cracks at the indentation corners and assuming that these cracks have a half-penny shape). When the investigated indent only presented one corner crack instead of four (which is the case for the following indents: Syalon 101 Vickers 2 N, Syalon 101 Vickers 1 and 2 N, Syalon 050 Vickers 500 mN), two values were calculated: one assuming there was one entire subsurface half-penny crack and one considering only half of this value (as only one crack was visible on surface).

As presented in Table 4.11 for all indents studied, the predicted crack surface area considerably differs from the actual total crack surface area calculated from the 3D reconstruction. This observation is contradictory with the use of classical models to determine fracture toughness in this ceramics. Interestingly, the difference is lower for the higher load studied (5 N) which may indicate that as the load increases, the difference found between predicted and actual crack surface areas would decrease. These results also highlight the fact that even when there is no surface crack, some subsurface damage is found which is not taken into account in classical model of resistance to fracture.

Table 4.11: Comparison between the predicted crack surface area and the crack surface area measured from 3D reconstruction.

Indent studied	**Load** (N)	**Predicted crack surface area (Anstis model)** (μm^2)	**Total crack surface area (3D reconstruction)** (μm^2)	**Difference** (%)
Syalon 101 Vickers	0.5	0	17	-
Syalon 101 Vickers	1	0	82	-
Syalon 101 Vickers	2	177 or 89	340	92 or 282
Syalon 101 Vickers	5	2166	934	57
Syalon 101 Vickers	5	1466	1177	20
Syalon 101 Vickers	5	623	903	45
Mean value 5 N	*5*	-	*1005*	*41*
Syalon 101 Cust. tip	0.5	0	126	-
Syalon 101 Cust. tip	1	127 or 63	388	206 or 516
Syalon 101 Cust. tip	2	322 or 161	1210	276 or 652
Syalon 050 Vickers	0.5	54 or 27	53	2 or 96
Syalon 050 Vickers	1	239	153	36
Syalon 050 Vickers	2	615	443	28

As cracking is mostly diffuse in Syalons 101 and 050 (a high number of microcracks has been observed), an energy approach would be more appropriate in order to quantify the damage in the material. As indentation curves permit the study of the plastic energy dissipated during the indentation process, this plastic energy has been compared to the total crack surface area found during 3D reconstruction of the crack patterns. Table 4.12 presents the total crack surface area measured from 3D reconstructions and the average plastic energy dissipated during the indentation process for the twelve indents studied with the FIB. The corresponding curves are plotted in Figs. 4.72 to 4.74.

A strong correlation is clearly visible between the variation of W_p with the indentation load and the variation of the total crack surface area with the indentation load. This correlation is valid for the indents performed in Syalon 101 or Syalon 050 indented with a Vickers or a customized tip. It is interesting to notice the existence of this strong correlation despite the fact that FIB tomography has influenced considerably the calculated crack surface area.

Table 4.12: Total crack surface area measured from 3D reconstructions and average plastic energy dissipated during the indentation process for the indents studied with the FIB.

Indent studied	**Load (N)**	**Total crack surface area (μm^2)**	**W_p (10^{-7}J)**
Syalon 101 Vickers	0.5	17	1.28±0.03
Syalon 101 Vickers	1	82	3.8±0.1
Syalon 101 Vickers	2	340	10.8±0.4
Syalon 101 Vickers	5	934	45±3
Syalon 101 Vickers	5	1177	45±3
Syalon 101 Vickers	5	903	45±3
Mean value 5 N	*5*	*1005*	*45±3*
Syalon 101 Cust. tip	0.5	126	3.9±0.2
Syalon 101 Cust. tip	1	388	11.0±0.3
Syalon 101 Cust. tip	2	1210	32±1
Syalon 050 Vickers	0.5	53	1.12±0.08
Syalon 050 Vickers	1	153	3.2±0.2
Syalon 050 Vickers	2	443	9.0±0.5

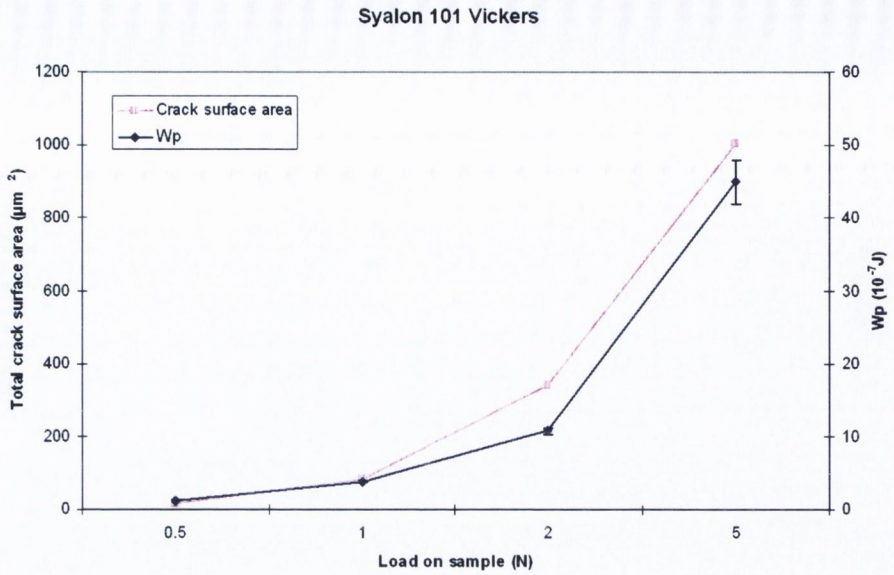

Figure 4.72: Variation of the total crack surface area measured from 3D reconstruction and of the average plastic energy dissipated during the indentation process for the Vickers indentations performed in Syalon 101.

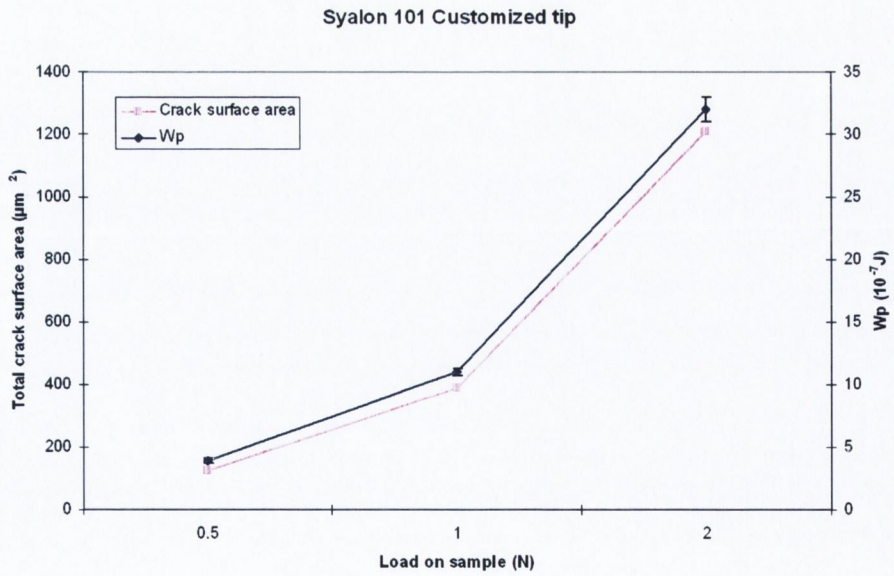

Figure 4.73: Variation of the total crack surface area measured from 3D reconstruction and of the average plastic energy dissipated during the indentation process for indentations performed with the customized tip in Syalon 101.

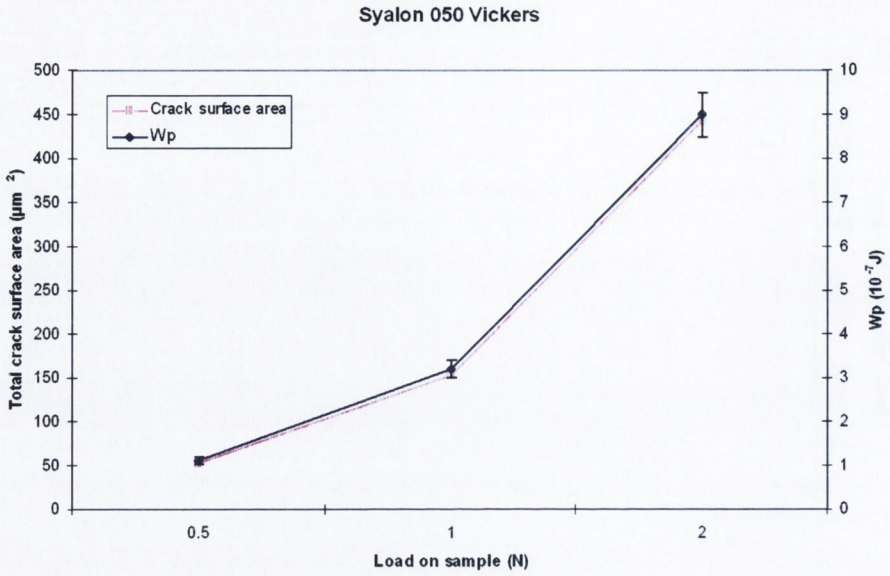

Figure 4.74: Variation of the total crack surface area measured from 3D reconstruction and of the average plastic energy dissipated during the indentation process for the Vickers indentations performed in Syalon 050.

Chapter 5

Discussion

Wear is a huge issue for ceramics used in biomaterials and in order to simulate this process in those ceramics, indentation is a technique often used as this test is very close to wear processes. Indentation tests simulate the behavior of a particle pressed into the surface of the material and to study consequences on the material properties. However, accessing subsurface damage created during indentation is a critical issue and few solutions currently exist. Methods previously cited in the literature review, like decoration of cracks or ceramographic polishing, suffer from a lack of accuracy and may introduce significant changes in the post-indentation cracks. The new method developed in this project uses a combined approach indentation - FIB tomography - 3D reconstruction in order to investigate fracture behavior and to try to quantify fracture resistance of ceramics at the microscale. This new technique has highlighted the inaccuracy of classical models at small scales. It has also revealed a strong correlation existing between the plastic energy dissipated through indentation and the total crack surface area measured underneath the indent site. However, an influence of FIB tomography on post-indentation crack area has been identified and has highlighted the need for additional work on this technique in order to use it as a relevant tool to study the influence of microstructure on fracture behavior.

The work done in this project has investigated fracture behavior of micro-indented porous polycrystalline alumina and Syalons 101 and 050. The development of the combined approach of indentation-FIB tomography-3D reconstruction has also highlighted many issues concerning the Indentation Crack Length (ICL) method for the characterization of fracture properties of ceramics at the microscale. A discussion on the contribution of this new approach to the study of fracture resistance of these ceramics is also presented. Finally, the relevance of the indentation technique in the measurement of fracture properties is discussed.

5.1 On the investigation of fracture properties of alumina

The high variation in the indentation curves obtained in polycrystalline alumina cannot be attributed to an insufficient number of tests. In fact, from the viewpoint of statistics, if the number of tests is not big enough, the average value is expected to differ significantly from the bulk value measured with conventional methods. In this study however, 178 good tests have been identified for D2 and 112 good tests for L2. This represents a significant number of tests. However, the results still present a large scatter in measured mechanical properties. This high variation can be attributed to the influence of local microstructure as previously highlighted by Gong et al. [25]. In fact, even for the highest load tested (10.2 N), the corresponding average maximum indentation depth is 5.8 μm for both D2 and L2. These values are on the same order of magnitude as the average grain sizes of D2 and L2 (4.7±2.0 μm and 9.7±3.8 μm respectively). This is also visible on SEM micrographs of 5 N indents made in D2 and L2 (Fig. 4.5) as the size of the residual impression is on the same order of magnitude as the grain size. Consequently, microstructure will influence the indentation response of the material at this scale. For instance, presence of microstructural features like grain boundaries or pores in the area indented or cracking during loading will lead to an increase in the penetration depth. Furthermore, the cracks formed will affect the material stiffness and allow the indenter to reach higher penetration depths. An interesting result is that the coefficient of variation of h_{max} exhibits a decreasing tendency with increasing the maximum load. This is an indirect support to the influence of microstructure on the measured properties: as the load increases, the indentation zone of influence expands and the differences between local features tend to be averaged. This result is in accordance with the findings of Gong et al. [25] who conducted nanoindentation tests on a high-purity, dense, 0.9 μm average grain size alumina ceramic at loads ranging from 8 to 500 mN. A difference with their experiment is the amount of porosity present in our samples (7.0 % for D2 and 3.3 % for L2).

At the indentation loads investigated, E and H are expected to be a measure of local properties. The average values of E and H which are useful at the bulk level, are expected to have high variations in polycrystalline alumina at the microscale due to the influence of the local microstructure. Thus E and H values vary significantly depending on the indent location. In fact, calculation of H depends on the contact area A at peak load and therefore on $1/h_c^2$. Furthermore,

E depends on $\sqrt{A}$ and therefore on $1/h_c$ but also depends on the stiffness S which is evaluated at h_{max}. Knowing that h_c also depends on h_{max} and S helps to understand why the scatter found in the maximum penetration depth induces a large variation in the measured material properties. Furthermore, in the loads investigated in this study, micro-cracking occurs (a critical load of 200 mN for cracking in alumina has been reported [94]) and as highlighted by Petit et al. [69] and Krell et al. [94], micro-cracking induces an increase in material compliance and penetration depth and thus affects the calculated values of E and H. This will also contribute to the large scatter observed in E and H values. This also suggests that the amount of scatter may perhaps be correlated to the amount of microcracking and is worthy of further study. This scatter is in accordance with the findings of Petit et al. [69] who observed variations in the range 5-10% in the indentation Young's modulus of a polycrystalline alumina. They have concluded that their indentation results were representative of the bulk material property even though their residual imprint size (11 μm) was only three times bigger than their mean grain size (3.8 μm). In this case, the indentation may only concern a few grains, thus the properties measured are more local and strongly influenced by microstructural features than representative of the bulk material. Another fact also tends to support the hypothesis of the influence of microstructural inhomogeneity on the material response to micro-indentation. When fitting the unloading curves with the power law described in Eq. 5.1, a large scatter of B and m values was observed at each load.

$$P = B\,[h - h_f]^m \tag{5.1}$$

In fact, Pharr et al. [152], explained Eq. 5.1 by the use of an 'effective indenter' whose geometry is determined by the shape of the plastic hardness impression during indentation. In this case, the fitting parameters B and m are functions of E and H of the material tested. As a consequence, a large variation in B and m would indicate that E and H vary significantly from one indentation site to another and thus that the properties measured are local properties.

Concerning fracture analysis, calculation of fracture toughness by the ICL method was not possible as the crack patterns obtained did not match the requirements necessary to use conventional fracture toughness models (defined explicitly in the literature review). In fact, the porous alumina samples showed poor reproducibility in the crack patterns for the loads studied. This is consistent with the observations of Ponton et al. [62] who noticed that crack patterns in polycrystalline ceramics became random and erratic when the indent size was

close to the mean grain size. Conventional equations are based on the assumption that surface cracks propagate radially from the indent corners. This was not the case in this study as the observed cracks were tortuous, sometimes departing from the side of the indent or not following a radial line from the indent corner. All these observations mean that there were significantly more free surfaces created during cracking than if cracks were propagating radially from the indent corners. Furthermore, most of the cracks had short lengths which means that they lay within the dimension of the deformed region. In those cases, trying to apply a conventional indentation fracture toughness equation would give meaningless results.

These experiments done in alumina have confirmed the fact that for this material at the microscale, a method to quantify resistance to fracture is missing as the existing models are not valid anymore.

An interesting result from subsurface analysis using FIB-tomography is the fact that increasing load seems to lead to an increasing tendency to form deep lateral cracks under the indents. It has been shown that at high loads, lateral cracks tend to divert upwards toward the surface, resulting in material removal at the surface. This phenomena, called chipping is highly damaging for the material.

This preliminary study done on alumina has highlighted the fact that indentation tests allow the measurement of local properties E and H. This result is of great interest in the study of local fracture, as this project aims to investigate the local damage or fracture as it happens at small scale in ceramics used in biomaterials for instance. Local fracture is influenced by local properties like E and H so it is interesting that indentation technique can capture these local variations. This study on alumina has also shown that local microstructure has a great influence on local E and H. It has also revealed the inaccuracy of the ICL method to characterize fracture resistance in these ceramics at the microscale. Finally, it has established a protocol for this project and set up the reconstruction technique. However, because of technical issues (it was impossible to visualize grain boundaries during FIB tomography), this study has been carried on with SiAlON materials.

5.2 On the investigation of fracture properties of Syalon 101 and 050

5.2.1 Analysis of Young modulus and hardness

As previously observed in alumina, there was a high variation in indentation curves in Syalon 101 and 050 in the range of loads studied. This can again be attributed to the influence of microstructure as the maximum depth reached (6.2 μm for 10 N) is on the same order of magnitude as the average grain size (1.9 μm). This result is supported by the fact that as the load increases, the coefficient of variation of the maximum depth decreases, meaning that there is less dispersion in the results due to the decreasing influence of local microstructure.

Calculations of hardness for Syalon 101 and Syalon 050 over all loads tested with the Vickers tip in this study have given the following values: 18.7 GPa for Syalon 101 and 22.0 GPa for Syalon 050, which are significantly different from the bulk values given by the manufacturer (respectively 14.7 GPa and 19.6 GPa). The hardness value given by International Syalons was calculated at 2.942 N ($Hv_{0.3}$ microhardness test) which is on the same range of scale as our experiments. However, hardness calculated by International Syalons is based on the contact area of the residual impression while hardness calculated in this work uses the contact contact area evaluated at peak load. If there is significant elastic recovery (which is the case for our samples), the two values may differ considerably. During this study, hardness was found to decrease with the load applied. This apparent indentation size effect (i.e, hardness increasing when load decreases) cannot be related to the indentation size effect described by Nix and Gao [6](detailed in the Literature Review) which is usually observed with indentation tests at scales on the order of one micron, as the size of the tests presented here is significantly bigger than that. It should also be noticed that no pile-up effect was visible on indents made with a Vickers tip, which could have lead to an overestimation of the hardness value at small load and therefore to a wrong observation of apparent indentation size effect. No evident explanation was found to describe the difference found for Young's modulus between the manufacturer value and the one from this study. In all loads studied in this project, E was always found lower than the manufacturer specifications for both Syalons 101 and 050.

There was a decrease observed in hardness and Young's modulus values for both Syalon 101 and Syalon 050 when increasing the maximum peak load. This decrease in H and E values is a size effect which may be due to the material

itself and the growing influence of microstructural parameters when decreasing the load.

E and H are measures of elastic and plastic behavior in a material. Fracture at small scale is influenced by local E and H and, as already found in alumina, local values of E and H are experiencing large variations in Syalons 101 and 050 due to the local microstructure. Indentation is therefore a useful technique to capture this variability in E and H and this variability should be reflected in the plastic and elastic energies of indentation.

5.2.2 Analysis of energy dissipated through indentation

Analysis of indentation curves was performed in order to check if elastic and plastic energies of indentation were reflecting local variations as E and H were doing and then to check if these energies could be related to any local fracture property. Study of indentation curves has provided access to the total energy W_{tot} dissipated through indentation as well as the elastic part W_e of this energy. Thus, it was possible to deduce the plastic energy W_p from each experiment.

Variations of W_e and W_p were observed for both Syalons 101 and 050 and as these values are linked to E and H properties, these variations are also expected to come from the influence of local microstructure.

In order to assess whether the material response to load changed with increasing indentation load, the ratio of the total plastic energy over the total indentation energy (W_p/W_{tot}) was calculated. This ratio was found to slightly increase with the maximum load applied for both Syalon 101 and Syalon 050. This result means that there is no real change in the elastic-plastic response of the material when increasing the indentation load and therefore that the mechanisms involved in the indentation response are the same over the range of loads studied.

For the purposes of this work, the plastic energy W_p was divided into three contributions: plastic energy coming from dislocation movements (E_p), energy dissipated through densification (E_d) and energy dissipated through fracture (E_f). Transformation induced by shear also exists but is not applicable in SiAlONs. In most ceramics, dislocations are present in the crystalline structure but are unable to move due to the high strength of the covalent bonds holding the atoms together. As a consequence, prior to the application of a force large enough to induce dislocation movements, other defects present in the ceramic will be overloaded, causing the ceramic to fail. The plastic energy due to dislocation movements is therefore very low in hard ceramics and its contribution to the total plastic energy is minor compared to fracture energy and densification energy.

Densification during indentation is an important parameter in ceramics because it is related to the microporosity that is often present in sintered ceramics. However, this is not the case for Syalon 101 and Syalon 050 where a liquid phase is formed during sintering which leads to an intergranular glass on cooling. Therefore, the remaining porosity in Syalons 101 and 050 is only due to the presence of few macropores and has been estimated as 0.05 % for Syalon 101 and as 1.3 % for Syalon 050 of the total volume fraction. In polycrystalline ceramics, the influence of the volume fraction porosity P on the Young's modulus can be estimated by the equation $E(P) = E_0(1 - 1.9\ P + 0.9\ P^2)$ where $E(P)$ is the Young's modulus of the porous material and E_0 the modulus of the corresponding dense material. Similarly, porosity affects flexural strength according to the equation: $\sigma_{fs} = \sigma_0 \exp(-nP)$ with n being a geometrical factor reflecting the shape of the pores (this factor is usually between 2 and 4). These two equations have been plotted in Fig. 5.1 with n=3 and both show that for P less than 5 %, the influence on E and σ_{fs} is quite low. As the porosity calculated in Syalons 101 and 050 is 0.05 % and 1.3 % respectively, one might expect the influence of porosity to be quite small on the material properties and therefore the contribution of the densification energy to the total plastic energy to be low compared to the contribution of the fracture energy. As a result, the total plastic energy calculated from the indentation curves will be considered as being mainly the energy dissipated through fracture. The high number of cracks observed underneath the indents studied with the FIB constitutes another support to this assumption.

This study has shown that there was a strong correlation between the variation of plastic energy with indentation load and the variation of total crack surface area with load for the two materials studied and for the two different indenters. This result is very interesting in the study of local fracture as it links the results given by an indentation test to one important fracture parameter. This result will be discussed in greater detail in section 5.3.1. It is important to note that material failure will not only depend on the total crack surface area but also on the crack shape, size and localization. Therefore, the crack size distribution was investigated and the contributions of the different cracks to the total surface area studied.

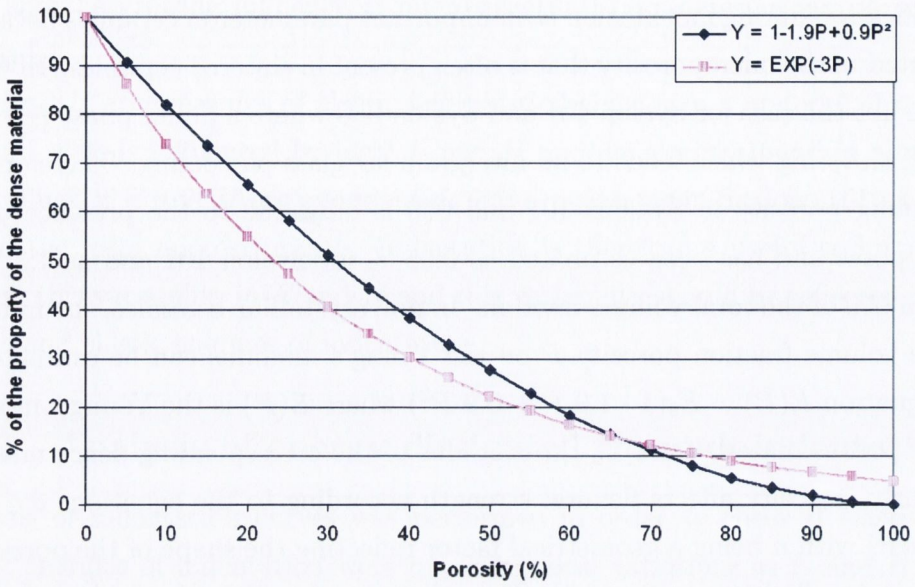

Figure 5.1: Variation in material property with porosity according to two different equations.

5.2.3 Relationship between crack size and microstructural scale

For every indent studied with FIB tomography, each crack was reconstructed individually in order to calculate its crack surface area. Then the distribution of the crack surface areas was investigated for each indent (histograms are presented in section 4.2.3.1). For the purpose of associating these results with microstructural features, the histograms obtained were correlated with the area of an equivalent grain. The β-sialon grains present in Syalon 101 have an average grain size of 1.9 μm so the equivalent grain was taken as a spherical particle of diameter equal to 1.9 μm. Therefore, the area of this equivalent grain is given as $(1.9/2)^2\Pi \simeq 2.8$ μm^2. Three intervals were then defined for the crack surface areas found for each indent:

- small cracks (S): cracks with a surface area less than or equal to the area of an equivalent grain. These cracks will be strongly influenced by local microstructure
- medium cracks (M): those with a surface area lying between the area of an equivalent grain and ten times this area.
- large cracks (L): those with a surface area greater than ten times the area of

an equivalent grain. These cracks will probably be subject to little influence from the local microstructure.

In addition to β-sialon grains, Syalon 050 also contains α-sialon grains but the latter could not be differentiated from β-sialon grains on the SEM micrographs. Therefore, the same equivalent grain was taken for both materials.

The results are presented in Table 5.1 and the contributions of small, medium and large cracks to the total crack surface area for the different loads investigated in Syalons 101 and 050 are drawn in Figs. 5.2, 5.3 and 5.4.

Table 5.1: Contribution of small, medium and large cracks to the total crack surface area in Syalons 101 and 050 indented at different loads with the customized and Vickers tips.

Indent	**Load (N)**	**Fraction of surface area of the concerned cracks over the total crack surface area**		
		From 0 to 2.8 μm^2	**From 2.8 to 28 μm^2**	**More than 28 μm^2**
Syalon 101 Vickers	0.5	100%	0%	0%
Syalon 101 Vickers	1	31%	29%	40%
Syalon 101 Vickers	2	14%	17%	69%
Syalon 101 Vickers num7	5	6%	4%	90%
Syalon 101 Vickers num18	5	7%	10%	82%
Syalon 101 Vickers num20	5	15%	17%	68%
Average value (5 N indents)	*5*	*9%*	*11%*	*80%*
Syalon 101 Cust. tip	0.5	17%	60%	22%
Syalon 101 Cust. tip	1	9%	39%	52%
Syalon 101 Cust. tip	2	9%	16%	75%
Syalon 050 Vickers	0.5	17%	83%	0%
Syalon 050 Vickers	1	9%	32%	59%
Syalon 050 Vickers	2	6%	9%	85%

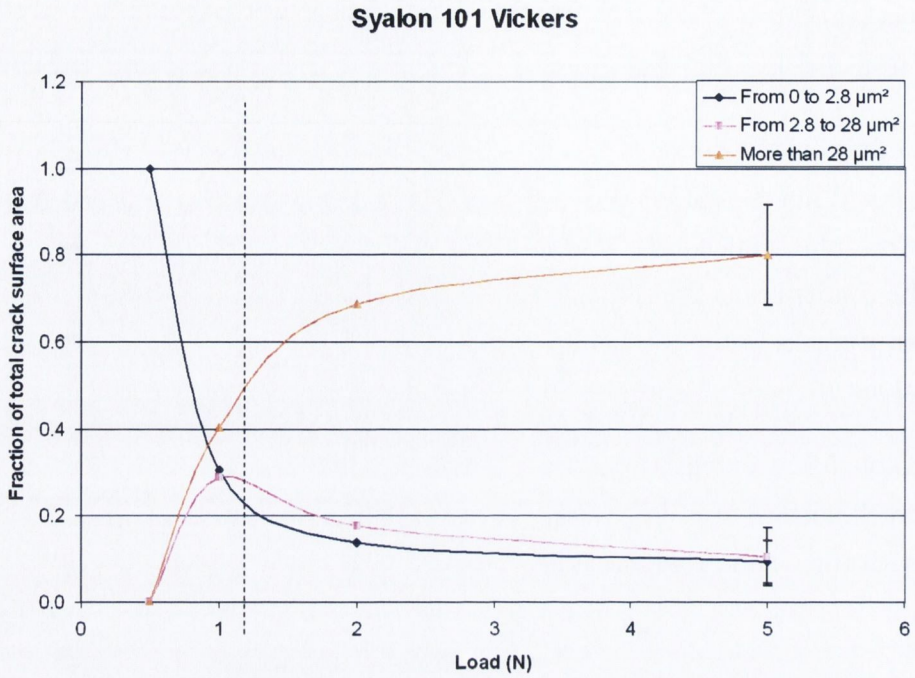

Figure 5.2: Contribution of small, medium and large cracks to the total crack surface area in Syalon 101 indented at different loads with the Vickers tip.

According to these graphs, contributions of S and M cracks to the total crack surface area decrease dramatically when the load increases in Syalon 101. On the contrary, as the load increases, the contribution of large cracks increases considerably. This dramatic change in the contributions of these three types of cracks appears to occur between 1 and 2 N. Above this threshold, the surface area of L cracks represent the majority of the crack surface area and therefore will determine the material resistance to fracture. However, some care should be taken when saying that large cracks are not strongly influenced by local microstructure. This statement is in contradiction with the observed tortuous crack paths, crack bridgings and crack deflections observed during reconstruction of subsurface cracks. In fact, as indentation is a quasi-static process, cracks grow slowly and are influenced by the local microstructure while growing. These large cracks can therefore be seen as a coalescence of microcracks in areas where tensile stress is maximum. Nevertheless, as the load increases, the stresses become higher and are less influenced by local heterogeneities, leading to the formation of cracks following a more classical path on average, even if they are often deflected locally. On the contrary, small cracks are strongly influenced by local stresses. This might

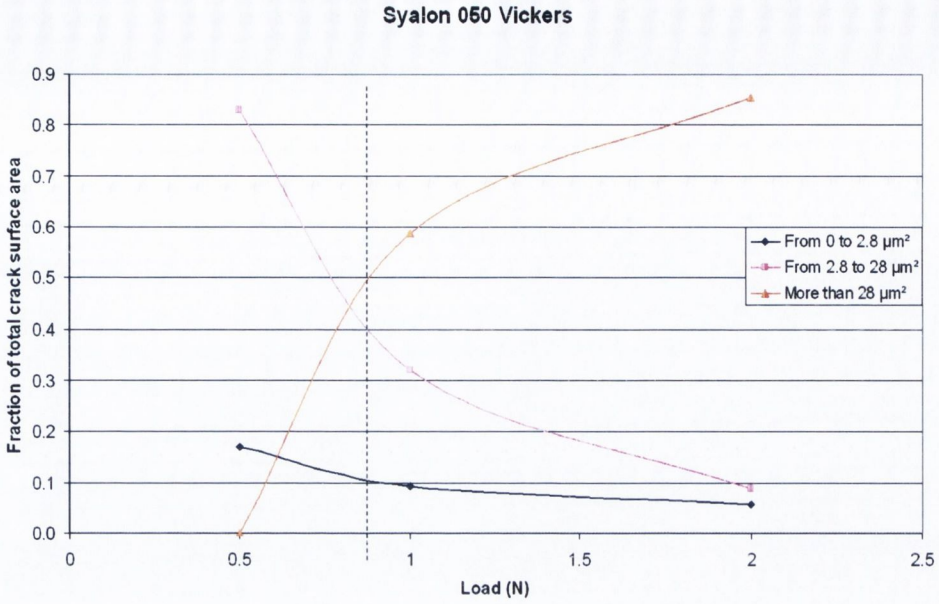

Figure 5.3: Contribution of small, medium and large cracks to the total crack surface area in Syalon 050 indented at different loads with the Vickers tip.

explain why well-defined crack shapes have been observed at 5 N in Syalon 101 (for instance, the partial half-penny crack) compared to the cracks found at 500 mN. Interestingly, surface cracking threshold was found to be between 3 and 4 N in Syalon 101 when observing the indents with the SEM. This threshold is just above the one found previously in the contributions of small, medium and large cracks. Therefore, it might be suggested that cracks appear on the surface when coalescence of subsurface microcracks has reached this threshold.

Below 1 N in Syalon 101 indented with the Vickers tip, the total crack surface area is significant, even if there is no surface crack. Most of the energy is dissipated through microcracking and the resulting crack pattern looks more like damage than fracture.

For Syalon 050, there is also a dramatic change in contributions of S, M and L cracks to the total crack surface area. This change occurs between 0.5 N and 1 N, a bit lower than for Syalon 101 indented with a Vickers tip but the difference between them is not significant. As in Syalon 101, contributions of S and M cracks to the total crack surface area decrease dramatically when the load increases while contribution of large cracks increases considerably. The surface cracking threshold was found to be between 2 and 3 N so the same explanation as in Syalon 101 can be suggested.

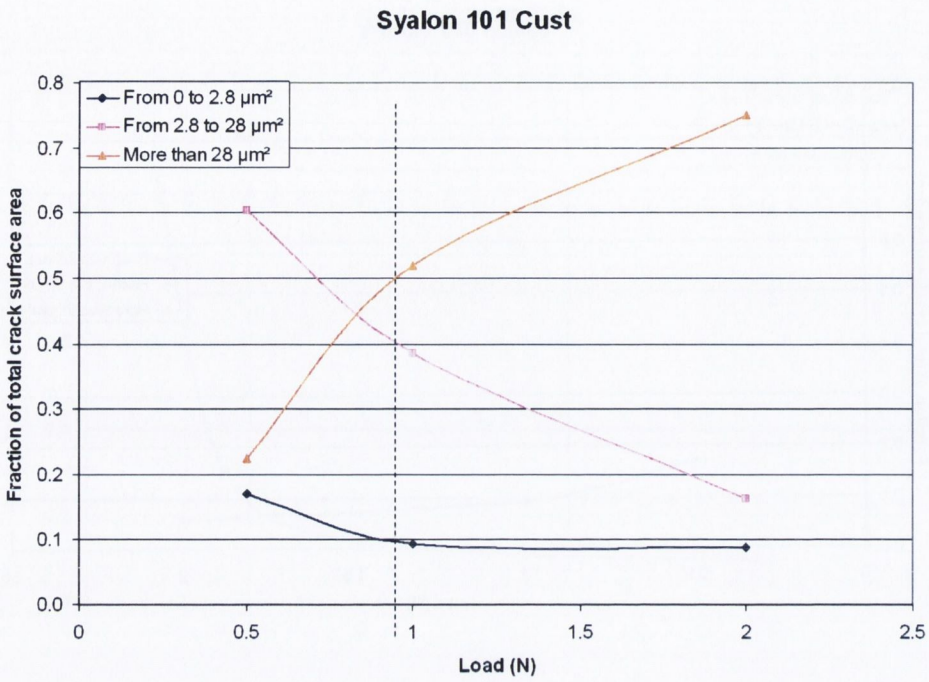

Figure 5.4: Contribution of small, medium and large cracks to the total crack surface area in Syalon 101 indented at different loads with the customized tip.

Interestingly, there is also a dramatic change in S, M and L crack contributions to the total crack surface area for Syalon 101 indented with the customized tip. Contributions of S, M and L cracks follow the same variations as in Syalon 101 indented with a Vickers tip but the change in their contributions seems to happen at a lower load with the customized tip than with the Vickers tip although this difference is not really significant.

It can be concluded from this study that there is no real difference between Syalon 101 and Syalon 050 concerning the variations with the indentation load of contributions of S, M and L cracks to the total crack surface area. These two materials differ on their crystal structure, their composition being nearly identical. It might then be hypothesized that crystal structure doesn't have a significant influence on the variations of the crack size distribution with the load applied for these two SiAlON ceramics studied.

All these conclusions should be moderated by the fact that the total crack area has been modified by the FIB process, as described in the Results chapter. The influence of the FIB process is probably higher at high loads at it modifies the local stress fields remaining after indentation which is higher for higher loads.

However,the influence of the FIB itself is unlikely to explain all the dramatic changes in contributions of S, M and L cracks when load increases.

5.2.4 Influence of random local microstructure

The three Vickers indents at 5 N in Syalon 101 were studied in order to investigate the influence of random local microstructure. Results concerning 3D reconstruction of these three indents are summarized in Table 5.2. These indents were made in the same conditions. The same amount of energy was given to the material and they only differ by the location of the indentation. They have been chosen depending on their surface behavior: indentations num7 and num18 present four well-defined corner cracks but of different length and the predicted crack surface areas based on conventional models are respectively 2166 μm^2 and 1466 μm^2. On the contrary, indentation num20 only shows two surface cracks and the predicted crack surface area is 623 μm^2. FIB tomography reveals that the situation underneath the surface is the opposite: there are far more cracks underneath indent num20 (265 cracks) than underneath the two others (122 cracks for indent num18 and 66 for num7). For indent num7 which has big surface cracks, results show less cracks underneath the surface. This means that there was a very high tensile stress near the surface, leading to the opening of long surface cracks. On the contrary, for indent num20 which has only two shorter surface cracks, lots of cracks were observed below the surface, meaning that tensile stress was lower on surface than for indent num7 and more distributed inside the volume of the material. These results show the high influence of random local microstructure on local stress fields during the indentation process. Local microstructure highly disturbs the idealized stress field patterns, which results in different cracking behavior: surface cracking or cracking more distributed inside the volume of the material. In the last case (indent num20), the material may have a higher resistance to fracture than in the case of indent num7. This is correlated by the fact that the contribution of large cracks to the total crack surface area is lower for indent num20 than for indent num7 (68 % vs 90 %).

In the three cases however, the total crack surface area found with the 3D reconstruction is quite similar. Consequently, even if the total crack surface area is an important parameter to determine fracture properties, this experiment shows that in order to quantify fracture behavior, crack localization and size need to be determined.

Table 5.2: Contributions of S, M and L cracks to the total crack surface area, total number of cracks and total crack surface area of the three 5 N Vickers indents performed in Syalon 101.

Indent	Fraction of surface area of the concerned cracks over the total crack surface area			Total number of cracks	Total crack surface area (μm^2)
	From 0 to 2.8 μm^2	From 2.8 to 28 μm^2	More than 28 μm^2		
101V 5N num7	6%	4%	90%	66	934
101V 5N num18	7%	10%	82%	122	1177
101V 5N num20	15%	17%	68%	265	903

5.2.5 Comparison between Syalon 101 and Syalon 050

Results obtained during indentation and following the 3D reconstruction enable a comparison of fracture behavior of Syalons 101 and 050. For the same indentation load, W_{tot} is lower in Syalon 050 than in Syalon 101. W_p is also lower in Syalon 050. Assuming densification and dislocation mechanisms can be neglected, W_p is associated with the fracture energy E_f, which means that fracture energy is lower for Syalon 050 than for Syalon 101. The same crack propagation mechanisms are observed in Syalon 101 and in Syalon 050 (crack bridging and crack deflection). For the same indentation load applied, the same types of cracks are observed in Syalon 101 and Syalon 050 but cracks are bigger in Syalon 050. This result, combined with the fact that Syalon 050 has a greater total crack surface area than Syalon 101 for the same indentation load, tends to indicate that fracture process would be easier in Syalon 050 than in Syalon 101 on the range of loads investigated (which would confirm what the manufacturer claims at macroscale for fracture toughness). These two materials differ by their phase composition, their phase assemblage but also by their porosity. The lower fracture resistance of Syalon 050 can be related to one of these three parameters or to a combination of them. Syalon 050 is in fact more porous than Syalon 101 and porosity influences significantly crack formation and propagation. Porosity can be linked to a reduction of fracture (as some energy is associated to densification) but pores can also favor crack formation and propagation.

In the field of materials design, it is of greater interest to obtain diffuse cracks inside the structure than large cracks which may lead to the material failure. It would therefore be better to keep the use of one material under the load where microcracks starts to coalesce to form larger cracks. In order to increase fracture resistance of a material, it would be interesting to obtain diffuse cracking in the material for the highest load possible. In the case of Syalons 101 and 050, there

is no significant difference between the load threshold where larger cracks tend to dominate. Another solution to increase fracture resistance of a material would be to decrease the total crack surface area and for this parameter, Syalons 101 and 050 considerably differ.

5.3 Discussion on the combined indentation-FIB tomography technique in this study

In order to access fracture behavior of ceramics at the microscale, indentation tests are routinely performed and fracture toughness deduced from the length of surface cracks (ICL method) using elastic, elastic-plastic or residual stress models, with the Anstis model being the most frequently used. These models are used despite the fact that many of the assumptions underlying them are not valid at the small scale as previously highlighted in the Literature Review.

The techniques used in this project have highlighted the fact that fracture toughness determined using the ICL method was not relevant in the case of ceramics at the microscale. Surface crack analysis has shown that none of the basic assumptions of these models was valid at this scale. The observed surface cracks often do not match the requirements for the ICL method, with cracks emanating from the sides of the indents rather than from one corner, having a length inferior to the diagonal length and a very tortuous shape. The indentation crack shape and length also varied considerably from one indent to another for the same load applied. Moreover, all indentations performed with the customized tip present a significant amount of pile-up. All these issues have been previously noticed by several authors [68, 153]. Solomah [68] presented a list of issues commonly encountered when trying to measure length of surface cracks in order to apply the ICL method to many ceramic materials. Quinn et al. [67] have also pointed out the fact that even if surface cracks can be measured, the theory behind the ICL method was not valid in order to determine fracture resistance of ceramics. The work done in this study has confirmed the issues highlighted by Solomah concerning surface cracks and has also permitted the comparison of actual subsurface crack shapes and areas with the idealized crack patterns (half-penny or shallow radial cracks) on which ICL models are based. Using FIB tomography, this work has confirmed that subsurface cracks don't follow well defined paths and has shown the presence of numerous microcracks present underneath the indent and diffuse inside the material. This study has also shown the huge influence of microstructure which locally disturbs idealized stress fields: crack deflection and

crack bridging were two phenomena encountered for every indentation volume reconstructed. Following these observations, the huge difference observed between the predicted crack surface area and the actual one is not really surprising and again supports the irrelevance of the ICL method in the case of ceramics, especially at small scale. Finally, FIB tomography of indents with no surface crack has revealed the presence of significant subsurface microcracking. This microcracking is not taken into account in any classical model but needs to be accessed when looking at fracture resistance of the material.

5.3.1 Correlation between indentation results and subsurface crack analysis

As cracking observed underneath the indents was mainly done by microcracks and longer cracks not following classical paths, an energy approach was considered in order to quantify fracture behavior of these ceramics. The combined method of indentation-FIB tomography used in this study had the advantage of accessing both the energy dissipated during indentation and the total crack surface area from the 3D reconstruction. Therefore, this technique has permitted the study of the variations with load of these two values for two different materials (Syalon 101 and Syalon 050) and for two different indenter geometries (Vickers and customized tip). A strong correlation was observed between the variation of plastic energy with indentation load and the variation of total crack surface area with load for the two materials studied and for the two different indenters. The relationship between the plastic energy and the total crack surface area observed for Syalon 101 indented with the Vickers and customized tips as well as for Syalon 050 indented with the Vickers tip is shown in Figs. 5.5, 5.6 and 5.7.

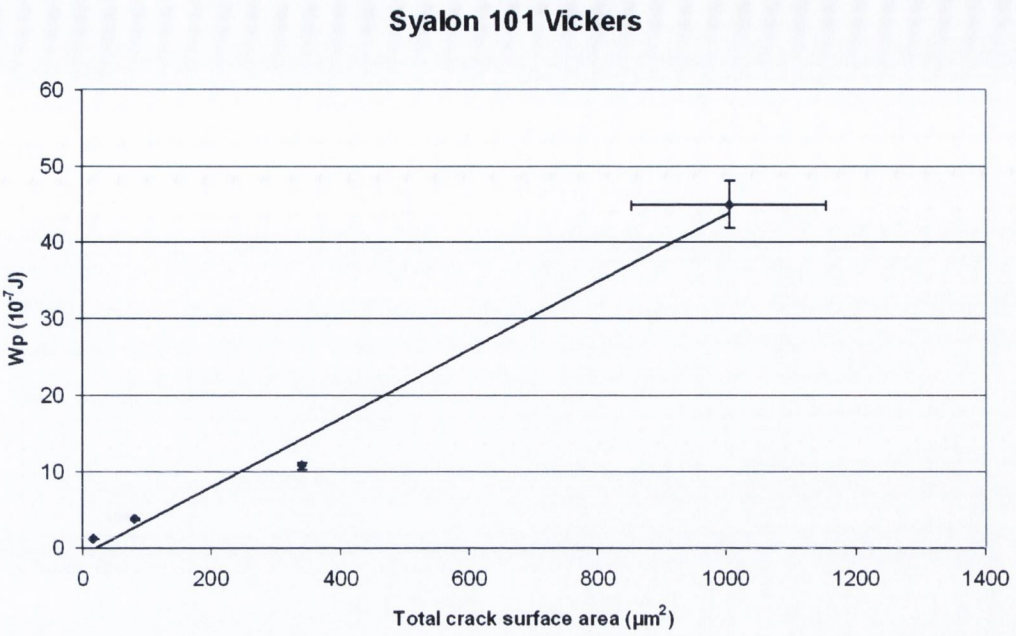

Figure 5.5: Variation of plastic energy with total crack surface area for Syalon 101 indented at different loads with the Vickers tip.

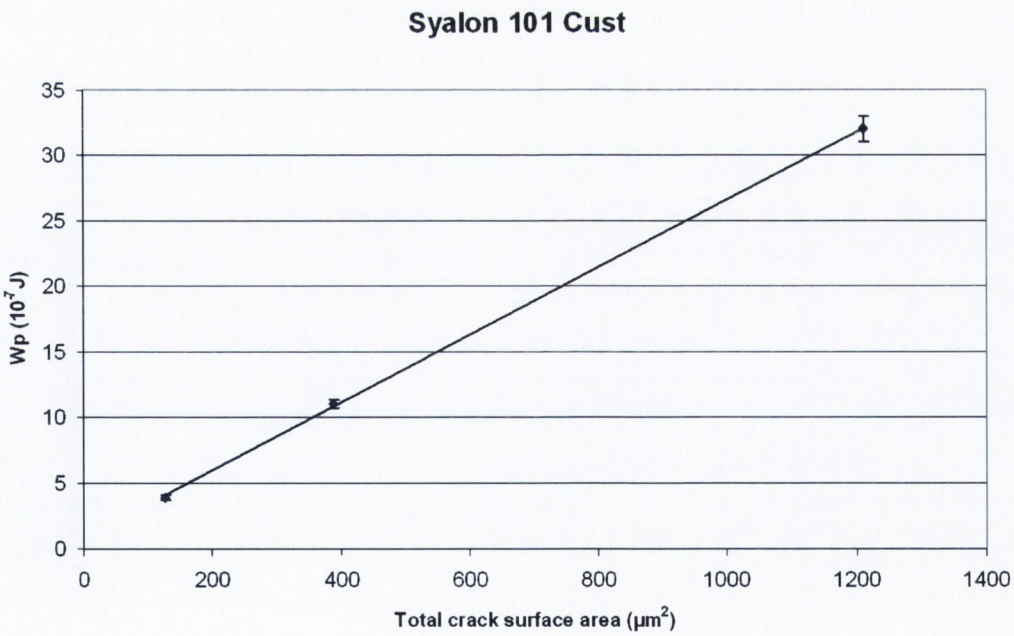

Figure 5.6: Variation of plastic energy with total crack surface area for Syalon 101 indented at different loads with the customized tip.

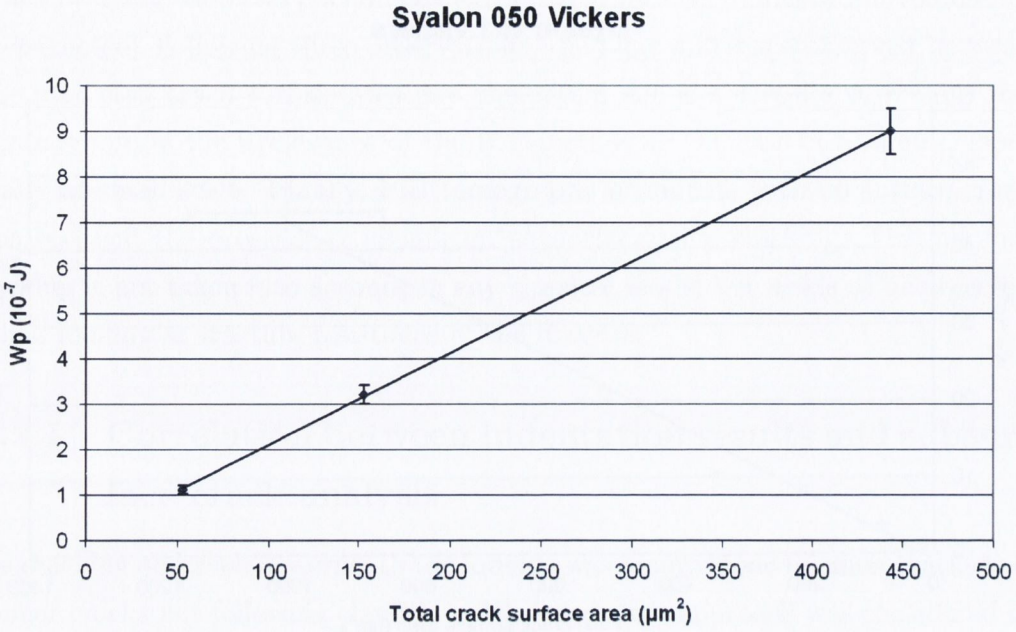

Figure 5.7: Variation of plastic energy with total crack surface area for Syalon 050 indented at different loads with the Vickers tip.

This strong correlation can be explained by the existing relationship between plastic energy dissipated during an indentation test and the total surface area of the cracks formed during this test. In fact, the main contributions to the plastic energy W_p are the plastic energy coming from dislocation movements (E_p), the energy dissipated through densification (E_d) and the energy dissipated through fracture (E_f). Other dissipation mechanisms also exist (heat for instance) but have minor contributions to W_p than E_p, E_d and E_f. The plastic energy due to dislocation movements is low in hard ceramics like SiAlONs. In fact, in ceramics like SiAlONs where the bonding is highly covalent, there are few dislocation motions. This is due to the fact that in these ceramics, the covalent bonds are relatively strong, there are few slip systems and dislocation structures are complex. Therefore, these materials will tend to fail before reaching the load necessary for dislocation movements. In the case where the samples experienced pile-up (when indenting with the customized tip), the material pushed out looked like broken pieces or grains which have been moved after cracking has occurred. Thus it is considered as coming from microcracking and not from dislocation movements. The contribution of E_p to W_p is therefore minor compared to the contribution of E_f. This assumption is consistent with publications of Wang et al. [154] and Giannakopoulos et al. [155]. They described shear stresses in alumina

and silicon nitride as being more likely associated with microcracking than with dislocation movements.

As previously discussed in section 5.2.2, energy dissipated through densification can be neglected in Syalons 101 and 050 compared to energy dissipated through fracture because of the high density of these ceramics. In Syalon 101 and Syalon 050, a liquid phase is formed during sintering which leads to an intergranular glass on cooling. Therefore microporosity is low in these ceramics and the remaining porosity is only due to the presence of few macropores inside the material. Consequently, contribution of the densification energy to the total plastic energy can be neglected compared to the contribution of the fracture energy. Therefore, plastic energy calculated from indentation curves is nearly entirely dissipated through fracture processes and can be used to approximate the fracture energy in the case of SiAlON ceramics in the range of loads investigated. Fracture energy, according to the definition proposed by Griffith, is the energy associated with the formation of new surfaces. The fracture energy and the total crack surface area are linked by a term called the surface energy per unit area γ (also called specific surface energy). γ represents the amount of increase of free energy when the area of surface increases and is a material property. For instance, γ will have a different value for the α, β and intergranular phases. For a sample containing several phases like Syalon 101 or Syalon 050, γ will then be a combination of these different values depending on the percentage of the different phases in the sample composition. A relationship between plastic energy and total crack surface area is thus expected and explains the strong correlation found between the variation of plastic energy with indentation load and the variation of total crack surface area with load. Nevertheless, it is interesting to notice that this strong correlation exists despite the change induced by FIB tomography on the calculated crack surface area.

5.3.2 Development of a FIB-SEM imaging technique for the study of subsurface cracks in insulating brittle materials

A new fully automated method was implemented with the FIB in order to study and reconstruct subsurface cracks created during the indentation tests. This technique was developed to solve issues arising from a long automatic acquisition process, the insulating nature of the SiAlON specimens and the introduction of minimal damage to the original cracks resulting from indentation. The software

tool provided by the FIB manufacturer was completely inadequate in handling problems associated with sectioning a highly insulating ceramic. Therefore, a customized script was written in order to automate the serial-sectioning experiments. A number of phenomena related to the highly insulating nature of SiAlONs ceramics were identified and solved.

One of the main issues concerned charging effects on the electron induced secondary electron images (E-SE images) taken during FIB tomography and the fact that these effects could impede 3D reconstruction. On newly cut cross-section images taken by the SEM, distortions and strong voltage contrast (strong bright and dark regions appearing on the flat cross-section face due to non-even charge distribution) were observed. In an attempt to minimize this effect the energy of the incident electron beam and the image scan parameters were varied. The former approach was employed to try to balance the primary charge incident upon the cross-section face during scanning with that leaving the face in the form of secondary and back-scattered electrons [156, 107]. An electron beam energy of 5 keV was found to offer good spatial resolution imaging, sufficient to resolve clearly the microscale cracks and to be the best compromise between reducing levels of voltage contrast and maximizing the contrast needed to differentiate the amorphous and crystalline phases. Further reduction in the levels of voltage contrast due to electrical charging were obtained by choosing a low beam current (0.40 nA, to reduce the amount of implanted charge) and by using a relatively quick scan rate (dwell time = 3 μs) averaged over 16 frames. Images acquired, in which less charge was implanted (dwell time = 30 μs), over a single frame exhibited far stronger voltage contrast.

One unwanted contrast feature that the optimization of beam energy, current and image acquisition parameters could not solve was the presence of shadow effects from the side walls. This effect, which obscures important microstructural and crack features, is due to charging and is material dependent. A suggested approach to overcome this problem is by milling a 'U-shaped' trench around the investigated sample location prior to the serial sectioning process [107, 105, 113]. However, in the study of subsurface cracks, this technique was unsuitable as the creation of the 'U-pattern' would induce significant changes in the stress fields surrounding the indent and lead to the opening or closing of cracks through stress relief.

Charging effects during electron imaging also resulted in a brightness gradient from the top to the bottom of the cross-section. This brightness gradient as well as the shadow effects from the side walls can induce difficulties during

segmentation by introducing different grey levels within the same phase. Thus, data segmentation by a global threshold value was not longer possible. As only few filters were available for segmentation in Avizo, a customized script has been written in Matlab to overcome this issue. This script uses linear filters and two local thresholds in order to transform the grey level images to binary ones (with the intergranular phase in white and the grains in black). Then a filter to remove small objects (noise) was used and the binary images obtained were superimposed to the original ones to check the filtering process. Binary images were then segmented in Avizo using a global threshold.

The second main issue was due both to charging effects and to the long duration of each experiment. It concerned the alignment of the ion and electron beams. It was clear that to develop an automated serial-sectioning routine that would yield image data of high enough quality for 3D reconstruction, dynamic adjustment of both the FIB and SEM processes would be required.

Commonly, when performing serial-sectioning with the manufacturer supplied software, the ion beam automatically mills slices of a specified thickness and assumes that the specimen stays effectively in the same position throughout the process. This assumption is a critical one as any change in the effective specimen position will lead to irregularity of the slice thickness and affect the spatial resolution of the 3D reconstruction. For all material types, poor mounting of the sample or mechanical drift of the sample stage could cause a variation in this effective position. However, these effects are usually negated by strong sample mounting and the fact that the ratio of the slice thickness/slice milling time is usually larger than the nominal mechanical drift rate. In the case of the highly insulating SiAlON samples studied in this project, an initial observation of beam deflection due to local electrostatic charging suggested that some method of ion-beam position checking and re-alignment would be required in order to maintain the consistency of slice thickness. For this purpose, a pair of reference markers, crosses, were initially milled out of the RoI and images of them recorded. Prior to the milling of each slice, the script acquired an ion beam secondary electron image and utilized image recognition to assess the strength of the beamshift drift-correction to be applied. As the volume of the slices to be milled was large a relatively high ion beam current, 3.0 nA, was employed. Repeated imaging of the crosses using such a large beam current resulted in gradual erosion so a method of periodically updating the reference images was also employed. The effectiveness of the drift-correction procedure and resulting quality of the slicing was analyzed by forming image stacks from both the uncorrected and drift corrected ion in-

duced secondary electron images (I-SE images) as presented in the Experimental Methods chapter. The stack of I-SE images was also used to check the variation in thickness of the milled slices (this is critical to the spatial resolution of the reconstruction along the slicing direction).

Considering the duration of each experiment (typically twelve to fifteen hours) and the presence of charging effects, a drift of the scanning electron beam can also occur. Introducing markers, the traditional technique for correcting this drift, was not possible in this study as milling these references would change local stress fields. During the serial sectioning procedure it was observed that the level of drift of the E-SE images was small enough that it could be corrected for later in post-processing of the E-SE image stack. Therefore, drift-correction of the E-SE images was not automatically performed during FIB tomography in order to reduce the overall run time. Furthermore, the focus of the electron beam was automatically adjusted to compensate for the slight increase in working distance that occurs as the cross-section face is sequentially milled.

The last issue to be overcome concerned the accumulation of negative charges on the material during FIB tomography. In fact, the slice milling and imaging procedure inflicts first positively charged ions then negatively charged electrons upon the cross-section face. While the charges are indeed opposite it would not be expected that they should cancel each other out. During FIB tomography, a problematic linear increase in brightness was observed to occur. This resulted in saturation of areas of the E-SE images, obscuring both microstructural and crack features, in the latter part of the serial sectioning sequence. To deal with this, two E-SE images were acquired per slice, the first using the detector amplifier conditions (contrast and brightness) set at the start of the run and the second utilizing a compensating brightness reduction. The magnitude of the brightness reduction was empirically determined over several sectioning runs and applied as a linear correction with slice number. This automated reduction of brightness has successfully avoided obscuration of image features due to saturation.

The fully automated slice&view experiment using FIB developed in this project has enabled the study and reconstruction of 3D crack structure following an indentation in a highly insulating ceramic material. This new method minimizes charging effects and corrects electron and ion beams drifts. It also enables the reconstruction of the microstructure and of the crack pattern as well as the calculation of the total crack surface area.

5.3.3 Influence of FIB process on indentation cracks

This work has also investigated the influence of the FIB process on the total indentation crack area. This influence can be noticed by three observations: the fact that some cracks have opened on the platinum layer which has been deposited after the indentation test, the presence of the same dominant crack patterns in all 3D reconstructions and the significant difference in crack density found between the first and the second half of the indents studied during FIB tomography. The change induced in existing stress fields by the ion beam during a slice&view experiment has already been described by Inkson et al. [118] and Elfallagh et al. [125, 120] in several publications. According to their work on soda-lime-silicate-glass, creation of new free surfaces during FIB tomography induces a relief of existing stresses. This stress relief leads to the opening of new cracks or to the closing of existing cracks. This interpretation has been checked using the Finite Elements model of indentation developed in Trinity College Dublin. Simulations of material removal process using the ion beam have shown that when removing material in the first part of the indent, the new FIB cut surface induces a relaxation of the high compressive stresses remaining from indentation, thus opening new cracks. On the contrary, when FIB tomography starts the second half of the indent, a considerable part of the compressive zone has already been removed which can lead to a reduction of the stressed environment in the second half of the indent. This in turn has lead to the closing of some cracks in this reduced stress environment and explains the observed reduction in crack density in the second half of the indent studied. Therefore during unidirectional tomography, in the first half of the indent more cracks are observed than in the second half. This result also explains why the number and size of the cracks observed in the first half will be bigger than the number and size of the cracks resulting only from the indentation process. On the contrary, the number and size of the cracks observed in the second half of the indent will be lower than the number and size of the cracks only due to indentation.

Another phenomenon can influence the density of cracks observed. Material removed by the ion beam can be sputtered into existing cracks [118, 119, 125, 120], masking their presence if the cracks are small. This will accentuate the difference observed in the density of cracks between the two halves of the indent as cracks in the second half are already smaller due to the stress relief previously described.

The work done by Inkson et al. [118] tends to confirm the explanations above. They have noticed that when FIB trenches are cut simultaneously on two opposite sides of an indent, they observe the same crack density on the two opposite cross-

sections.

The fact that dominant cracks are observed in the first half of all indents (a partial half-penny crack emanating from the indent corner where the FIB tomography begins, few shallow or deep lateral cracks and one or two shallow radial cracks) regardless of the microstructure also indicates that these cracks may largely be due to the FIB process which relaxes existing stresses in the first half of the indent studied.

The influence of the FIB on indentation cracks may be significant. However, there are variations observed in crack patterns and in the total crack surface area depending on the indent studied. This means that cracks observed during 3D reconstruction are not all due to the FIB process and are therefore coming from the indentation test. As FIB sputtering induces changes in residual stress fields, one might expect existing cracks to undergo an alteration of their topography, length and width of opening. However, Elfallagh et al. [120] found good correspondence between the major crack morphologies investigated with the FIB and the ones identified using optical methods. This result tends to indicate that the influence of FIB processing on indentation cracks would be mainly on their length and width of opening but more experiments are needed to check this assumption.

Despite the change induced by FIB tomography on the total indentation crack area and therefore on the calculated crack surface area, there is still a strong correlation found between the variation of plastic energy with indentation load and the variation of total crack surface area with load. A possible explanation is that the intensity of the stress fields remaining after indentation is proportional to the load applied. If the change in crack surface area due to the FIB process is also proportional to the intensity of the stress fields then this change would also be proportional to the load applied. In this case, the variation of the crack surface area calculated from 3D reconstruction with the load applied will be proportional to the surface area of cracks only issued from the indentation test. This would mean that by applying a scaling factor for the influence on the FIB on the curve of variation of the calculated total crack surface area with the load applied, we would access the true variation of the indentation crack surface area with load, before invasive FIB sectioning.

In order to check this hypothesis, future work is needed to quantify indentation residual stresses at different loads and to check if these two values are proportional. The change in crack surface area due to the FIB process should also be quantified as well as its variation with residual stress fields. This would quantify precisely the influence of FIB tomography on crack surface area calcu-

lated from 3D reconstructions. It would also identify the cracks opened mainly during the FIB process.

Nevertheless, this new technique accesses both quantitative (total crack surface area and its link to plastic energy) and qualitative information (localization and shape of subsurface cracks). In the case of Syalons 101 and 050 where there was a good contrast between phases, this technique has also permitted to study crack-microstructure interactions.

With some additional work on the technique (to find a way to measure texture during FIB tomography for instance) and on other materials of different microstructures, this technique could then be a useful tool for the development of materials more resistant to fracture.

5.4 Relevance of indentation technique in the study of fracture properties

In the characterization of small scale fracture in ceramics where failure mechanisms are often different from the ones at bulk level, classic tests done at the macro level like Single-Edge V-Notched Beam (SEVNB) or Chevron Notched Beam (CNB) are not applicable. Therefore, measuring small scale fracture properties of ceramics is a critical issue and indentation could help to sort of this problem. In fact, indentation is a non-destructive technique as it only requires a small volume of material. It is also very suitable to test materials at the microscale and this test is close to wear processes. Some studies have pointed out issues existing about the relevance of the indentation technique and in particular of the ICL method in the determination of fracture resistance of ceramics [67, 153]. It is true that contrary to standardized fracture toughness tests (like SEVNB or CNB) which are based on the rapid propagation of a single well-defined crack, indentation test produces a complex three-dimensional crack system with interacting cracks. Moreover, after indentation, the material is left with significant residual stresses and damage around the cracks. These complex residual stress fields are dependent on the indentation load and on the microstructure in the case of ceramics. This study has confirmed that the use of the ICL method was not relevant in the calculation of fracture resistance at small scale in ceramics (cf. section 5.3) but it has also pointed out the fact that indentation might still be of interest in the determination of fracture resistance of those ceramics (cf. section 5.3.1). In fact, indentation technique allows the investigation of the effect of the indenter shape on stress fields. When used with FIB tomography it enables the

study of crack patterns and crack localization and can also be used to study the effect of microstructure and composition on crack patterns and fracture behavior. Finally, the existing correlation between indentation energy and the total crack surface area is of great interest in order to estimate small scale fracture resistance of ceramics.

5.4.1 Variation of the stress fields through the indenter shape

This work has shown that indentation is an interesting technique to vary the stress fields and then look at the corresponding material response. In fact, it is possible to vary the stress fields through a variation in the indenter geometry and thus look at different situations. The use of the customized tip has permitted the increase in plastic energy during an indentation test, the elastic energy remaining the same. The total crack surface area calculated from 3D reconstruction was bigger with the customized tip than with the Vickers and there were also more cracks close to the surface. This means that fracture resistance of Syalon 101 was probably lowered by the use of the sharper customized tip. Different geometries of the indenter represent different shapes of a wear particle. A wear particle is usually a grain pulled out which remains on the material surface and acts as a small indenter. These experiments with the customized tip suggest that it may be better to use equiaxed grains so that if they are pulled out, they will act more as a Vickers than a customized tip and therefore cause less damage to the material.

5.4.2 Access to crack size distribution and crack localization when in combination with FIB tomography

The combined indentation-FIB tomography approach has shown its usefulness in the investigation of subsurface fracture. Crack size distribution and crack localization are two parameters which can be determined using FIB tomography. These parameters are crucial to characterize small scale fracture and can be assessed with great accuracy during FIB tomography. 3D reconstruction of the crack patterns also allows quantification of crack surface area inside the indented volume.

5.4.3 Study of the effect of microstructure and composition on crack patterns and cracking behavior

Another interest of the combined indentation-FIB tomography technique concerns investigations on the influence of microstructure on fracture properties of materials. FIB tomography also allows investigation of crack-microstructure interactions and different microstructures can be tested and the corresponding crack patterns investigated in order to design materials more resistant to fracture.

5.4.4 Access to total crack surface area through indentation energy

More importantly, indentation tests give an easy access to the energy dissipated during indentation and this energy might be related to fracture behavior of the material. In the case of ceramics experiencing few dislocation movements and densification mechanisms, plastic energy calculated from indentation tests can be linked to energy dissipated through fracture. This study has shown a strong correlation between W_p and the total crack surface area, both values following the same variations with the maximum indentation load. It might thus be possible to estimate the total crack surface area through an indentation test although there is still a need to quantify the relationship between W_p and the total crack surface area for the materials studied.

Accessing total crack surface area as well as crack distribution and sizes would determine small scale fracture behavior of these ceramics. This work has used FIB tomography to assess crack size distribution and crack location (deep cracks or cracks close to the surface) but a more practical method is needed as FIB tomography can't be used routinely. The influence of the FIB process on total indentation crack area cannot also be neglected. Further work is needed in order to see if these parameters (localization of cracks and crack size distribution) can be assessed through an indentation test, maybe through variations of local properties like E and H. Nevertheless, this project has shown that the indentation technique promises to reveal the exact mechanisms which contribute to the fracture resistance of ceramics.

Chapter 6

Conclusions

The growing use of ceramic devices in MEMS and biomaterials has led to new difficulties in the characterization of fracture properties of these materials at the microscale. Wear for instance is a huge issue for biomaterials as small particles pulled out from the material will remain on the specimen surface, induce more damage to the material and cause inflammatory responses. Classic methods which are accurate to determine fracture toughness at the macroscale are inappropriate to estimate local fracture properties which are decisive at the microscale. Indentation, which is a technique often performed to simulate wear process, can access local properties like hardness and Young modulus. In fact, this project has shown that in both alumina and SiAlONs, local E and H measured by indentation were different from bulk properties in the range of loads investigated. This study also aimed to check if indentation was a relevant technique to assess small scale fracture properties. In order to investigate this, a study of subsurface cracks was implemented. However, accessing subsurface cracks created during indentation is a challenging issue as classical methods (described in the literature review) considerably alter post-indentation cracks. A new method was therefore proposed and tested in this project on alumina, Syalon 101 and Syalon 050. The new technique developed in this project is based on FIB tomography and overcomes issues arising from dealing with highly insulating materials. It also enables the study of subsurface cracks with minimal damage to the original cracks resulting from indentation. The combined indentation-FIB tomography approach presented in this project has permitted the study of fracture properties of alumina and Syalons 101 and 050 at the microscale.

6.1 Main results

In summary, the main findings of this work are:

- The strong influence of local microstructure on local E and H which considerably differ from bulk properties.

- The inaccuracy of the ICL method to characterize fracture resistance in the ceramics investigated (alumina and Syalons) at the microscale. In all cases, fracture surface calculated by the ICL method is considerably different from the actual crack surface area and actual crack patterns completely differ from idealized crack patterns. Furthermore, significantly large amounts of subsurface cracks form when there is no observed surface cracks.

- A strong correlation found between the plastic energy dissipated through indentation and the total crack surface area measured underneath the indent site for the two materials studied and for the two different indenters. This result indicates that indentation might be a relevant test in the study of small scale fracture as this technique can capture the total crack surface area which is one important local fracture property.

- Concerning crack size distribution, the presence of a threshold in the maximum indentation load applied for the two materials investigated. Below this threshold, there is a significant number of subsurface microcracks. This microcracking is not taken into account in any classical model but needs to be assessed when looking at fracture resistance of the material. Above this threshold, coalescence of microcracks occurs to form larger cracks which are influenced by dominant stress fields even if they are locally deflected by local stress fields. These larger cracks represent the majority of the total crack surface area and therefore will determine the material resistance to fracture. This study has revealed that fracture process would be easier in Syalon 050 than in Syalon 101 on the range of loads investigated.

- The development of a new FIB-SEM imaging technique. This technique can be applied to other insulating brittle materials in the study of subsurface cracks following indentation or scratch tests.

- The usefulness of the combined approach indentation - FIB tomography - 3D reconstruction. First, it enables the study of subsurface crack size distribution and localization. Second, this technique allows the study of crack-microstructure interactions and can be used to test different microstructures

in order to design materials more resistant to fracture. Toughening mechanisms like crack deflection and crack bridging were visible in the case of Syalons 101 and 050 where there was a good contrast between the different phases.

6.2 Limitations

There are two main limitations to the findings of this work. The first one is the influence of FIB processing on the indentation crack surface area. By releasing some indentation residual stress fields, FIB tomography leads to the opening of new cracks or to the closing of existing cracks. This phenomenon has an influence on the calculated crack surface area, although the extent of this influence is unclear. However the FIB still represents an advance in the techniques used to investigate subsurface cracks as it induces less changes to indentation cracks than other methods.

The second limitation lies in the assumption that plastic energy from indentation is only due to fracture. In this study, the energies dissipated through densification and through dislocation movements have been neglected compared to the energy dissipated through fracture for the two materials studied (Syalons 101 and 050) but this might not be possible for other materials or in a different range of indentation loads.

6.3 Future work

A significant influence of FIB tomography on the total post-indentation crack area has been identified and has highlighted the need of additional work on this technique in order to use it as a relevant tool to investigate fracture behavior of ceramics at small scale. Future work is needed to quantify indentation residual stresses at different loads as well as changes in those residual stress fields with the FIB process. It would then be possible to estimate the area of cracks opened or closed during the FIB process and therefore to assess the original crack surface area coming from the indentation process. From this, it would be possible to quantify the relationship between the plastic energy and the total crack surface area.

This detailed work has established the importance of assessing subsurface crack patterns. However, the FIB technique used in this study is not suitable for a routine use. Additional work is therefore needed on this technique in order to find

another method to assess subsurface crack size distribution and crack localization more easily, maybe through correlations with variations in local parameters like E and H.

Finally, this indentation-FIB tomography-3D reconstruction technique could be a useful tool for the development of materials more resistant to fracture. Additional work on materials of different microstructures is needed in order to understand and quantify the interactions between microstructure and fracture process in ceramics at the microscale.

This project has shown that indentation was a relevant technique to access local fracture properties. With further developments, this technique could be a useful tool in the determination of fracture resistance of ceramics at the small scale.

Bibliography

1. Walraven, J. A. volume Vol.1 of *Proceedings. International Test Conference 2003 (IEEE Cat. No.03CH37494)*, 828–33 (IEEE, Charlotte, NC, USA, 2003).

2. Lawn, B. R. *Journal of Materials Research* **19**(1), 22–29 (2004).

3. Nemeth, N. N. *CARES/Life Used for Probabilistic Characterization of MEMS Pressure Sensor Membranes.* NASA, Glenn Research Center, (2002).

4. Liew, L.-A., Zhang, W., An, L., Shah, S., Luo, R., Liu, Y., Cross, T., Dunn, M. L., Bright, V., Daily, J. W., Raj, R., and Anseth, K. *American Ceramic Society Bulletin* **80**(5), 25–30 (2001).

5. Sedel, L. and Janot, C. *Biomatériaux.* INSERM - Faculté de Médecine Lariboisière - Paris, (1997).

6. Nix, W. D. and Gao, H. *Journal of the Mechanics and Physics of Solids* **46**(3), 411–425 (1998).

7. Peng, Z., Gong, J., and Miao, H. *Journal of the European Ceramic Society* **24**(8), 2193–2201 (2004).

8. Ren, X. J., Hooper, R. M., Griffiths, C., and Henshall, J. L. *Journal of Materials Science Letters* **22**(15), 1105–1106 (2003).

9. Zhang, T.-Y., Xu, W.-H., and Zhao, M.-H. *Acta Materialia* **52**(1), 57–68 (2004).

10. Tho, K. K., Swaddiwudhipong, S., Hua, J., and Liu, Z. S. *Materials Science and Engineering: A* **421**(1-2), 268–275 (2006).

11. Kreuzer, H. G. M. and Pippan, R. *Acta Materialia* **55**(9), 3229–35 (2007).

12. Mirshams, R. A. and Parakala, P. *Materials Science and Engineering A* **372**(1-2), 252–260 (2004).

13. Krell, A. *Materials Science and Engineering A (Structural Materials: Properties, Microstructure and Processing)* **A245**(2), 277–84 (1998).

14. Armstrong, R. W. volume 19 of *Int. J. Refract. Met. Hard Mater. (UK)*, 251–5 (Elsevier, Ixtapa, Mexico, 2001).

15. Armstrong, R. W. and Cazacu, O. *International Journal of Refractory Metals and Hard Materials* **24**(1-2), 129–134 (2006).

16. Carlton, C. E. and Ferreira, P. J. *Acta Materialia* **55**(11), 3749–3756 (2007).

17. Anstis, G. R., Chantikul, P., Lawn, B. R., and Marshall, D. B. *Journal of the American Ceramic Society* **64**(9), 533–8 (1981).

18. Middlemiss, S. and King, R. P. *International Journal of Mineral Processing* **44-45**, 43–58 (1996).

19. Steinbrech, R. W. *J. Eur. Ceram. Soc.* **10**, 131–42 (1992).

20. Quinn, J. B., Sundar, V., and Lloyd, I. K. *Dental materials : official publication of the Academy of Dental Materials* **19**(7), 603–611 (2003).

21. Chantikul, P., Bennison, S. J., and Lawn, B. R. *Journal of the American Ceramic Society* **73**(8), 2419–27 (1990).

22. Tomaszewski, H., Boniecki, M., and Weglarz, H. *Journal of the European Ceramic Society* **20**(14-15), 2569–74 (2000).

23. Tomaszewski, H., Boniecki, M., and Weglarz, H. *Journal of the European Ceramic Society* **21**(8), 1021–6 (2001).

24. Mencik, J. and Swain, M. V. *Journal of Materials Research* **10**(6), 1491–501 (1995).

25. Gong, J., Peng, Z., and Miao, H. *Journal of the European Ceramic Society* **25**(5), 649–54 (2005).

26. Green, D. J. *An introduction to the mechanical properties of ceramics. 8.13: Fractography p266-269.* Cambridge : Cambridge University Press, (1998).

27. Green, D. J. *An introduction to the mechanical properties of ceramics. 8.4: Nucleation and formation of cracks p216-217.* Cambridge : Cambridge University Press, (1998).

28. Griffith, A. A. *The phenomena of rupture and flow in solids*, volume A221. Philosophical Transactions of the Royal Society of London, (1920).

29. Inglis, C. E. *Stresses in a Plate Due to the Presence of Cracks and Sharp Corners*, volume 55. Transactions of the Institute of Naval Architects, (1913).

30. Obreimoff, J. W. *The Splitting Strength of Mica*, volume A. Proceedings of the Royal Society of London, (1930).

31. Irwin, G. *Fracturing of metals, ASM Cleveland* (1948).

32. Barenblatt, G. I. *Advanced Applied Mechanics* **7** (1962).

33. Rice, J. R. *Journal of Applied Mechanics* **35**, 379–386 (1968).

34. Green, D. J. *An introduction to the mechanical properties of ceramics. 8.6: Stress intensity factor solutions p224-231.* Cambridge : Cambridge University Press, (1998).

35. Irwin, G. *Fracture Handbook of Physics*, volume 6. Springer, Berlin, (1958).

36. Green, D. J. *An introduction to the mechanical properties of ceramics. 8.10: Mixed mode fracture p247-248.* Cambridge : Cambridge University Press, (1998).

37. Rice, J. R. *J. Mech. Phys. Solids* **26**, 61–78 (1978).

38. Olagnon, C., Chevalier, J., and Pauchard, V. *Journal of the European Ceramic Society* **26**(15), 3051–3059 (2006).

39. Krell, A., Pippel, E., Woltersdorf, J., and Burger, W. *Journal of the European Ceramic Society* **23**(1), 81–9 (2003).

40. Green, D. J. *An introduction to the mechanical properties of ceramics. 8.11: Microstructural aspects of crack propagation p248-264.* Cambridge : Cambridge University Press, (1998).

41. Swanson, P. L., Fairbanks, C. J., Lawn, B. R., Mai, Y. W., and Hockey, B. J. *Journal of the American Ceramic Society* **70**(4), 279–289 (1987).

42. Bennison, S. J. and Lawn, B. R. *Acta Metallurgica* **37**(10), 2659–2671 (1989).

43. Chen, Y., Xu, H., Kibble, K. A., and Hall, R. *Materials & Design* **21**(5), 453–459 (2000).

44. *British Standards BSI 14425-1* (2003).

45. Gogotsi, G. A. *Ceramics International* **29**(7), 777–784 (2003).

46. Lawn, B. R. and Evans, A. G. *Journal of Materials Science* **12**(11), 2195–9 (1977).

47. Lawn, B. R., Fuller, E. R., and Wiederhorn, S. M. *Journal of the American Ceramic Society* **59**(5-6), 193–7 (1976).

48. Lawn, B. R. and Fuller, E. R. *Journal of Materials Science* **10**(12), 2016–24 (1975).

49. Boussinesq, J. *Application des potentiels l'tude de l'quilibre et du mouvement des solides lastiques.* Paris, France: Gauthier-Villars, (1885).

50. Burghard, Z. *Behaviour of glasses and polymer-derived amorphous ceramics under contact stress.* PhD thesis, Max-Planck-Institut für Metallforschung, Stuttgart, (2004).

51. Lawn, B. *Fracture of brittle solids. 8.1: Crack propagation in contact fields: blunt and sharp indenters p250-263.* Cambridge : Cambridge University Press, (1993).

52. Marsh, D. M. *Plastic Flow and Fracture of Glass*, volume 282. Proceedings of the Royal Society of London Series A - Mathematical and Physical Sciences, (1964).

53. Lawn, B. R., Evans, A. G., and Marshall, D. B. *Journal of the American Ceramic Society* **63**(9-10), 574–81 (1980).

54. Cook, R. F. and Pharr, G. M. *Journal of the American Ceramic Society* **73**(4), 787–817 (1990).

55. Hertz, H. *Miscellaneous papers by Heinrich Hertz*, volume 92. J. Reine Angew. Math., (1881).

56. Hagan, J. T. and Swain, M. V. *Journal of Physics D (Applied Physics)* **11**(15), 2091–102 (1978).

57. Lawn, B. R. and Swain, M. V. *Journal of Materials Science* **10**(1), 113–22 (1975).

58. Niihara, K., Morena, R., and Hasselman, D. P. H. volume 5 of *Fracture Mechanics of Ceramics*, 97–105 (Plenum Press, New York, NY, USA, Universal Park, PA, USA, 1983).

59. Palmqvist, S. *Method att bestamma segheten hos sproda material, sarskilt hardmetaller*, volume 141. Jernkontorets Ann., (1957).

60. Green, D. J. *An introduction to the mechanical properties of ceramics. 8.14: Contact-damage processes p269-278.* Cambridge : Cambridge University Press, (1998).

61. Marshall, D. B., Lawn, B. R., and Evans, A. G. *Journal of the American Ceramic Society* **65**(11), 561–6 (1982).

62. Ponton, C. B. and Rawlings, R. D. *Materials Science and Technology* **5**, 961–976 (1989).

63. Stevenson, A. N. J. and Hutchings, I. M. *Journal of Materials Science Letters* **15**(8), 688–690 (1996).

64. Evans, A. G. and Charles, E. A. *Journal of the American Ceramic Society* **59**(7-8), 371–2 (1976).

65. Liang, K. M., Orange, G., and Fantozzi, G. *Journal of Materials Science* **25**(1A), 207–14 (1990).

66. Harding, D. S., Oliver, W. C., and Pharr, G. M. volume 356 of *Materials Research Society Symposium - Proceedings*, 663–668 (Materials Research Society, Pittsburgh, PA, USA, Boston, MA, USA, 1995).

67. Quinn, G. D. and Bradt, R. C. *Journal of the American Ceramic Society* **90**(3), 673–680 (2007).

68. Solomah, A. G. volume 156 of *Ceramic Transactions*, 153–159 (American Ceramic Society, Nashville, TN., United States, 2004).

69. Petit, F., Vandeneede, V., and Cambier, F. *Materials Science and Engineering: A* **456**(1-2), 252–260 (2007).

70. Lemaitre, J. *Engineering Fracture Mechanics* **25**(5-6), 523–537 (1986).

71. Mazars, J. and Pijaudier-Cabot, G. *International Journal of Solids and Structures* **33**(20-22), 3327–3342 (1996).

72. Lee, U., Lesieutre, G. A., and Fang, L. *International Journal of Solids and Structures* **34**(33-34), 4377–4397 (1997).

73. Krajcinovic, D. and Fonseka, G. U. *Journal of Applied Mechanics* **48**(4), 809–815 (1981).

74. Zioupos, P. *Materials Science and Engineering: C* **6**(1), 33–40 (1998).

75. Oliver, W. C. and Pharr, G. M. *Journal of Materials Research* **7**(6), 1564–83 (1992).

76. Pharr, G. M. volume A253 of *Mater. Sci. Eng. A, Struct. Mater., Prop. Microstruct. Process. (Switzerland)*, 151–9 (Elsevier, Il Ciocco, Italy, 1998).

77. Hay, J. L. and Pharr, G. M. *Materials Park* , 232–243 (2000).

78. Oliver, W. C. and Pharr, G. M. *Journal of Materials Research* **19**(1), 3–20 (2004).

79. Fischer-Cripps, A. C. *Nanoindentation. Appendix 3: Common Indenter Geometries p191-194.* New York, N.Y. ; London : Springer, (2002).

80. Martin, M. and Troyon, M. *Journal of Materials Research* **17**(9), 2227–34 (2002).

81. Fischer-Cripps, A. C. *Surface and Coatings Technology* **200**(14-15), 4153–4165 (2006).

82. Sneddon, I. N. *International Journal of Engineering Science* **3**, 47–57 (1965).

83. ISO14577. *ISO Central Secretariat, 1 rue de Varembé, 1211 Geneva 20, Switzerland* (2002).

84. Bolshakov, A. and Pharr, G. M. *Journal of Materials Research* **13**(4), 1049–58 (1998).

85. Pharr, G. M., Bolshakov, A., Tsui, T. Y., and Hay, J. C. Thin-Films - Stresses and Mechanical Properties VII. Symposium, 109–20 (Mater. Res. Soc, Boston, MA, USA, 1998).

86. Tsui, T. Y., Oliver, W. C., and Pharr, G. M. *Journal of Materials Research* **11**(3), 752–9 (1996).

87. Zeng, K. and Chiu, C. H. *Acta Materialia* **49**(17), 3539–51 (2001).

88. Taljat, B. and Pharr, G. M. *International Journal of Solids and Structures* **41**(14), 3891–904 (2004).

89. Kese, K. O., Li, Z. C., and Bergman, B. *Journal of Materials Research* **19**(10), 3109–19 (2004).

90. Kese, K. O., Li, Z. C., and Bergman, B. *Materials Science and Engineering A (Structural Materials: Properties, Microstructure and Processing)* **404**(1-2), 1–8 (2005).

91. Kese, K. and Li, Z. C. *Scripta Materialia* **55**(8), 699–702 (2006).

92. VanLandingham, M. R. *Journal of Research of the National Institute of Standards and Technology* **108**(4), 249–265 (2003).

93. Shuman, D. J., Costa, A. L. M., and Andrade, M. S. *Materials Characterization* **58**(4), 380–389 (2007).

94. Krell, A. and Schadlich, S. *Materials Science and Engineering A (Structural Materials: Properties, Microstructure and Processing)* **A307**(1-2), 172–81 (2001).

95. Pharr, G. M., Harding, D. S., and Oliver, W. C. Size: 13 p. (, United States, 1992).

96. McGrouther, D. and Munroe, P. R. *Microscopy Research and Technique* **70**(3), 186–194 (2007).

97. Munroe, P. R. *Materials Characterization* **60**(1), 2–13 (2009).

98. Giannuzzi, L. A. and Stevie, F. A. *Micron* **30**(3), 197–204 (1999).

99. Reyntjens, S. and Puers, R. volume 11 of *J. Micromech. Microeng. (UK)*, 287–300 (IOP Publishing, Uppsala, Sweden, 2001).

100. Sugiyama, M. and Sigesato, G. *Journal of Electron Microscopy* **53**(5), 527–536 (2004).

101. Wirth, R. *Chemical Geology* **261**(3-4), 217–229 (2009).

102. Inkson, B. J., Wu, H. Z., Steer, T., and Mobus, G. Fundamentals of Nanoindentation and Nanotribology II. Symposium (Mater. Res. Soc. Symposium Proceedings Vol. 649), 7–7 (Mater. Res. Soc, Boston, MA, USA, 2001).

103. Moon, R. J., Xie, Z. H., Hoffman, M., Munroe, P. R., and Cheng, Y. B. volume 156 of *Ceramic Transactions*, 49–58 (American Ceramic Society, Nashville, TN., United States, 2004).

104. Steer, T. J., Mobus, G., Kraft, O., Wagner, T., and Inkson, B. J. Fundamentals of Nanoindentation and Nanotribology II. Symposium (Mater. Res. Soc. Symposium Proceedings Vol. 649), 3–7 (Mater. Res. Soc, Boston, MA, USA, 2001).

105. Schaffer, M., Wagner, J., Schaffer, B., Schmied, M., and Mulders, H. *Ultramicroscopy* **107**(8), 587–597 (2007).

106. Uchic, M. D., Groeber, M. A., Dimiduk, D. M., and Simmons, J. P. *Scripta Materialia* **55**(1), 23–8 (2006).

107. Holzer, L., Indutnyi, F., Gasser, P. H., Munch, B., and Wegmann, M. *Journal of Microscopy* **216**, 84–95 (2004).

108. Williams, R., Bhattacharyya, D., Viswanathan, G. B., Banerjee, R., and Fraser, H. L. *Microscopy and Microanalysis* **10**(SupplementS02), 1178–1179 (2004).

109. Claves, S. R., Bandar, A. R., Misiolek, W. Z., and Michael, J. R. *Microscopy and Microanalysis* **10**(SupplementS02), 1138–1139 (2004).

110. Kammer, D., Mendoza, R., Barnett, S. A., and Voorhees, P. W. *Microscopy and Microanalysis* **11**(SupplementS02), 72–73 (2005).

111. Williams, R. A., Uchic, M., Dimiduk, D., and Fraser, H. L. *Microscopy and Microanalysis* **12**(SupplementS02), 1234–1235 (2006).

112. Kato, M., Ito, T., Aoyama, Y., Sawa, K., Kaneko, T., Kawase, N., and Jinnai, H. *Journal of Polymer Science Part B: Polymer Physics* **45**(6), 677–683 (2007).

113. Matthijs De Winter, D., Schneijdenberg, C., Lebbink, M., Lich, B., Verkleij, A., Drury, M., and Humbel, B. *Journal of Microscopy* **233**(3), 372–383 (2009).

114. Wang, Y. Z., Revie, R. W., Phaneuf, M. W., and Li, J. *Fatigue and Fracture of Engineering Materials and Structures* **22**(3), 251–6 (1999).

115. Steer, T. J., Mobus, G., Kraft, O., Wagner, T., and Inkson, B. J. *Thin Solid Films* **413**(1-2), 147–54 (2002).

116. Xie, Z. H., Munroe, P. R., Moon, R. J., and Hoffman, M. volume 255 of *Wear (Netherlands)*, 651–6 (Elsevier, Netherlands, 2003).

117. Xie, Z. H., Munroe, P. R., McGrouther, D., Singh, R. K., Hoffman, M., Bendavid, A., Martin, P. J., and Yew, S. *Journal of Materials Research* **21**(10), 2600–2610 (2006).

118. Inkson, B. J., Leclere, D., Elfallagh, F., and Derby, B. *Journal of Physics: Conference Series* **26**(1), 219–22 (2006).

119. Elfallagh, F. and Inkson, B. J. *Journal of Physics: Conference Series* **126**, 1–4 (2008).

120. Elfallagh, F. and Inkson, B. J. *Journal of the European Ceramic Society* **29**(1), 47–52 (2008).

121. Holzapfel, C., Schaf, W., Marx, M., Vehoff, H., and Mucklich, F. *Scripta Materialia* **56**(8), 697–700 (2007).

122. Lube, T. *Journal of the European Ceramic Society* **21**(2), 211–18 (2001).

123. Xie, Z. H., Hoffman, M., Moon, R. J., Munroe, P. R., and Cheng, Y. B. *Journal of the American Ceramic Society* **87**(11), 2114–2124 (2004).

124. Wu, H. Z., Roberts, S. G., Mbus, G., and Inkson, B. J. *Acta Materialia* **51**(1), 149–163 (2003).

125. Elfallagh, F. and Inkson, B. J. *Journal of Microscopy* **230**(2), 240–251 (2008).

126. Munro, R. G. *Journal of the American Ceramic Society* **80**(8), 1919–28 (1997).

127. He, Z. and Ma, J. *Materials Science and Engineering A* **361**(1-2), 130–135 (2003).

128. Bae, I. J. and Baik, S. *Journal of the American Ceramic Society* **80**(5), 1149–1156 (1997).

129. Bae, S. I. and Baik, S. *Journal of Materials Science* **28**(15), 4197–204 (1993).

130. Fang, J., Thompson, A. M., Harmer, M. P., and Chan, H. M. *Journal of the American Ceramic Society* **80**(8), 2005–12 (1997).

131. Gavrilov, K. L., Bennison, S. J., Mikeska, K. R., and Levi-Setti, R. *Journal of Materials Science* **38**(19), 3965–72 (2003).

132. Ahn, J. H., Lee, J.-H., Hong, S.-H., Hwang, N.-M., and Kim, D.-Y. *Journal of the American Ceramic Society* **86**(8), 1421–3 (2003).

133. Lartigue-Korinek, S., Carry, C., and Priester, L. *Journal of the European Ceramic Society* **22**(9), 1525–41 (2002).

134. Park, C. W. and Yoon, D. Y. *Journal of the American Ceramic Society* **83**(10), 2605–2609 (2000).

135. Prendergast, I. D., Budworth, D. W., and Brett, N. H. *Transactions and Journal of the British Ceramic Society* **71**(1), 31–6 (1972).

136. Sato, E. and Carry, C. *Journal of the American Ceramic Society* **79**(8), 2156–60 (1996).

137. Tzing, W. H. and Tuan, W. H. *Journal of Materials Science Letters* **18**(14), 1115–17 (1999).

138. Voytovych, R., MacLaren, L., Gulgun, M. A., Cannon, R. M., and Ruhle, M. *Acta Materialia* **50**(13), 3453–63 (2002).

139. Hah, S. R., Fischer, T. E., Gruffel, P., and Carry, C. volume 181-183 of *Wear (Switzerland)*, 165–77, (1995).

140. Iio, S., Yamamoto, H., and Mitsuoka, T. volume 21 of *Ceramic Engineering and Science Proceedings*, 461–468 (American Ceramic Society, Westerville, OH, USA, Cocoa Beach, FL, USA, 2000).

141. Krefetz, S. B. and Fischer, T. E. *Wear* **211**(1), 141–145 (1997).

142. Rittidech, A., Portia, L., and Bongkarn, T. *Materials Science and Engineering A (Structural Materials: Properties, Microstructure and Processing)* **438-440**, 395–8 (2006).

143. Sathiyakumar, M. and Gnanam, F. D. *Ceramics International* **28**(2), 195–200 (2002).

144. West, G. D., Perkins, J. M., and Lewis, M. H. *Journal of the European Ceramic Society* **27**(4), 1913–18 (2006).

145. Touchefeu, S. (2008).

146. Lawn, B. R. and Marshall, D. B. *Journal of the American Ceramic Society* **62**(7-8), 347–350 (1979).

147. Chantikul, P., Anstis, G. R., Lawn, B. R., and Marshall, D. B. *Journal of the American Ceramic Society* **64**(9), 539–43 (1981).

148. Casellas, D., Caro, J., Molas, S., Prado, J. M., and Valls, I. *Acta Materialia* **55**(13), 4277–4286 (2007).

149. Kremer, J. R., Mastronarde, D. N., and McIntosh, J. R. *Journal of Structural Biology* **116**(1), 71–76 (1996).

150. Jiang, D., Thomson, K., Kuntz, Joshua, D., Ager, Joel, W., and Mukherjee, Amiya, K. **56**(11), 959–962 (2007).

151. Mijangos, I. *Scale effects in indentation fracture toughness measurements of brittle ceramics arising from crack-microstructure interactions.* PhD thesis, Trinity College Dublin, (2010).

152. Pharr, G. M. and Bolshakov, A. *Journal of Materials Research* **17**(10), 2660–71 (2002).

153. Ghosh, A., Kobayashi, A., Li, Z., Henager, C. J., and Bradt, R. *Technical report PNL-SA-16927* (1991).

154. Wang, Y. and Hsu, S. M. *Wear* **195**(1-2), 112–122 (1996).

155. Giannakopoulos, A. E. and Larsson, P. L. *Mechanics of Materials* **25**(1), 1–35 (1997).

156. Goldstein, J., Newbury, D., Joy, D., Lyman, C., Echlin, P., Lifshin, E., Sawyer, L., and J., M. *Scanning Electron Microscopy and X-ray Microanalysis.* Springer, New York, USA, (2003).

Appendix A
Characteristics of FIB tomographies performed

Table A.1: Characteristics of FIB tomographies performed.

Indents studied **3D reconstruction performed**	**Volume removed** **X (μm) * Y (μm) * Z (μm)**	**Ion beam** **current (nA)**	**Number** **of slices**	**Sectioning step** **size (nm)**
Syalon 101 V 500 mN	11 * 13 * 8	3.0	130	100
Syalon 101 V 1 N	20 * 25 * 8	0.92	250	100
Syalon 101 V 2 N	26 * 30 * 8	3.0	300	100
Syalon 101 V 5 N num7	50 * 55 * 10	6.5	220	250
Syalon 101 V 5 N num18	48 * 55 * 10	6.5	220	250
Syalon 101 V 5 N num20	40 * 45 * 10	3.0	450	100
Syalon 101 C 500 mN	16 * 17 * 8	3.0	170	100
Syalon 101 C 1 N	24 * 25 * 10	3.0	250	100
Syalon 101 C 2 N	30 * 37 * 10	3.0	370	100
Syalon 050 V 500 mN	16 * 17 * 8	3.0	170	100
Syalon 050 V 1 N	20 * 24 * 10	3.0	240	100
Syalon 050 V 2 N	30 * 33 * 12	3.0	330	100
Other indents studied				
Syalon 101 V 1 N	20 * 25 * 8	0.28	250	100
Syalon 101 C 1 N	25 * 26 * 10	2.8	260	100
Syalon 050 C 500 mN	16 * 17 * 8	3.0	170	100
Syalon 050 C 1 N	24 * 25 * 10	3.0	250	100
Syalon 050 C 2 N	30 * 37 * 10	3.0	370	100

V = Vickers indenter tip

C = customized indenter tip

Appendix B
Other views of the 3D reconstructions

Figure B.1: Top view of a 3D reconstruction of a Vickers indentation at 500 mN in Syalon 101. Each crack has been meshed and is represented with a different color. The surface is in green.

Figure B.2: Side view of a 3D reconstruction of a Vickers indentation at 500 mN in Syalon 101.

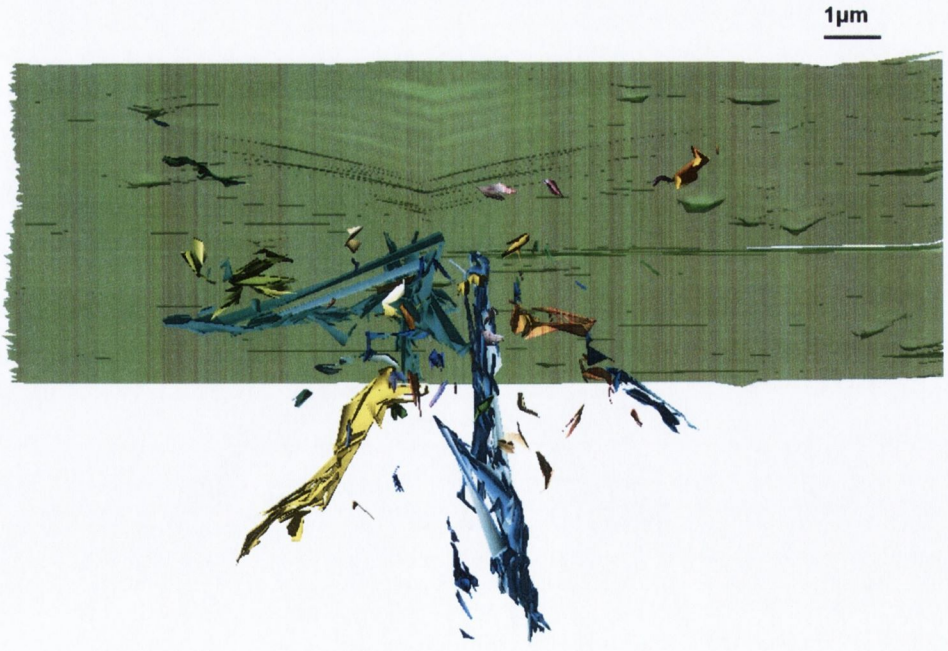

Figure B.3: Top view of a 3D reconstruction of a Vickers indentation at 1 N in Syalon 101.

Figure B.4: Side view of a 3D reconstruction of a Vickers indentation at 1 N in Syalon 101.

Figure B.5: Top view of a 3D reconstruction of a Vickers indentation at 2 N in Syalon 101.

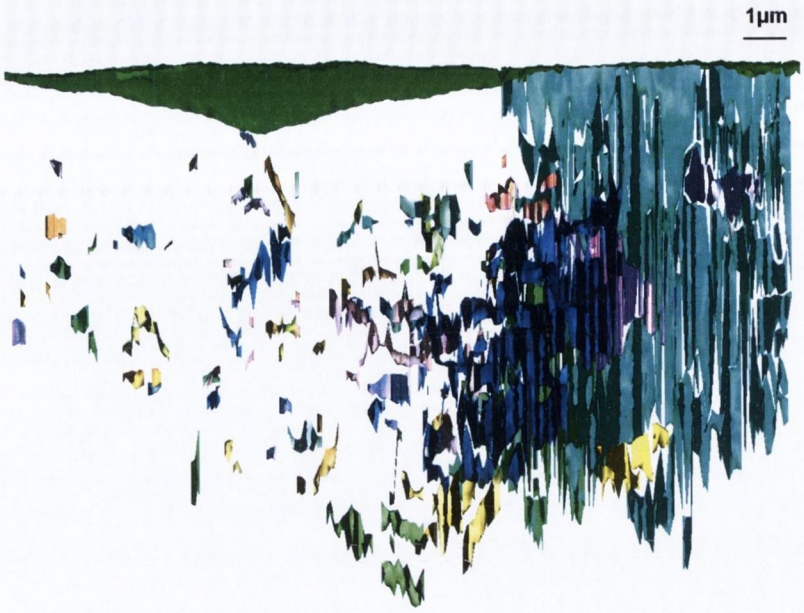

Figure B.6: Side view of a 3D reconstruction of a Vickers indentation at 2 N in Syalon 101.

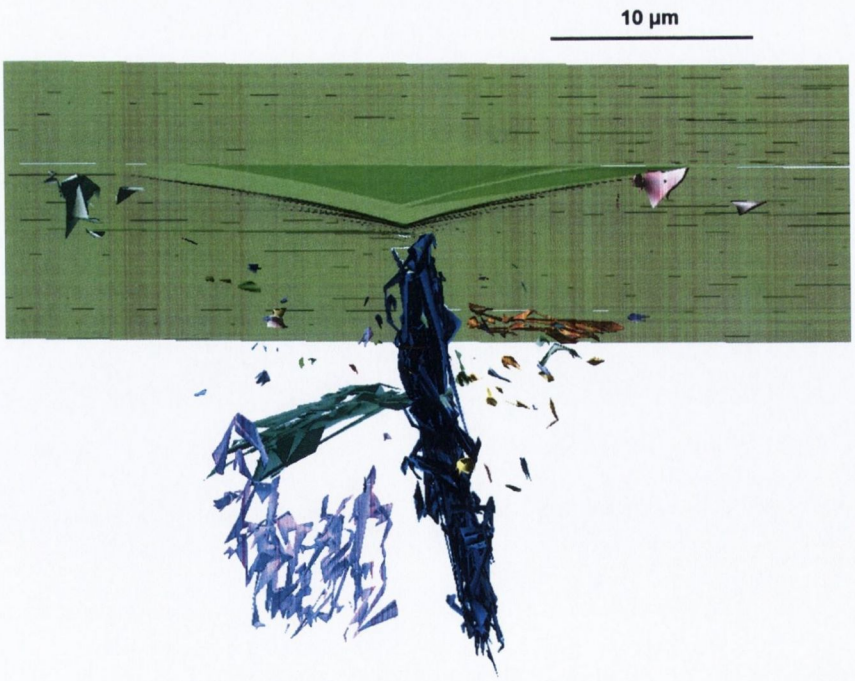

Figure B.7: Top view of a 3D reconstruction of a Vickers indentation at 5 N (indent num7) in Syalon 101.

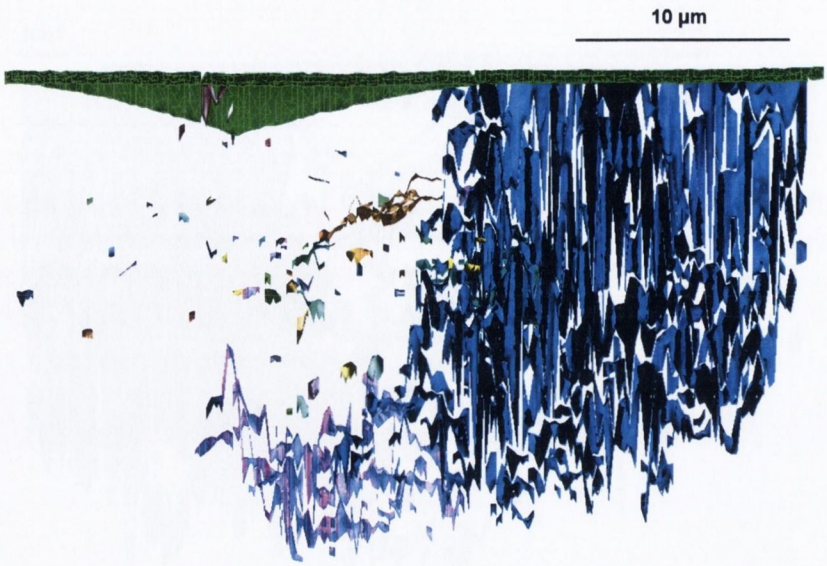

Figure B.8: Side view of a 3D reconstruction of a Vickers indentation at 5N (indent num7) in Syalon 101.

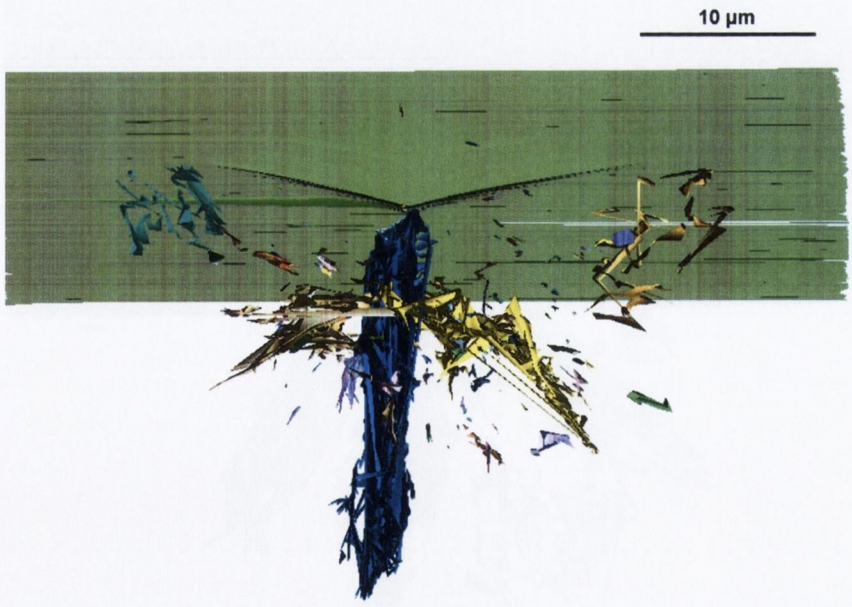

Figure B.9: Top view of a 3D reconstruction of a Vickers indentation at 5 N (indent num18) in Syalon 101.

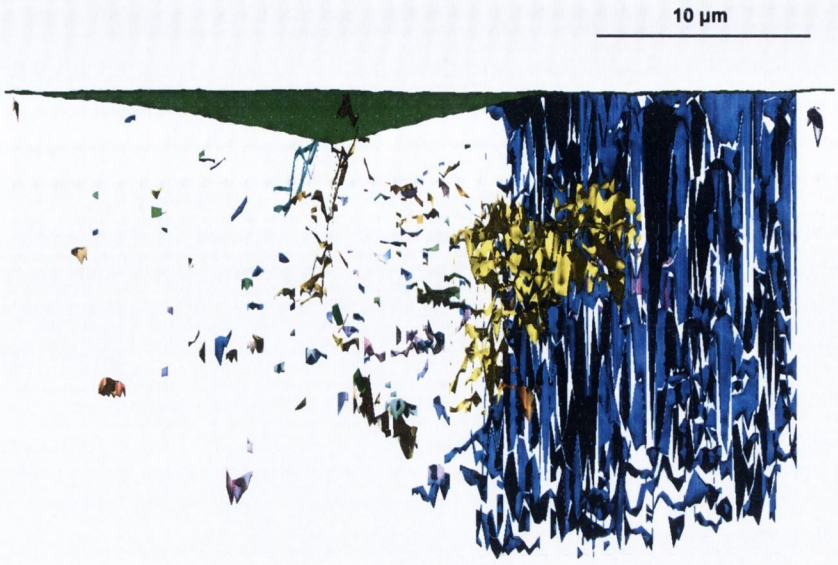

Figure B.10: Side view of a 3D reconstruction of a Vickers indentation at 5N (indent num18) in Syalon 101.

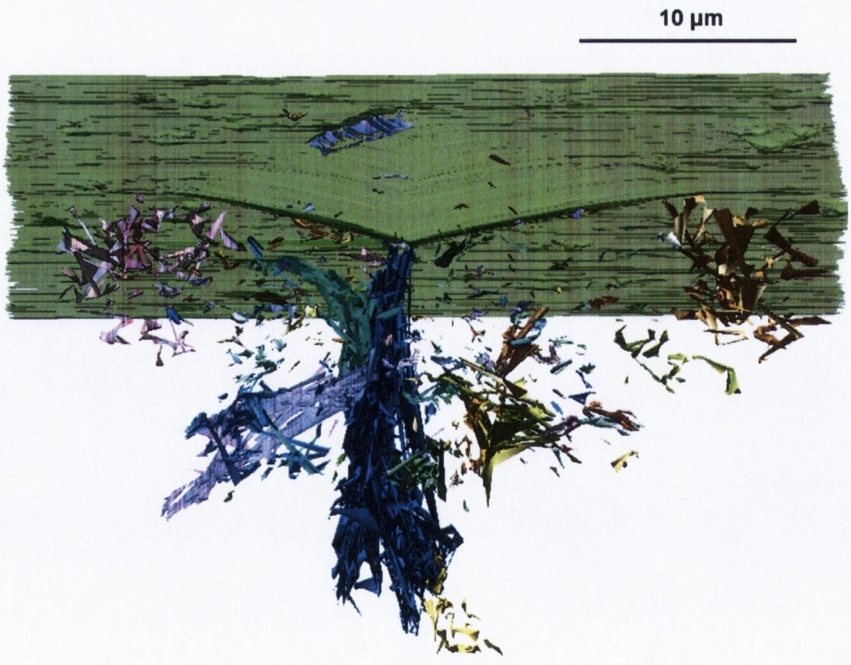

Figure B.11: Top view of a 3D reconstruction of a Vickers indentation at 5 N (indent num20) in Syalon 101.

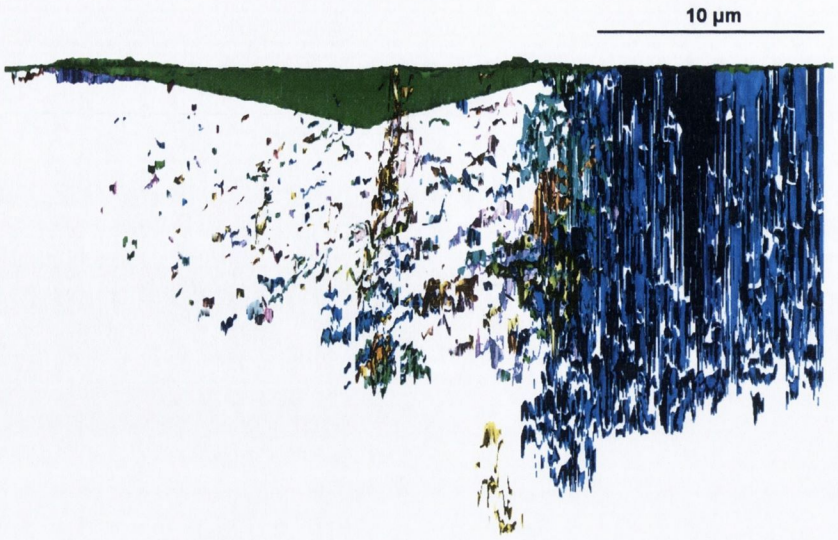

Figure B.12: Side view of a 3D reconstruction of a Vickers indentation at 5N (indent num20) in Syalon 101.

Figure B.13: Top view of a 3D reconstruction of an indentation performed with the customized tip at 500 mN in Syalon 101.

Figure B.14: Side view of a 3D reconstruction of an indentation performed with the customized tip at 500 mN in Syalon 101.

Figure B.15: Top view of a 3D reconstruction of an indentation performed with the customized tip at 1 N in Syalon 101.

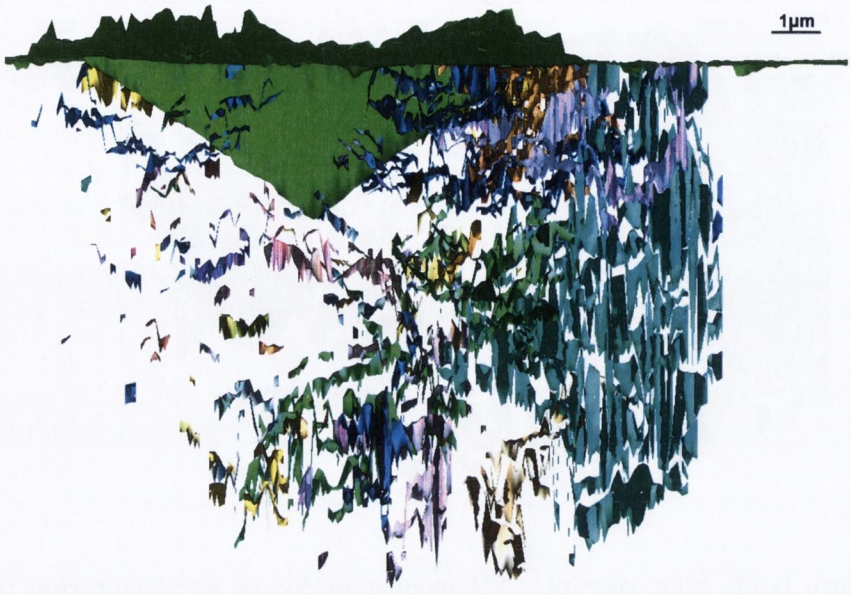

Figure B.16: Side view of a 3D reconstruction of an indentation performed with the customized tip at 1 N in Syalon 101.

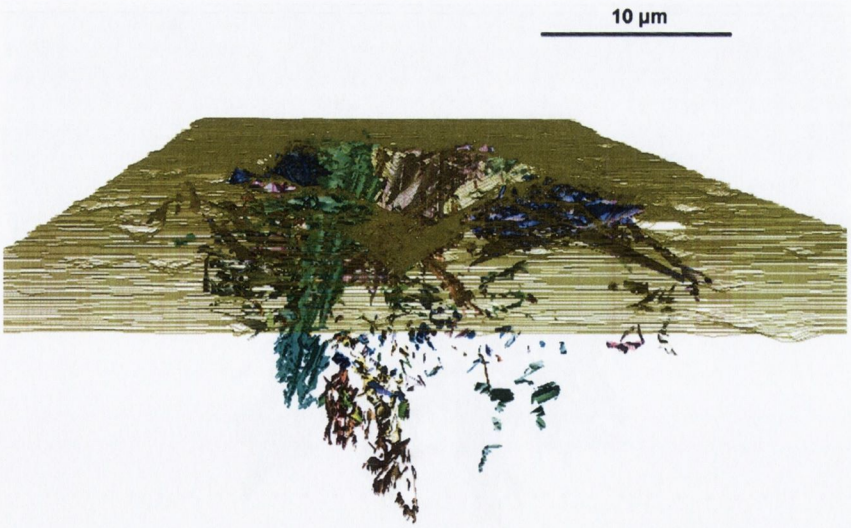

Figure B.17: Top view of a 3D reconstruction of an indentation performed with the customized tip at 2 N in Syalon 101.

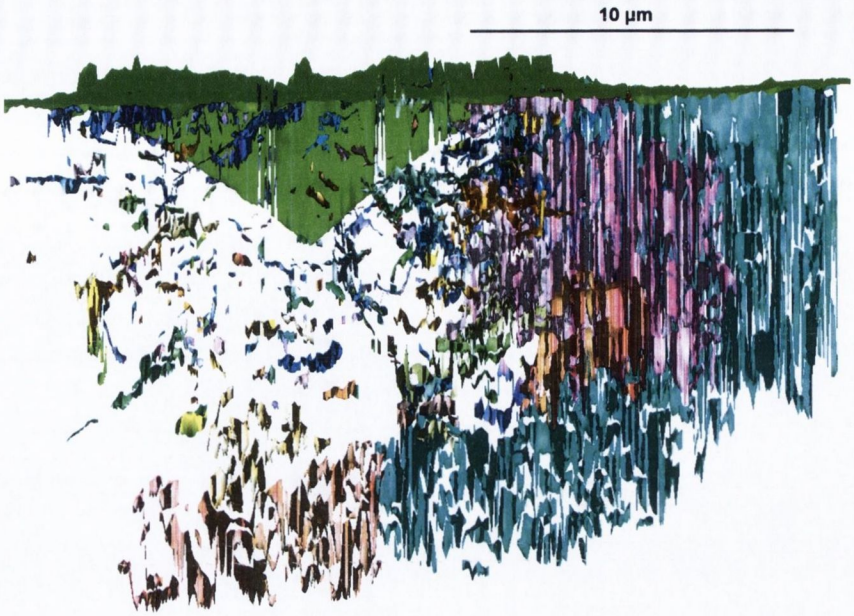

Figure B.18: Side view of a 3D reconstruction of an indentation performed with the customized tip at 2 N in Syalon 101.

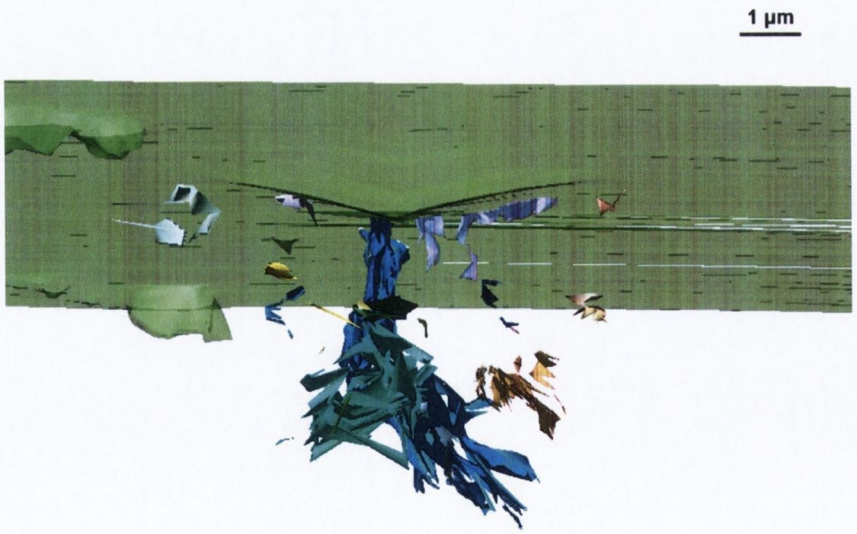

Figure B.19: Top view of a 3D reconstruction of a Vickers indentation at 500 mN in Syalon 050.

Figure B.20: Side view of a 3D reconstruction of a Vickers indentation at 500 mN in Syalon 050.

Figure B.21: Top view of a 3D reconstruction of a Vickers indentation at 1 N in Syalon 050.

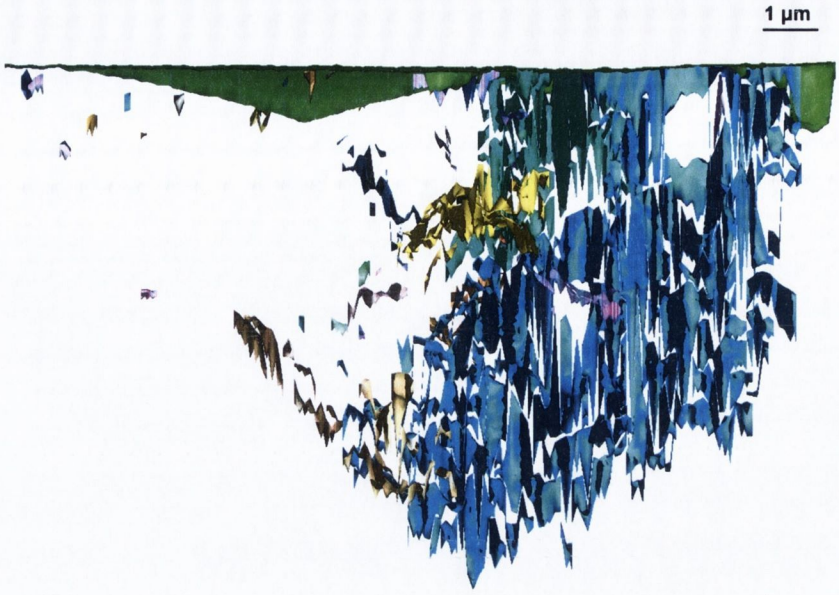

Figure B.22: Side view of a 3D reconstruction of a Vickers indentation at 1 N in Syalon 050.

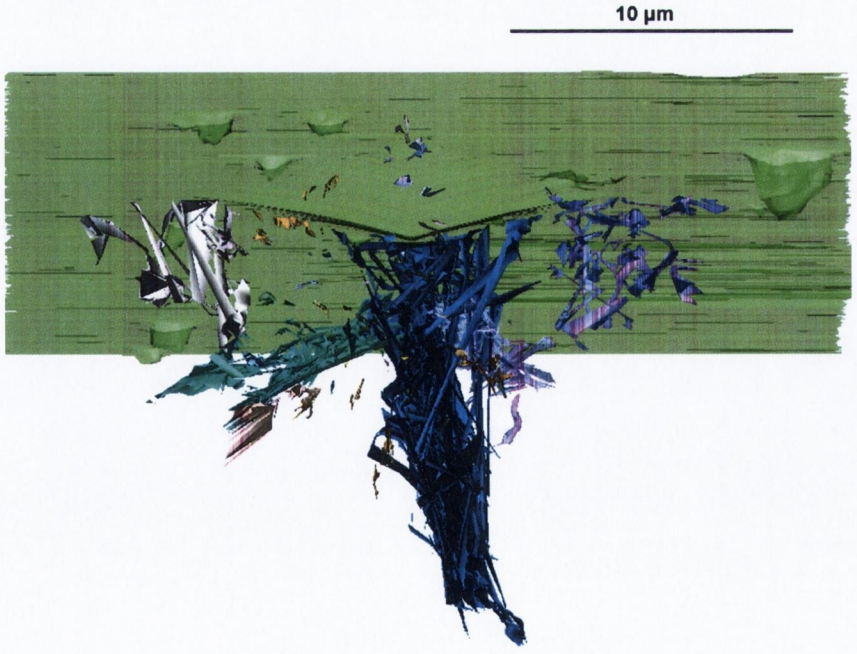

Figure B.23: Top view of a 3D reconstruction of a Vickers indentation at 2 N in Syalon 050.

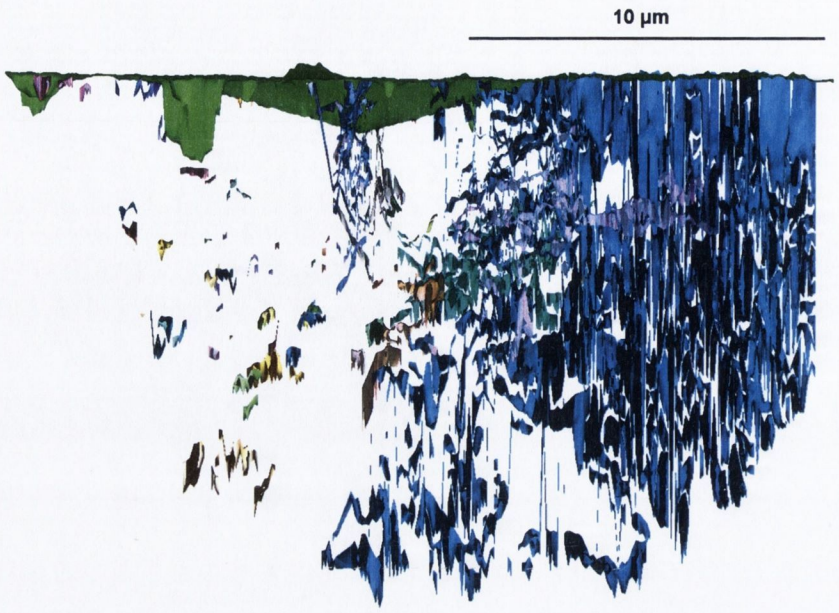

Figure B.24: Side view of a 3D reconstruction of a Vickers indentation at 2 N in Syalon 050.